BERTRAM

5th Numerical Towing Tank Symposium

29. September - 1. October 2002

Pornichet / France

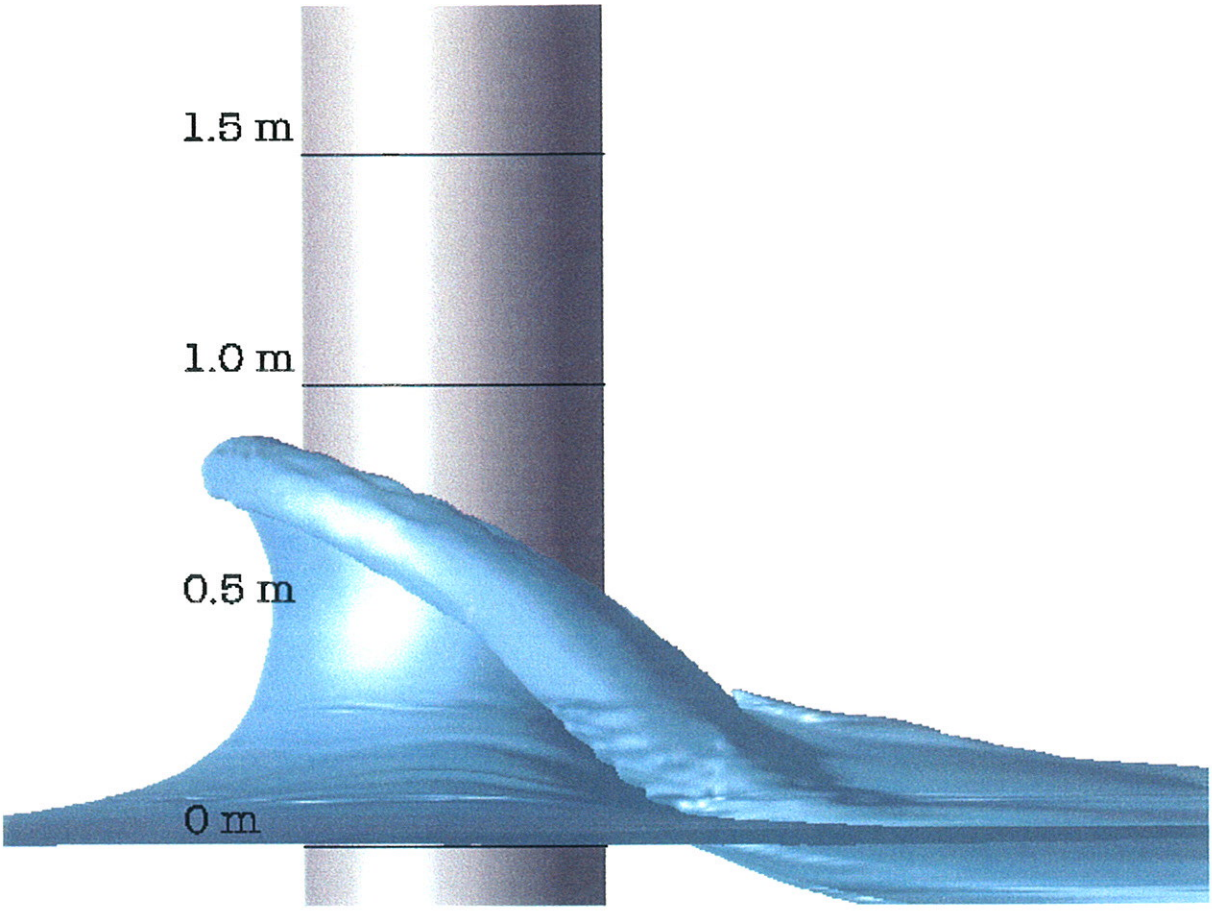

Gerard Delhommeau, Michel Visonneau (Ed.)

LABORATOIRE DE MECANIQUE DES FLUIDES - UMR 6598 DU CNRS
ECOLE CENTRALE DE NANTES
BP 92101
44321 NANTES CEDEX 3, FRANCE

Sponsored by

Office of Naval Research

CD adapco Group

Chantiers de l'Atlantique/Alstom

Région des Pays de la Loire

5^{th} Numerical Towing Tank Symposium, 29. September - 1. October 2002, Pornichet / France

Papers are ordered in alphabetical order of first author :

"Comparison between SPH and VOF Free Surface Flow Simulation"
Y. Andrillon, M. Doring, B. Alessandrini, P. Ferrant

"An Experimental Study on Water Shipping"
M. Barcellona, M. Greco, E. Pequinot, M. Landrini

"Modeling Appendages in RANSE Simulations of Aerodynamic Flows around Ship Superstructures"
V. Bertram, O. El Moctar, D. Schmode

"Forward Speed Effects on Diffraction-Radiation Computations"
J.P.Boin, M.Guilbaud, M.Ba

"Seakeeping Simulation of Fast Hard Chine Vessels using RANSE"
M. Caponnetto

"Numerical Simulation of 2-phase Flows by Smoothed Particle Hydrodynamics" Ⓧ
A. Colagrossi, M. Landrini

"Level-set Simulation of the Vortical Flow Generated by a Surface-piercing Body"
G. Colicchio, M. Landrini, J. Chaplin

"Investigations of Tip Vortex Cavitation Inception on Hydrofoils Deduced from Propeller Blades"
F. Deniset, V. Navaza, J.Y. Billard, F. Hauville

"Unsteady Navier-Stokes Equations : A Fully Coupled Method for Unstructured Meshes"
E. Didier, B. Alessandrini

"Shape Optimization in a Complex Numerical Framework : Advances and Limitations"
R. Duvigneau , M. Visonneau

"A New Potential /Ranse Approach for Water Wave Diffraction"
P. Ferrant, L. Gentaz, D. Le Touzé

"Unstructured Multigrid Method for Ship Flows"
T.Hino, N. Hirata

"Numerical Simulation of Propeller-Rudder Interface"
J-M. Laurens, F. Grosjean

"RANSE Simulations for Cavitating Hydrofoils"
O. Lindenau., H. Streckwall, V. Bertram

"Numerical Investigation of Viscous Flow around Costa Bulbs"
L. Luebke

"Towards Ship Performance Improvement Using mode FRONTIER"
J.J. Maisonneuve

"Development of an Unstructured Pressure-Correction Solver Based on Triangle Meshes"
T. Mikkola

"Farfield Dispersive Waves and the Radiation Condition"
F. Noblesse, C. Yang

"Numerical Simulation of Ship Flows under Self-Propulsion Condition with Contrarotating Propellers"
K. Ohashi, N. Hirata, T. Hino

"The Role of Transition on the Performance Characteristics of Hydrofoils"
V. Papakonstandinou, G. Tzabiras, S. Voustinas

"An Adaptative Quadtree Surface Marker Method for Fully Non-Linear Wave Simulations"
C. Santos, D. Greaves

"Investigation of Two-Dimensional Transom Waves Using Inviscid and Viscous Free-Surface Boundary Conditions at Model and Full-Scale Ship Reynolds Numbers"
J. Schweighofer

"Study of Three RANS Body Force Propeller Models"
C. D. Simonsen, J. Cross-Whiter

"Planing Boat in Waves"
H. Soeding

"Resistance and Self-Propulsion Factors Prediction for Practical Ship Hulls by CFD"
N. Takada, T. Hoshino, S. Ishikawa, S. Higaki

"Domain Decomposition with Implicit Coupling and Non-Matching Grids"
A. van der Ploeg

"Verification of Navier-Stokes Solutions - a Study on an Analytical Test Case"
S. Werner, B. Regnström, L. Larsson

"An Approach of Ship Manoeuvring by Simultaneous Computation of Viscous Flow and Ship Motion"
Y. Xing, G. Jensen, I. Hadzic, M. Peric

Comparison between SPH and VOF Free Surface Flow Simulation

Y. Andrillon, M. Doring, B. Alessandrini, P. Ferrant
Laboratoire de Mécanique des Fluides
Ecole Centrale de Nantes-CNRS
yann.andrillon@ec-nantes.fr

1 Introduction

The free surface flow simulation sees its limits unceasingly pushed further. One of the last great difficulty in this domain has been the problem of reconnections of interfaces, occurring in flows with breaking waves. Within the last ten years, with the advent of the free surface capturing methods initiated by Hirt & Nicholls[6] the numerical solution of these flows has become possible. Nevertheless, an other approach has been recently introduced to simulate this kind of flow. This approach, named 'Smooth Particles Hydrodynamics", comes from the astrophysics. Monaghan[9] first applied it to free surface flows. This method is really different from both free surface capturing and free surface tracking methods, indeed it is an meshless and lagrangian approach. Thus it is more versatile in the simulation of complex flows. During the NuTT's 01, Tulin[4] showed its robustness and accuracy. In this paper we present a comparison between a "Volume Of Fluid" method using the Fully Coupled technique and the "SPH" method. The flow case investigated in this comparative study is the classical dam breaking problem.

2 SPH Solver

The SPH method belongs to a new type of numerical methods : meshfree methods. In this kind of methods a set of interpolating points is chosen in the medium. This points are associated with an interaction function (Kernel function) which is used to discretise the partial differential operators. In the case of free surface flows, the equations to be solved are Navier-Stokes equations (1, 2) and an equation of state for the pressure called Tait's equation (3). SPH is usually a compressible lagrangian method, but if Mach number remains below 0.1 during the whole simulation, the flow can be regarded as incompressible.

$$\frac{d\vec{v}}{dt} = \vec{g} - \frac{\nabla P}{\rho} + \overrightarrow{a_{viscous}} \tag{1}$$

$$\frac{d\rho}{dt} = -\rho.\nabla.\vec{v} \tag{2}$$

$$P = \frac{1}{7}c^2(\rho^7 - 1) \tag{3}$$

To discretise previous equations, variables are convoluted with the kernel function which tends to a Dirac distribution. In this paper the chosen kernel is the cubic spline kernel introduced by Monaghan :

$$W(q = \frac{|\vec{r}|}{h}) = C \begin{cases} \frac{2}{3} - q^2 + \frac{1}{2}q^3 & \text{if } 0 \leq q < 1 \\ \frac{1}{6}(2-q)^3 & \text{if } 1 \leq q < 2 \\ 0 & \text{else} \end{cases} \tag{4}$$

with C a constant set to ensure $\int W = 1$.

Then the values of a function and its gradient can be determined in the following way :

$$f(\vec{r}) \approx \int_D f(\vec{x}) W(\vec{r}-\vec{x}) d\vec{x} \tag{5}$$

The next equation is obtained via integration by parts by neglecting the surface term which is null for interior particles as kernel function cancels itself for $\frac{|\vec{r}|}{h} \geq 2$.

$$\nabla f(\vec{r}) \approx \int_D \nabla f(\vec{x}) W(\vec{r}-\vec{x}) d\vec{x} = \int_D f(\vec{x}) \nabla W(\vec{r}-\vec{x}) d\vec{x} \tag{6}$$

This kind of discretisation is second order in space, and to enhance the numerical performance, such as conservation of angular momentum, the formulae are symmetrized following Monaghan[9] :

in the mass equation and in the momentum equation :

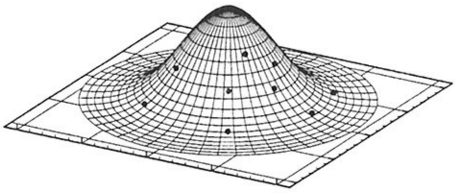

FIG. 1: Cubic Spline Kernel centered on grey particle

$$-\rho.\nabla.\vec{v} = \nabla.(\rho\vec{v}) - \nabla\rho.\vec{v} \tag{7}$$

$$-\frac{\nabla P}{\rho} = \nabla\frac{P}{\rho} - \frac{P}{\rho^2}\nabla\rho \tag{8}$$

Then the following numerical scheme can be deduced, where i-subscripted variables correspond to i^{th} particle :

$$\frac{d\vec{x_i}}{dt} = \vec{v_i} \tag{9}$$

$$\frac{d\vec{v_i}}{dt} = \vec{g} - \Sigma_j\, m\,(\frac{P_i}{\rho_i^2} + \frac{P_j}{\rho_j^2})\nabla W(\vec{r_i} - \vec{r_j}) \tag{10}$$

$$\frac{d\rho_i}{dt} = -\Sigma_j\, m\,(\vec{v_i} - \vec{v_j})\,\nabla W(\vec{r_i} - \vec{r_j}) \tag{11}$$

This ordinary differential equation system can be integrated in time by schemes such as Runge-Kutta, Leap-Frog, Predictor-Corrector to ensure second order convergence in time.

3 Free Surface Capturing Solver

The second solver involved in this comparative study, employs the 'Volume Of Fluid' method which has been investigated by several authors as Ubbink[12], Perić[10, 3] and Didier[5]. Briefly, this method has for principle to calculate the flow in the two fluids (air and water), considered as one single fluid whose physical properties vary across the interface. The physical characteristics ρ and μ are determined using the value of an additional variable (c) the volume fraction, given in equation (12). The value of (c) is such that, if a cell is filled with fluid 1, (c=0), and if it is filled with fluid 2, (c=1). The behaviour of the free surface is calculated through an additional advection equation (13). Consequently, the computation is performed on one a large fixed grid, which is one of the advantages of the method.

$$\rho = \frac{c\rho_1 + (1-c)\rho_2}{\rho_1} \qquad \mu = \frac{c\mu_1 + (1-c)\mu_2}{\mu_1} \tag{12}$$

$$\frac{\partial c}{\partial t} + \overrightarrow{\nabla} \cdot (c\overrightarrow{u}) = 0 \tag{13}$$

The flow is calculated using the incompressible Navier-Stokes equations which drive the motion of the fluid. In order to discretise the system, their dimensionless conservative form, as presented below (14, 15), is employed using a fully implicit finite volume method. To ensure the accuracy of the solver, the integrals are approximated to second order and the flux approximation is evaluated with a deferred correction. One critical issue of the VOF method is the choice of the differencing schemes employed to solve the convective term of the volume fraction equation. Low order schemes like central differencing schemes are not suitable because bounded solution is not ensured. And other differencing schemes like first-order upwind scheme are too diffusive, smear the interface and introduce artificial mixing of the two fluids over a wide region. Therefore high order mixing schemes have been designed for this application such as the CICSAM scheme developed by Ubbink[12]. It preserves a sharp transition zone with a checked boundedness criterion.

$$\begin{aligned}\int_V \frac{\partial \rho u_i}{\partial t} dV + \int_S \rho u_i \left(\vec{u}.\vec{n}\right) dS + \int_S P\,\vec{i}_i.\vec{n}\, dS + \int_S \frac{\mu}{Re}\left(\vec{\nabla}\vec{u}.\vec{n}\right) dS \\ = \int_V \frac{1}{Re}\left(\vec{\nabla}\mu\right).\left(\vec{\nabla}.\vec{u}\right) dV + \int_V \rho \frac{1}{Fr^2}\frac{\vec{g}}{g} dV\end{aligned} \tag{14}$$

$$\int_S \vec{u}.\vec{n}\, dV = 0 \tag{15}$$

As indicated before the system is built through a Fully Coupled method. Numerically this technique presents the advantage of accelerating the velocity-pressure coupling and fasten the convergence. More precisely, the Rhie and Chow[11] velocity flux reconstruction is applied to the conservation of momentum Navier-Stokes equation to obtain a single system using the pressure, the velocity and an added variable the second velocity. The solution is calculated with an iterative algorithm BiCGSTAB-ϖ using an incomplete LU decomposition preconditionner.

The VOF solver capabilities have been checked on different applications [1, 2], such as the flow in a sloshing tank or the simulation of a Rayleigh-Taylor instability.

4 Results

4.1 Dam breaking

To compare the two methods usual test case of the dam breaking has been chosen. This test case is typically employed to demonstrate the ability of codes to compute transient fluid flow with breaking free surface. The corresponding experiment has been made by Martin et Moyce[7], and more recently by Koshizuka[8]. The dimension of the initial water column is $a = 0.146$ m large and $2a = 0.292$ m high, and the tank is 0.584 m large. The flow, at first stage, presents the collapse of the column with a tongue of fluid propagating towards the opposite wall of the tank. Then the fluid strikes the right vertical wall, and goes up along it. During the next stage a breaking wave moves backward, then the flow is damped as in a sloshing tank. The data available from the experiment consists in pictures which show the time evolution of the breaking water wave, and secondary data such as the position of the wave front on the vertical and horizontal walls.

FIG. 2: secondary data description.

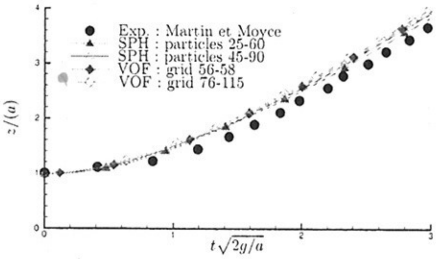

FIG. 3: water position on the left vertical wall

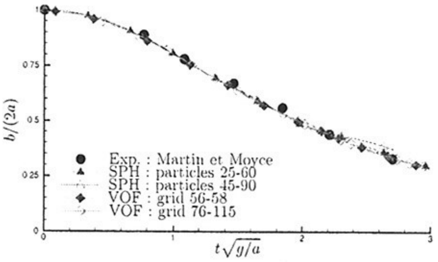

FIG. 4: water position on the horizontal wall

The comparisons between numerics and experiments are presented in figures 3 and 4. If the simulated position on the left vertical wall is in good agreement with the experimental one, the position of the wave front on the horizontal wall is less accurate. The "VOF" and the "SPH" show the same advance on the experimental result.

Indeed this difference could be explained by the slip condition used on the wall. This difference doesn't appear on the vertical wall , due to a lower speed. Another explanation is linked to the capturing of the interface. On the horizontal wall the tongue of water is so thin that the calculation in the VOF method of the iso-value $c = 0.5$ position is dubious. And, for the same reason it is difficult to find precisely the interface in the distribution of particles in the "SPH" method.

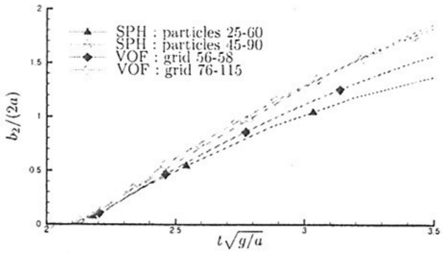

FIG. 5: water position on the right vertical wall

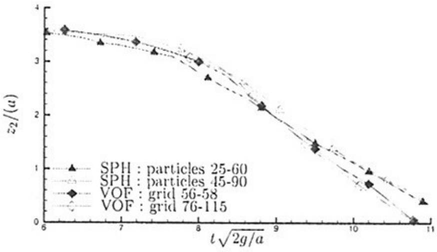

FIG. 6: position of the wave breaking

On the last plots, two other comparisons between "SPH" and "VOF" results are showed. In figure 5 the temporal evolution of the leading edge on the right vertical wall is followed. Stronger differences appear between the different configurations of grid, and of numbers of particles respectively. We suppose that the origin of these differences can be explained in the same manner as for the horizontal front wave evolution. The differences are increased by the thinness of the water on the wall. The fourth characteristic of the flow studied is the speed of the backward wave. In this case the two set of numerical data are similar. Unfortunately, there is no experimental data to validate this result.

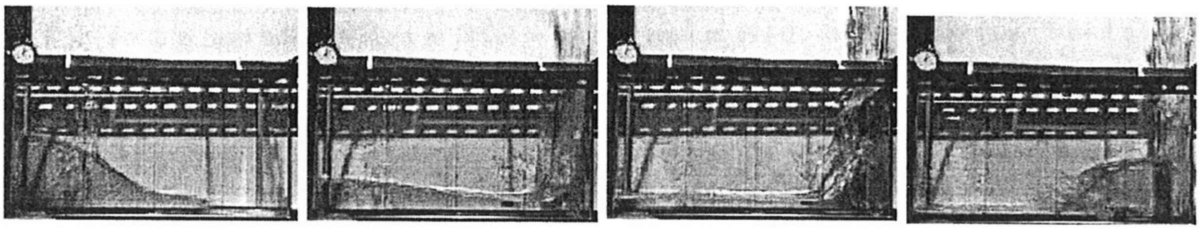

(a) Experiments

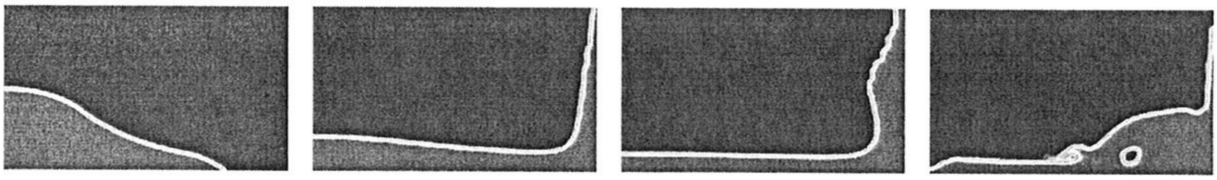

(b) VOF simulation

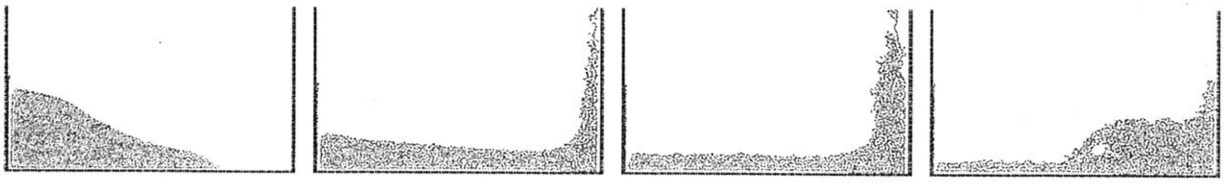

(c) SPH simulation

FIG. 7: free surface at $t = 0.2$ s,$t = 0.4$ s,$t = 0.6$ s and $t = 0.8$ s

As it has been written before, different pictures of the flow are available, and figures 7(a), 7(a) and 7(a) present the free surface profiles for the experiment and for the two numerical methods. globally, the free surface given by the numerical simulations are close to the experimental one, nevertheless the size of the bubble created in the SPH calculation is underestimated. But, one has to remember that the SPH code is a one single fluid solver and consequently the influence of the second fluid is neglected. However, it has been remarked that by increasing the number of particles the size of the bubble is more and more accurate. More simulations are thus necessary to explain the origin of this difference.

4.2 Dam breaking with obstacle

This second test case uses the same geometry defined before, with the addition of an obstacle. This results in a more complex flow. In practice, after the leading edge reaches the obstacle a tongue of fluid continues its movement towards the opposite wall, and the strike of the fluid on the wall is more violent. In this application, during the first 0.4 s the flow of the different numerical simulations is in good concordance with the experimental data. After 0.5 s, the free surface evolution of the SPH is less accurate than the VOF one. Practically, the tongue of water connecting the obstacle and the right wall falls down abnormally. The explanation of this phenomena is the same as for the under estimating of the bubble in the previous application. Figure 9(a) gives the pressure field in both air and water. The difference of pressure between the two sides of the tongue of water hitting the right wall is clearly depicted, confirms that the influence of air on the water flows cannot be neglected, which explains the difference between VOF and SPH results.

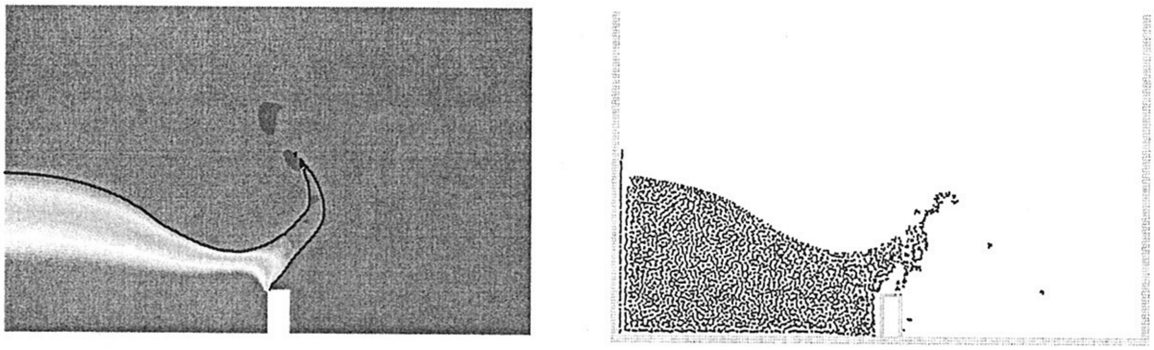

(a) VOF simulation

(b) SPH simulation

FIG. 8: Free surface at $t = 0.2$ s

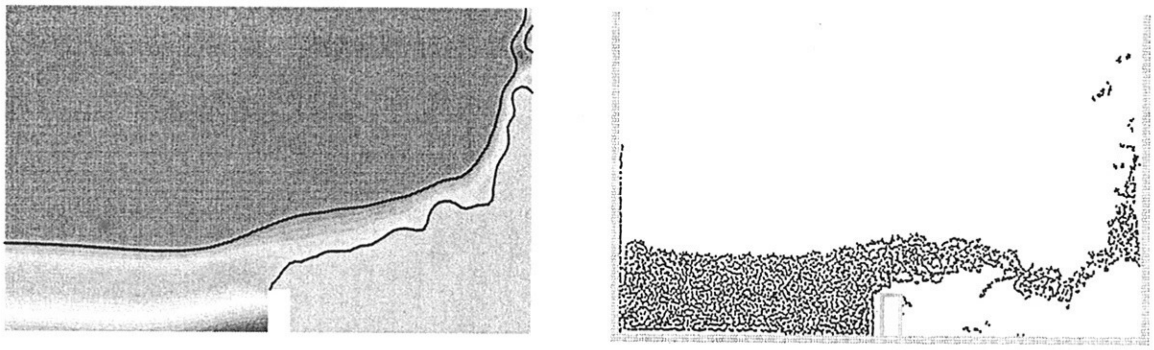

(a) VOF simulation

(b) SPH simulation

FIG. 9: Free surface at $t = 0.35$ s

5 Conclusion

The comparisons given in this paper demonstrate the ability of the SPH method to simulate complex free surface flows, and the accuracy of the SPH results against experimental and VOF simulation, including local flow characteristics such as the position of the leading edge on the wall. However, as in the SPH simulation the influence of the second fluid is neglected, some details flow are inaccurately predicted such as the flow with fluid 2 confined in a bubble. Then the future work is to consider the second fluid in the SPH method and to validate the different codes on other applications. In the long term, we plan to evolve the different codes to the 3D applications.

Références

[1] Y. Andrillon and B. Alessandrini. A 2D+T VOF fully coupled formulation for calculation of breaking free surface flow. In *24^{th} Symposium on Naval Hydrodynamics*. July 2002.

[2] Y. Andrillon and B. Alessandrini. A fully-coupled VOF method for free surface simulation. In S. F. L. R C T Rainey, editor, *International Workshop on Water Waves and Floating Bodies*. April 2002.

[3] R. Azcueta, S. Muzaferija, and M. Perić. Computation of water and air flow around ships. In *EUROMECH*, pages 121–131. 1998.

[4] A. Colagrossi, M. Landrini, and M. P. Tulin. A lagrangian meshless method for free surface flow. In 4^{th} *Numerical Towing Tank Symposium*. 2001.

[5] E. Didier. *Simulation D'écoulements À Surface Libre sur Des Maillages Destructurés*. Ph.D. thesis, Ecole Centrale de Nantes, 2001.

[6] C. W. Hirt and B. D. Nicholls. Volume of fluid (VOF) method for the dynamics of free boundaries. *Journal of Computational physics*, 39 :201–225, 1981.

[7] W. J. M. J C Martin and. An experimental study of the collapse of liquid columns on a rigid horizontal plane. *Philos. Trans. Soc. London*, A244 :312–324, 1952.

[8] S. Koshizuka and Y. Oka. Moving particle semi-implicit method : Fully lagrangian analysis of incompressible flows. In *European Congress on Computational Methods in Applied Sciences and Engineering*. ECCOMAS, 2000.

[9] J. J. Monaghan. Smoothed particle hydrodynamics. *Annu. Rev. Astron. Astrophys.*, 30 :543–574, 1992.

[10] S. Muzaferija, M. Peric, P. Sames, and T. Schellin. A two-fluid navier-stokes solver to simulate water entry. In *22nd Symposium on Naval Hydrodynamics*, pages 638–649. The National Academy of Sciences, 2000.

[11] C. M. Rhie and W. L. Chow. A numerical study of the turbulent flow past an isolated airfoil with trailing edge separation. *AIAA J.*, 21 :1525–1532, 1983.

[12] O. Ubbink. *Numerical Prediction of Two Fluid Systems with Sharp Interfaces*. Ph.D. thesis, Imperial College, 1997.

An Experimental Study on Water Shipping

Marco Barcellona, *Marilena Greco*, *Eric Pequinot* and *Maurizio Landrini*

INSEAN, *The Italian Ship Model Basin*, Roma, Italy. maulan@waves.insean.it

Introduction

Shipping of water on ship deck and related loads represents an important concern for the safety, and should be taken into account even at the design stage. Despite this fact a full knowledge about this phenomenon is still far to be achieved. In particular, the relationships between water shipping severity, geometry and motion of the ship and sea-state parameters are not yet understood.

In this paper, the water on deck caused on a restrained ship model in head waves is studied experimentally. These conditions are relevant, for instance, for FPSOs, which are ships operated most of the time as oil platforms, without forward motion.

Three geometries have been considered to investigate the the role of the bow shape, for several incoming wave steepness. The models have been equipped with transparent-material deck and the water shipping is studied by image analysis. In two cases, the pressure field on the deck has been measured. Finally, impact loads on a vertical wall to mimic a deck structure have been measured.

Experimental set-up

The experiments have been performed in the towing tank No. 2 at INSEAN, (220 m long, 9 m wide and 3.6 m deep). The geometrical parameters and the incident-wave conditions have been chosen by taking into account information from occurred FPSOs water-on-deck accidents and their usual operational conditions (*cf.* also [2]).

The adopted ship models are shown in figure 1.

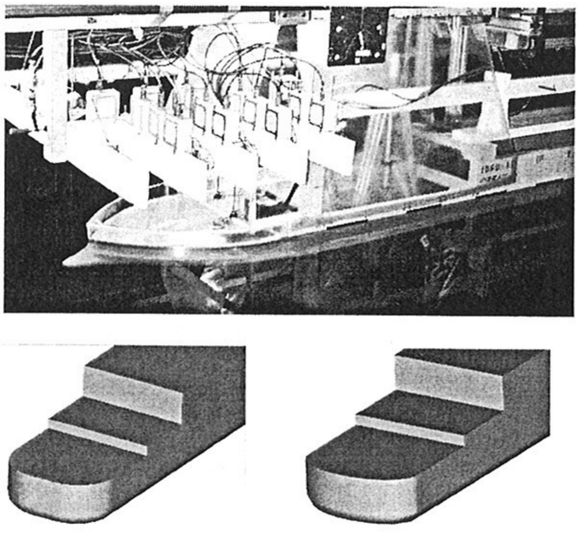

Fig. 1: Side view of the used ship models: Esso Osaka (top photo), circular bow (left-bottom drawing) and elliptical bow (right-bottom drawing).

The first model (top picture) is a Esso Osaka ship model (1:70 scale, length $L \simeq 4.44$ m, $D/L \simeq 0.064$, $B/L \simeq 0.17$). Since the model is restrained from oscillating during the experiments, to handle realistic heights of water relative to the deck for representative design condition, the upper portion of the bow has been modified and the freeboard reduced to $f/L \simeq 0.015$. The ship bow has a conventional bulb, but this is likely to be not relevant for water shipping (*cf.* i.e. [1]).

The other two models have main geometric parameters similar to the first model ($L \simeq 4$ m, $D/L \simeq 0.07$, $B/L \simeq 0.17$ and $f/L \simeq 0.016$). To simplify future numerical computations, simple barge-shape geometries have been used with rectangular cross section. Actually, to prevent possible vortex shedding phenomena, the corners have been rounded with a radius of curvature $r/L = 0.02$. The bows are, respectively, circular (left) with radius $R/B = 0.5$ and elliptical (right) with large half-axis equal to $B/2$ and ratio between axes about 3.8. For all the models, a Plexiglas vertical wall has been located at $d/L = 0.13$ from forward perpendicular.

The incident waves are obtained by wave focusing. In particular, by a linear decrease of the wavemaker frequency to obtain a train of waves with increasing phase speed. This leads to the focusing of the generated waves in a point coinciding, in the chosen set up, with the forward perpendicular of the models. The resulting wave packet is characterized by central wave peak, preceded and followed by two smaller peaks. The wave generation process has been tuned to obtain a single water-shipping event as result of the interaction of the hull model with the largest wave peak. This is similar to the real case, where the phenomenon, caused by an irregular sea-state, is usually recorded as a single or (at most) as a few events. In our experiments, each wave packet is characterized by an identical amplitude a for all the generated wave components. A wave-steepness parameter $k_c a$ is defined for the wave packet, where $a = H/2$ is the wave amplitude and k_c is the wavenumber related to the mean frequency f_c in the spectrum, kept fixed together with the frequency bandwidth Δf during the tests, and respectively equal to 0.6 Hz and 0.4 Hz. The characteristic wavelength can be defined as $\lambda_c = 2\pi/k_c = 4.33 \text{ m} \sim \mathcal{O}(L)$. In the wave packet, the shortest and the longest wave components correspond to $\simeq 0{\cdot}5L$ and to $\simeq 2{\cdot}6L$, respectively. The wave steepness $k_c a$ has been varied between 0·125 and 0·25.

The tank dimensions, the scale of the experiment and the use of wave packets ensure that the tests reproduce water-on-deck casualties in deep and open waters.

Video images have been obtained by using color and black-white cameras with a frame rate equal to 25 and 30 Hz, respectively, to get side and top views of the phenomenon. A series of piezoelectric pressure gauges, figure 2, have been distributed on a regular squared-cell grid (see figure 3, circular bow in the top and elliptical bow in the bottom). In this way the pressure evolution along the deck during each event has been recorded. Actually, only ten transducers were available and each test condition has been repeated twelve times to give the complete map of the pressure distribution on the deck. Clearly, this procedure relies on a good repeatability of the experiments.

PUT PRESSURE SENSORS CHARACTERISTICS

A load cell has been mounted behind the vertical wall on the deck to measure the horizontal force caused by the interaction between the impacting shipped water. The vertical wall has been mounted on a low friction linear bearing to reduce possible errors and dynamic effects related to the wall-supporting structure have been verified by hammer tests in dry conditions.

PUT THE LOAD CHARACTERISTICS

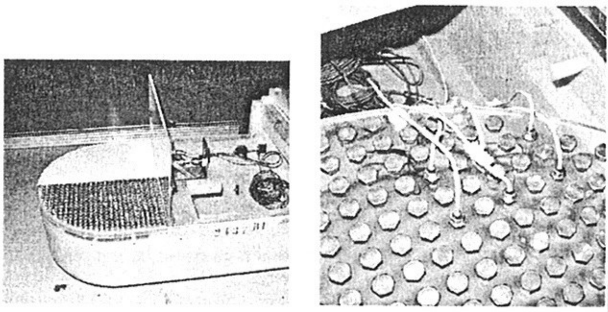

Fig. 2: Experimental set-up. Pressure gauges.

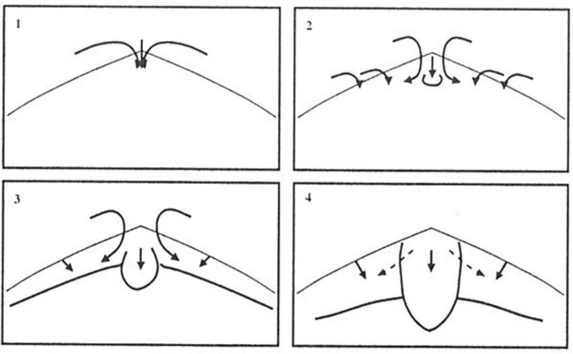

Fig. 4: Esso-Osaka model: sketch of the flow evolution during the water shipping, top-captain view. Time increases from left to right and from top to bottom.

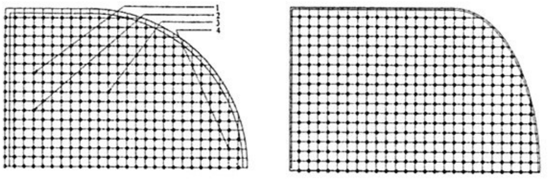

Fig. 3: Distribution of pressure gauges for the circular (left) and the elliptical (right) bows.

Bow-shape influence on the water-shipping evolution

Background Two-dimensional water-on-deck experiments discussed in [1] have shown that the water shipping starts in the form of a wave plunging and hitting the deck in proximity of the bow of the restrained model. The formation of a cavity entrapping air has been observed. Later the cavity is stretched downstream by the main flow along the deck and eventually breaks and collapses. Also, due to the impact, the water front plunging onto the deck splits in two jets: one moving downstream along the deck, the other one propagating upstream, toward the bow edge. The latter enhances the detachment of the air cavity from the deck.

The present three-dimensional experiments confirm the occurrence of a water front-plunging phase at the beginning of the shipping of fluid on the deck. In general, the water invades the deck first from the fore portion, where the wave elevation exceeds earlier the freeboard. Then the shipping develops along the bow sides, with a non uniform (decreasing) maximum freeboard exceedance going from the fore portion towards the superstructure. Although these aspects do not vary qualitatively when changing the geometry, we have noted some relevant modifications of the water-shipping features which will be presented in some detail.

ESSO OSAKA In this case, figure 4, the sharp and slender geometry of the bow contributes in causing two main plunging flows from the two sides of the deck (sketch 1). These fronts, moving inwards, impact each other along the centerline (sketch 2) and are then deviated outwards (sketch 3). The water entering the ship deck from the forward portion and that from the sides feed a tongue-shaped fluid structure (sketch 4), growing in time and propagating towards the vertical wall with increasing velocity. The water exceeds the freeboard also along the bow sides and a tubular cavity entrapping air is observed, with cross sectional area decreasing from the ship centerline along the bow sides. The water shipped from the side edges, evolves into two water fronts with smaller height and moving at an oblique angle. These lateral water fronts will also impact with the wall. After the impact with the wall, the water runs up, with spray formation and fragmentation of the free surface. Under the restoring action of gravity, the upward fluid motion is slowed down and then reversed into a waterfall, overturning onto the deck.

Circular Bow In this case, the water exceeds the freeboard almost uniformly along the fore portion of the bow, figure 5 (time increases from left to right and from top to bottom). A plunging phase is observed, resulting in a water impact with the deck. Similarly to the two-dimensional experiments, two flow jets are generated. The first picture shows the flow just after the initial plunging. The forward jet is characterized by a non-smooth leading front. The darker region behind it, indicated by the arrow, corresponds to the wetted region of the deck, while closer to the edge the presence of the air cavity is detectable. The water front remains roughly two dimensional in the region closer to the ship centerline. Near the bow sides, the flow enters almost perpendicular to the deck edges and it is then deviated to reconcile with the quasi-two dimensional flow in the inner region (second picture). The air tube initially entrapped near the bow detaches from the deck because of the backward jet following the impact of the plunging (third picture). Just behind the

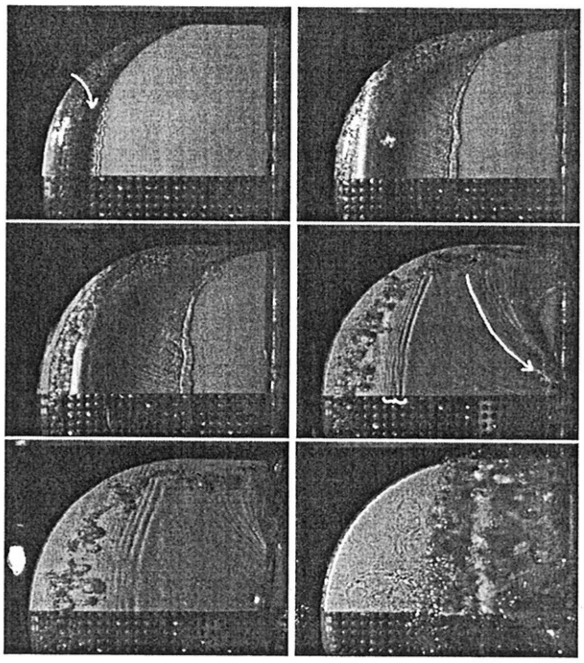

Fig. 5: Top view of the water shipping in case of the circular-bow shape. The time increases from left to right and from top to bottom. The wave packet has $k_c a = 0.2$ and $\lambda/L = 1\cdot08$.

water front, short wavelengths can be seen on the free surface (second and third pictures), maybe related to surface-tension effects. A second system of short waves appears later (indicated by the parenthesis in the fourth picture). The latter is probably caused by a contraction-rarefaction evolution of the cavity observed before its collapse. Also, close to the deck edges, where the longitudinal and the transverse flows have to reconcile, an oblique-moving water flow (indicated by the arrow in the fourth picture) is observed. This thickens the front near the centerline. The final impact with the superstructure is found starting from the centerline and spreading laterally. Similarly to the ESSO OSAKA model, water run-up and backward overturning are observed.

Elliptical Bow Also in the elliptical-bow case, figure 6 (time increases from left to right and from top to bottom), the initial stages of the water shipping appear well two-dimensional at the fore portion of the ship bow. After the impact of the initial plunging onto the deck, the jet moving towards the bow induces a backward wave motion. The forward moving water front is not smooth, similarly to the circular bow case. Also, similarly to the circular case, when the backward jet reaches the bow the cavity is detached from the deck. The following evolution is characterized by strong shape deformations and, eventually, by the fragmentation of the air cavity into finer bubbles. These are (partly) convected by the flow along the deck.

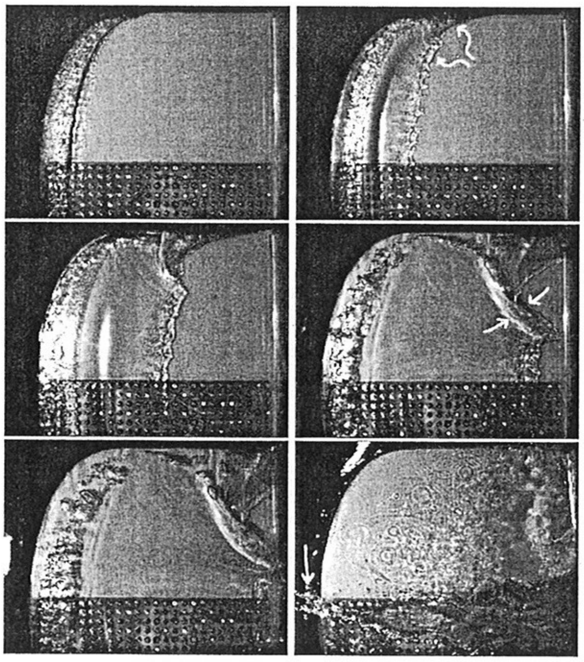

Fig. 6: Top view of the water shipping in case of the elliptical-bow shape. The time increases from left to right and from top to bottom. The wave packet has $k_C a = 0.2$ and $\lambda/L = 1{\cdot}08$.

At the same time, the plunging water front from the fore bow interacts with the front of the flow entering the deck along the sides. The two water fronts form an angle of about 90 degrees, and the resulting flow moves along an intermediate direction with curved fronts (see the marked area in the second picture). The radius of curvature of the front, is very small at the beginning and enlarges as the water flow develops along the deck. This process is qualitatively similar to the collision along the ESSO OSAKA centerline of the two plunging water fronts coming from the sides of the deck. In both cases we have a convergence of two flow structures related to the presence of a bow portion with sufficiently small radius of curvature. Here, the flow is strongly three-dimensional near the interaction of the two fronts, and quasi two dimensional near the centerline. The region of interaction between the two fronts is thicker than the surroundings (see marked area in the fourth picture) and propagates inwards and downstream, progressively destroying the quasi-two dimensional front along the centerline. Also for this bow geometry, two short wave systems are observed during the evolution: one, generated at the initial stage of the water shipping, moving just behind the leading front and probably caused by surface tension effects, the other one, appearing later and likely related to the evolution of the cavity before its collapse. By comparing the fourth frames for the circular- and the elliptical-shaped bows we note a strong similarity, though for the latter the interaction front is thicker and induces a more pronounced three-dimensionality.

The water front impacts with the superstructure in a rather non-uniform manner. The wall is first reached from the sides, then the region with the interacting fronts impacts and, finally, the inner portion of water shipped from the central bow region hits the structure. As it can be expected, the run up of the water is quite complex. The backward plunging is concentrated around the centerline, while along the wall sides it is not clear if a massive backward phase occurs or if there is a gentler run-down.

Differently than in the two-dimensional case, now part of the shipped water flows out laterally. As a result, a smaller amount of water falls back against the deck.

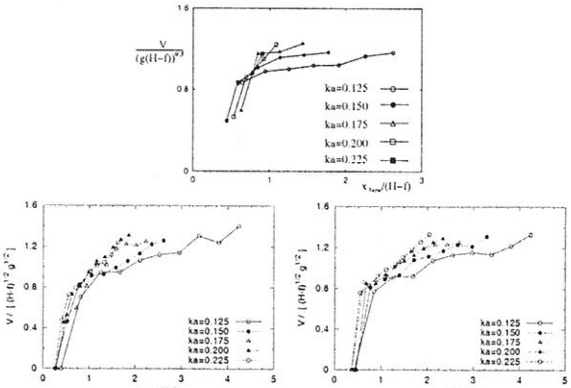

Fig. 7: Water front velocity along the deck centerline. Incoming-wave steepness and bow-shape influence Top: ESSO OSAKA, left bottom: circular bow, right bottom: elliptical bow.

Concerning the water-front velocity along the ship centerline, the values estimated by images (see figure 7), shows that the distance from the bow from where on the dispersion effects can be neglected, is not particularly influenced by the bow geometry. From the flow visualizations, we would expect such distance reduces going from the Esso-Osaka to the elliptical bow, the quantitative confirmation of this fact would require a finer velocity evaluation. Figure 8 shows the backward plunging flow from the side view, respectively, in the case of the Esso-Osaka (left) and of the elliptical model (right). In the Esso-Osaka case the spray associated with the plunging is more pronounced, the backward overturning seems to be always characterized only by one flow structure. Differently, there are two flow structure for the elliptical bow. One, observable in the picture, is quite concentrated in terms of spray. The other (not visible in the picture), with an important part of spray, reaches a higher height and impacts further on along the deck, towards the fore bow. For all the ship geometries, the water-off-deck phenomenon caused by the wall reflection modifies the flow-field conditions around the ship bow with respect to the diffracted wave field without water-on-deck occurrence. Therefore, in case of repeated water-shipping events, the second water on deck depends on incident-wave con-

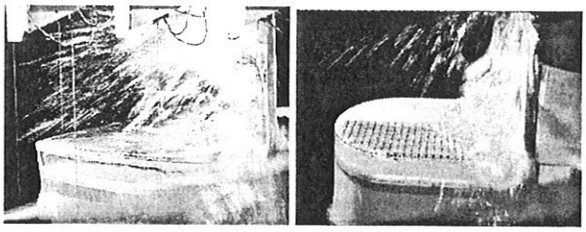

Fig. 8: Backward plunging wave during the late stages of the water shipping. Left: Esso-Osaka ship model. Right: elliptical bow.

ditions modified both by diffraction and by the off-deck flow associated with the previous event.

Wave-steepness influence on the water-shipping evolution

For all the considered bow shapes, a steepness increase causes a stronger three-dimensionality on the water-on-deck phenomenon. Neighbor water layer interaction enlarges, the leading water front propagating along the ship deck appears less regular. The cavity tube initially formed near the bow tends to become less uniform in the ship beam direction. Moreover, the existence of a second backward flow structure at the late stages of the water shipping is enhanced by a greater steepness. By increasing the incoming wave steepness, the non-dimensional water-front velocity (see figure 7) slightly increases and the establishment of the shallow water-conditions tends to be delayed in space (that is a greater distance from the bow is needed for the dispersion effects to become negligible) and time.

Green-water loading: pressure evolution along the deck

The pressure distribution along the circular-bow deck is shown in the left plots of figure 9 for time increasing from top to bottom. The right plots of the same figure give the top view of the corresponding flow configurations. The considered case corresponds to an incident wave packet with steepness $k_c a = 0{\cdot}2$ and wavelength $\lambda = 4{\cdot}33$ m. As we can see, before the water impacts with the wall (first and second pictures) the higher pressure values are located near the bow, where the amount of water is larger. From the results it is not clear how strong the increase of pressure due to air-cushion effects. Probably, a denser distribution of pressure gauges is needed. Moreover, pressure measurements become more difficult when bubbles are present, and actually, in some cases, unphysical negative pressure values have been recorded.

Interestingly, a pressure rise on the deck is observed at the bottom of the deck structured when the water impacts against it (fourth frame). As it can be expected, the maximum pressure is recorded near the centerline and decreases approaching the deck edges. The longitudinal extension of the pressure rise due to the impact is also relatively large (about one fourth of the deck length). Later, last frame, a second rise of the pressure is recorded. It is slightly more concentrated near the ship centerline, though with a longer longitudinal extension. By comparing with the video images, we can see that this is related to the backward plunging wave occurring during the water run-down phase.

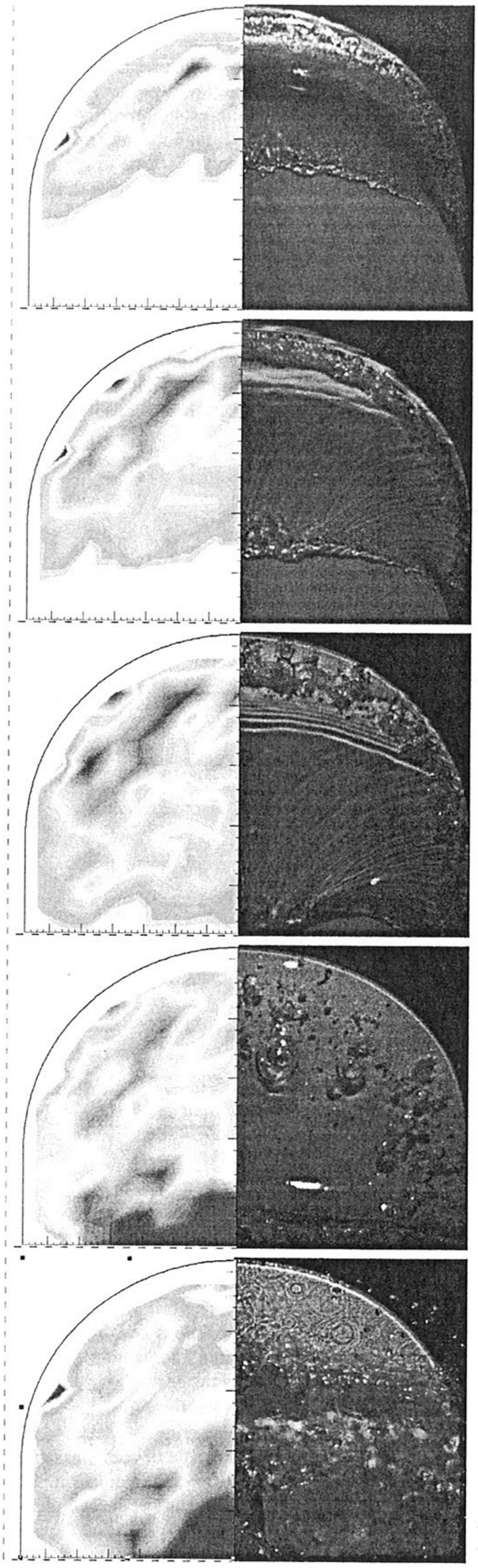

Fig. 9: Circular bow: pressure evolution onto the deck (left) and related flow configuration from a top view (right). The time increases from top to bottom. The wave packet has $k_c a = 0{\cdot}2$ and $\lambda = 4{\cdot}33$ m.

Qualitatively, the main features of the above described pressure evolution are rather similar for the two analytical geometries (the pressure distribution on the deck has not been measured for the ESSO OSAKA). The maximum pressure on the deck is recorded at the beginning of the impact with the wall and it is smaller for the elliptical bow shape, figure 10, for all the considered wave steepnesses, with the exception of the smallest one. The maximum pressure increases as the incoming-wave steepness increases, and the growth rate is slightly larger for the circular-bow geometry than the elliptical one.

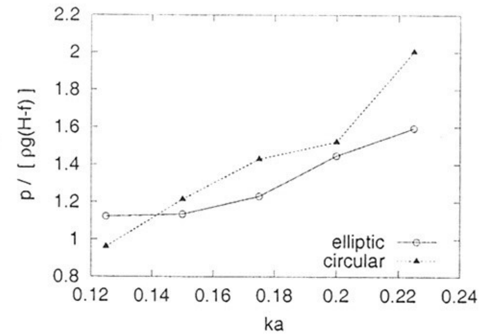

Fig. 10: **Influence of the incoming-wave steepness and of the bow shape on the maximum pressure on the deck.**

Green-water loading: force evolution on the vertical wall

Generally speaking, the time evolutions of the force acting on the vertical wall shows a first peak associated with the initial impact of the water. A secondary peak is observed, more pronounced in the case of the circular bow shape (*cf.* figure 11). Such peak is related to the later backward water overturning hitting the underlying layer of water. The maximum value of the horizontal force along the vertical wall is given in figure 12. This increases almost uniformly going from the circular to the elliptical bow. This is due to the different way the water hit the wall. Although the water-front velocity along the ship centerline is not very different, for the elliptical bow the main impact with the wall is associated with the mentioned flow structures generated by the interacting fronts. The latter are faster than the inner water front (*cf.* fourth frame of figure 6). For both ships, the maximum force increases as the steepness increases, but it becomes less sensitive to this parameter in the region of higher steepnesses. This reflects the trend of the maximum freeboard exceedance at the focusing point with the steepness.

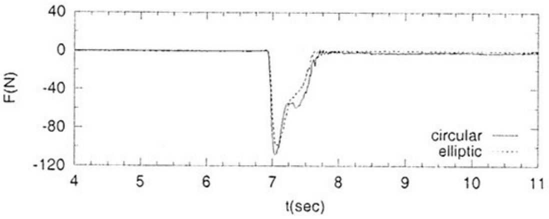

Fig. 11: **Time evolution of the horizontal force acting along the wall. The wave packet has $k_c a = 0{\cdot}2$ and $\lambda = 4{\cdot}33$ m.**

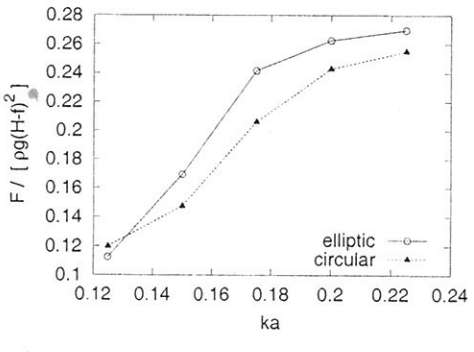

Fig. 12: **Influence of the incoming-wave steepness and of the bow shape on the the maximum horizontal force on the vertical wall.**

Surface-tension and viscous effects

In all the studied cases and for all the ship models, short wavy structures following the leading water front have been observed. The related wavelengths were of the order of one centimeter. This is a spatial scale where surface-tension effects could matter. Thus a possible explanation is connected with the surface tension effects excited by the high curvature of the initial plunging wave hitting the deck. This fact has to be accounted for when transferring the experimental results to the full scale.

Concerning the viscous effects, the global Reynolds number is sufficiently large but locally viscosity could matter during the evolution of the shipped water. In the boundary layer formed near the deck surface the flow is slowed, and the leading front is forced to become more rounded (steeper) near the deck. However if the boundary layer is sufficiently thin the water front can be roughly characterized as a wedge-shaped structure forming a relatively small angle with the deck. The smaller such angle is when the water hits the wall the better it is in terms of the structure safety (see *i.e.* Greco (2001)). A rough estimate of the boundary layer thickness can be obtained by assuming the thickness grows as in the case of the steady boundary layer for a flat plate. This gives a square-root growing. According to the estimated mean water front velocity along the deck the thickness remains sufficiently small and reaches a value of the order of one millimeter near the vertical wall position.

Repeatability of the experiments

As an example of repeatability of the model tests, figure 13 shows the time evolution of the wave elevation measured at the undisturbed focusing point and figure 14 gives the time record of the horizontal force on the wall, in the case of the circular bow. As we can see the results are in satisfactory agreement, confirming a good test repeatability. Figure 15 shows the time evolution of the pressure at locations 1-4 along the deck, in the case of the circular bow (*cf.* left sketch of figure 3) and of the same wave packet. The results agrees sufficiently each other, although some discrepancies have been observed (see plot for location 4). Probably, these are related to the occurrence and the development of bubbles due to the initial cavity formation, which are very sensitive to the local-flow conditions involved.

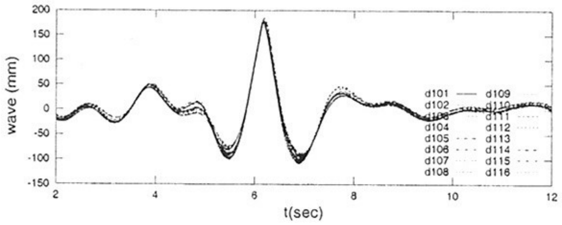

Fig. 13: **Repeatability analysis: time evolution of the wave elevation measured at the focusing point in the case of the circular-bow geometry. The wave packet has $k_c a = 0{\cdot}2$ and $\lambda = 4{\cdot}33$ m.**

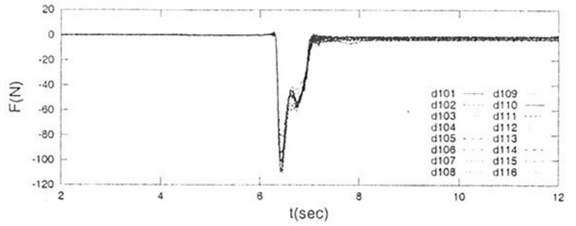

Fig. 14: Repeatability analysis: time evolution of the horizontal force acting along the wall in the case of the circular-bow geometry. The wave packet has $k_c a = 0{\cdot}2$ and $\lambda = 4{\cdot}33$ m.

Conclusions

A three-dimensional water-on-deck analysis has been presented by comparing three different bow geometries. The bow-shape influence on the water-on-deck features and on the green-water loading on deck structures has been discussed. The results showed that by taking a more 'two-dimensional' bow geometry not necessarily the resulting flow onto the deck will have more pronounced two-dimensional character. In particular, the elliptical ship is characterized by an flow interaction process giving rise to a jet structure with velocity growing during its evolution. This is similar to the tongue-shaped flow occurring in the Esso-Osaka case. For both of them, it is related to the presence of a sufficiently small radius of curvature in the bow geometry. The water-on-deck associated with the circular-bow seems to be the most two-dimensional one. Here the smoother bow geometry counteracts the interaction process. The incoming wave steepness has been varied and its influence on both the global features of the water shipping and on its effects on the deck structures have investigated. Possible relevant factors in terms of the deck and wall design have been indicated.

Acknowledgements INSEAN research activity is supported by the Italian *Ministero delle Infrastrutture e Trasporti* through INSEAN Research Program 2000-02.

References

[1] M. Greco (2001), *A Two-dimensional Study of Green-Water Loading*, Ph.D. dissertation, Dept. Marine Hydrodynamics, NTNU, Trondheim, Norway.

[2] M. Greco, O.M. Faltinsen and M. Landrini (2002), *Water Shipping on a Vessel in Head Waves*, Proc. of 24^{rd} ONR Symp. on Naval Hydrodynamics, Fukuoka, Japan.

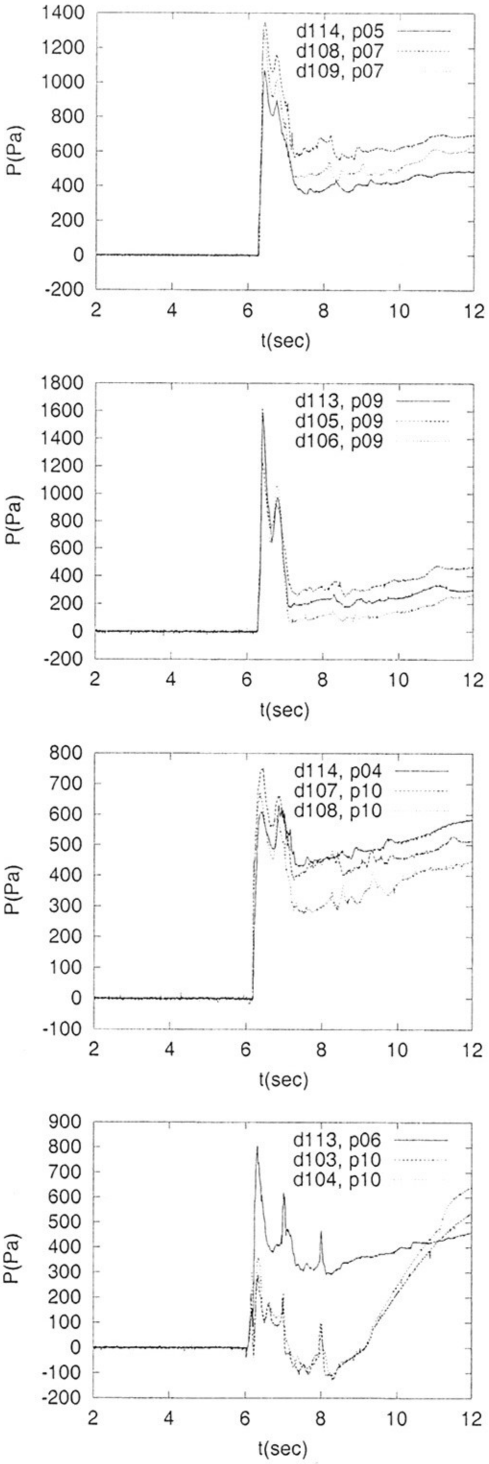

Fig. 15: Repeatability analysis: time evolution of the pressure at locations 1-4 (going from left to right and from top to bottom) along the deck of the circular bow (*cf.* top sketch of figure 3). The wave packet has $k_c a = 0{\cdot}2$ and $\lambda = 4{\cdot}33$ m.

Modeling Appendages in RANSE Simulations of Aerodynamic Flows around Ship Superstructures

Volker Bertram, ENSIETA, bertravo@ensieta.fr
Daniel Schmode, TU Hamburg-Harburg, d.schmode@tu-harburg.de
Ould M. El Moctar, Germanischer Lloyd, moct@germanlloyd.org

El Moctar et al. (2001), El Moctar and Bertram (2002), Lindenau et al. (2002), Schmode and Bertram (2002), presented aerodynamic CFD applications of the Hamburg Ship Model Basin HSVA for assorted ships. Ship superstructures feature many filigree appendages such as railings, antennae, deck equipment etc. An approximate modeling of these appendages is vital in wind tunnel tests to ensure sufficiently turbulent flow. A geometric modeling of these appendages in CFD simulation is impossible as this would require an excessive number of cells. We have now investigated appropriate modes to model the effect of the appendages on global flow pattern around ships, employing the commercial RANSE solver Comet. Comet is based on the finite-volume method to discretize the fundamental differential equations. We solve as usual the equations of conservation of mass and momentum, coupling pressure and velocity by the SIMPLE algorithm. We employed here the standard k-ε model. Comet offers the option of using baffle elements, i.e. partially permeable cell faces. Baffle elements are e.g. commonly employed in flow simulations to model forests without modeling each individual tree. Baffle elements are introduced by adding a source term on the control volumes adjacent to the baffle surfaces:

$$-\int_S r v_{\mathrm{sup}} \cdot dS$$

S is the baffle cell surface of a control volume. v_{sup} is the average velocity in the control volume. r is given by: $r = \rho\,(a+b|v_{sup}|)$. a and b are user-specified input. The baffle elements thus affect only the momentum equations directly.

We selected the antennae mast of the Superfast Ferry, Schmode and Bertram (2002), as a suitable representative of an appendage to ship superstructures. We limited ourselves in this study to wind coming directly from ahead. The mast is "filigree", but is expected to have a significant influence on the flow field around the downstream ship funnel. The 12 m mast was meshed with 3 grids of successive fineness, Fig.1. The computational domain extended 25 m upstream of the mast, 45 m downstream, 30 m to the side, 15 m to the top. Symmetry in y was exploited.

Fig.2 shows the turbulent kinetic energy and the absolute value of the velocity. The turbulent energy specified at the inlet dissipates rapidly, before the flow hits the mast. At the mast, new turbulence is generated. The wake of the mast is clearly visible in the plots of the velocity magnitude. The figures show also that we have not yet reached grid independent solutions, but a common pattern emerges. The turbulence is dissipated faster on the coarse grid (numerical dissipation error), the wake less pronounced.

Instead of the geometrical mast, we then employed a triangular area with height of the mast and width of its side wings. The area of this triangle is approximately three times as large as the projected geometric area of the mast. This was intended to account for the additional blockage due to the boundary layer around the mast. We assumed that the mast decelerates the flow velocity proportional to the velocity. We selected thus a=0 and varied b, as we could not find any suitable values in the literature. We expected a suitable value to lie somewhat above the geometric ratio of 1:3, say b=0.4. Fig.3 shows results for various values of b. Agreement is poor in all cases, particularly for turbulence. While the poor results may be due to wrong choice of parameters, we decided to abandon the research on baffle elements until we obtain new insight from related flow simulations.

Since the baffle elements were rather disappointing, we investigated next whether a very simplified geometry would give acceptable results. We modeled the mast by a slender block of same height. The grid had almost the same number of cells as the medium grid for the "exact" geometry. The results, Fig.4, are encouraging. Wake and turbulence are slightly larger than in the exact geometry model, but deemed acceptable for our purposes. At present, the best recommendation we can give for aerodynamic CFD simulations for ships is thus a strongly simplified modeling of the appendages.

EL MOCTAR, O.M.; GATCHELL, S.; BERTRAM, V. (2001a), *RANSE simulations for aerodynamic flows around ship superstructures*, 4th Num. Towing Tank Symp., Hamburg

EL MOCTAR, O.M.; BERTRAM, V. (2002), *Computation of viscous flow around fast ship superstructures*, 24th Symp. Naval Hydrodyn., Fukuoka

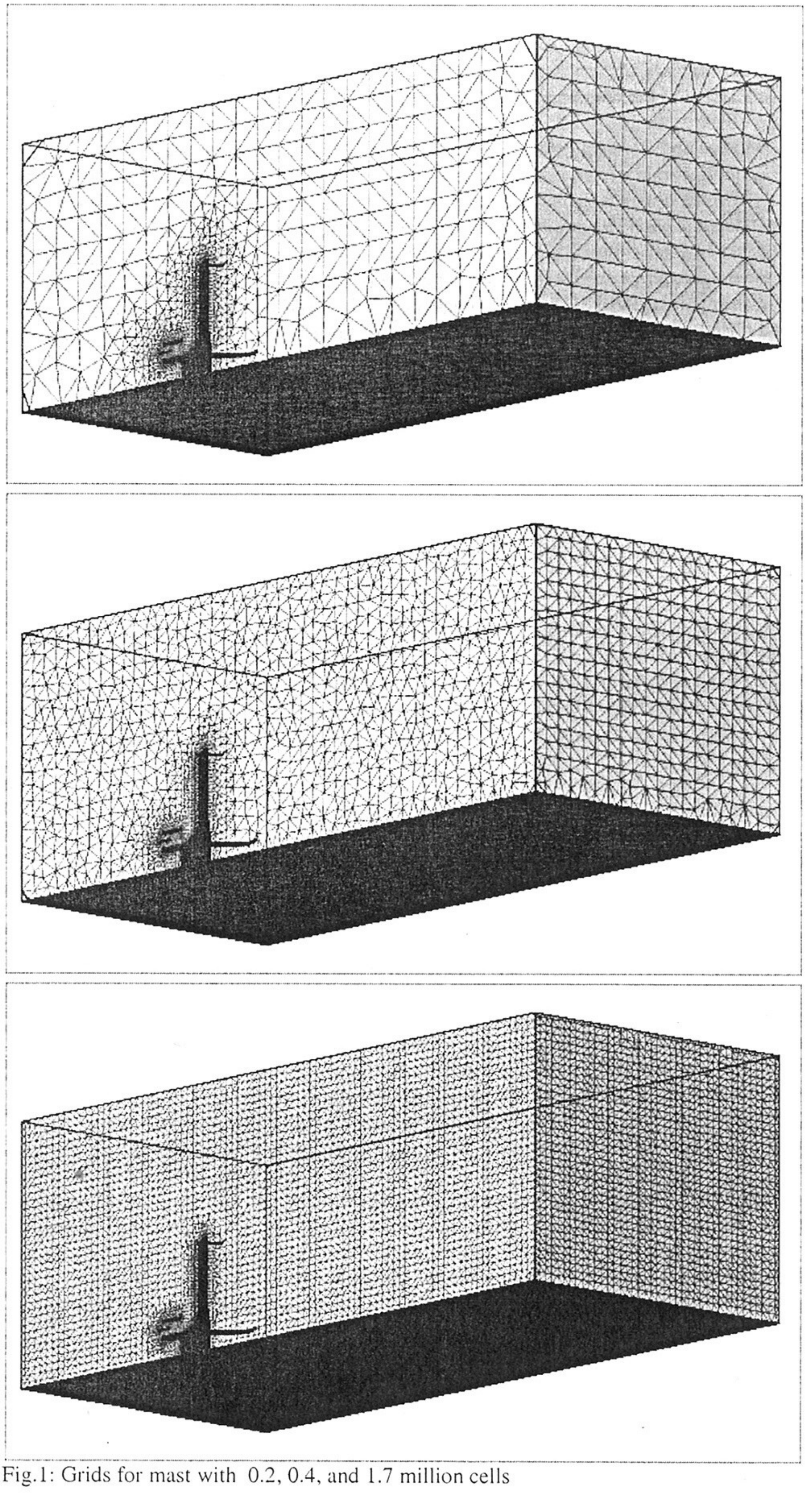

Fig.1: Grids for mast with 0.2, 0.4, and 1.7 million cells

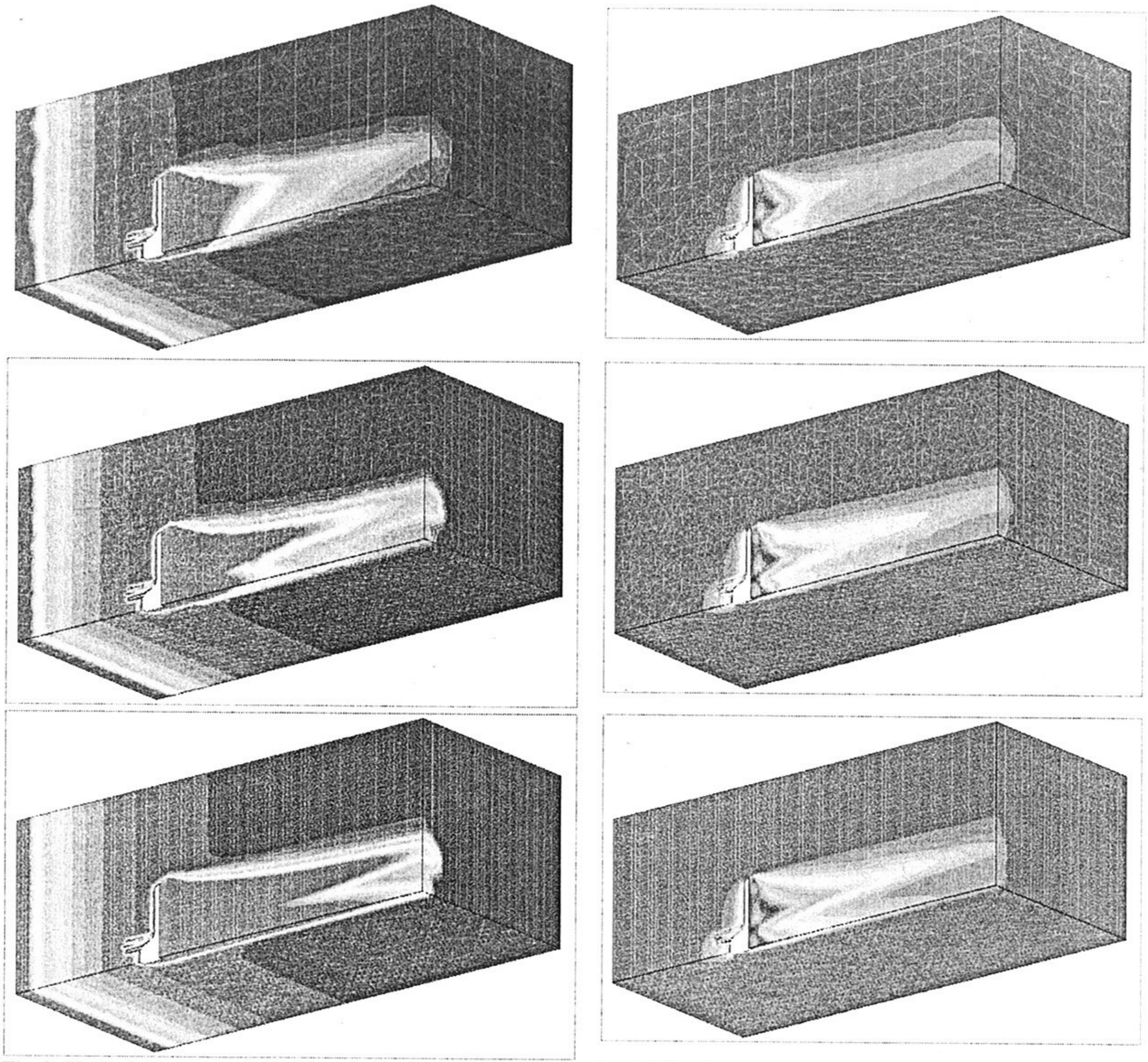

Fig.2: Turbulent energy k (left) and absolute value of velocity (right) for 3 grids, geometric model of mast

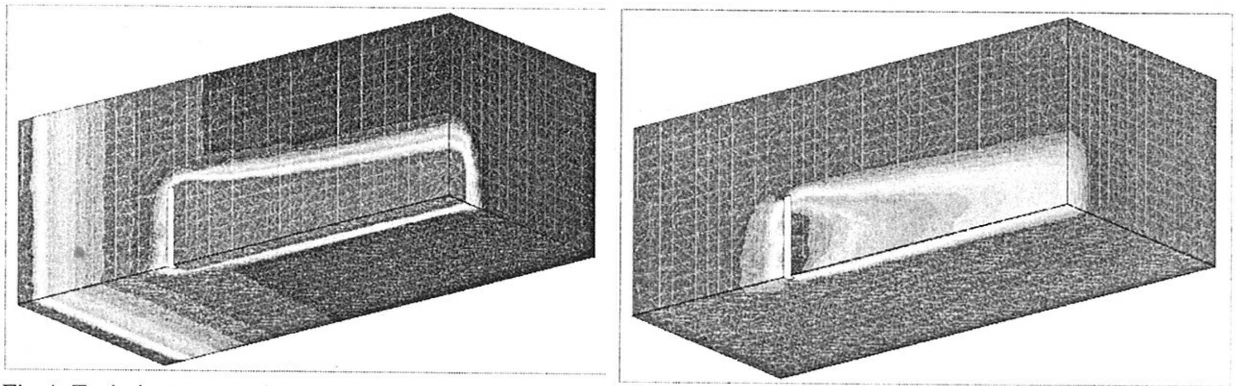

Fig.4: Turbulent energy k and absolute value of velocity for simple block

LINDENAU, O.; BERTRAM, V.; EL MOCTAR, O.M.; GATCHELL, S. (2002), *Aerodynamic simulations for an SES employing virtual reality post-processing techniques*, HIPER'02, Bergen

SCHMODE, D.; BERTRAM, V. (2002), *Aerodynamic flow computations for a Superfast ferry*, 3rd High-Performance Marine Vehicles Conf. HIPER'02, Bergen

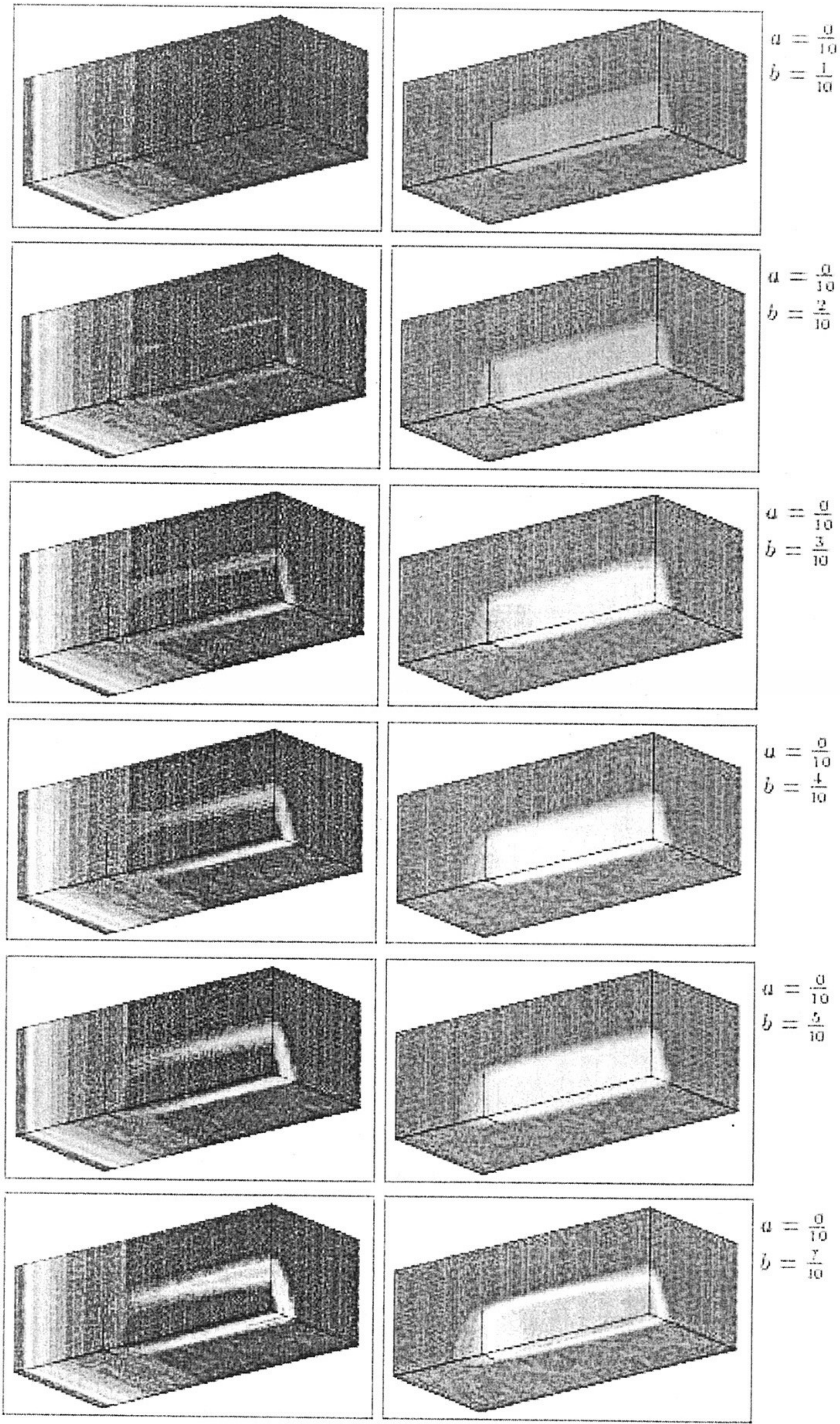

Fig.3: Baffle elements with a=0 and various values for b

Forward speed effects on diffraction-radiation computations

J.P.Boin[1], M.Guilbaud[1] and M.Ba[2]
Laboratoire d'Etudes Aérodynamiques (UMR CNRS n°6609)
[1]CEAT-University of Poitiers, 43 rue de l'Aérodrome 86036 Poitiers, France
Tel.: 33-5-49-36-60-27; Fax: 33-5-49-36-60-01; e-mail michel.guilbaud@lea.univ-poitiers.fr;
jeanphilippe.boin@free.fr
[2]ENSMA, 1 rue C. Ader, BP 40109, 86960 Futuroscope Chasseneuil Cedex, France
Tel.: 33-5-49-49-80-87; Fax: 33-5-49-49-80-89; e-mail: ba@lea.ensma.fr

Introduction

We have presented recently seakeeping computations, code Aquaplus (Nantes) and Poseidon (Poitiers), in the frequency domain, with the diffraction-radiation with forward speed Green function in a linear formulation, Delhommeau et al. [1], Ba et al. [2]. The main feature of these methods is to replace the computations of the Green function or of its derivatives by their boundary integration after having interchange the boundary and Fourier integrations, reducing thus the difficulties of calculations. A Stokes theorem is used in order to transform the boundary integrations into contour ones which are performed analytically, see Boin [3] or Maury [4] for details. As we intent to develop the computer code Poseidon in case of lifting flows, all the different cases of integration appearing in the expressions, deduced from the 3rd Green identity, to calculate the unsteady velocity potential and the velocity in a first order panel method have been studied. They concern integrations on panels, on waterline segments, on semi-infinite strips of the function itself or of its first or second derivatives. We use the this Green function as defined by the formulation of Guevel and Bougis [5], modified later by Delhommeau [6], and by Ba and Guilbaud [7] to obtain a practical method of computation. The analysis of the difficulties is presented and the influence of the forward speed has been considered. Finally, added-mass and damping coefficients on a semi-submerged ellipsoid are presented for various Froude numbers. The influence of the coupling with the steady potential either uniform, double body or Neumann-Kelvin flows, is considered, for a Wigley hull and a VLCChull, following Fang [8], but with the unsteady Green function corresponding to forward speed.

Problem to solve

The diffraction-radiation irrotational flow of an inviscid and incompressible fluid around a ship hull having a constant forward speed U is considered. A frame of coordinates fixed to the mean position of the body is used. The velocity potential can be separated into steady f_s and unsteady $\tilde{f}e^{iwt}$ parts, with w, the angular frequency. Both have to satisfy the Laplace equation, the body and the corresponding linearized free-surface boundary conditions and convenient conditions at infinity. In most of the studies, the potential f_s is taken as the potential of the uniform free-stream flow, but other choices can be done, [8]. The 3rd Green's formula leads to an integral equation, involving the corresponding Green function $\tilde{G}e^{iwt}$ and its derivatives, enabling to compute the potential and, by derivation, the velocity. This last equation, after discretisation of the body, leads to a linear system of equations through the body condition. After having solved this system, the pressure can be computed (involving both potential and its derivative for the unsteady part) and by integration on the body, forces and moments. The main difficulty is to compute the influence coefficients of the system, corresponding for a first order panel method, to the calculations of the integrations of the Green function or of its derivatives on an elementary panel S_j or on elementary segment C_j of the waterline if no lifting flow is considered:

$$\iint_{S_j} \tilde{G}dS; \quad \int_{C_j} \tilde{G}dy; \quad \iint_{S_j} \frac{\partial \tilde{G}}{\partial n_{M'}} dS; \quad \int_{C_j} \frac{\partial \tilde{G}}{\partial n_{M'}} dy$$

In the case of lifting flow, a doublet distribution on the body central plane and on semi-infinite strips extending from the trailing edge (where a Kutta-Joukowsky condition has to be satisfied) to downstream infinity with intensity, $\tilde{\mu}$, is considered. This intensity, proportional to the circulation, is linked to the intensity at the trailing edge x_{TE} on each strip k, $\tilde{\mu}_{TE_k}$. In the wake, the doublet intensity is related to $\tilde{\mu}_{TE_k}$, see Nontakaew et al. [9], by :

$$\tilde{\mu}_k(M,\omega) = \tilde{\mu}_{TE_k} e^{i\omega(x_M - x_{TE})/U_\infty}$$

So, extra integrations of the following quantities have also to be performed:

$$\iint_{S_j} \frac{\partial \tilde{G}}{\partial n_{M'}} dS ; \iint_{\Sigma_{h}} e^{i\omega(x_M - x_{TE})/U_\infty} \frac{\partial \tilde{G}}{\partial n_{M'}} dS \ ; \iint_{S_j} \frac{\partial^2 \tilde{G}}{\partial n_M \partial n_{M'}} dS ; \iint_{\Sigma_{h}} e^{i\omega(x_M - x_{TE})/U_\infty} \frac{\partial^2 \tilde{G}}{\partial n_M \partial n_{M'}} dS \ ,$$

where Σ_{h} is a semi-infinite strip of the wake

Numerical method and accuracy of the boundary integrations

The formulation of the diffraction-radiation with forward speed Green function, derived in [5], is used. The Green function is divided in three terms $\tilde{G} = G_0 + G_1 + conjg(G_2)$. The first one G_0 is the Rankine terms (including the source and its symmetric with respect to the free-surface); the two other ones, G_1 and G_2 are the Froude dependant part and are defined by integrals. For example, for G_1 :

$$G_1(M,M') = \frac{1}{\pi Lo} \left\{ \int_0^{\pi/2} \frac{K_1[g_1(K_1\xi) + g_1(K_1\xi')] - K_2[g_1(K_2\xi) + g_1(K_2\xi')]}{\sqrt{1+4\tau\cos\theta}} d\theta \right\}$$

G_2 has a similar definition but is more complex (several integrals and an extra term). The poles appearing in G_1 and G_2 are very similar to pole K_j defined by:

$$K_j = \frac{1 + a_j 2\tau\cos\theta + (i)^{2i}\sqrt{1 + a_j 4\tau\cos\theta}}{2F^2\cos^2\theta}, j = 1 \text{ to } 4, \text{with } a_j = 1 \text{ if } j = 1,2 \text{ or } a_j = -1 \text{ if } j = 3,4.$$

where $i = \sqrt{-1}$. $F = U/\sqrt{gL}$ is the Froude number and $\tau = \omega U/g$, the Brard parameter, L the body length; details can be found in [3]. Using a Stokes theorem, the various integrations of the functions G_1 and G_2 on a polygonal panel with m nodes are transformed into a contour integral:

$$I_s = \iint_s \frac{d^2}{d\chi^2} f(\chi)\, ds' = \sum_{k=1}^{m} C_k \frac{f(\chi_{k+1}) - f(\chi_k)}{\chi_{k+1} - \chi_k}$$

where $\chi = K\xi \ or \ K\xi'$ are complex linear functions of the Cartesian coordinates and K is one of the pole (a non zero complex). The numerical integration of the Fourier integrals are performed through a Adaptive Simpson method, using a size of the integration step decreasing when the integrand has steep variation, [9].

The difficulty of the computations of these Fourier integrals can be directly related to the power α of poles of the Green function, or more precisely to the power of the trigonometric functions included into it (the weaker the power of the cosine, the larger the oscillations of the integrand). Table 1 presents the powers of the poles involved in the calculations.

Values of α	$\int_s ds'$	$\int_{y'_2}^{y'_2} dy'$	$\iint_\Sigma ds'$	Function
$G(M,M')$	2	0	0	-2
$\partial G(M,M')/\partial x_i$	0	-2	-2	-4
$\partial^2 G(M,M')/\partial x_i \partial x_j$	-2	-4	-4	-6

Table1 : Power of the cosine in the Fourier integrals

Grey zones in table 1 are for the computations not used in a classical panel method. From this table, the different calculations can be classified by a level of difficulty, from level 1 to level 7, figure 1. The difficulties decrease for the various integrations when compared to the function itself. For a given field point, the computation of the velocity induced by the wake ($\alpha = -4$; level 7) is the most difficult to perform. Three calculations involve the same power of cosine (α = -2; level 4 to 6), $\iint_{s_j} \partial^2 G / \partial x_i \partial x_j ds'$ on a panel, $\int_{y'_1}^{y'_2} \partial G / \partial x_i dy'$ on the waterline and $\iint_{\Sigma_{BI}} \partial G / \partial x_i ds'$ in the wake. Other factors enable here to classify the difficulties. The waterline integral is always the most difficult, due to $z'=0$. The integral on the unsteady wake uses two successive numerical integrations, in z' and the other in θ. The waterline integration of the Green function and the integration of the first derivative on a panel are simpler (α=0; level 2 and 3). For the same reasons as previously, the integration on the waterline is the more difficult to calculate of the two. Finally, the simplest calculation is for the boundary integral of G on a panel (α = 2; level 1).

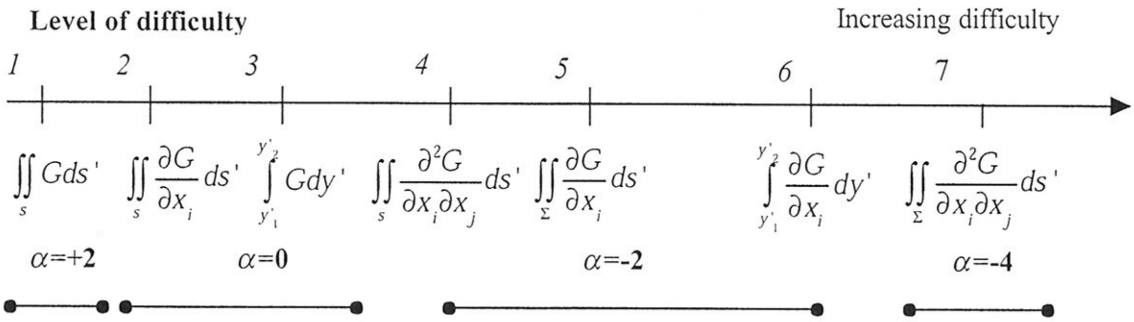

Figure 1 : Scale of the difficulties of the calculations for the Fourier integrations

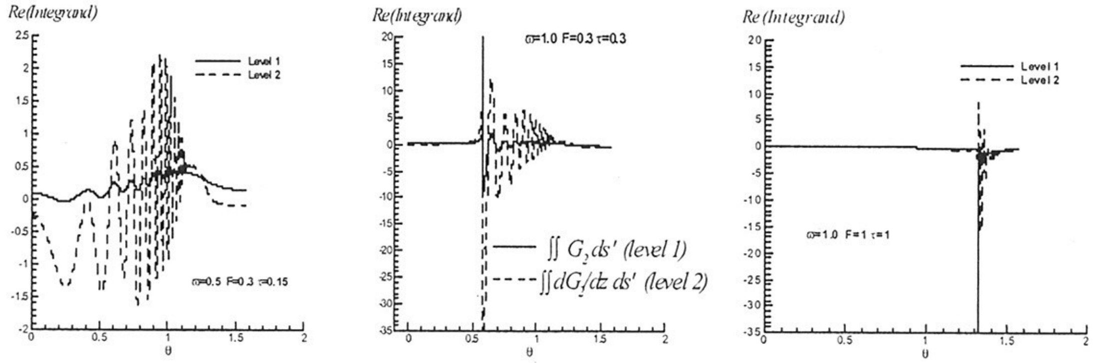

Figure 2 : Integrands of levels 1 and 2 for function G_2

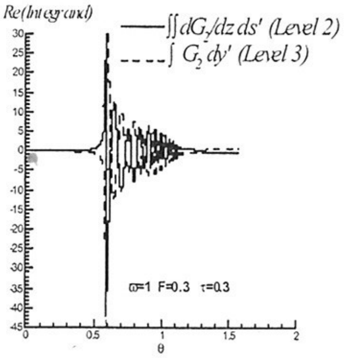

Figure 3 Integrands of levels 2 and 3 for function G_2

As an example, we illustrate the behaviour of the integrands for a given field point $M(-2,1,-0.1)$ and a source panel defined by 4 nodes : $M'_1\left(X=\sqrt{3}/4, Y=0.25, 0\right)$, $M'_2(-X,-Y,0)$; M'_3 and M'_4 are under the two previous ones but with $z=-1$. Calculations are performed for 2 values of the Froude number, F=0.3 and 1, with a reduced circular frequency, ν = 0.5 and 1; (with $\nu = w\sqrt{L_0/g}$, Lo= 1m), corresponding to τ=0.15, 0.3 and 1. Figure 2 and 3 plot the real part of the integrand in θ for function G_2 only, (more difficult to calculate). The amplitudes of the oscillations for G_1 have similar shape but are about 10 times smaller than for G_2. The comparison of the integration of the Green function and of its z derivative over a panel, figures 2, shows that the integrand is more oscillating as the difficulty level increases. It can be observed that the amplitudes of the oscillations of the functions increase with t. For τ>1, the absolute values of the integrands become very weak with weak oscillations. Some exceptions to the predictions of Table 1 occur: a more difficult integration on a waterline segment of the Green function than on the integration of the first derivative on a panel is predicted, but the integrands are quite similar, (cf. figure 3 for the comparison of the integrands of the z-derivative of G_2 on a panel and of the function on a waterline segment). This fact can be explained because the panel contour includes a branch on the free surface and that the difficulties tied to the segment at z'=0 are present in the two integrals.

Close to the free-surface, the integrands oscillate with an indefinitely increasing amplitude and frequency. To illustrate this problem, the behaviour of the integrand of the Green function on a waterline segment is studied for two different depths of submersion of the field point M ($z=-10^{-3}$ and -10^{-5}) and two Froude numbers $F=0.3$ and 1 on figure 4 in the same conditions as previously. As predicted, the difficulties appear for $\theta \rightarrow \pi/2$, due to the poles. If $z \neq 0$, the integral tends also to zero but less and less rapidly, with an increasing frequency of the oscillations when $z \rightarrow 0$. The integration is still possible if enough points are chosen. But for z=0, there is no more convergence and this frequency tends to infinity for $\pi/2$. Then the integral is no more defined. Close to the free-surface, integrals are calculated using an extrapolation for the value at z=0, because the integrals on the Green function (or derivatives) have no oscillation when the field point describes the z-axis. As the Froude number increases, the oscillations are shifted closer to $\theta = \pi / 2$.

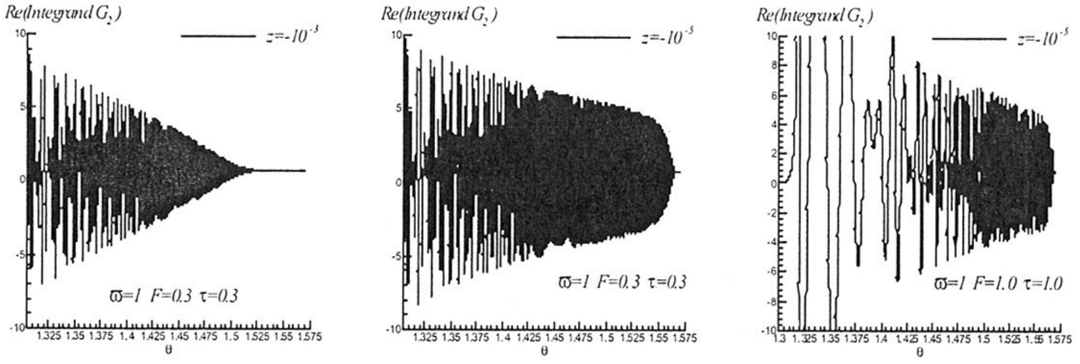

Figure 4: Behaviour of the real part of the integrand for G_2 close to the free surface,

Added-mass and damping coefficients

Semi-submerged ellipsoid

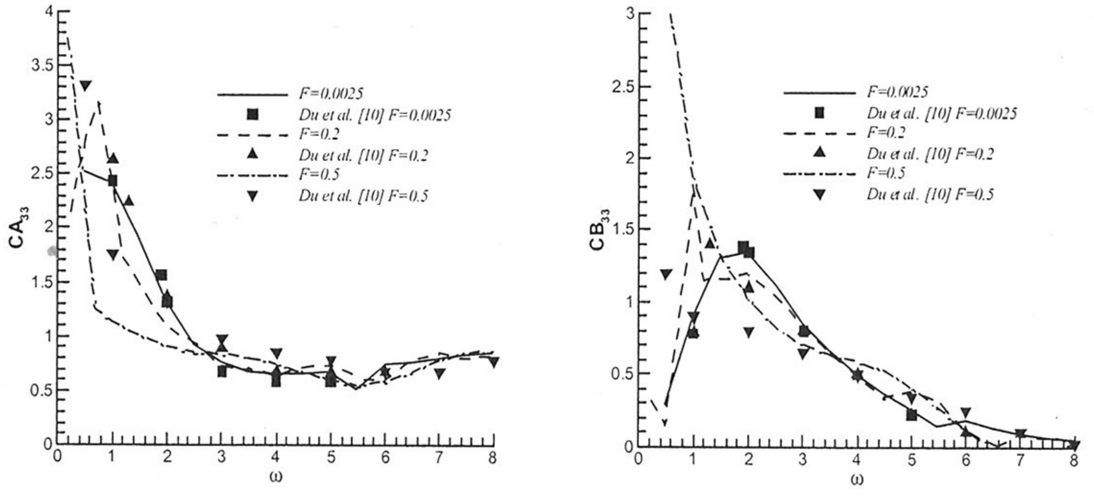

a) Added-mass *b) Damping*

Fig. 5 Unsteady coefficients on a surface-piercing ellipsoid (1:8) versus the reduced frequency at various Froude numbers

Added mass a_{ij} and damping coefficients b_{ij} are given by:

$$a_{ij} = \frac{1}{w^2}\Re\left[-r\iint_S (iw - \nabla f_s \cdot \nabla) n_i f_j ds\right]; b_{ij} = \frac{1}{w}\Re\left[-r\iint_S (iw - \nabla f_s \cdot \nabla) n_i f_j ds\right]$$

where f_s represents the potential of the steady flow. Figure 5 plots the results of the added-mass and damping coefficients A_{33} and B_{33} for heave motion versus the reduced frequency $\tilde{\omega}$ for the surface-piercing ellipsoid (axis ratio 8:1), already studied by Du et al. [10], at various Froude numbers with a number of panels N=480. The results of the present method are in good agreement with the ones of [10] at lower Froude numbers F; as F increases, some discrepancies appear, may be due to the different methods of calculation of the waterline integral which become more difficult to compute accurately. Influence of the forward speed is effective only at low frequency and decreases when this frequency increases.Except at the lower values of the frequency, A_{33} decreases and B_{33} increases as the Froude number increases.

Wigley hull

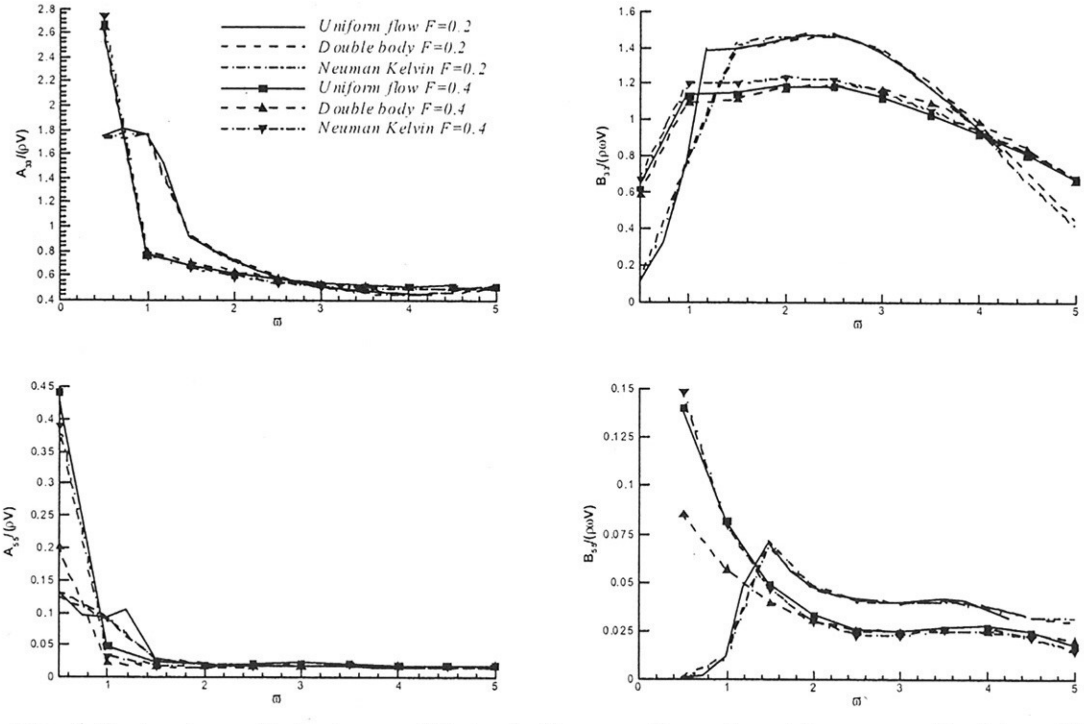

Fig. 6 Unsteady coefficients on a Wigley hull versus the reduced frequency (F=0.2 and 0.4)

The influence of the choice of the steady potential is important. This problem has been study in [8], using as steady flow potential either the one of uniform flow or the one of Neumann-Kelvin flow, but with an unsteady Green function not accounting for the forward speed (only encounter frequency assumption). Here the three different steady flow potentials are used. The unsteady flow is here one of the 6 different radiation potentials $f_j, j = 1 \, to \, 6$. Figure 6 plots pure added-mass and damping coefficients for heave and pitch motions versus the non dimensional frequency for the three different steady potentials (uniform, double body and Neumann-Kelvin) for F=0.2 and 0.4. The results at F=0.2 for the uniform flow as steady potential have been shown to be in good agreement with other method of calculations for Series 60 hulls or Wigley hull, [1,2] and [3]. As already mentioned in [8], for Series 60 or Wigley hulls, the influence of the steady potential is weak, particularly for heave motion, and restricted to lower values of the frequency. Figure 6 shows, particularly for pitch motion, that this influence, always restricted to low frequencies, increases with the Froude number; the double body calculations give lower values of both added-mass and damping coefficients. The difference decreases as the frequency increase and become quite negligible for v >2.5.

VLCC hull

Similar results are given on figure 7 for a VLCC hull at F=0.2. Here also, the influence of the steady potential chosen is negligible on A_{33} but for the others coefficients, it can be observed on the whole set of the values of the frequency. For A_{55}, the values of the added-mass coefficients increases from the Neumann-Kelvin, to the double body and to the uniform flow steady potential; for the damping coefficients, A_{33} or B_{55}, for the same steady potentials, these coefficients increases.

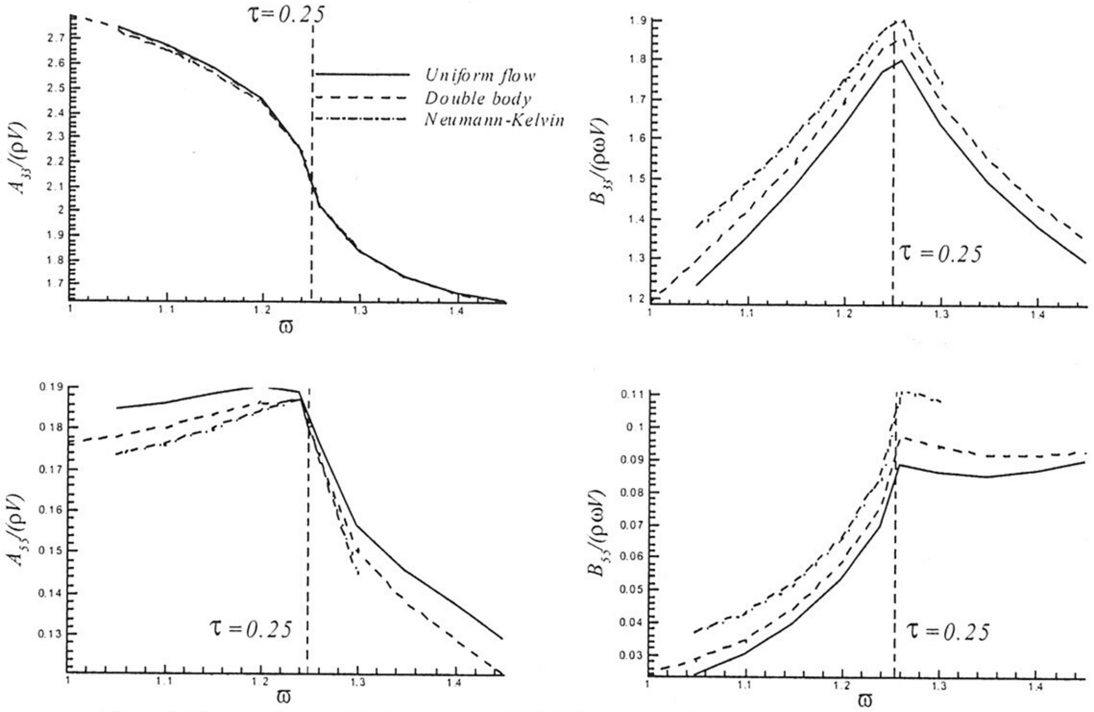

Fig. 7 Unsteady coefficients on a VLCC versus the reduced frequency (F=0.2)

References

[1] Delhommeau G., Maury C., Boin J.-P., Guilbaud M. and Ba M., "Influence of waterline integral and irregular frequencies in seakeeping computations", 4th Num. tank Symposium, Hamburg, 2001.

[2] Ba M., Boin J.-P., Delhommeau G., Guilbaud M. et Maury C., "Sur l'intégrale de ligne et les fréquences irrégulières dans les calculs de tenue à la mer avec la fonction de Green de diffraction-radiation avec vitesse d'avance", C.R. Acad. Sci. Paris, t.329, Série IIb, 141-181, 2001.

[3] Boin J.-P., "Calcul des efforts hydrodynamiques sur un navire soumis à une houle régulière; applications d'une méthode de singularités de Kelvin", Thèse de doctorat, Université de Poitiers, 2001.

[4] Maury C., "Etude du problème de tenue à la mer avec vitesse d'avance quelconque par une méthode de singularité de Kelvin", Thèse de doctorat, Ecole Centrale et Université de Nantes, 2000.

[5] Guével P. and Bougis J., "Ship motions with forward speed in infinite depth", Int. Ship. Progress, **29**, 103-117, 1982.

[6] Delhommeau G., "Les problèmes de diffraction-radiation et de résistance de vagues: Etude théorique et résolution numérique par la méthode des singularités", Thèse de doctorat d'état, Ecole Centrale et Université de Nantes, 1987.

[7] Ba M., and Guilbaud M., "A fast method of evaluation for the translating and pulsating Green's function", Ship Tech. Res., **42**, 68-80, 1995.

[8] Fang M.-C., "The effect of steady flow potential on the motions of a moving ship in waves", J. of Ship Res., **44**, 1, 14-32, 2000.

[9] Nontakaew U., Ba M. and Guilbaud M., "Solving a radiation problem with forward speed using a lifting surface method with a Green's function", Aerospace Science and Technology, **8**, 533-43, 1997.

[10] Du S., Hudson D.A., Price W.G. and Temarel P., "Comparison of numerical evaluation techniques for the hydrodynamic analysis of a ship travelling in waves", *Trans. RINA*, **141**, 236-258, 1999.

Sea keeping simulation of fast hard chine vessels using RANSE

Mario Caponnetto
Rolla Research, Via Silva 5, Balerna (Switzerland)

Introduction

The design of an hard chine vessel requires, more then for other kind of boats and ships, a trade off between calm water resistance and sea keeping qualities. Following Savitsky theory the prismatic hull of minimal resistance, above a certain speed, if a flat hull. Even if we consider hulls more complex then a Savitky prism, the deadrise angle remains a fundamental parameter for calm water resistance and this angle should be minimized, whatever the other parameters are (beam, LCG...). Keeping all the rest fix, a flat hull generates more lift, allowing a lower trim angle (less wave drag) and less wetted surface (less friction drag). In waves a flat hull is one of the worst shape we can image. Large impact pressures are suddenly generated as the waves hit the bottom; this creates structural problems as well as vertical accelerations that can be hardly sustained by the crew. In practice a deadrise angle is always necessary but the amount of vee-shape depends on speed, boat dimensions and expected waves size. Modern boats are seldom prismatic, and have a deadrise angle that varies along the boat length. Depending on the applications, this angle may vary from 10/20 degrees at the transom to 20/50 degrees near to the bow, where impact pressure are expected to be higher. This so called "warped" hulls pose new problems to the naval architects. First, Savitky theory can't be used to calculate calm water trim and resistance of warped hulls. Second, there is a lack of data usable to predict sea-keeping qualities of warped (but even prismatic) hulls. Reasonably the more deadrise angle we give the better the sea keeping qualities, and worst the calm water performances, will be, but when to stop?
A couple of years ago we started trying to answer the problem of calm water calculation of fast hard chine vessels, bypassing the somehow crude approximations of the Savitky theory. The method we investigated to deal with this problem is a RANSE solver where the complex behavior of the free surface is computed with a special kind of VOF (Volume of Fluid) method. The commercial code ***Comet*** was tested among others, giving the best results (ref. 1, 2). Since then, many hulls have been tested, designed and optimized by our Company and the method is now a valuable tool for a number of leading shipyards in the nautical market. The step forward required by the designers is the possibility to compute sea keeping. The natural way to approach this problem is to use the unsteady and moving mesh capabilities of ***Comet***; some of the results obtained by now will be presented in the paper.

1. Overview of the method

1.1 Main features of the solver

For both steady (calm water) and unsteady (sea keeping) computations, a Finite Volume Method is used to solve the Navier-Stokes equations. Turbulence, of minor importance for this type of problem, is approximated using a K-epsilon model. The main feature of the code is the possibility to solve very complex behaviors of the free surface, typical of planing hulls. The Front Capturing Method built in the program can easily compute spray, breaking and overturning waves, detachment and reattachment of the flow along the chine, the side hull and the transom, and, in some extent, the ventilation of the hull. Details of the method can be found if ref. 3, 4.

1.2 Mesh generation

Structured or unstructured meshes can be handle by ***Comet***, as well as blocks of cells with not matching vertices. As far as the hull is a conventional hard chine vessel, we have found that the best results in terms of precision, as well as time spent to generate the mesh, are obtained with a structured mesh formed by hexahedral cells. This approach is somehow mandatory, as will be explained later, if the hull must be moved in a time domain simulation.

A Fortran code has been developed to build the structured mesh. The code loads the geometry of the hull and generates all the files needed to the solver (vertex coordinates, cells, regions…). The stretching of the cells in regions were a higher or lower resolution of the flow is required, can be easily controlled playing on a number of parameters. In general we want to increase cell density near to the hull and the free surface. Moreover the hull is placed in space giving in input a value for the trim and the sink, but in theory we can give all the 6 degrees of freedom. The hull, deck and transom are discretised. Special care is dedicated to the proper definition of the chine and the spray rails. Flaps, tunnels and skeg can be also modeled. A typical surface mesh of the hull is shown in figures 1 and 2.

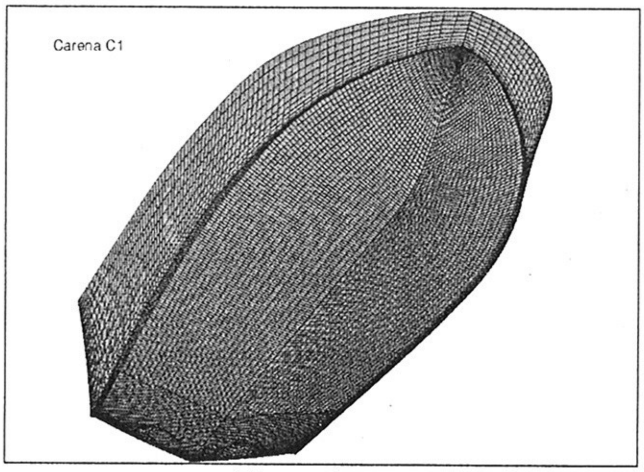

Figure 1

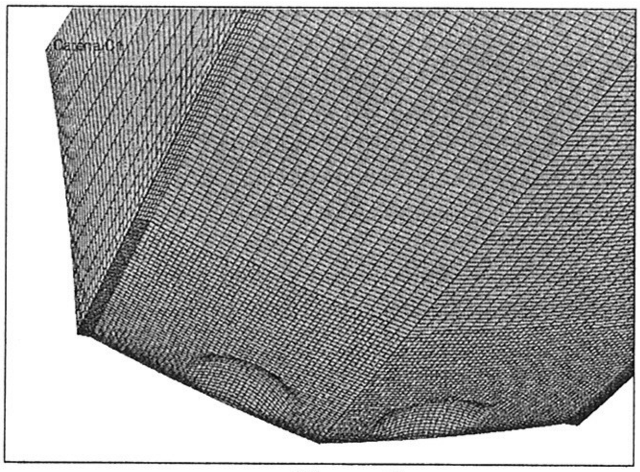

Figure 2

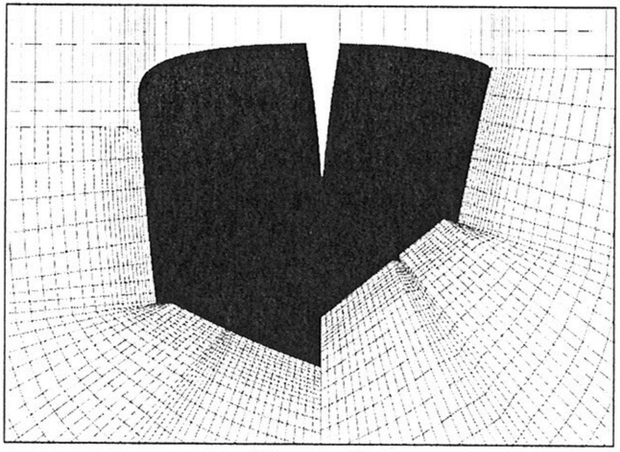

Figure 3

Figure 3 shows crosscuts of the volume mesh in two transversal planes near to the bow (right) and the stern (left). Local refinements can be done (as visible in figure 2) splitting a cell in a number of sub-cells.

The time required to build all the files needed to feed the solver is very short; about 10 seconds for a typical mesh having 200.000 cells.

1.3 Moveable mesh

In a sea keeping simulation the hull will change its relative position in the calculation domain at each new time step. By now we are dealing only with two degrees of freedom (trim and sink), since only bow waves are considered. Surge movements can be of some importance with higher waves, and can be added in the simulation, but this possibility haven't been tested yet.

At each time step updated values for the trim and sink will be supplied to the mesh program to built the new mesh. The cell vertices along the external boundary of the computational domain remains fixed, while those over the hull are moved rigidly of the right amount. All the vertices in between will be consistently moved of a fraction of the hull movements, but keeping the same topology. Cells and vertices numeration remains the same. Each cell will keep its "identity" and will be formed by the same vertices, simply moved of a small quantity. In this way the solver can restart without the additional efforts needed to interpolate the old variable (pressure, velocity...) to the new cells; computational time and convergence rate is speeded up.

1.4 Boundary, initial conditions and time step

Regular bow waves or a "sequence" of waves with different lengths and highs can be generated. Since no surge movement is considered, the boat is fixed longitudinally in an "average" flow having a speed opposite to the boat speed Vb. Sinusoidal waves are enforced at the inlet; calling Lw the length of the wave and Hw its high, the wave profile at the inlet (h) will vary with time (t) in the following way:

$$h = \tfrac{1}{2} Hw * \cos(\omega_e t) \quad where: \quad \omega_e = \omega + \frac{Vb}{g}\omega^2 \quad and \quad \omega = \sqrt{\frac{2\pi g}{L_w}}$$

At the inlet both air and water are blown in the domain. The cells whose centroid lies below h will inject water, the remaining air. Since h changes with time, there are cells that will change periodically the injected phase. The cells whose boundary surface is intersected by the local free surface will have a mixed phase proportional to the area below and above the free surface. Pressure and velocity boundary conditions are enforced. Above the free surface the air speed and pressure are set to Vb and Patm. Below the expressions for the pressure, horizontal and vertical velocities of a linear Airy wave (ref. 5) are used, but shifted from the undisturbed water level (h=0) to the actual free surface. This approximation has proven to produce in practice very regular waves, whose length and high can be easily controlled, as far as the slope of the wave is not too high.

The initial free surface is flat, the flow is initialized with V=Vb and the pressure is P=Patm for the air and P=Patm +rho*g*z for the water. This pressure condition is also applied to the outlet. To allow a smooth launch of the computation, the real wave high at in inlet is let to grow linearly from zero to Hw in about one encounter period.

Time step remains constant during the simulation and its value is normally set according to a Courant number of 0.15, calculated with the boat speed and the average length of the cells along the hull. For each time step a maximum of 30 iterations is allowed to reach convergence. The simulation is carried on until about 10 waves are encountered, but usually the phenomenon becomes periodic at the third or fourth encountered wave.

1.5 Forces and moments calculation

At the end of each time step the pressure over the hull is know and the vertical force and moment around the center of gravity can be calculated. Vertical and angular accelerations are then used to compute the new trim and sink for the next time step.

A problem arise from some numerical fluctuation of the calculated pressure distribution and forces between an iteration and the next one. Due to this small oscillations, even in calm water, a boat left free to heave and trim should manifest continuous small movement around the mean position. This problem has been found to be amplified in the unsteady calculations.

To prevent this phenomenon a quadratic least square fit of the vertical force (and moment) is performed on a number of time steps preceding the last one (figure 4). The fitting function is extrapolated to the next time step to compute an average force and moment suitable to calculate the trim and sink changes.

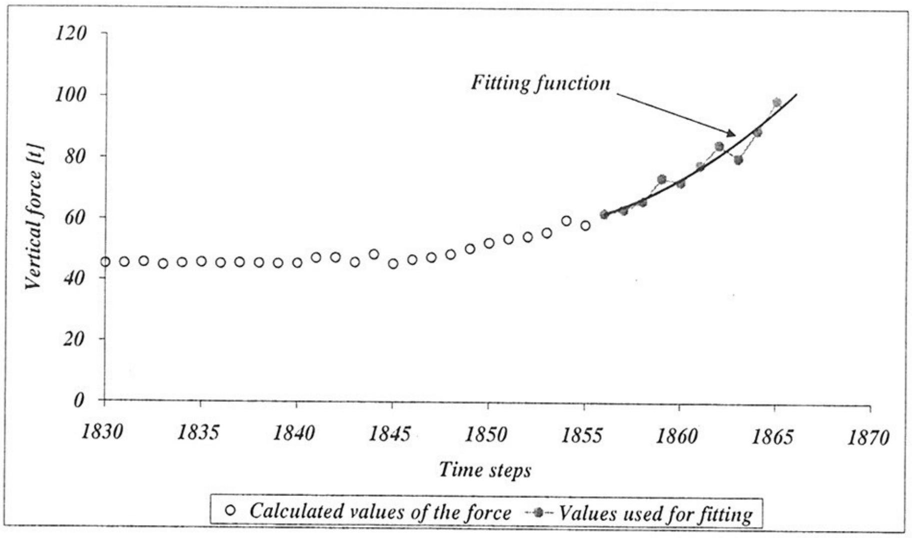

Figure 4

2. *Sample cases*

The code has been already used to perform sea keeping calculation for a number of planing hulls. Typically we have to deal with boats whose length ranges between 15 to 40 meters, and speed from 25 to 60 knots and above. For this kind of applications we have a lack of experimental data (in full or model scale) useful to validate the method.

What has been done by now is to check the robustness of the method and to perform convergence and mesh sensitivity tests. What can be said is that the accelerations computed are realistic. The code is very robust, since typically 5000 time steps are completed without crashes in the 90% of the cases. As far as accelerations are concerned, the results are converged with about 100.000 cells (for one half of the physical domain considering the lateral symmetry of the problem). Changes of hull geometry give qualitatively the expected results, and this is important in the perspective to rank different boats at the design stage.

It must be pointed out that, at difference of the typical behavior of conventional ships in waves, whose largest non linearity is the out coming of the bow off the water, very extreme situations have be encountered in our simulations. Sometimes the entire hull comes out of the water and then brutally hits the new incoming wave, rising the water above the deck.

Two cases are presented in the next figures as examples. In figure 5 a 24 meter boat moving at 45 knots is shown when coming near completely out of the water in a regular sea with Lw=30 m and Hw=2 m. Figure 6 shows the bow impact of a 35 meter yacht at 30 knots in similar wave conditions.

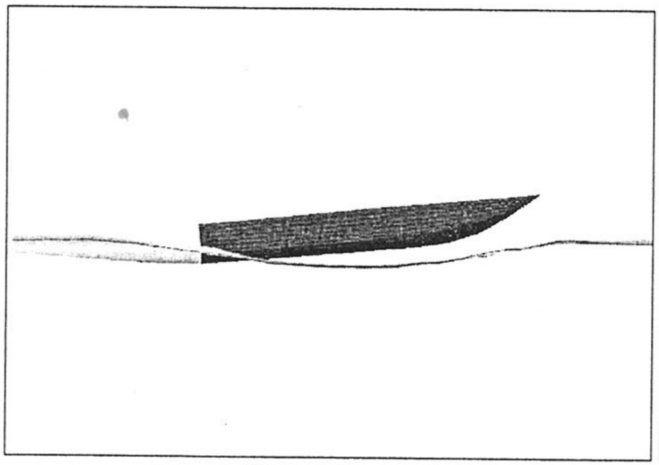

Figure 5

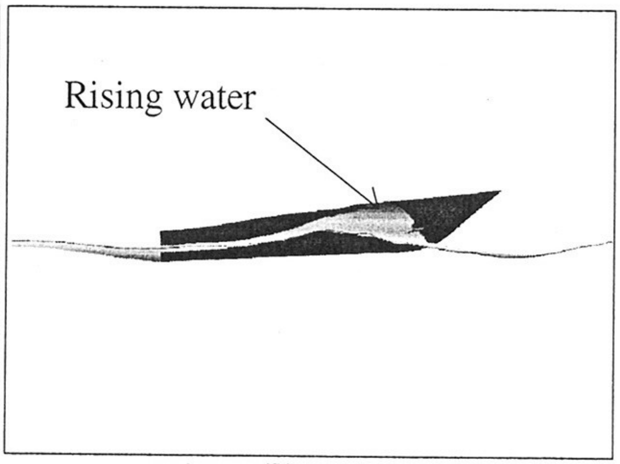

Figure 6

In these cases pressure impacts are huge, and probably to neglect hull flexibility, but instead considering the hull as a rigid body, doesn't respect sufficiently the real of the phenomenon. Moreover surge motion should probably be considered.

The next three figures show some samples of the trim, sink and vertical acceleration of the center of gravity time histories. The boat in question is 35 meter long and is running at 45 knots. Two waves are considered, Lw=20 m, Hw=1 m and Lw=30 m, Hw=1.5 m.

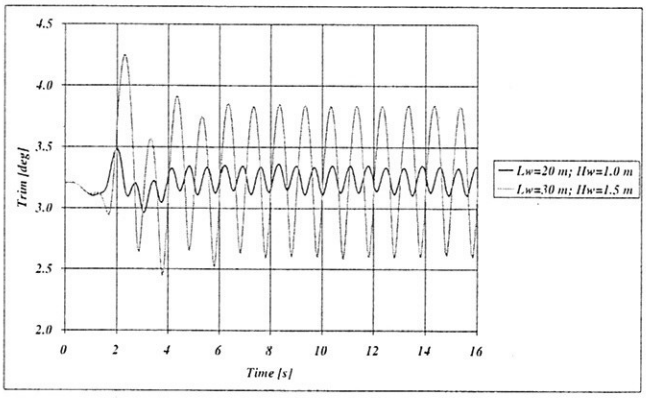

Figure 7

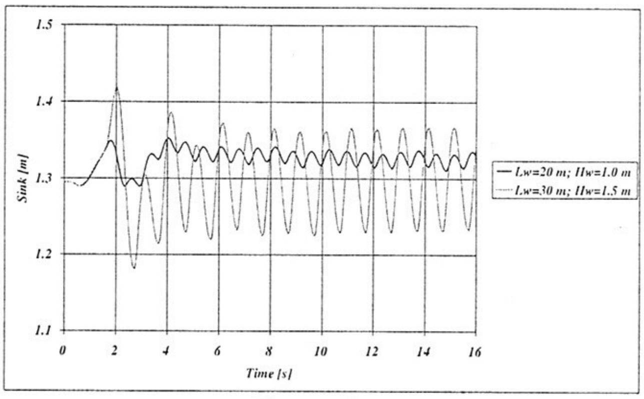

Figure 8

An other useful quantity derived is the time history of the drag, that integrated over time can give the "average" increase of drag, allowing an estimation of the speed reduction in waves. A sample is presented in figure 10, where the computation has been performed for a 90' Open yacht.

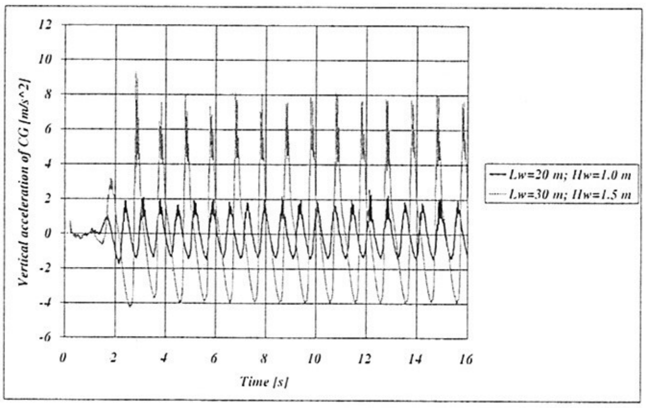

Figure 9

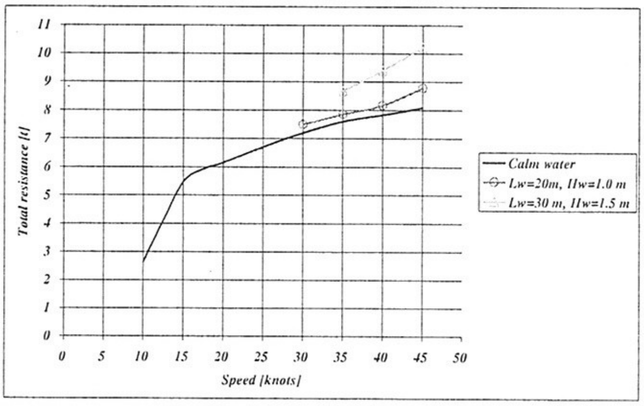

Figure

The next figures show the calculated pressure distribution, and the corresponding trim of the hull, at three different instants of the simulation. In the first frame be boat is nearly out of the water and there is only a small vee-shaped high pressure region ahead of the transom. After that the hull, falling down, hits the water all along the keel, and the impact pressure is maximum. The water is partly deflected by the spray rails. Finally the bow enters the incoming crest. Of course these data can be very useful for structural calculations.

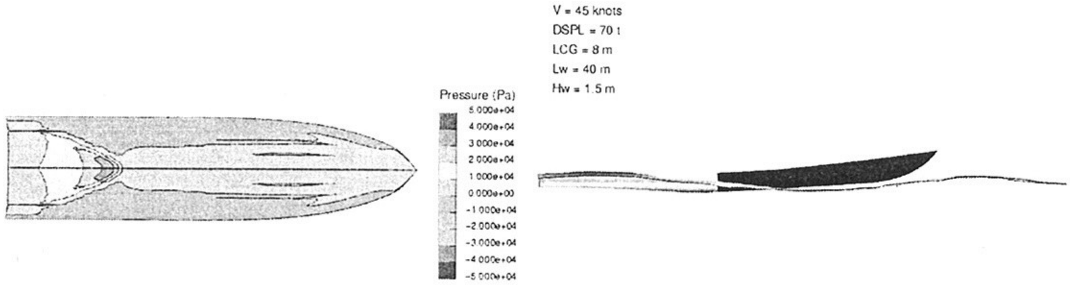

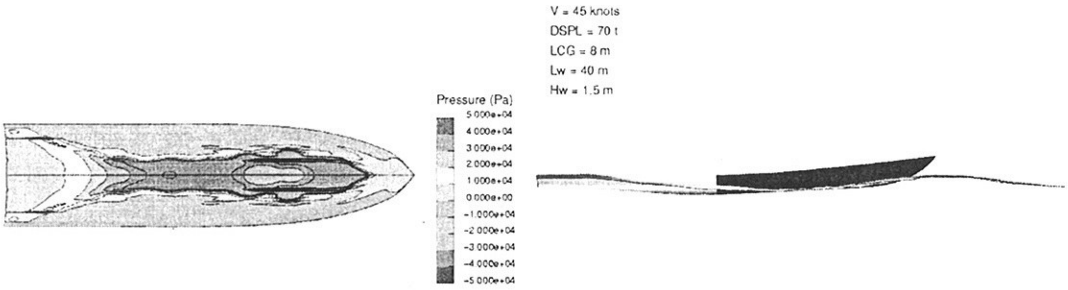

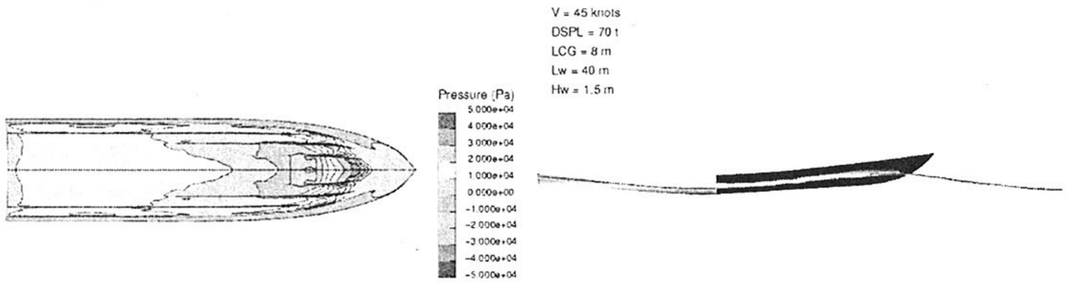

3. Conclusions

In the paper the need of a tool able to predict the sea keeping performances of hard chine vessels has been pointed out. The method investigated to face the problem if an unsteady CFD solver where the free surface is calculated using a VOF method. A code has been developed to allow the movement of the structured mesh with time. The boat is free to trim and sink, under the effect of regular bow waves generated at the inlet. The results obtained in the first tested case are still to be validated, but the code has been proven to be robust and supply qualitatively satisfactory results.

4. References

1. CAPONNETTO, M., "*Numerical Simulation of Planing Hulls*". Proceeding of the 3rd Numerical Towing Tank Symposium, 9-13 September, Tjärnö, Sweden.

2. CAPONNETTO, M. "*Practical CFD Simulations for Planing Hulls*". HIPER '01, 2-5 May, Hamburg, Germany.

3. FERZIGER, J, H, PERIC, M, "*Computational Methods for Fluid Dynamics*". Springer editions.

4. COMET version 2.00, User Manual.

5. BERTRAM, V. "*Practical Ship Hydro Dynamics*". Butterworth-Hainemann editions.

Numerical Simulaton of 2-Phase Flows by Smoothed Particle Hydrodynamics

Andrea Colagrossi and *Maurizio Landrini*

INSEAN, *The Italian Ship Model Basin*, Roma, Italy.
maulan@waves.insean.it

Introduction

Tulin and Landrini (2000), Landrini *et al.* (2001a, 2001b) applied the Smooth Particle Hydrodynamics method (SPH, see *e.g.* Monaghan 1988) to capture the basic features of wave breaking around ships. In particular, it has been highlithed and discussed the basic link between breaking processes, vorticity generation and air capturing. The latter implies the need of multi-phase modeling to study the long-term evolution of such flows. On this ground, we developed a two-phase version of the SPH method, Colagrossi *et al.* (2002), which improved the applicability of SPH to these problems. In this paper, we further extend this development and present the algorithmical details of the present SPH implementation. As a practical example, we consider the two-phase version of the classical dam-break problem, *e.g.* Colicchio *et al.* (2000). Namely, an initially rectangular column of heavy fluid is surrounded by a lighter one. Both media are contained within a rectangular tank.

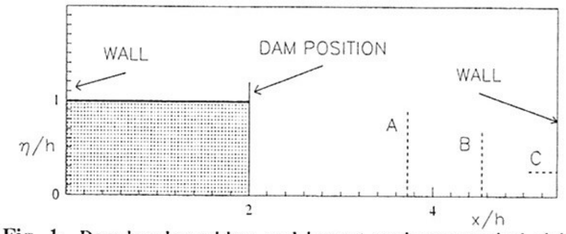

Fig. 1: Dam-break problem and impact against a vertical rigid wall. The geometrical parameters are chosen according to the experiments performed by Zhou *et al.* (1999) A-B: wave-gauges. C: pressure-transducer.

Basic aspects of the SPH method

In Smooth Particle Hydrodynamics, the fluid is divided into a collection of N particles interacting each other through evolution equations of the general form:

$$\begin{aligned} \frac{d\rho_i}{dt} &= -\rho_i \sum_j \mathcal{M}_{ij} \\ \frac{d\boldsymbol{u}_i}{dt} &= -\frac{1}{\rho_i} \sum_j \mathcal{F}_{ij} + \boldsymbol{f}_i \\ \frac{d\boldsymbol{x}_i}{dt} &= \boldsymbol{u}_i \end{aligned} \qquad (1)$$

The interaction terms $\mathcal{M}_{ij}$, $\mathcal{F}_{ij}$ follow from the Euler equations and contain the density ρ_i, the velocity $\boldsymbol{u}_i$ and the pressure p_i of the particles. The last equation in (1) describes the motion of the i-th particle.

The interaction terms $\boldsymbol{\mathcal{F}}_{ij}$ model (at least) the pressure interactions and contain the pressure p_i which here is uniquely determined by the value of the density ρ_i through a state equation of the form

$$p(\rho) = P_0 \left[\left(\frac{\rho}{\rho_0} \right)^{\gamma} - 1 \right] . \qquad (2)$$

The parameters P_0, ρ_0, γ are chosen to have maximum density oscillations of order of $\mathcal{O}(1\%)$ around the reference value ρ_0. In practice, this is accomplished by choosing the sound speed $c_s = dp/d\rho$ ten times or more larger than the highest fluid velocity expected in the physical problem. We note that the use of the actual speed of sound in water would imply a time-step too small for any practical use.

In this way, the solution of the Poisson equation for the pressure is avoided and the method does not require the solution of an algebraic problem. Therefore, the memory occupation is proportional to the number of particles, and the efficiency is rather high. The particles can be arbitrarily scattered over the fluid domain leading to a completely grid-free method.

The interaction terms can be computed independently of each other, resulting in an explicit method which can be easily implemented on parallel computers.

The method is rather robust, even for large free-surface fragmentation and folding, efficient, and relatively easy-to-code at least in its most naive implementation. Modeling of no-slip body boundary conditions and of turbulent flows are less obvious. Finally, the stability analysis of the method represents a difficult task. Some of these issues are discussed by Colagrossi *et al.* (2001).

Implementation details

The actual form of the interaction terms follows by discretizing the interpolation integral

$$\langle u(\boldsymbol{x}_P) \rangle = \int_\Omega u(\boldsymbol{x}^*)\, W(\boldsymbol{x}_P - \boldsymbol{x}^*; h)\, dV^* . \qquad (3)$$

In the original method, Monaghan adopted the following approximation to the velocity field and its gradient

$$\langle \boldsymbol{u}_i \rangle \simeq \sum_j \boldsymbol{u}_j\, W_{ji}\, dV_j \, , \quad \langle \nabla \boldsymbol{u}_i \rangle \simeq \sum_j \boldsymbol{u}_j \otimes \nabla W_{ji}\, dV_j \, . \qquad (4)$$

Here and in the following discrete approximations, the kernel function W_{ji} is evaluated at the points $\boldsymbol{x}_i$, $\boldsymbol{x}_j$, and the gradient operator ∇ is taken with respect to the variable $\boldsymbol{x}_i$. We note that $dV_j = m_j/\rho_j$, namely each particle carries a constant mass m_j during the evolution. Also, Monaghan proposed locally conservative expressions for the divergence and gradient operators:

$$\begin{aligned} div(\boldsymbol{u}_i) &= \sum_j (\boldsymbol{u}_j - \boldsymbol{u}_i) \cdot \nabla W_{ji} \frac{m_j}{\rho_i} \\ \nabla \mathcal{A}_i &= \sum_j (\mathcal{A}_j - \mathcal{A}_i) \nabla W_{ji} \frac{m_j}{\rho_i} \end{aligned} \qquad (5)$$

and put the pressure gradient in the form:

$$\nabla p_i = \sum_j \left(\frac{p_j}{\rho_j^2} + \frac{p_i}{\rho_i^2} \right) \nabla W_j(\boldsymbol{x}_i)\, m_j \, , \qquad (6)$$

The latter is based on the use of the identity:

$$\nabla p = \nabla \left(\frac{p}{\rho} \right) + p \frac{\nabla \rho}{\rho^2} \qquad (7)$$

For free-surface flows (that is for a one-fluid system) the last term vanishes at the free surface and smooth out the presence of the density gradient which is, in principle, defined only in the fluid side. For interface flows, the pressure is continuous and generally different from zero while the density jumps sharply across the interface. This is a source of numerical instabilities, mainly when dealing with large density difference in the two-fluids (see Colagrossi *et al.* 2002). To avoid this, we use the discrete approximations

$$\begin{aligned} div(\boldsymbol{u}_i) &\simeq \sum_j (\boldsymbol{u}_j - \boldsymbol{u}_i) \cdot \nabla W_{ji}\, dV_j \\ \langle \nabla \boldsymbol{u}_i \rangle &\simeq \sum_j (\boldsymbol{u}_j - \boldsymbol{u}_i) \otimes \nabla W_{ji}\, dV_j \end{aligned} \quad . \tag{8}$$

The divergence and gradient operators now read:

$$\begin{aligned} div(\boldsymbol{u}_i) &= \sum_j (\boldsymbol{u}_j - \boldsymbol{u}_i) \cdot \nabla W_{ji} \frac{m_j}{\rho_j} \\ \nabla \mathcal{A}_i &= \sum_j (\mathcal{A}_j - \mathcal{A}_i) \nabla W_{ji} \frac{m_j}{\rho_j} \end{aligned} \quad . \tag{9}$$

The main difference between (9) and Monaghan's (5) is the use of m_j/ρ_j instead of m_j/ρ_i, which becomes crucial for small density ratios. Moreover, by using (9) and following Bonet (1999), we compute the pressure gradient as

$$\nabla p_i = \sum_j (p_j + p_i) \nabla W_{ji}\, dV_j \ . \tag{10}$$

Equations (9-10) are still locally conservative.

Equations (8) for the velocity field are complete to the zeroth order. For the density, we adopted a first-order interpolation proposed by Belytschko *et al.* (1998):

$$\langle \rho_i \rangle = \sum_j \rho_j\, W_j^{MLS}(\boldsymbol{x}_i)\, dV_j \tag{11}$$

where the modified kernel is computed through:

$$W_j^{MLS}(\boldsymbol{x}_i) = [\beta_0(\boldsymbol{x}_i) + \beta_1(\boldsymbol{x}_i)(x_i - x_j) + \beta_2(\boldsymbol{x}_i)(y_i - y_j)]\, W_{ij}$$

$$\boldsymbol{\beta}(\boldsymbol{x}_i) = \begin{pmatrix} \beta_0 \\ \beta_1 \\ \beta_2 \end{pmatrix} = \boldsymbol{A}^{-1}(\boldsymbol{x}_i) \begin{bmatrix} 1 \\ 0 \\ 0 \end{bmatrix}$$

$$\boldsymbol{A}(\boldsymbol{x}_i) = \sum\nolimits_j W_j(\boldsymbol{x}_i)\, \bar{\mathbf{A}}_{ij}$$

$$\bar{\mathbf{A}}_{ij} = \begin{bmatrix} 1 & (x_i - x_j) & (y_i - y_j) \\ (x_i - x_j) & (x_i - x_j)^2 & (y_i - y_j)(x_i - x_j) \\ (y_i - y_j) & (y_i - y_j)(x_i - x_j) & (y_i - y_j)^2 \end{bmatrix}$$

which is computationally more expensive because of the inversion of the 3×3 matrix $\boldsymbol{A}$ for each fluid particle $\boldsymbol{x}_i$. This formulation allows to obtain a more regular pressure distribution and an improved energy conservation even for the one-fluid problem. As an example, figures 2-3 show the energy evolution and the fluid configuration, respectively, obtained by three different interpolation schemes in case of the free-surface flow after a dam-break. In figure 2, ΔE is the potential energy imbalance corresponding to the static configurations, respectively, before the dam break and with the fluid distributed along the horizontal bottom. In particular, interpolation (11) and the Shepard interpolation (*cf.* Colagrossi *et al.* 2001) are used for schemes A and B, respectively, while scheme C is the Monaghan method. Before the impact against the vertical wall placed at the right end of the dry horizontal bottom, the energy conservation is nearly superimposed for all considered formulations, though the pressure distributions (top plot in figure 3) show high-frequency oscillations which are smoothed out by the Shepard formulation and suppressed by the MLS formulation. After the impact (mid plots in figure 3), the energy conservation deteriorates greatly for the standard scheme. Schemes A and B show better performance, though the energy loss increases as well. The backward overturning (bottom plots in figure 3) is accompanied by a further increase of the energy loss. On this ground, we adopted the interpolation scheme (3) also for developing the two-phase version of the method.

Another modification of the present implementation is related to the Monaghan's *XSPH* velocity correction. This correction takes into account the neighbors velocities through a mean velocity evaluated within the particle support, i.e.

$$\boldsymbol{u}_i = \boldsymbol{u}_i + \frac{\epsilon}{2} \sum_j \frac{m_j}{\bar{\rho}_{ij}} (\boldsymbol{u}_j - \boldsymbol{u}_i) W_{ji} \qquad \bar{\rho}_{ij} := \frac{\rho_i + \rho_j}{2} \ .$$

For particles i close to the two-fluids interface the mean density $\bar{\rho}_{ij}$ is wrongly evaluated and the *XSPH* correction leads to wrong results. In our implementation, when considering one medium, the XSPH correction is computed without considering influence of the other media possibly present.

We now consider in more detail the formulation for two fluids, say, X and Y, without any constraint on the density ratio ρ_X/ρ_Y. We assume $\rho_Y/\rho_X \leq 1$.

As discussed Hoover (1998), using the pressure gradient in the form (6) implies fictitious surface-tension effects which are not detected in the present implementation. In particular, studying the rising-bubble problem, Colagrossi *et al.* (2002) observed the fragmentation of the bubble and, for small density ratio, the dispersion of the light fluid within the other one. This has requested the explicit modeling of surface-tension effects. A possible strategy is based on the evaluation of $\nabla \hat{\boldsymbol{n}}$ at the interface, Morris (2000). A simpler and more efficient algorithm is based on the modified state equation

$$p(\rho) = P_0 \left[\left(\frac{\rho}{\rho_0} \right)^{\gamma} - 1 \right] - \bar{a} \rho^2 \tag{12}$$

where the last term models Van der Waals cohesion force, as suggested by Nugent and Posch (2000). The pressure gradient

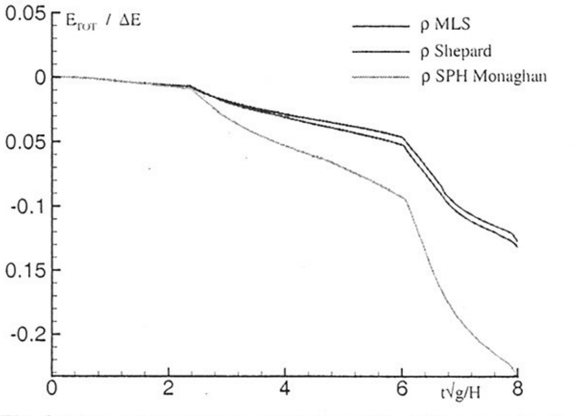

Fig. 2: Dam-break problem. Evolution of the total energy by the three different interpolation schemes: MLS interpolation, Shepard interpolation and Monaghan SPH.

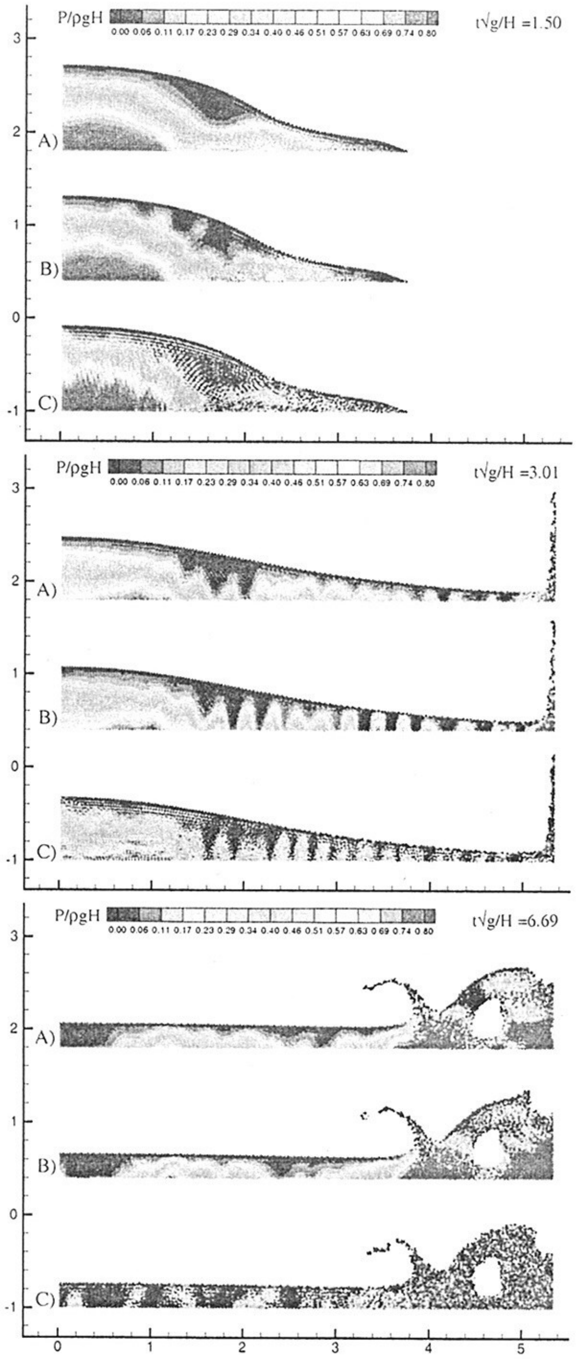

Fig. 3: Dam-break problem. Pressure contours by three different interpolation schemes: A) MLS interpolation, B) Shepard interpolation, C) Monaghan SPH.

becomes

$$\begin{aligned} \nabla p_i &= \sum_j (p_j + p_i)\nabla W_j(\boldsymbol{x}_i)\, dA_j \\ &- \bar{a}\sum_j (\rho_j^2 + \rho_i^2)\nabla W_j(\boldsymbol{x}_i)\, dA_j \ . \end{aligned} \tag{13}$$

In the present computations, the modified state equation has been used only for the lighter fluid. In particular, the discrete version of the extra term reads

$$-\bar{a}\sum_{j\in Y} (\rho_j^2 + \rho_i^2)\nabla W_j(\boldsymbol{x}_i)\, dA_j \ . \tag{14}$$

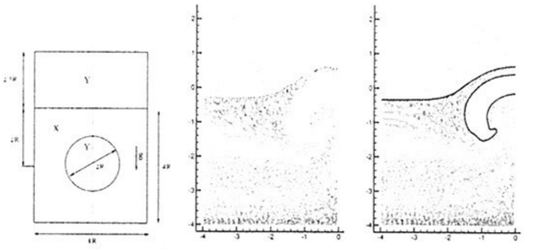

Fig. 4: Rise of a gas bubble through the water. Left: sketch of the problem and adopted nomenclature. Center: standard SPH solution. Right: improved model. $\rho_Y/\rho_X = 0{\cdot}5$, $t\sqrt{(g/R)} = 4{\cdot}427$. The solid lines in the right plot represent a Navier-Stokes solution based on the Level-Set algorithm for capturing the interface.

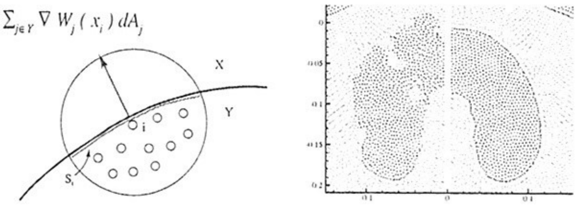

Fig. 5: Modeling of surface-tension effects in case of a gas bubble rising through the water (*cf.* Fig. 4)

For the purpose of discussion, we note that (14) can be approximated as

$$-2\bar{a}\rho_{0Y}^2 \sum_{j\in Y} \nabla W_j(\boldsymbol{x}_i)\, dA_j \ . \tag{15}$$

Therefore, because of the kernel properties, the summation in (15) is zero for a particle totally embedded within its own phase and results in a vector normal to the interface as the particle approaches it. The parameter $-\bar{a}$ allows to control the strength of the cohesion force. This is qualitatively shown in the left plot of figure 5, together with the comparison of the solution obtained with and without surface-tension modeling (right plot).

In the present implementation, we use the state equations

$$\frac{p_X(\rho)}{P_0} = \left(\frac{\rho}{\rho_{0X}}\right)^{\gamma_X} - 1 \qquad \frac{p_Y(\rho)}{P_0} = \left(\frac{\rho}{\rho_{0Y}}\right)^{\gamma_Y} - 1 \tag{16}$$

with $\gamma_X = 7$ and $\gamma_Y = 1.4$, for the heaviest and the lightest fluid respectively, and the corresponding sound speeds are

$$c_X = \sqrt{\frac{P_0\,\gamma_X}{\rho_{0X}}} \qquad c_Y = \sqrt{\frac{P_0\,\gamma_Y}{\rho_{0Y}}} \ . \tag{17}$$

The reference pressure P_0 is usually chosen to achieve a small compressibility for the X-phase, that is $U_{X\,max}/c_X \ll 1$ where $U_{X\,max}$ is the expected order of magnitude of the fluid velocity for the considered problem. We note that both (6) and (10) imply that for a uniform non-zero pressure the exchanged force between the particles is non-zero. Therefore the chosen form of the state equation ensures that for $\rho(\boldsymbol{x}) = \rho_0$ the pressure is zero and the fluid stays at rest.

From eq. (17), we note that for small density ratio ρ_Y/ρ_X the sound speed in the phase Y is much larger than in the heavier phase, and therefore the compressibility is relatively smaller in air than in water. Typical state diagrams pratically adopted are shown in figure 6. It is evidenced that to operate in the same pressure range (as needed by the interface dynamic condition) the lighter fluid Y needs to be modeled by a steeper state curve, hence with a higher sound speed. In the computational practice,

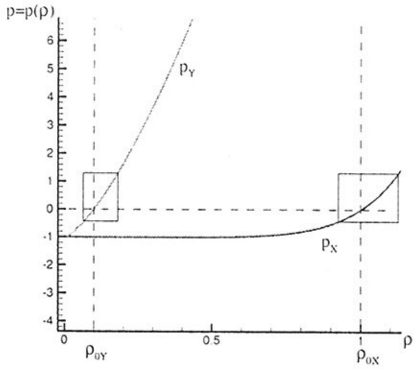

Fig. 6: State-equation diagrams for the two phases showing that to operate in the same pressure range the lighter fluid needs a steepest density-pressure characteristic curve.

since the method stability is related to the speed of sound, as the density ratio decreases the time step Δt decreases largely to prevent unstable evolutions in the lighter phase. Moreover, as discussed in Colagrossi *et al.* (2001), to increase the stability properties, a numerical viscous term of the form $\alpha c h$ is usually introduced in the practical implementation. Therefore, the difference in the sound speed of the two media implies using different viscous coefficients α to achieve the same numerical viscosity in both phases.

Two-phase modeling of dam-break and impact problems

We discuss the application of the two-phase version of the SPH method to the flow originated after a dam-break and the impact of the following water front against a fixed vertical wall. In spite of its simplicity, this problem embeds several features related to practical hydrodynamic circumstances, *e.g.* slamming and green-water loads on deck and deck-structures.

The plots in figure 7 gives a first idea of the effect of the density ratio on the global evolution of the collapse of the water reservoir (initial length $L/H = 2$). The main features of the flow evolution are the same for both cases: after the heavy fluid has been released, a liquid tongue develops along the bottom, and eventually impacts against the right vertical wall. The fluid runs up and then collapses backwards in the form of a large punger, hitting the underlying liquid sheet and forming a cavity entrapping the lighter fluid. The results for the air-water density ratio (left) can be compared with those for a hundred times heavier upper fluid (right). Before the impact, the main differences are the slope and the propagation speed of the water front along the horizontal bottom. In particular, for $\rho_Y/\rho_X = 0{\cdot}1$, the motion is slower and the front is blunter than in case of air-water density ratio. After the impact, a smaller run up is observed for $\rho_Y/\rho_X = 0{\cdot}1$ and the following evolution is further and further delayed with respect to the air-water case. Also, in the latter case, the splash up generated by the backward plunger is more vigorous.

Figure 8 summarizes the effect of changing the density ratio on the main geometrical parameters characterizing the impact flow. The limiting case $\rho_Y/\rho_X = 0$ corresponds to water moving in a vacuum. The top plot shows that the slope of the water front increases rapidly as the weight of the upper fluid increases. This is related to the larger inertia of the upper fluid which inhibits increasingly the water motion. The maximum run up, center plot, increases as the density ratio approaches the air-water case. Finally, the area of the entrapped cavity generated by the collapse of water attains a minimum value for $\rho_Y/\rho_X \simeq 0{\cdot}01$ and increases both for larger and for smaller density ratios.

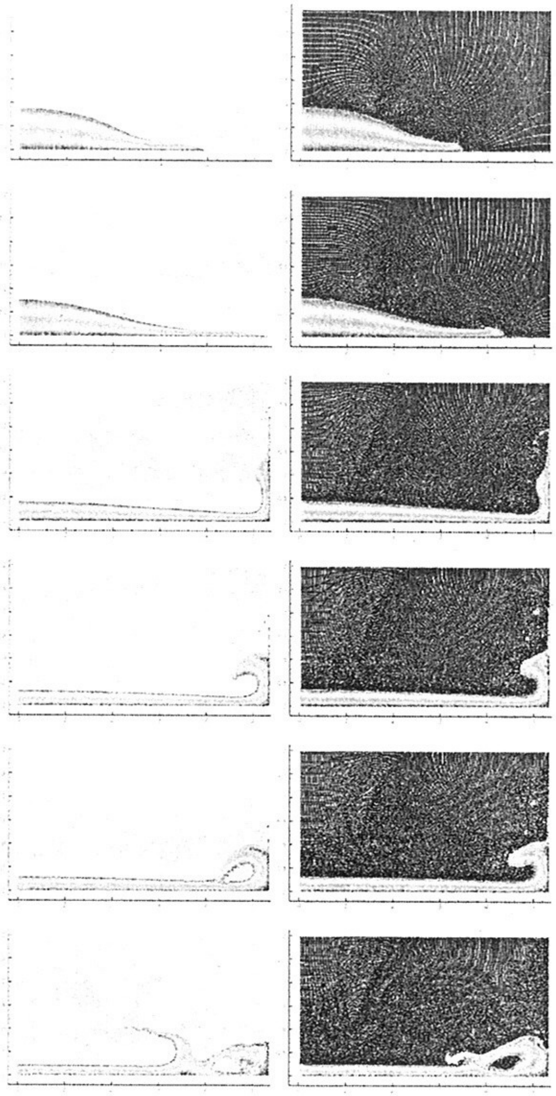

Fig. 7: Two-phase simulation of the flow after a dam break. Left: $\rho_Y/\rho_X = 0{\cdot}001$. Right: $\rho_Y/\rho_X = 0{\cdot}1$. Time increases from top to bottom.

As it can be expected, the impact of the water front against the vertical structure is accompained by large slamming loads, mainly depending on the velocity and on the slope of the impacting water front, at least in the initial stage. This can be inferred from figure 9, where the pressure at the wall foot is compared with the SPH numerical simulations. The first large pressure rise for $t/\sqrt{gL} \simeq 2{\cdot}4$ corresponds to the impact of the water front with the wall and both the numerical simulations recover reasonably well the measurements. The overshoot observed experimentally is probably related to details of the starting conditions and cannot be further commented. Greco (2001) evidenced that the backward plunging water front induces a second pres-

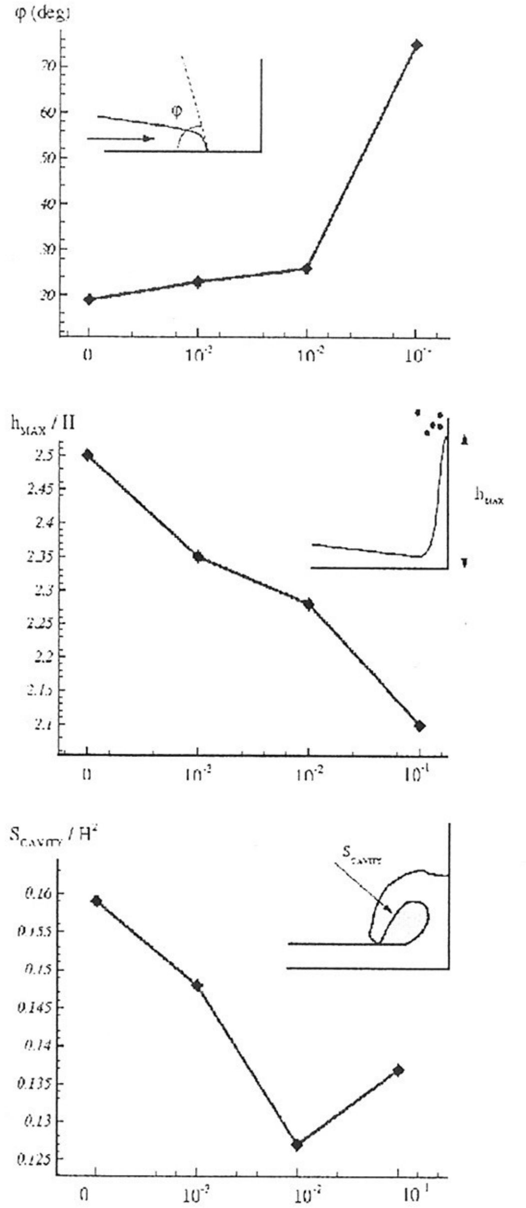

Fig. 8: Two-phase simulation of the flow past a dam break. Effect of density ratio on: slope of the water front at the impact (top), maximum run up (center), area of the entrapped cavity (bottom).

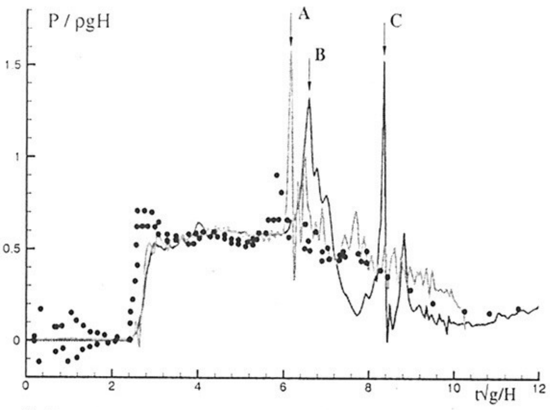

Fig. 9: Pressure evolution on the veritical wall. Solid lines: two-phase ($\rho_Y/\rho_X = 10$, green line) and free-surface flow ($\rho_Y/\rho_X = 0$, red line) simulations. Symbols: experimental data from Zhou *et al.* (1999).

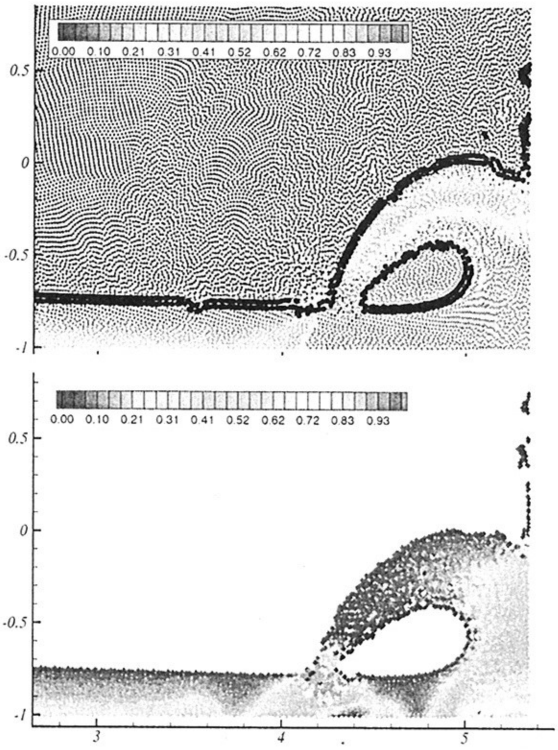

Fig. 10: Dam-break flow simulation and impact against a vertical wall: color contours of the pressure field corresponding to the pressure peak A in figure 9. Top: two-phase simulation ($\rho_Y/\rho_X = 10$). Bottom: free-surface simulation ($\rho_Y/\rho_X = 0$).

sure peak on the vertical wall. This is also observed in figure 9, *cf.* peak A. This phenomenon can be further discussed by means of the pressure contours at this time instant, which corresponds to the formation of closed cavity, as shown in figure 10 for $\rho_Y/\rho_X = 10$ and 0 (top and bottom plots respectively). In the air-water case, the pressure rise inside the air cavity is felt also in a large water region, near the corner. Clearly, this air-cushion effect is not observed in the free-surface flow modeling, and a limited pressure rise is localized around the plunger tip impinging on the underlying layer of water. Actually, see peak B in figure 9, the free-surface simulation shows a delayed pressure rise which can be related with the fast circulatory flow around the entrapped cavity shown in figure 11. The reliability of the latter result is clearly affected by the lack of modeling of the entrapped air. For $\rho_Y/\rho_X = 0$, the final collapse of the empty cavity results in the large pressure peak C which is considered totally unphysical. On the other hand, on a longer time scale, the two-phase simulation gives a rather realistic pressure evolution and the slow decay of the measurements is captured rather well.

Actually, high frequency oscillations are predicted which are not present in the measurements. In the numerics, these pressure fluctuations are associated with the oscillation of the entrapped air bubble, and the number of the available experimental samples does not allow a fine judgement. Generally

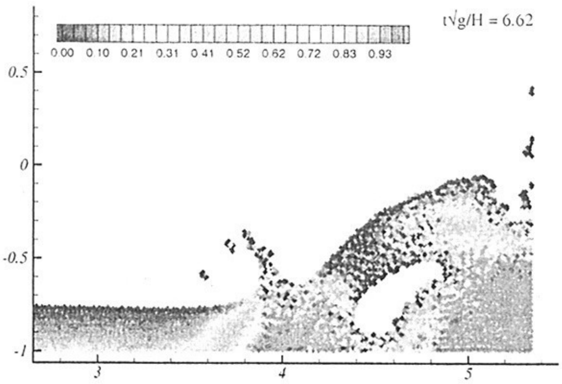

Fig. 11: Dam-break flow simulation ($\rho_Y/\rho_X = 0$) and impact against a vertical wall: color contours of the pressure field corresponding to the pressure peak B in figure 9.

speaking, beside other parameters, the dynamic behaviour of such flow field is characterized by the non-dimensional quantity $P_0/\rho_X U^2$. For $P_0/\rho_X U^2 \ll 1$, the dynamic reaction of the lighter fluid is weak and the bubble can be more easily entrapped, and large volume variations can be observed. For larger values, say $P_0/\rho_X U^2 > 1$, the volume variations are relatively smaller and either the fluid tends to escape before the cavity closure, or the surrounding liquid fragments and the cavity disappears. So far, we have not developed a complete exploration of the effects of this parameter which is left for future work.

Acknowledgements INSEAN research activity is supported by the Italian *Ministero delle Infrastrutture e Trasporti* through INSEAN Research Program 2000-02.

References

[1] A. Colagrossi, M. Landrini, M. P. Tulin (2001), *A Lagrangian Meshless Method for Free-surface Flows* Fourth Numerical Towing Tank Symposium, Hamburg.

[2] G. Colicchio, A. Colagrossi, M. Greco, M. Landrini (2002), *Free-surface Flow After a Dam break: A Comparative Study.* Ship Tech. Res. **49**/3.

[3] A. Colagrossi, M. Landrini, M.P. Tulin (2000), *Near Shore Bore Propagation and Splashing Processes: Gridless Simulations*, Monterey (CA), OEL Tech. Report 00-224.

[4] W.G. Hoover (1998), *Isomorphism Linking Smooth Particles and Embedded Atoms*, Physica A, **260**, pp. 244-254.

[5] J.J. Monaghan (1988), *An Introduction to SPH*, Comp. Phys. Comm. **48**, pp. 89-96.

[6] J.J. Monaghan (1996), *Gravity currents and solitary waves*, Physica D **98**, pp. 523-533.

[7] J.J. Monaghan, A. Kocharyan (1995), *SPH simulation of multi-phase flow*, Comp. Phys. Comm. **87**, pp. 225-235.

[8] J.J. Monaghan (1997), *Implicit SPH Drag and Dusty Gas Dynamics*, J. Comput. Phys. **138**, pp. 801-820.

[9] J.J. Monaghan, R.A.F. Cas, A.M. Kos, M. Hallworth (1999), *Gravity currents descending a ramp in a stratified tank*, J. Fluid Mech. **379**, pp. 39-69.

[10] J.P. Morris (2000), *Simulating Surface Tension with Smoothed Particle Hydrodynamics*, Int. J. Numer. Methods Fluids, **33**, pp. 333-353.

[11] J. Bonet, T.-S.L. Lok (1999), *Variational and Momentum Preservation Aspects of SPH Formulations*, Comput. Methods Appl. Mech. Engrg. **180**, pp. 97-115.

[12] T. Belytschko, Y. Krongauz, J. Dolbow, C. Gerlach (1998), *On the Completeness of Meshfree Particle Methods*, Int. J. Numer. Mech. Engng. **43** pp. 785-819.

[13] S. Nugent, H.A. Posch (2000), *Liquid Drops and Surface Tension with Smoothed Particle Applied Mechanics*. Physical Review E, **62** (4), pp. 4968-4975, Part A

[14] S. Zhang, D.K.P. Yue, K. Tanizawa (1996), *Simulation of Plunging Wave Impact on a Vertical Wall*, J. Fluid Mech. **327** pp. 221–254.

[15] M. Landrini, A. Colagrossi, M. P. Tulin (2001a), *Breaking Bow and Stern Waves: Numerical Simulations*, Proc. of 16th Int. Work. Water Waves Float. Bodies, Hiroshima (Japan).

[16] M. Landrini, A. Colagrossi, M. P. Tulin (2001b), *Numerical Studies of Breaking Bow Waves Compared to Experimental Observations* 4th Numerical Towing Tank Symposium, Hamburg (Germany).

[17] M. P. Tulin, M. Landrini (2000), *Breaking Waves in the Ocean and around Ships* Proc. of 23rd ONR Symp. on Naval Hydrodynamics, Val de Reuil, France.

[18] Z. Q. Zhou, J. O. De Kat, B. Buchner (1999), *A Nonlinear 3–D Approach to Simulate Green Water Dynamics on Deck*, Proc. 7th Int. Conf. Num. Ship Hydrod., Nantes, Ed. Piquet, J., pp. 5.1–1, 15.

Level-set Simulation of the Vortical Flow Generated by a Surface-piercing Body

Giuseppina Colicchio [1,2], *Maurizio Landrini* [1] and *John Chaplin* [2]

1 INSEAN, *The Italian Ship Model Basin*, Roma, Italy. maulan@waves.insean.it
2 *Department of Civil & Environmental Engineering*, Southampton University, UK

1 Introduction

The flow field around a ship is extremely complex, even for the simplest case of motion through calm water with constant forward speed. In particular, many vortical structures are originated by the ship motion. Some of them are directly related to ship breaking waves (Landrini *et al.* 2001). In other cases, vorticity is created at the hull boundary and shed along and downstream the ship.

In this paper, we report our ongoing investigations aimed to gain fundamental understanding of the fluid dynamic processes connected with the motion of a ship. In particular, we consider a two-dimensional prototype problem consisting in a vertical flat plate, piercing the air-water interface, and moving forward with known velocity. This rather simple problem is meant to be roughly representative of the fluid phenomena occurring around the bow of a blunt ship and near a transom stern.

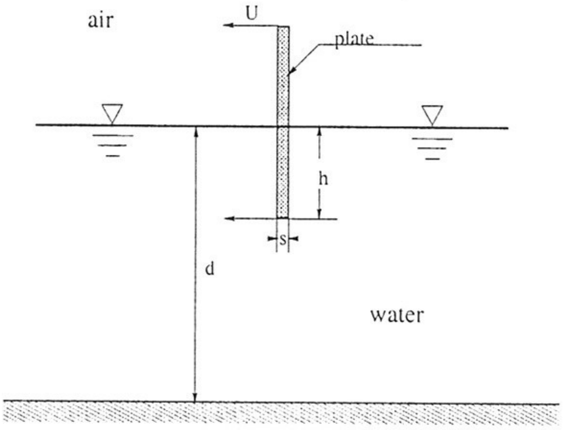

Fig. 1: Sketch of the considered problem and nomenclature adopted.

The problem is studied numerically by a Navier-Stokes solver with a Level-Set technique to capture the air-water interface. Details of the method are presented and numerical results are discussed. Preliminary data from a companion experimental investigation, still in its infancy, are presented.

2 Numerical modeling

Background fluid-flow solver We assume that the evolution of a two-fluid system is governed by the Navier-Stokes equations

$$\begin{aligned} \nabla \cdot \boldsymbol{u} &= 0 \\ \rho \frac{D\boldsymbol{u}}{Dt} &= -\nabla p + 2\nabla \cdot \mu \boldsymbol{D} + 2\sigma\kappa\delta_S \boldsymbol{n} + \rho \boldsymbol{g} \end{aligned} \tag{1}$$

where the density ρ and the dynamic viscosity μ vary sharply across the interface. The term $2\sigma\kappa\delta_S\boldsymbol{n}$ is the capillary force, with σ the surface tension, $\boldsymbol{n}$ the normal to the interface, κ half the interface curvature and the Kroneker delta δ_S is equal to unity on the interface and zero elsewhere. Finally,

$$(\boldsymbol{D})_{ij} = D_{ij} = \frac{1}{2}\left(\frac{\partial u_j}{\partial x_i} + \frac{\partial u_i}{\partial x_j}\right)$$

is the rate of strain tensor.

A second-order approximation in time of Eq. (1) can be written as:

$$\begin{aligned} \frac{\boldsymbol{u}^{n+1}-\boldsymbol{u}^{n}}{\Delta t} &= -\frac{\nabla p^{n+1/2}}{\rho^{n+1/2}} - [(\boldsymbol{u}\cdot\nabla)\boldsymbol{u}]^{n+1/2} \\ &+ \frac{[2\nabla\cdot\mu\boldsymbol{D}]^{n+1/2}}{\rho^{n+1/2}} + \frac{[2\sigma\kappa\delta_S\boldsymbol{n}]^{n+1/2}}{\rho^{n+1/2}} + \boldsymbol{g} \end{aligned} \tag{2}$$

and it is solved through a predictor-corrector scheme. To simplify the following description, we name with $F(\boldsymbol{u})$ the terms that will be approximated through the Taylor expansion in the two steps, that is

$$F(\boldsymbol{u}) = -(\boldsymbol{u}\cdot\nabla)\boldsymbol{u} + \frac{2\nabla\cdot\mu\boldsymbol{D}}{\rho} + \frac{2\sigma\kappa\delta_S\boldsymbol{n}}{\rho} + \boldsymbol{g}$$

In the predictor step, the density at the time $n+1/2$ is substituted with that at $n-1/2$, and the term $[F(\boldsymbol{u})]^{n+1/2}$ is obtained through a Taylor expansion form the previous time steps. The term containing the pressure gradient is written as:

$$\frac{\nabla p^{n+1/2}}{\rho^{n-1/2}} = \frac{\nabla p^{n+1/2}}{\rho^{n-1/2}} - \frac{\nabla p^{n-1/2}}{\rho^{n-1/2}} + \frac{\nabla p^{n-1/2}}{\rho^{n-1/2}}$$

and the two-steps procedure to obtain the new velocity becomes:

$$\tilde{\boldsymbol{u}} = \boldsymbol{u}^{n} + \Delta t\left\{[F(\boldsymbol{u})]^{n+1/2} - \frac{\nabla p^{n-1/2}}{\rho^{n-1/2}}\right\}$$

$$\boldsymbol{u}^{n+1} = \tilde{\boldsymbol{u}} + \Delta t\left\{-\frac{\nabla p^{n+1/2}}{\rho^{n-1/2}} + \frac{\nabla p^{n-1/2}}{\rho^{n-1/2}}\right\}$$

In case of incompressible fluids, the previous equation becomes

$$\frac{\nabla\tilde{\boldsymbol{u}}}{\Delta t} = \nabla\left(\frac{\nabla(p^{n+1/2}+p^{n-1/2}}{\rho^{n-1/2}}\right)$$

and it gives a first guess for $p_0^{n+1/2}$, $\boldsymbol{u}_0^{n+1/2}$ and $\rho_0^{n+1/2}$. In the iterative corrector procedure the term $[F(\boldsymbol{u})]^{n+1/2}$ is obtained through a centered Taylor expansion, and the pressure gradient is written as

$$\frac{\nabla p_k^{n+1/2}}{\rho_{k-1}^{n+1/2}} = \frac{\nabla p_{k-1}^{n+1/2}}{\rho_{k-1}^{n+1/2}} + \frac{\nabla p_c}{\rho_{k-1}^{n+1/2}}$$

with $k = 1, 2, \ldots$ the iterative step. For the predictor part

$$\begin{aligned} \tilde{\boldsymbol{u}} &= \boldsymbol{u}^{n} + \Delta t\left\{[F(\boldsymbol{u})]^{n+1/2} - \frac{\nabla p_{k-1}^{n+1/2}}{\rho_{k-1}^{n+1/2}}\right\} \\ \boldsymbol{u}_k^{n+1} &= \tilde{\boldsymbol{u}} - \Delta t\frac{\nabla p_c}{\rho_{k-1}^{n+1/2}} \end{aligned}$$

and using the divergence-free condition

$$\frac{\nabla\tilde{\boldsymbol{u}}}{\Delta t} = \nabla\left(\frac{\nabla p_c}{\rho_{k-1}^{n+1/2}}\right)$$

From which we can work out pressure, velocity, density and viscosity at the new iterative step until the convergence is satisfied.

For the spatial discretization, we have used staggered grid and x- and y-derivatives have been calculated using a second-order approximation and ENO schemes.

Interface capturing The interface between the fluids is traced using a the level-set function ϕ. A narrow band around the interface is characterized by its signed distance from the air-liquid interface. It is used as well to smooth the discontinuity of density and viscosity at the free surface. In particular the density is written as $\rho = f(\phi)$. So the continuity equation becomes:

$$\frac{\partial \rho}{\partial \phi}\left(\frac{\partial \phi}{\partial t} + \boldsymbol{u} \cdot \nabla \phi\right) = 0$$

that is the transport equation for the distance function.

As the velocity field $\boldsymbol{u}$ is not compatible with the displacement of a proper distance function a reinitialization of ϕ is necessary after a given number of time steps. The reinitialization, as introduced by Osher and Sethian [2], uses the equation

$$\frac{\partial \phi}{\partial \tau} + \left(\frac{\nabla \phi \cdot \nabla \phi}{|\nabla \phi|} - 1\right) \mathrm{sign}(\phi) = 0 \tag{3}$$

where ϕ evolve in the pseudo time τ until stationary conditions are obtained. The standard solving procedure is based on an ENO scheme for the calculation of the spatial derivatives. In such schemes, an error is introduced at the interface and [3] proposed to solve Eq. (3) by

$$\phi^{l+1}_{i,j} = \begin{cases} \phi^{n}_{i,j} - \Delta\tau\left(\mathrm{sign}(\phi^{0}_{i,j})|\phi^{l}_{i,j}| - D_{i,j}\right) & \text{interface cell} \\ \phi^{n}_{i,j} - \Delta\tau \mathrm{sign}(\phi^{0}_{i,j})\left(\dfrac{\nabla\phi^{l}_{i,j}\nabla\phi^{l}_{i,j}}{|\nabla\phi^{l}_{i,j}|} - 1\right) & \text{otherwise} \end{cases}$$

where

$$D_{i,j} = \frac{2\phi^{0}_{i,j}}{\sqrt{\dfrac{(\phi^{0}_{i+1,j} - \phi^{0}_{i-1,j})^2}{\Delta x^2} + \dfrac{(\phi^{0}_{i,j+1} - \phi^{0}_{i,j-1})^2}{\Delta y^2}}} .$$

Though this procedure reduces the rounding error caused by the level-set reinitialization, some smoothing is still visible and further improvement is gained by using, for the interface cells,

$$D^{m}_{i,j} = \frac{\phi^{0}_{i,j}}{\sqrt{A+B}}$$

$$A = \frac{\phi^{0}_{i+1,j}\left(\frac{\phi^{0}_{i+1,j}}{2} - \phi^{0}_{i,j}\right) + (\phi^{0}_{i,j})^2 + \phi^{0}_{i-1,j}\left(\frac{\phi^{0}_{i-1,j}}{2} - \phi^{0}_{i,j}\right)}{\Delta x^2}$$

$$B = \frac{\phi^{0}_{i,j+1}\left(\frac{\phi^{0}_{i,j+1}}{2} - \phi^{0}_{i,j}\right) + (\phi^{0}_{i,j})^2 + \phi^{0}_{i,j-1}\left(\frac{\phi^{0}_{i,j-1}}{2} - \phi^{0}_{i,j}\right)}{\Delta y^2}$$

This formulation does not smooth the oscillations at the interface, hence a weighted combination of the two methods has been introduced at the interface:

$$\phi^{l+1}_{i,j} = \phi^{n}_{i,j} - \Delta\tau((\mathrm{sign}(\phi^{0}_{i,j})|\phi^{l}_{i,j}| - (a_{rs}D_{i,j} + a_m D^{m}_{i,j}))$$

and, from our experience, $a_{rs} = 0{\cdot}8$ and $a_m = 0{\cdot}2$ results the best choice.

3 Discussion

The considered problem is characterized by the following non-dimensional groups

$$Fr = \frac{U_M}{\sqrt{gh}}, \quad Re = \frac{\rho_w U_M h}{\mu_w}, \quad We = \frac{h \rho_w U_M^2}{\sigma}$$

where h and U_M are the initial submergence and the maximum velocity of the plate, respectively. The subscript w indicates the water properties. In the following, lengths are made non dimensional by h, and the force values are divided by $\rho g h$.

In the numerical simulation, the plate velocity is described by a Heaviside function $U(t) = U_M H(t)$. Figures 2-3 show the Navier-Stokes (laminar) simulation for Fr=0·8 and Re$\simeq \mathcal{O}(10^6)$. Surface-tension effects have not been modeled (We=∞). At the beginning, the fluid runs up along the forward side of the plate (moving from left to right) and is sucked down on the lee side. At the same time, the starting vortex appears and progressively grows as time passes, until it is shed downstream the plate. After that, a relatively small amount of vorticity is injected in a rather thin shear layer.

On the forward side, the water reaches the maximum run up and then slightly falls down, accompanied by the formation of a plateau of water whose extension in the forward direction increases as time passes. The water front steepens gradually and a forward-plunging jet appears. As the breaking process develops, the water level on the upstream side of the plate decreases and, later on, increases again, maybe in a cyclical fashion, though the length of simulation is too short for a definitive judgment. The breaking process is characterized by the formation of a cavity entrapping air and the splashing up of the water after the impact of the plunging jet. As observed in experiments (Bonmarin 1989) and numerical simulations (Tulin and Landrini 2000), the splash up may evolve into another breaking cycle with the formation of a second forward-plunging jet and a (possibly weaker) second splash-up structure according to the strength of the initial breaking front. So far, we have not investigated this process on a long time scale and the simulation is stopped before the first splash up completely collapses down, under the action of the gravity. In any event, this breaking process is an important source of vorticity, besides the vorticity created at the body boundary, though in the former case the phenomenon is intrinsically inviscid and related to the change of topology of the fluid domain.

On the lee side, the starting vortex sucks down the interface which evolves into a backward breaker. Also in this case, a cavity entrapping air is formed and a residual clockwise circulatory region is observed. Closer views of the rotational regions created upstream and downstream through the breaking process are given in figure 4.

Figure 5 shows the pressure force acting on the plate for $Fr = 0{\cdot}8$ and the separate contributions coming from right and left sides. The force is positive in the positive x-direction. At the (impulsive) start, a high overpressure on the left side and a deep depression on the right one (pressure impulse) are observed. This phenomenon is soon to decrease, leaving a positive force on the left side and a negative force on the right, the latter mainly due to a depressional area around the lower tip of the plate. This depression becomes the core of the nascent vortex, and its separation is accompanied by the first peak of the right force. After the starting vortex is detached, the pressure decreases again around the lower tip and the force acting on that side is dominated by gravitational effects. On the left side, after the sudden start, the continuous piling up of water results in the the peak load synchronized with the maximum run up. As soon as the water front propagates away from the solid boundary, the force decreases and does not show any signature of the interface breaking observed immediately after. In the final part of the simulation, the small-amplitude oscillations of the left force are due to the oscillation of the water level on the forward side of the plate.

For smaller Froude number a similar evolution is observed, and it is not reported for the limited space available. For Fr=1·2, figure 6, a more vigorous vortex shedding is found without any breaking events of the interface downstream the plate. Interestingly, for this speed the interface moves down and reaches the edge of the plate, resembling the case of a dry transom stern in a ship. In general, for all the considered cases, on the upstream side the interface evolves into a forward-plunging jet,

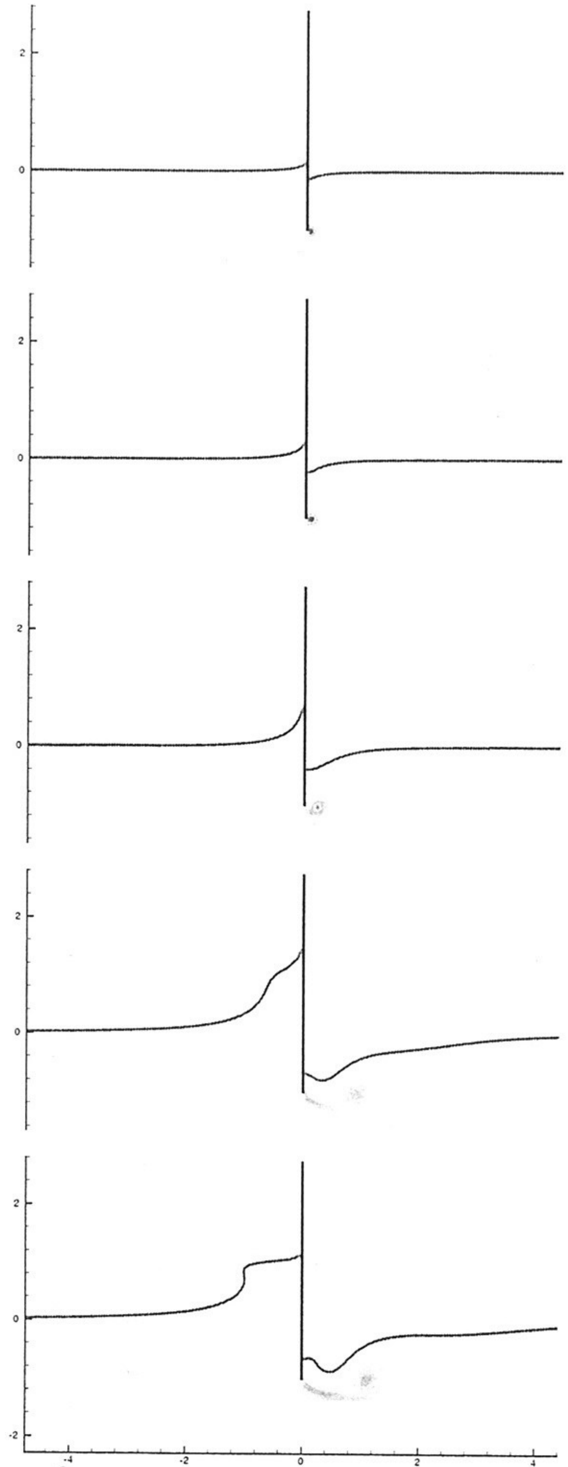

Fig. 2: Interface and vorticity field in water for Fr= 0·8. Non-dimensional time increases from top to bottom (τ =0·12, 0·24, 0·45, 1·53, 2·7).

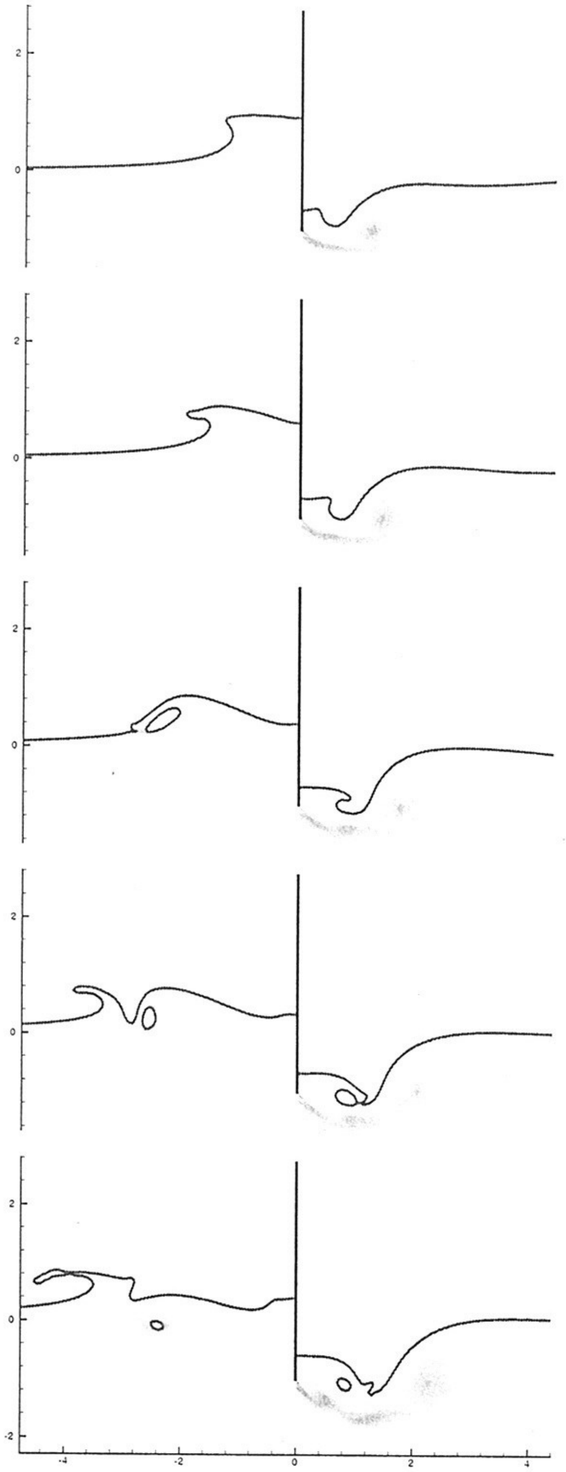

Fig. 3: Interface and vorticity field in water for Fr= 0·8. Non-dimensional time increases from top to bottom (τ =3·06, 3·69, 4·68, 5·67, 6·39)

with strength increasing with the Froude number.

Similar numerical computations has been performed in [5] for the inviscid free-surface problem, with a vortex sheet emanating from the sharp immersed edge of the plate by using a suitable Kutta condition. They have evidenced the presence of three regimes as for the interaction between the free surface and the vortex sheet, namely a *subcritical* regime, $Fr < 0{\cdot}7$, where no significant interactions between a single branched spiral vortex and the interface occurs before the breaking events; a *transcritical* regime, $0{\cdot}7 < Fr < 1{\cdot}0$, where the free surface stretches the vortex sheet, causing its roll up, even though the interaction is limited; a *supercritical* regime, $Fr > 1{\cdot}0$, where the vorticity affects significantly the free-surface motion. For the pre-breaking regime, our results are consistent with these find-

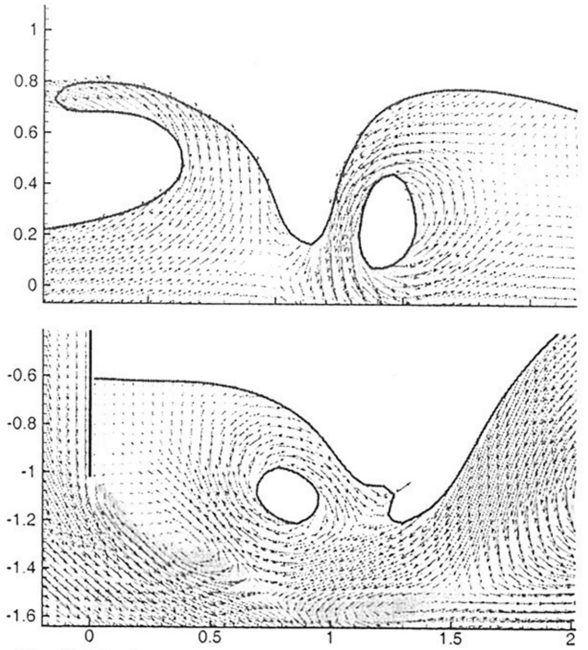

Fig. 4: Velocity fields near the cavity entrapping air originated by the folding and breaking of the interface for Fr=0·8. Top: forward cavity. Bottom: backward cavity.

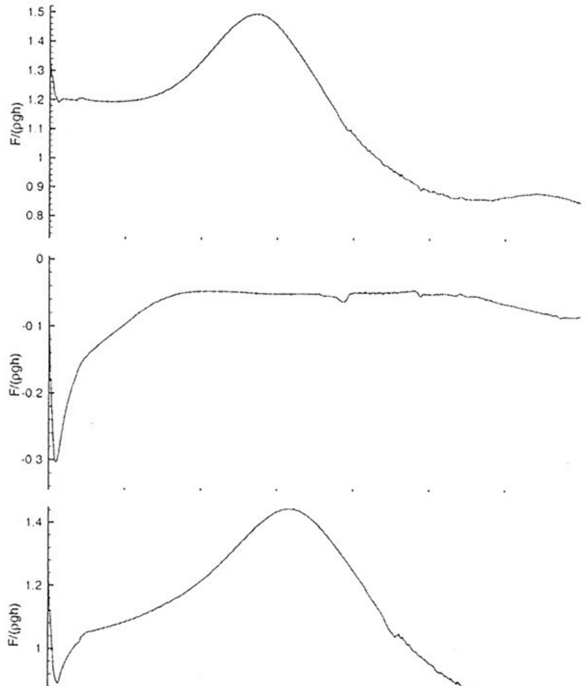

Fig. 5: Pressure loads acting on the left (top) and the right (center) sides of the plate for Fr= 0·8. The resulting force is plotted in the bottom figure.

ings. The present numerical method can be used to investigate further the viscous features of the vorticity-interface interaction, as well as the post-breaking evolution. For example, figures 3 and 7 show that a new vortex is shed because of the downwash induced by the breaking.

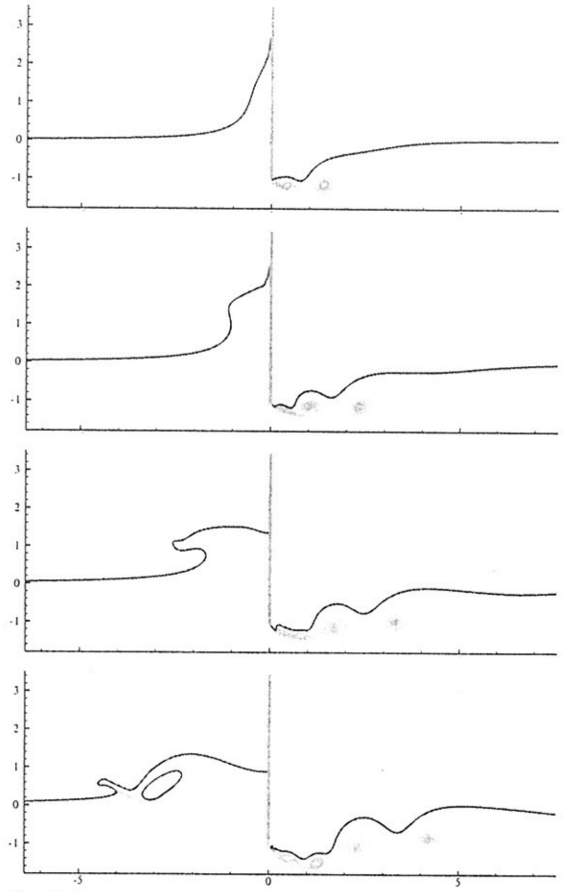

Fig. 6: Interface and vorticity field in water for Fr= 1·2. Non-dimensional time increases from top to bottom (τ =0·6, 1·2, 1·8, 2·4)

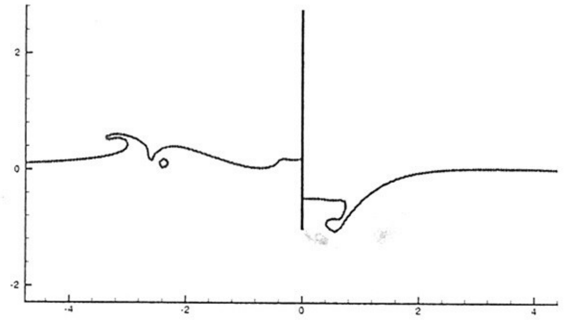

Fig. 7: Interface and vorticity field in water for Fr= 0·6. and τ = 3.

Never the less, our numerical scheme still presents some problem related to the numerical diffusion of the interface across the surface cells, which presently limits our analysis capability. The most important feature of the surface capturing schemes, above all of the one adopting the level set, is the possibility to leave the mesh unaltered throughout the calculation as the interface is followed using an analytical function ϕ directly linked to density and viscosity. As the interface is smeared over at least two cells, there is a diffusion error in the solution of the Poisson equation which has to be added to the numerical diffusion error in the calculation of the convection term and to the error in the mass conservation.

Likely, the effect of these errors is a wrong approximation of the mass transport in the area where high vorticity is generated. For example, on the upper part of the plunging jets there is a vortex whose wrong numerical handling create sometimes a *nose-up* effect. However, it can be reduced using an appropriate advection scheme as the superbee scheme. Also, we note that the size of the submerged air bubbles decreases in time because of the present limits of the method. Therefore, further improvements are needed to handle accurately on a longer time scale the post-breaking evolution.

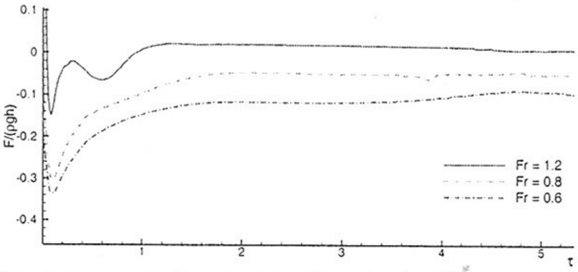

Fig. 8: Pressure load on the right of the plate for different Froude number.

Figure 8 shows the forces acting on the right side of the plate for different velocities. As the maximum velocity increases, the depressional area downstream of the plate becomes deeper, causing a shift of the forces to higher values. At higher Froude number, we observe an oscillation in the force diagram because of the vortex shedding. This is apparent for $Fr = 1{\cdot}2$. Interestingly, for this case, the force on the right side vanishes because of the reaching of dry conditions. second vortex, later no more effects can be noticed on that side of the

4 First experimental results

We briefly report our preliminary results from experiments performed in a flume 420 mm wide, 18 m long and a still water depth of 700 mm. An aluminum vertical plate is towed along the flume, and the initial draft is 47 mm, see figure 9 Displacement and velocity are measured by an optical encoder and used to drive the numerical simulations. Comparison of numerical and experimental results for $Re \simeq 33000$, $We \simeq 10000$ and $Fr \simeq 1$ are ongoing. Standard water density, viscosity and surface tension have been used, though fluorescent material has been added to the water, and temperature and pressure conditions have not been monitored. Figure 11 shows the experimental and the numerical evolutions for the corresponding instants of time. The agreement is qualitatively rather good, and also the vortical structures luckily evidenced by some ventilation effects are visible. Actually, some disturbances on the free surface downstream the plate (now moving from left to right) are detectable, partly due to some leakage from the sides of the plate and the walls of the flume. The plunging of the upstream jet is delayed in case of the numerical simulation because of the problems previously mentioned. Also, some influence of surface tension can also be seen: the jet observed in the experiments is more rounded than the numerical one.

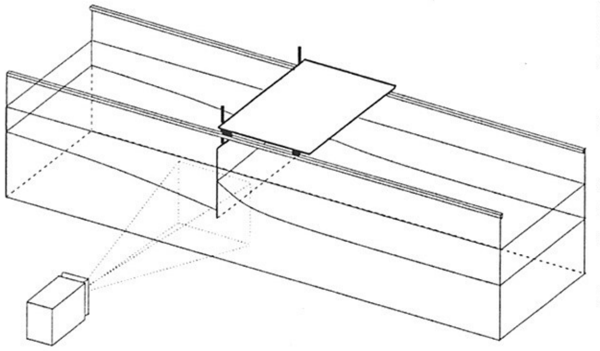

Fig. 9: Experimental set up

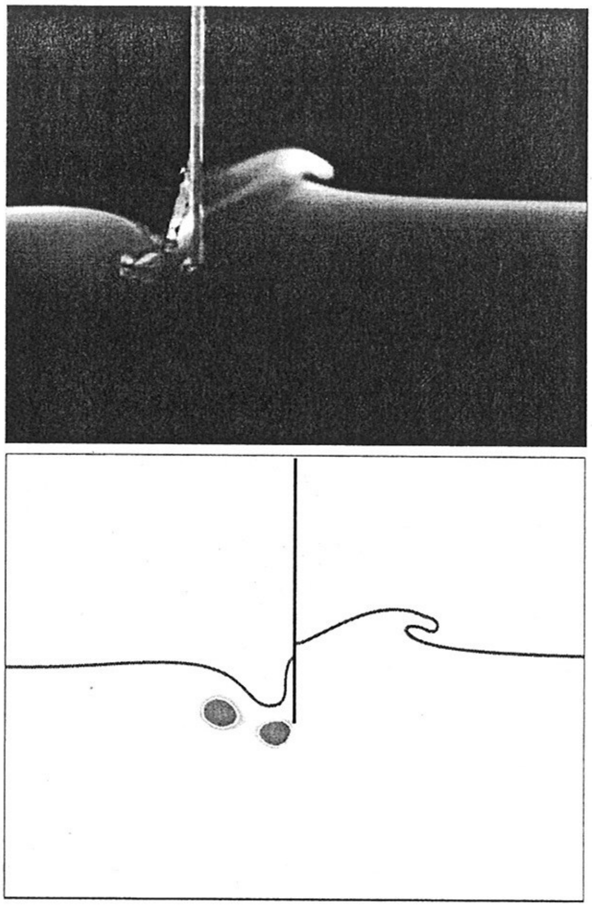

Fig. 10: simulation with surface-tension effects modeled. The superbee scheme has been applied. ($t = 0{\cdot}37$ s)

We have just modeled the surface tension and figure 10 reports a very preliminary, yet encouraging, result.

Acknowledgements INSEAN research activity is supported by the Italian *Ministero delle Infrastrutture e Trasporti* through INSEAN Research Program 2000-02.

References

[1] Bonmarin P. (1989), Geometric properties of deep-water breaking waves, *J. Fluid Mech.*,**209**, pp. 405-433.

[2] Sussman M., Smereka P. and Osher S. (1994), A Level Set Approach for Computing Solutions to Incompressible Two-Phase Flow. *J. Comp. Physics* **114**, pp. 146-159 (1994).

[3] Russo G. and Smereka P. (2000), A remark on computing distance functions. *J. Comp. Physics* **163**, pp. 51-67 (2000).

[4] Tulin M.P. and Landrini M. (2000), Breaking waves in the ocean and around ships, In: *Proc. 23rd Symp. Naval Hydrod.*, Rouen (Fr).

[5] Tsai W.T. and Yue D.K.P. (1993), Interaction between a free surface and a vortex wheet shed in the wake of a surface-piercing plate. *J. Fluid Mech.* **257**, pp. 691-721.

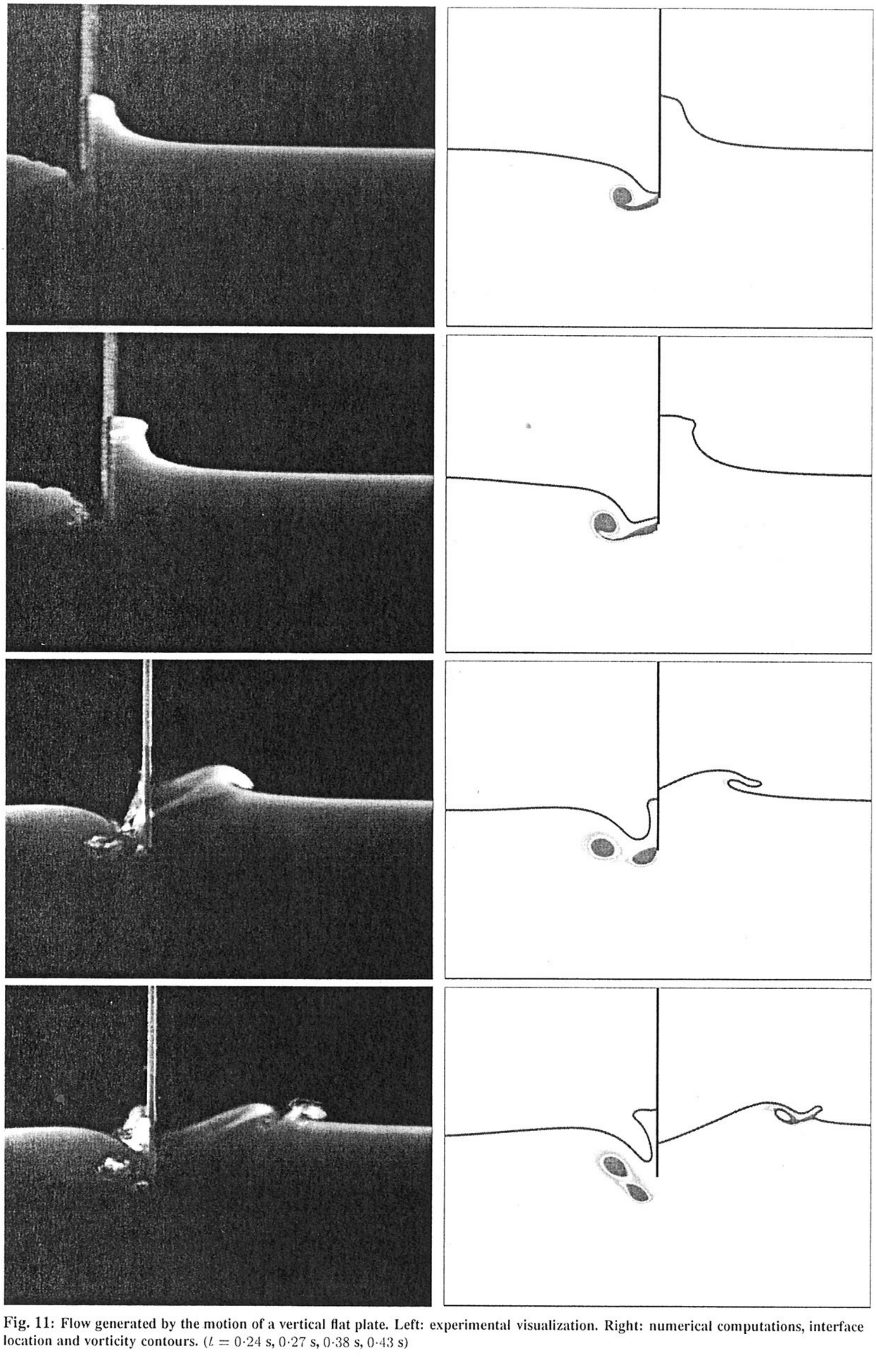

Fig. 11: Flow generated by the motion of a vertical flat plate. Left: experimental visualization. Right: numerical computations, interface location and vorticity contours. ($t = 0{\cdot}24$ s, $0{\cdot}27$ s, $0{\cdot}38$ s, $0{\cdot}43$ s)

INVESTIGATIONS OF TIP VORTEX CAVITATION INCEPTION ON HYDROFOILS DEDUCED FROM PROPELLER BLADES

F. DENISET[*] V. NAVAZA[*] J.Y. BILLARD[*] F. HAUVILLE[*]

- [*] IRENav (Institut de Recherche de l'Ecole Navale), 29240 Brest Naval, France

ABSTRACT

For the same ship propeller project, two propellers with identical propulsive performances and similar geometry present totally different behaviors of tip vortex cavitation (TVC) during behind hull trials. The aim of this work is to analyze the blade tip vortex flow both numerically and experimentally. For that purpose, an original method is proposed which transforms the propeller blades' geometry into corresponding hydrofoils. The RANS (Reynolds Averaged Navier-Stokes) computations are compared to LDV (Laser Doppler Velocimetry) measurements conducted in the ENCT (Ecole Navale Cavitation Tunnel). A good agreement is found between the computed and measured TVC inception conditions. A particular attention is paid to the velocity and pressure distributions computed in the very near field close to the tips of the two hydrofoils. These results highlight differences between the two propeller blade tip vortex flows.

NOMENCLATURE

Propeller parameters

P1 and P2	Propellers
D	Propeller diameter [m]
R_{max}	Propeller radius [m]
r	Local radius [m]
$R = r / R_{max}$	Dimensionless local radius
$\frac{H}{D}(R)$	Reduced pitch law
$C_{0.7}$	Chord [m] of section R = 0.7
U_∞	Ship speed [m/s]
n, ω	Propeller rotational speed [rps,rad.s^{-1}]
P_v	Vapor pressure [Pa]
P_{ref}	Reference pressure [Pa]
ν	Dynamic viscosity [m^2/s]
$J = \frac{U_\infty}{n D}$	Advance coefficient
$J_{nominal}$	Nominal advance coefficient

T	Propeller thrust [N]
Q	Propeller torque [N.m]
$V_{0.7}$	Leading edge velocity [m/s] at R=0.7

$$V_{0.7} = \sqrt{U_\infty^2 + (0.7\,\pi\,n\,D)^2}$$

$Re = \frac{V_{0.7}\,C_{0.7}}{\nu}$	Reynolds number
$K_T = \frac{T}{\rho n^2 D^4}$	Thrust coefficient
$K_Q = \frac{Q}{\rho n^2 D^5}$	Torque coefficient
$\eta = \frac{J}{2\pi}\frac{K_T}{K_Q}$	Efficiency
σ_n and $\sigma_{0.7}$	Cavitation inception numbers

$$\sigma_n = \frac{P_{ref} - P_v}{\frac{1}{2}\rho\,n^2 D^2} \qquad \sigma_{0.7} = \frac{P_{ref} - P_v}{\frac{1}{2}\rho\,V_{0.7}^{\;2}}$$

Hydrofoil parameters

H1 and H2	Hydrofoils deduced from P1 and P2 at nominal operating condition
X	Axial coordinate [m]
Y	Vertical coordinate [m]
Z	Spanwise coordinate [m]
S	Hydrofoil area [m^2]
V_0	Inlet velocity [m/s]
β	Incidence angle [degrees]
$\varphi_J(R)$	Hydrofoil incidence law [degrees]
F_P	Lift force [N]

$Re = \frac{V_0\,C_{0.7}}{\nu}$	Reynolds number
$C_L = \frac{F_P}{\frac{1}{2}\rho S V_0^2}$	Lift coefficient
$C_p = \frac{P - P_{ref}}{\frac{1}{2}\rho V_0^2}$	Pressure coefficient
$\sigma_{tunnel} = \frac{P_{ref} - P_v}{\frac{1}{2}\rho V_0^2}$	Cavitation inception number

INTRODUCTION

TVC inception depends on several factors, like water quality (Arndt & Keller 1992, Shen & al. 2001), model scale (Keller 2001), the geometry of the blade tip (Pauchet & al. 1994, Fruman & al. 1995, Kuiper 2001) or vortex intensity. This has been highlighted by numerous studies conducted on hydrofoils mounted in cavitation tunnels. In this work, we focus on the influence of the blade tip geometry on TVC inception. In the past, hydrofoils have been tested in order to characterize the physical effects of different geometrical parameters (skew, cross-section...). However, the automatic extrapolation to propellers of the numerous results obtained on the hydrofoils remains difficult, particularly concerning TVC prediction. On the one hand, the geometries of the tested hydrofoils largely differ from those of the propeller blades. For example, the hydrofoils have usually rectangular or elliptical planforms, without any twist law, without any rake, and without any skew or a very limited one as compared to that of a propeller blade. On the other hand, the hydrofoils and propellers flow conditions are highly different because the hydrofoils are placed in the straight inlet flow of the tunnel test section whereas the propeller blades are rotating.

A method has been developed at IRENav which transforms a "rotating propeller blade" into a "hydrofoil mounted in a tunnel". The goal of this method is the characterization of propeller blade TVC behavior on a simple hydrofoil mounted in the ENCT. The hydrofoil geometry is deduced from the propeller blade by a geometrical transformation called "blade-to-hydrofoil" transformation (figure 1). The transformation, applied to the blades of two propellers, P1 and P2, allowed the study of the propellers TVC behavior through the vortex flow analysis around the two deduced hydrofoils. The method was validated by both experimental and numerical studies.

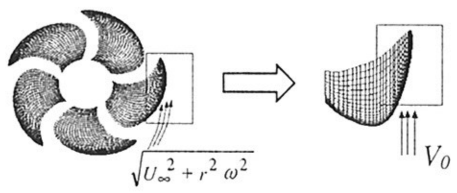

Figure 1 : Propeller blade and its deduced hydrofoil.

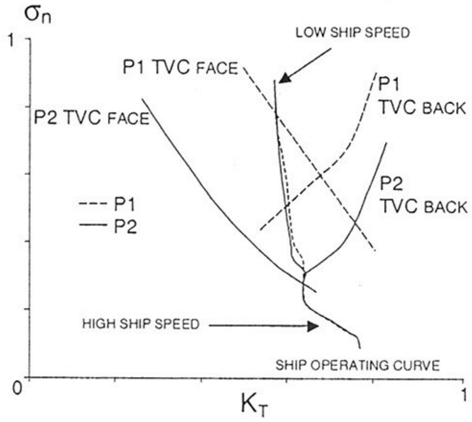

Figure 2 : P1 and P2 full-scale TVC inception curves. Tests conducted at MARIN's depressurized towing tank results.

First, we present the different TVC behaviors observed on the propellers P1 and P2 during cavitation tests conducted in a towing-tank. Second, the different stages of the "blade-to-hydrofoil" transformation are detailed. Then, the experimental devices and the RANS commercial flow solver Fluent5^{TM} are presented. Finally, the analysis of the experimental and numerical results allows the comparison of the TVC behavior on the two hydrofoils deduced from the blades of the propellers P1 and P2.

1. POSITION OF THE PROBLEM : P1 AND P2 CAVITATION TESTS RESULTS

The two propellers P1 and P2 have been designed for a same project. Both geometries and corresponding operating curves are very similar and provide the same thrust (identical K_T thrust coefficients) under their respective operating conditions given by the nominal value of the advance coefficient J. The behind-ship-hull propeller tests conducted in MARIN's depressurized towing tank on 1/16 scaled propeller models P1 and P2 have revealed similar cavitation behaviors, except for TVC, for which results are completely different. The McCormick (McCormick 1962) extrapolation at full scale of TVC inception curves resulting from these trials performed with models are presented in figure 2.

For low loads of the propeller blades, a cavitating tip vortex appears on the face of the blade (TVC face) whereas for high loads the cavitating tip vortex appears on the back (TVC back). The bucket is the region of this diagram where the TVC progressively disappears from the blade face and appears on the blade back. The bucket of propeller P2 is centered on the operating curve of the ship. This is not the case for propeller P1 and as the ship advance velocity is progressively increased, TVC appears earlier on P1 than on P2.

How to interpret these differences ? The propeller trials highlight the strong influence of loading conditions on TVC. As the main differences between the two geometries are concentrated in the tip region, we will focus our flow analysis on the blade tip, our "blade-to-hydrofoil" transformation will be defined in order to keep both this flow and the governing geometrical parameters unchanged.

2. BLADE TO HYDROFOIL TRANSFORMATION

Tip vortex investigations underline the strong influence of blade geometry and tip flow conditions on tip vortex roll-up and cavitation. Therefore, the transformation will take into account both the geometrical characteristics of the propeller blade and the flow conditions at the tip. For this study, we have chosen to keep constant a maximum of the blade geometrical characteristics to facilitate the interpretation and the exploitation of the results by the propeller designer.

2.1 Blade geometry and flow conditions at the tip

In the plane of the developed sections, the incident velocity magnitude depends on the rotation rate and ship advance velocity and consequently on the advance parameter J. It is given by the following expression:

$$U^{J}_{incid}(R) = \sqrt{U^{2}_{\infty} + (r\omega)^{2}} = U_{\infty}\sqrt{1 + \left(\frac{\pi R}{J}\right)^{2}} \qquad (1)$$

This velocity magnitude increases with the radius R. The velocity incidence angle, called hydrodynamic incidence, is defined as the angle between the inlet flow direction and the local section chord at the leading edge of each section. The hydrodynamic incidence law $\phi_J(R)$ is given by:

$$\phi_J(R) = \psi(R) - \alpha_J(R)$$

$$\text{with} \quad \left\{ \begin{array}{ll} \psi(R) & = \arctan\left(\dfrac{\frac{H}{D}(R)}{\pi R}\right) \\ \alpha_J(R) = & \arctan\left(\dfrac{J}{\pi R}\right) \end{array} \right\} \qquad (2)$$

As shown by expression (2), the hydrodynamic incidence depends both on the geometry through the blade reduced pitch law $\frac{H}{D}(R)$ and on the propeller operating conditions through the advance parameter value J.

2.2 Description of the transformation

The hydrofoil issued from the transformation will be placed in the tunnel uniform and straight inlet flow. Since the incident velocity on the blade sections is inscribed in the plane of the developed sections, the hydrofoil sections are constructed in these planes, and five out of six of the definition laws will be kept unchanged: thickness, camber, chord, rake and skew.

As the tunnel inlet flow is horizontal, to keep the hydrodynamic incidence law $\phi_J(R)$ unchanged, the reduced pitch law is transformed into an incidence law given by:

$$\phi_J(R) = \psi(R) - \alpha_J(R) \qquad (3)$$

Because of the J dependence of the hydrofoil incidence law, each propeller operating condition is represented by a specific hydrofoil, called H^{J}, each hydrofoil differing from the other by its incidence law.

In this work, we focus on the nominal operating condition. Then, the transformation is applied to the P1 and P2 propeller blades for their nominal operating conditions and the deduced hydrofoils are called $H1^{J\ \mathrm{nominal}}$ and $H2^{J\ \mathrm{nominal}}$, respectively, or simply: H1 and H2. Their incidence laws are given in figure 3. These two hydrofoils have been machined and tested.

The velocity magnitude at the leading edge of the blade sections, depending on the radius R (equation 1), cannot be reproduced on the hydrofoil sections (figure 4) because of the uniformity of the tunnel inlet flow. Consequently, due to the relative increase of inlet velocity on the hydrofoil sections close to the root, their loads are greater than those of the corresponding blade sections located close to the hub. During the tests, the overloading of the root has given rise to a sheet cavity sufficiently far from the tip to be of no consequence on the tip flow.

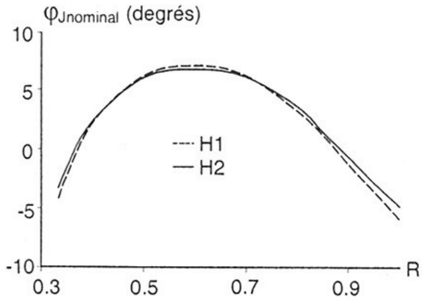

Figure 3 : Incidence laws of the hydrofoils H1 and H2.

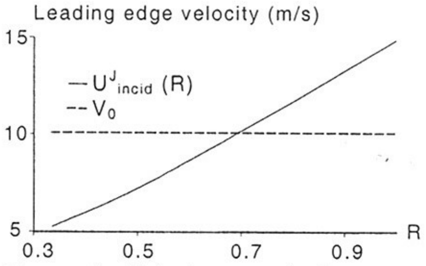

Figure 4 : Velocity magnitude at the leading edge of the blade and hydrofoil sections (Re=1.62 × 10⁶).

The global incidence of the hydrofoil can be modified by an angle β. This angle is measured from the center of the root section chord, $\beta = 0°$ being associated with the hydrofoil nominal operating condition. The incidence laws thus obtained, $\phi_\beta(R) = (\phi_{J\text{nominal}}(R) + \beta)$, are very close to the incidence laws of the specific hydrofoils $H1^J$ and $H2^J$, equation 3, when J is close to J_{nominal}. Indeed, the differences observed at the tip do not exceed 5% if $-1° < \beta < 1°$. Beyond 1 degree, the difference is increased. Consequently, propellers and hydrofoils tests results will be compared only for operating conditions very close to the nominal one.

3. EXPERIMENTAL SETUP

The cavitation tests are conducted for the hydrofoils H2 and H1 in the square test section 192 mm × 192 mm of the Ecole Navale Cavitation Tunnel (Navaza 2002). The spans of the hydrofoils are equal to 120 mm and represent 1/12 of the spans of the associated propellers blades. The hydrofoils cavitation tests are performed at $V_0 = 10$ m/s — the corresponding Reynolds number is then equal to 1.62×10^6, without any roughness on the stainless–steel hydrofoils and without germs' injection. The air content is close to 30%, and the free stream turbulence level is lower than 2%. The TVC inception detection is based on a visual criterion, with the help of a stroboscope which accentuates the liquid–vapor interfaces visualization. Inception is recorded as soon as a vapor filament becomes visible in the wake of the hydrofoil.

4. COMPUTATIONS

RANS computations - conducted with the commercial CFD code Fluent5™ - are essential in order to account for tip vortical structures, which are strongly linked to the boundary layer development on the hydrofoil. The H-structured grids allow the control of the cells repartition in sensitive regions like leading edge, boundary layer and tip region. The size of these grids reaches 700 000 cells. About 10 cells are located in the boundary layer and about 15 cells are transversally located in the tip vortex core. Grid independence is achieved by successive mesh refinements based on a criterion related to pressure. This vortex core refinement is a prerequisite to properly compute the tip vortex flow (Dacles–Mariani & al. 1995).
At the outlet (exit plane) of the computational domain a zero gradient condition, called "outflow", is imposed. Symmetry conditions are imposed on the tunnel walls.
In this work, we focus on TVC inception on the hydrofoil or in the near wake region, and on the circulation distribution. The over-diffusion of the tip vortex downstream the hydrofoil is not analyzed.

The computations performed with turbulent flow conditions (k–ε standard and k–ε RNG turbulence models) led to an overestimation of the vortex diffusion. Indeed, several authors have shown numerically and experimentally that the core of the vortex is a low turbulent region (See Dupont & Cerrutti 1992, Fruman & al. 1992, Viot & al. 1998, Berntsen & al. 2001). Therefore, the first flow analyzis has been based on the results of computations performed with laminar flow conditions.

5. RESULTS

5.1 Comparison of propeller P2 and hydrofoil H2 cavitation tests

The analysis of TVC on the hydrofoil and on the propeller blade underlines identical TVC back and TVC face behaviors. The propeller P2 and hydrofoil H2 TVC inception curves are compared in a (β, σ) diagram in figure 5, where σ is equal to σ_{tunnel} for the hydrofoil and $\sigma_{0.7}$ for the propeller. The K_T nominal value corresponds to the zero β value. For the nominal operating conditions of H2 and P2, TVC back appears in the wake, in an intermittent way, for the same cavitation inception number $\sigma_{tunnel} \approx \sigma_{0.7} \approx 0.45$. At the opposite, TVC face takes place in a high way. Moreover, for the same operating conditions, sheet back cavitation is more extended on the hydrofoil than on the blade. These three phenomena are explained by the blade-to-hydrofoil transformation which, for similar tip loadings, overloads the central and root hydrofoil sections as compared to the blade ones. In conclusion, the propeller and the hydrofoil TVC behave qualitatively and quantitatively in the same way when the flow conditions remain close to the nominal one. For higher and lower values of β, the comparison is not relevant.

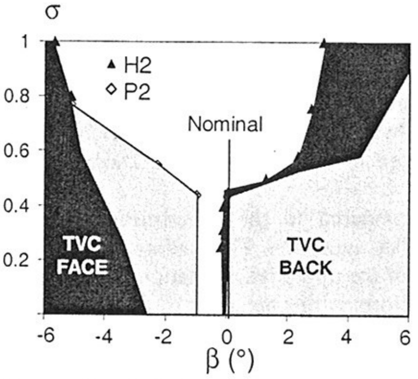

Figure 5 : TVC inception curves obtained in the cavitation tunnel of the SVA Potsdam for the propeller P2 and in the ENCT for the deduced hydrofoil H2.

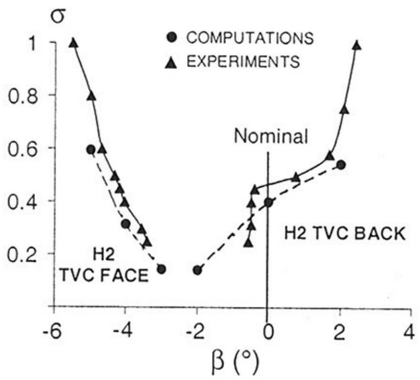

Figure 6 : H2 experimental and computational TVC inception curves (Re=1.62×10^6).

5.2 Comparison of hydrofoil H2 experimental and computational results

The RANS computations have been performed for H2 (β=0°, Re=1.62×10^6), with different mesh refinements. The validation of the computational results is made through the comparison between computed tangential velocity profiles and LDV measurements.

In the near field, the computed tangential velocity profiles through the H2 tip vortex and the LDV measurements are in good agreement. Far downstream, the maximum of the tip vortex tangential velocity is under-estimated and the radius of the viscous core is over-estimated (Viot & al. 1998). The computed pressure coefficient in the vortex core increases quickly downstream whereas the pressure coefficient estimated from the LDV measurements decreases in the near field, for H2 nominal operating conditions.

The theoretical prediction of cavitation inception from the knowledge of the initially subcavitating flow domain results from the comparison of the static pressure minimal value observed in the vortex with the vapor pressure value. Because of the downstream excessive diffusion introduced by the code, computations do not allow the prediction of TVC inception in the wake, i.e. close to the H2 nominal operating condition. When cavitation appears at the leading edge or in the near field —back and face leading edge vortex cavitation, the numerical prediction agrees with the experiments. The numerical TVC inception diagram, obtained from the computations performed for H2 and different β values, is compared to the experimental one in figure 6 and shows that only cavitation tests allow an accurate prediction of the hydrofoil cavitation bucket localization.

5.3 Comparison of hydrofoils H1 and H2 experimental and computational results

Experiments and computations have been conducted for the hydrofoil H1 in the same way as for H2. TVC inception diagrams and tip vortex characteristics are compared for the nominal operating conditions (β=0°, Re=1.62×10^6). At $\beta = 0°$, which corresponds to the nominal operating condition, H1 TVC back appears in an intermittent way, over the hydrofoil. When the cavitation number is decreased close to the H2 TVC back inception number, cavitation is still present at the tip of H1.

For the two hydrofoils, the tip vortex is located on the suction side and the path of the tip vortex behind the hydrofoil is lined up with the chord of the tip section. This observation highlights the importance of the choice of the reduced pitch value at the tip for a better TVC control.

The tangential velocity profiles show that the H1 tip vortex roll-up process occurs upstream as compared to the H2 one. At the tip, the vortex intensity of H1 is greater than H2's. These results explain the shift of the H1 TVC bucket towards the lowest loads (i.e. $\beta<0^\circ$) as compared to H2.

The computed pressure coefficients in the H1 and H2 tip vortex core are compared in figure 23. The minimum value of the pressure coefficient, reached on the hydrofoil itself and associated to the TVC inception number, is lower in the H1 tip vortex core than in the H2 one: $Cp_{min} = -0.6$ for H1 and $Cp_{min} = -0.3$ for H2. These results agree with the experiments and explain the shift of the H1 TVC bucket to a higher pressure level, as compared to H2.

CONCLUSION

An original method has been developed at IRENav to characterize propeller blades TVC behavior by help of hydrofoils mounted in a cavitation tunnel. The cavitation tests, conducted in the ENCT on the hydrofoil H2 deduced from a blade of the propeller P2, have shown TVC behaviors analogous to those observed during open water tests performed on propeller P2. Moreover, the propeller and hydrofoil TVC inception numbers are quantitatively comparable as soon as the operating conditions are close to the nominal one. These results provide, for the tested geometry, a first validation of the method.

The RANS computations conducted on hydrofoil H2 have been compared to the experimental results, particularly concerning the prediction of tip vortex characteristics and TVC inception. The leading edge vortex cavitation inception is well predicted. However, the accurate prediction of the tip vortex cavitation still remains a problem when inception occurs far downstream from the foil tip. Therefore, as this behavior is observed at the nominal conditions, experiments are still necessary to determine the TVC bucket localization.

The hydrofoils cavitation tests conducted in the ENCT indicate a better TVC behavior of H2 as compared to H1. This result is in agreement with the TVC observed on P1 and P2, and provides a second validation of the method in the case of the industrial problem to be solved in this work.

ACKNOWLEDGEMENTS

This work has been supported by John Crane Lips Defense Propulsion Systems. This contribution is gratefully acknowledged.

REFERENCES

Arndt, R.E.A, Keller, A.P. 1992. Water quality effects on cavitation inception in a trailing vortex. Journal of Fluids Engineering, Vol.114, pp.430.

Dacles-Mariani, J., Zilliac, G.G., Chow J.S., Bradshaw P. 1995. Numerical/Experimental study of a wingtip vortex in the near field. AIAA Journal, Vol.33, No.9, pp.1561–1568.

Fruman, D.H. 1995. The *Action Concertée Cavitation* research program and accomplishments. CAV'95: International Symposium on Cavitation , Deauville, France, pp.211-217.

Fruman, D.H., Cerrutti, P., Pichon, T., Dupont, P. 1995. Effect of hydrofoil planform on tip vortex roll-up and cavitation. Journal of Fluids Engineering, Vol.117, pp.162-169.

Fruman, D.H., Dugué, C., Pauchet, A., Cerrutti, P. and Briançon–Marjolet, L. 1992. Tip vortex roll–up and cavitation. 19th Symposium on Naval Hydrodynamics, Seoul, Korea.

Hsiao C.T., Pauley L.L. 1998. Numerical study of the steady-state tip vortex flow over a finite-span hydrofoil. Journal of Fluids Engineering, Vol.120, pp.345-353.

Keller, A.P. 2001. Cavitation scale effects – Empirically found relations and the correlation of cavitation number and hydrodynamic coefficient. CAV2001: Fourth International Symposium on Cavitation, Pasadena, USA.

Kinnas, S.A., H Lee, Mueller, A.C. 1998. Prediction of propeller blade sheet and developed tip vortex cavitation. 22nd Symposium on Naval Hydrodynamics, Washington D.C., USA, pp.182-198.

Kuiper,G. 2001. New developments around sheet and tip vortex cavitation on ship's propellers. CAV2001: Fourth International Symposium on Cavitation, Pasadena, USA.

McCormick, B.W. 1962. On cavitation produced by a vortex trailing from a lifting surface. ASME, Journal of Basic Engineering, pp.369-379.

Navaza, A.V. 2002. Influence de la géométrie d'extrémité de pales sur la cavitation de tourbillon marginal. Application aux hélices marines. Thèse de doctorat, University of Nantes, France.

Pauchet, A., Briancon-Marjollet, L., Gowing, S., Cerrutti,P., Pichon, T. 1994. Effects of foil size and shape on tip vortex cavitation occurrence. Second International Symposium on Cavitation, Tokyo, Japan.

Viot, X., Fruman, D.H., Deniset, F., Billard, J.Y. 1998. Numerical simulation of tip vortices roll-up. 22nd Symposium on Naval Hydrodynamics, Washington D.C., USA.

Unsteady Navier–Stokes equations: A fully coupled method for unstructured meshes

E. Didier* and B. Alessandrini**

* *Departamento de Engenharia Mecânica e Industrial,*
Universidade Nova de Lisboa, Faculdade de Ciências e Tecnologia,
Campus de Caparica, 2829-516 Caparica, Portugal
E–mail: deric@fct.unl.pt, Webmail : http://fct.unl.pt
** *Division Hydrodynamique Navale, Laboratoire de Mécanique des Fluides,*
Ecole Centrale de Nantes, 1 rue de la Noë BP 92101, 44072 Nantes Cedex 03, France
E–mail: alessandrini@ec-nantes.fr, Webmail : http://ec-nantes.fr

1. Introduction

The simulation of non–stationary flows requires accurate modeling of the non–linearities present in the Navier–Stokes equations. Due to the linearisation of these equations, it is necessary to perform one or more non–linear iterations during the simulation process.

However, traditional solution methods, like segregated method where momentum and pressure equations are solved successively, appear insufficient to deal with non–stationary flows simulation. These procedures, where the unknown factors are not given simultaneously, are called decoupled methods.

A fully coupled method of resolution is presented which solves simultaneously the momentum and pressure equations, by solving one only linear system coupling velocity and pressure unknowns [1]. The non–linear effects are thus handled better, and the non–linear residues convergence is accelerated. In this paper the proposed solution methods employs the finite volume formulation adapted to unstructured meshes [3] [4].

2. Numerical model

The bidimensional Navier–Stokes equations written in conservative form are integrated on each control volumes, and discretised using the cell–centered location of the velocity and pressure unknowns.

The mixed unstructured grid verifies the criteria of Delaunay triangulation. A wall mesh refinement, supporting quadrilateral control volumes, makes it possible to model directly the boundary layer, while preserving the mesh orthogonality.

The overall accuracy of the implicit schemes is second order in time and space. The three points Euler implicit scheme is used for discretisation time. Convectif and diffusive terms are discretised in space using deferred correction scheme [5] and centered differencing scheme respectively. For unstructured meshes it is difficult to keep the second order accuracy in implicit schemes based on compact molecules of discretisation; Since in this case only unknowns on both sides of the control volume interface are used. Compact schemes are thus more adaptable to ensure the solvability of the coupled linear system. In this case explicit corrections are requires so that the overall accuracy approaches the second order. The algebraic transport equation can be written as

$$u_{i_p} + C_{k \neq p}\, u_{i_{k \neq p}} + G_k p_k = F_{u_i} \quad \text{with} \quad i = 1, 2 \tag{1}$$

In this equation, index p defines a value of center control volume, index k defines value of nearest neighbors and center control volume$\{1, .., n, p\}$, u_i a component velocity with $i = (1, 2)$, p the dynamic pressure. The right member F_{u_i} contains explicit part resulting to the approximation schemes.

Secondary velocity unknown u_i^* is introduced, in order to write a relation between velocity at the center control volume, secondary velocity and the discrete pressure gradient.

$$u_{i_p} - u_{i_p}^* + G_k p_k = 0 \quad \text{with} \quad i = 1, 2 \tag{2}$$

A new algebraic equation is obtained for the secondary velocity:

$$u_{i_p}^* + C_{k \neq p}\, u_{i_{k \neq p}} = F_{u_i} \quad \text{with} \quad i = 1, 2 \tag{3}$$

This discret equation can then be write in a continuous differential form. So that by cancelation of the divergence operator a pressure equation is obtained. A Rhie and Chow mass flux reconstruction [7] allows to obtain a discret pressure equation.

$$(D_i)_k (u_i^*)_k - DG_k\, p_k = F_P \quad \text{with} \quad i = 1, 2 \tag{4}$$

3. Fully coupled solver method

The fully coupled linear system $Ax = b$ for the velocity and pressure unknowns can be written in the following form :

$$\begin{bmatrix} I & -I & G \\ C & I & 0 \\ 0 & D & -DG \end{bmatrix} \begin{bmatrix} U \\ U^* \\ p \end{bmatrix} = \begin{bmatrix} F_U \\ F_{U^*} \\ F_P \end{bmatrix}$$

The matrix A is a sparse matrix, non–symmetrical with a large dimension, made up of several blocks. Particularly the DG block concerning incompressible pressure equation is very ill–conditioned.

A preconditioning LU is applied to the matrix A. The preconditioning linear system is solved using the iterative solution method BiCGSTAB-w [8] [10]. The figure 1 presents the reduction order of the maximum normalized variation velocity during a time iteration, for flow calculation around a cylinder ($Re = 3000$). A six order reduction is rapidly obtained after five non–linear iterations.

The figure (figure 2) presents the residue convergence for the resolution of a simple problem of thermic diffusion in a square domain for a structured and an unstructured grid.

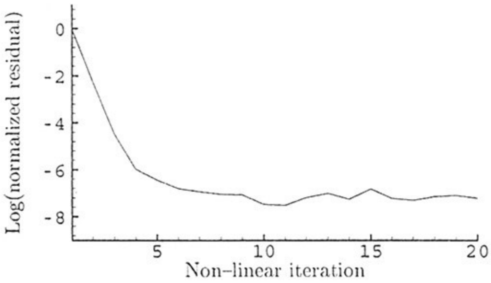

Figure 1. Non-linear iteration.

The residue convergence is faster for a structured grid than for the unstructured grid. First part convergence is identical but residue decreases very quickly for structured grid in the second part of the convergence process. That is certainly due to the multi-diagonal matrix structure of the linear system in the particular case of a structured grid. This diagonal structure associated with a preconditioning LU gives a better matrix conditioning, and thus a faster resolution by iterative methods.
This iterative resolution method BiCGSTAB-*w* preconditioned *LU* on unstructured grid requires once and an half times more iterations than for a structured grid. Nevertheless, it ensures a regular residue convergence.

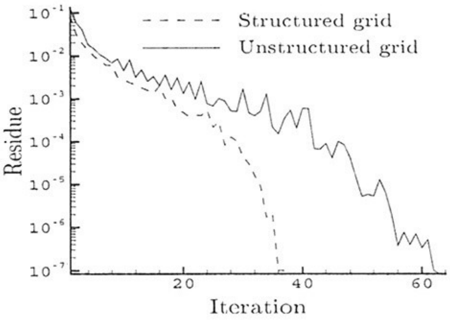

Figure 2. Residue convergence for a structured and an unstructured grid.

4. Numerical results

Flow around one cylinder, $Re = 3000$ *and* $Re = 9500$

For $Re = 3000$, the numerical results of circulation length normalized by cylinder diameter L/D are in very good agreement with experimental data [2] and with the numerical results from a vorticity-current function formulation [6] (figure 3). The circulation zone is however slightly over–estimated beyond that from non–dimensional time $t = 2$. The evolution of the first component of velocity profile on the principal axis of the wake is in accordance with experimental results [2]. For an non–dimensional time higher than $t = 2$ a slightly over–estimated of the minimal velocity is observed.

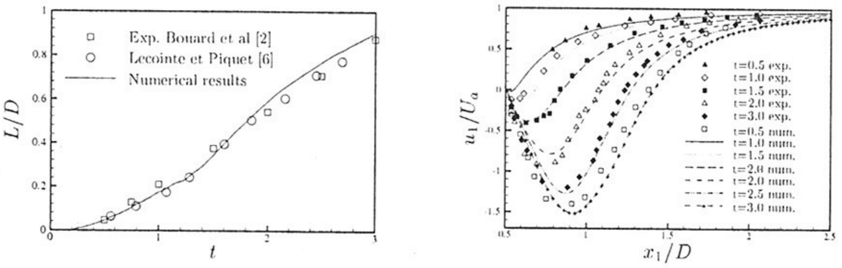

Figure 3. Circulation length and velocity profiles, $Re = 3000$.

For $Re = 9500$, the circulation length L/D and velocity profile of the first component on the principal axis of the flow for five different times are presented on figure 4. Numerical results are in very good accordance with the experimental data [2] and the numerical results for a vorticity–streamlines function [6]. The circulation length evolution is predicted with a good accuracy. Numerical results presented are in very good accordance with each experimental velocity profile. Only a small over–estimation of velocity can be noticed for $t = 1.8$.

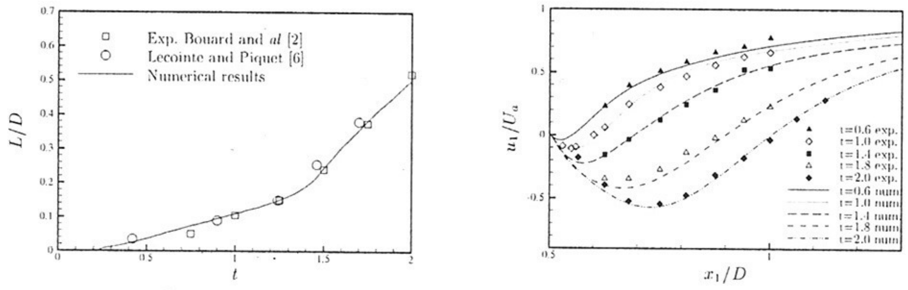

Figure 4. Circulation length and velocity profiles, $Re = 9500$.

Two cylinders coast at coast, $Re = 2200$

The figure 5 presents the temporal evolution position of internal and external vortex center, for center to center distance cylinders of $T/D = 1.5$, Reynolds number $Re = 2200$. Parameters a/D and b/D indicate respectively the position of the vortex center A or B compared with the cylinder edge, and distances between the vortex centers A or B.
Positions of the internal vortex A and external vortex B are relatively well estimated. Vortex velocity distance are in good agreement with experimental data [9]. The distance b/D between vortex A is slightly over–estimated whereas position center of vortex B presents a strong

similarity with experimental data. One can notice that the internal vortex is released more rapidly with higher velocity than the external vortex.

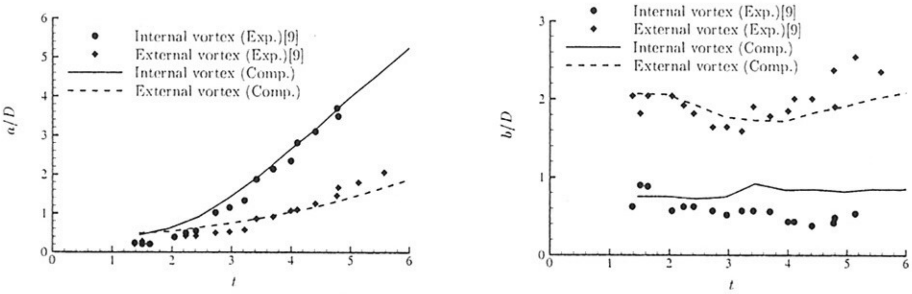

Figure 5. Evolution of a/D and b/D for two cylinders coast at coast $T/D = 1.5$, $Re = 2200$.

Two cylinders in tandem arrangement

Here we chose to validate the case of two cylinders in tandem arrangement, in laminar flow. The non–dimensional cylinder distance center to center T/D is equal to 2.

Figures 6 shows the mixte unstructured grid composed by 30000 cells used and the streamlines at a non–dimensional time $t = 15$ for a Reynolds number equal to 200. A computational time of 4 hours is necessary for simulation of a non–dimensional time $t = 15$, on workstation Compac, processor $EV6$, 500 MHz. Two stable symmetric circulation areas appear between the first cylinder and in front of the second cylinder. At the rear of the second cylinder, two instable large circulation are generated, and alternate vortex is released.

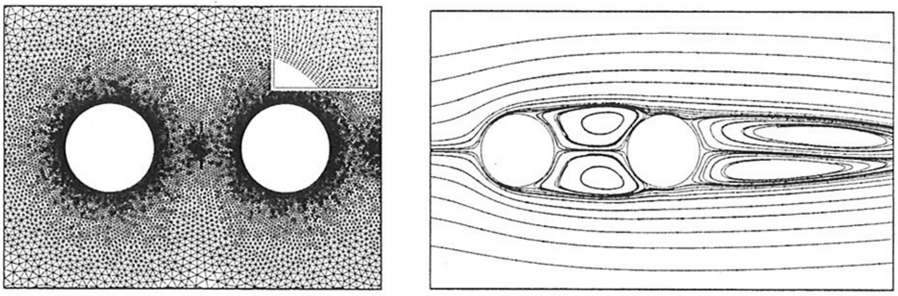

Figure 6. Grid around two cylinders in tandem arrangement and flow at non–dimensional time $t = 15$.

Figure 7 shows the non–dimensional drag coefficient C_d for each cylinder as a function of non–dimensional time t. These results are in agreement with experiments reported by Zdravkovich [11] which shows that for $T/D = 2$, the first cylinder experiences a drag coefficient C_d around 1 (for a single circular cylinder, $C_d = 1.35$). The second cylinder experiences a drag coefficient around -0.2. Computational values for drag coefficient present a very good agreement with experimental data. Particularly drag coefficient of rear cylinder is exactly -0.2, and an error lower than 2.5% is obtained for drag coefficient of front cylinder.

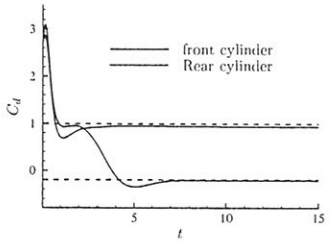

Figure 7. Drag coefficients for two cylinders, $Re = 200$, $T/D = 2$.

5. Conclusion

The results presented here show the ability of the fully coupled method based on the construction of one linear system in velocity and pressure in case of unstructured grids to reduce non-linear residues very quickly. Comparisons of predictions for different unsteady flows with experimental observations are in good agreement.

Further development of the method includes implementation of a turbulence model, in order to simulate turbulent flow.

REFERENCES

1. B Alessandrini and G Delhommeau A multigrid velocity–pressure–free surface elevation fully coupled solver for turbulent incompressible flow around a hull calculations *Proc 9th International Conference on Numerical Methods in Laminar and Turbulent Flows, Atlanta* 1995; 1173–1184.
2. R Bouard and M Coutanceau The early stage of development of the wake behind an impulsively started cylinder for $40 < Re < 10^4$ *Journal of Fluids mechanics* 1980; **101**,part3:583–607.
3. E Didier and B Alessandrini Simulation d'écoulements visqueux à surface libre pour des géométries complexes à l'aide de maillages déstructurés. $8^{ième}$ *Journées de l'Hydrodynamique, Nantes* 2001.
4. E Didier Simulation d'écoulements à surface libre sur des maillages déstructurés. *PhD Thesis, Ecole centrale de Nantes* 2001.
5. Khosla PK, Rubin SG. A diagonally dominant second-order accurate implicit scheme. *Computers fluids* 1974; **2**:207–209.
6. Y Lecointe and J Piquet Compact finite-difference methods for solving incompressible Navier–Stokes equations around oscillating bodies *Chapter 1985-04, Von Karman Institute, Lecture Series* 1985.
7. Rhie CM, Chow WL. A numerical Study of turbulent flow past an isolated airfoil with trailing edge separation. *AIAA Journal* 1983; **21**:179–195.
8. G L G Sleijpen and H A Van der Vorst Maintaining convergence properties of BiCGSTAB methods in finite precision arithmetic *Numerical Algorithms* 1995; **10**:203–223.
9. D Summer and S J Price and M P Paidoussis Investigation of impulsively started flow around side-by-side circular cylinders : application of particle image velocimetry *Journal of Fluids and Structures* 1997; **11**:597–615.
10. H Van der Vorst Bi-CGSTAB : a fast and smoothly converging varaint of bi-CG for the solution of nonsymetric linear systems *J. Sci. Stat. Comp.* 1992; **2**:218–231.
11. M Zdravkovich Review of flow interference between two circular cylinders in various arrangements *ASME* 1977.

Shape Optimization in a Complex Numerical Framework : Advances and Limitations

R. Duvigneau & M. Visonneau
LMF DMN, Ecole Centrale de nantes, 44321 Nantes, France

Introduction

Thanks to the progress in Computational Fluid Dynamics (CFD) during the last years, flow solvers are now integrated in fully automated design optimization procedures. In order to use these shape optimization tools in an industrial framework to solve realistic problems, some conditions are required. First, the flow solver implemented should be able to provide accurate predictions of complex flows, for high Reynolds number and realistic geometries. Indeed, one may expect to solve three-dimensional problems on unstructured grids, using sophisticated turbulence models. For hydrodynamics applications, free surface calculation methods are also required. This condition suppose to solve optimization problems in a complex numerical framework and will have strong consequences for the choice of the optimization strategy.

The second condition in order the design tool to be practically used concerns the computational costs. Since several expensive simulations have to be performed, the costs are usually prohibitive and the optimization strategy chosen should require as few evaluations as possible.

Then, the optimized shapes obtained should provide interesting solutions to the problem studied. Therefore, one may expect to find through the search the global optimum. Multi-objective solutions are also usefull, since opposite goals are often faced in practice. An other requirement is that the final shape is rather unsensitive to the physical or numerical parameters used.

This paper is devoted to the study of the optimization strategies which could be used to fulfil the conditions described previously. The difficulties arising from the use of a complex flow solver in the design procedure are particularly explored.

The ISIS flow solver

The flow solver ISIS, developed in our laboratory is included in the design procedure. It solves the incompressible Reynolds-Averaged Navier-Stokes Equations (RANSE) on unstructured grids, with a strongly conservative formulation. The discretization scheme uses a finite-volume method, generalized to unstructured meshes composed of arbitrary volume shapes. Thus, calculations involving complex grids may be taken into account. The flow variables are stored at the center of the control volumes, surface and volume integrals being evaluated using second order accurate approximations. The pressure-velocity coupling is performed by a SIMPLE-like algorithm. Several near-wall low-Reynolds number turbulence models, ranging from one-equation Spalart-Allmaras model, two-equation $k-\omega$ closures, to a full Reynolds stress transport $R_{ij}-\omega$ model are implemented in the flow solver. Free-surface calculations are also possible through surface-fitting or surface-capturing methods.

Optimization strategies

Several strategies may be considered to drive the search of the optimal shape. In order to reduce the computational costs, one may propose to use gradient-based methods, characterized by a superlinear convergence and an indepedance from the number of design parameters. However, the implementation of this strategy in a complex numerical framework is particularly tedious. Indeed, the evaluation of the derivatives of the cost function with respect to the design parameters relies on the differentiation of the flow solver, through the resolution of an adjoint equation [1]. Thus, this approach is still limited to middly complex problems, involving typically unviscid flows. Two alternative approaches may be considered to evaluate the derivatives : the automatic differentiation softwares and an incomplete evaluation of the gradient, neglecting the modifications of the flow. But these methods are still limited by the complexity of flow solver in the first case and the range of application in the second case. Moreover, gradient-based methods have several drawbacks. They can only consider one optimization criterion and are particularly sensitive to the numerical noise arising from the use of complex numerical methods and generating spurious local optima. Considering all these remarks, the gradient-based strategies are rejected in this framework. This choice has crucial consequences, since all other approaches are submitted to the "curse of dimensionality", the number of evaluations required being at least proportional to the dimension of the problem. Thus, the parameterization of the shapes should involve as few design variables as possible.

Derivative-free deterministic algorithms, such as the simplex method [3] based only on function values comparisons, may be easily implemented in the design procedure, since the flow solver is considered as a "black box", yielding both flexibility and robustness to solve complex optimization problems. Moreover, this kind of methods is less sensitive to the noisy errors. Nevertheless, they are limited to perform local optimizations including one criterion.

Therefore, stochastic methods, such as Genetic Algorithms (GAs), are particularly appealing. Indeed, they have the capability to perform global optimizations and solve multi-objective problems. Furthermore, their robustness to solve multi-modal problems has been shown several times in the past. As derivative-free methods, their implementation in the particular framework of complex CFD is quite easy [4]. However, this strategy is particularly expensive, since the number of evaluations is about ten times higher than the number required by deterministic methods. These costs make the use of genetic algorithms unrealistic for three-dimensional problems.

These observations look quite pessimistic. Although the ultimate optimization strategy does not exist yet, one may propose a realistic way, taking the best parts of the different strategies and using approximation methods to reduce the computational time. Genetic algorithms have two main drawbacks: the number of evaluations and the low local convergence rate. To reduce the number of evaluations through the flow solver, one may use the knowledge already collected on the problem to build local approximations replacing some expensive evaluations [8]. More precisely, all exact evaluations through the flow solver are stored in a database, whose entries are used to train Artificial Neural Networks (ANNs). They are employed to perform inexact pre-evaluations of the shapes at each generation, only the most promising shapes according to the ANNs pre-evaluations being exactly evaluated through the flow solver. In that way, the number of expensive evaluations may be significantly reduced, without loosing the interesting capabilities of genetic algorithms. Then, genetic algorithms are only expected to determine the overall characteristics of the optimal shape and the final local search is performed by a deterministic algorithm, which can quickly precisely define the shape.

This strategy, using hybrid genetic algorithms and neural networks, has been successfully applied to optimize the shape of a three-dimensional wing at the incidence 8°, at a location close to the salmon, with respect to the lift [5]. For this case, an unstructured mesh of about 800 000 cells was used, for a Reynolds number $Re = 2\,10^6$, the near-wall low-Reynolds number SST $k-\omega$ model being employed. The shape is described by 12 design parameters. The figure 1 representing the evolution of the cost function during the design procedure illustrates the strategy. The calculations are performed using a multi-block parallelization technique, on sixty R14000 processors. As seen, very complex problems may be solved using this strategy. Even if the costs remain quite large, the CPU time has been reduced more than five times with respect to a simple genetic algorithm. Although this approach has still some limitations, such as the number of design variables involved, it seems to be a realistic and promising way.

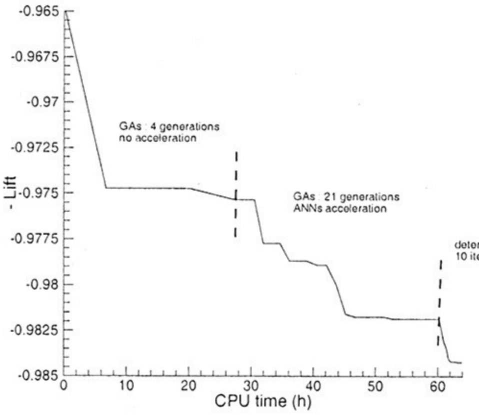

Figure 1: Evolution of the cost function

Shape parameterization and mesh update

When three-dimensional unstructured meshes are employed, the parameterization as well as the mesh update during the design process are difficult tasks. Indeed, a curvilinear representation of the shape is not available. Thus, the use of B-spline net representations for instance is tedious. The nodes coordinates on the shape and connectivities are the only knowledge which could be used. Therefore, a Free Form Deformation (FFD) technique [10] is used to control the shape perturbations during the design process. It consists in embedding in a box the object to be deformed, and then modifying the space in the box and the object inside by deforming the box, rather than modifying the object itself. In that manner, the shape of the object can be modified without even identifying its nature. This powerfull approach provides an easy-to-use solution, requiring only a few control points to control the deformation of the shape. However, this general technique may be inadequate to deal with a particular and specialized problem.

The automated mesh update is problematic, when unstructured grids using a near-wall turbulence modeling formulation is employed, since the grid volumes are highly stretched near the wall to fulfil the condition $y^+ \leq 1$. The spring analogy [7] previously used to deform two-dimensional meshes [3], may hardly be employed for three-dimensional problems. Therefore, one may recommend to smoothly deform the shape and the mesh by the FFD method at the same time, since the FFD approach relies on a spatial deformation. This strategy may be carried out for two-dimensional as well as three-dimensional grids and is obviously adequate for multi-block calculations. However, the quality of the resulting grid is not ensured. An example of deformation of a hybrid grid around the NACA 0012 airfoil is provided by the figures 2 to 4, using the spring analogy and the FFD method. As seen, the FFD method provides a smoother deformation, but the orthogonality of the grid near the wall is not maintained, contrary to the spring analogy. Nevertheless, the FFD method gives satisfactory results, when small perturbations are taken into account.

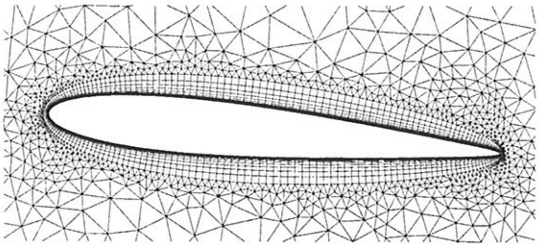

Figure 2: Initial mesh

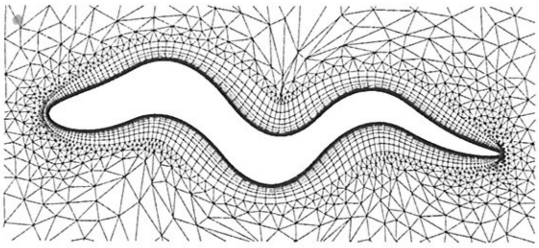

Figure 3: Spring analogy

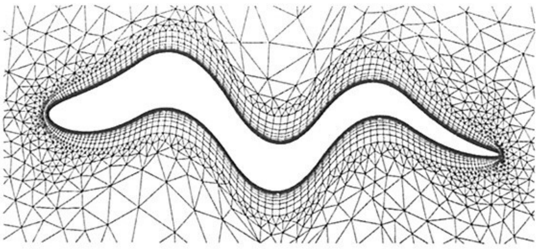

Figure 4: Free Form Deformation

Influence of turbulence modeling

The previous sections provide some solutions to solve optimization problems involving a complex flow solver. However, one should validate the results obtained and quantify the influence of the numerical and physical parameters on the design procedure. Indeed, some quantities have an influence on the resolution of the flow and thus on the optimal search. For instance the grid size, the stopping criteria, the discretization schemes, turbulence modeling, generate noisy errors during the evaluations [9]. A precise study concerning the role played by turbulence closures for hull shape optimization was performed in [6].

The flow around the KVLCC2 tanker is computed at full scale ($Re = 10^9$), using a structured mesh of about 400 000 volumes. Two turbulence models are tested: The eddy-viscosity SST $k - \omega$ model of Menter and a second-order closure $R_{ij} - \omega$ model. The goal of the optimization is to homogenize the longitudinal velocity field at the location of the propeller, modifying the stern of the ship described by 6 design variables. It was shown that the two models give different predictions of the wake for the initial shape, the longitudinal vortex generated being intensified by the second order closure [2]. However, these differences are less important at full scale than at model scale. We intend to quantify the influence of the turbulence modeling during the optimization process.

The figures 5 and 6 show the isowakes for the initial and final shapes. As seen, the optimal shapes are characterized by a far more intense longitudinal vortex homogenizing the flow and close to the vortices observed at model scale. This evolution during the design process enforces the influence of the turbulence modeling. The figure 7 and 8 represent the streamlines close to the wall. One may observe that the topology of the flow has changed and is finally similar to model scale flows. Therefore, some differences between the models appear, even at full scale. Looking at the optimized shapes (figure 9), similar trends are obtained, although some differences are noticed due to the fact that the second order closure provides a more intense prediction of the flow. Therefore, lower modifications may generate a more intense vortex. One may notice that the final shapes found correspond to U-shaped hull. The evolution of the cost function, given in figure 10, shows a reduction of 70% of the velocity mean deviation at the propeller location. The reduction is lower for the second order closure. This phenomena is maybe due to the presence of more complex turbulence structures in the wake, which are not described by the linear eddy-viscosity model.

Finally, this example underlines the influence of turbulence modeling in the framework of hull shape optimization. Although its role was a priori less important at full scale, it was shown that the choice of the turbulence model may have a crucial influence, when a sharp optimization process is performed.

Conclusion

This study explored different strategies to solve shape optimization problems involving complex flow solvers. As seen, the choice of the optimizer strongly depends on the framework and has crucial consequences. Genetic algorithms have several advantages over deterministic approaches. It was shown that their use is now realistic, providing that acceleration techniques are employed, such as inexact pre-evaluations through artificial neural networks. Some practical difficulties still exist, for instance the mesh update for three-dimensional problems. However, the main limitation may be the influence of turbulence modeling on the design process for some problems, since this modeling error cannot be controled, contrary to other numerical parameters, such as grid size or partial convergence.

References

[1] W. K. Anderson and V. Venkatakrishnan. Aerodynamic design optimization on unstructured grids with a continuous adjoint formulation. *Computers and Fluids*, 28(4):443–480, 1999.

[2] G. Deng and M. Visonneau. Comparison of explicit algebraic stress models and second-order turbulence closures for steady flows around ships. In *Proceedings of the Seventh International Conference onNumerical Ship Hydrodynamics*, Nantes, France, July 1999.

[3] R. Duvigneau and M. Visonneau. Shape optimization for incompressible and turbulent flows using the simplex method. AIAA Paper 2001–2533, June 2001.

[4] R. Duvigneau and M. Visonneau. Single- and multi-objective optimization for high-fidelity cfd using genetic algorithms. In *EUROGEN 2001 - Evolutionary Methods for Design, Optimisation and Control with Applications to Industrial Problems*, September 2001.

[5] R. Duvigneau and M. Visonneau. Hybrid genetic algorithms and neural networks for fast cfd-based design. AIAA Paper 2002–5465, September 2002.

[6] R. Duvigneau and M. Visonneau. On the role played by turbulence closures in hull shape optimization at model and full scale. In *24th ONR Symposium on Naval Hydrodynamics*, July 2002.

[7] C. Farhat, C. Degand, B. Koobus, and M. Lesoinne. Torsional springs for two dimensional dynamic unstructured fluid meshes. *Computational Methods in Applied Mechanics and Engineering*, pages 231–245, 1998.

[8] A.P. Giotis and K.C. Giannakoglou. *Eurogen 99, evolutionary algorithms in engineering and computer science*, chapter Single- and multi-objective airfoil design using genetic algorithms and artificial intelligence. John Wiley & sons, 1999.

[9] J.I. Madsen. Response surface techniques for diffuser shape optimization. *AIAA Journal*, 38(9):1512–1518, 2000.

[10] J.A. Samareh. A survey of shape parameterization techniques. In *CEAS/AIAA/ICASE/NASA Langley International Forum on Aeroelasticity and Structural Dynamics*, June 1999.

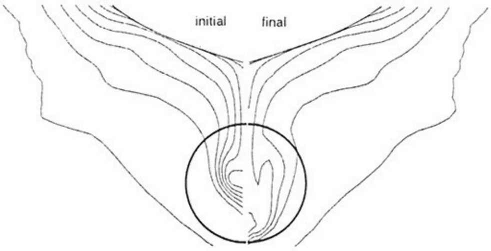

Figure 5: Isowakes for the SST $k - \omega$ model

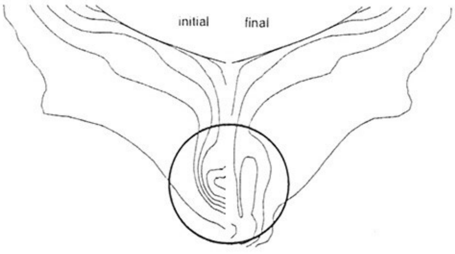

Figure 6: Isowakes for the $R_{ij} - \omega$ model

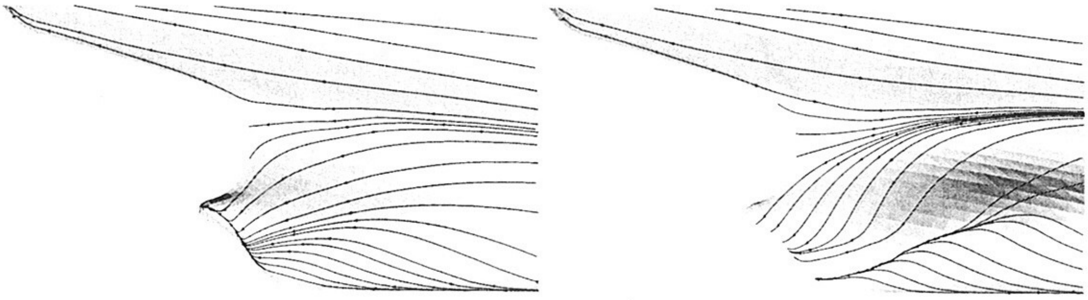

(a) Initial

(b) Final

Figure 7: Streamlines for the SST $k - \omega$ model

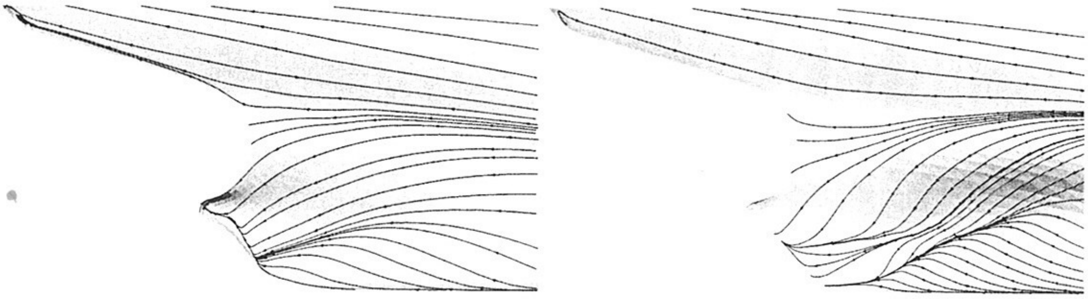

(a) Initial

(b) Final

Figure 8: Streamlines for the $R_{ij} - \omega$ model

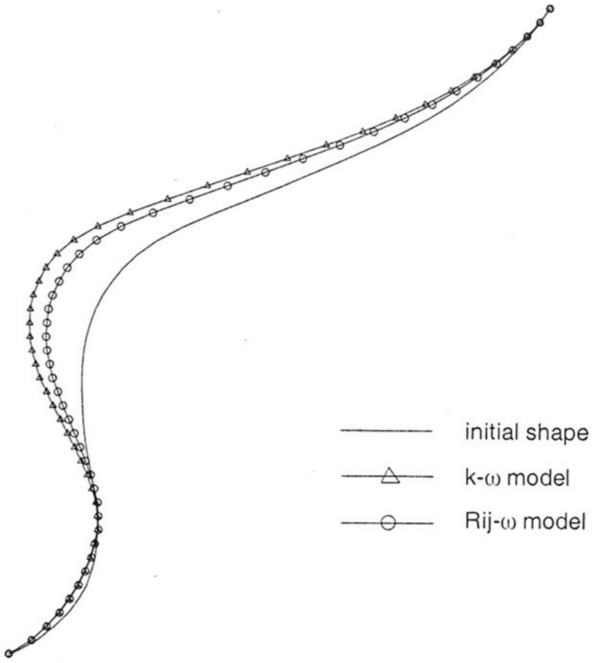

Figure 9: Initial and final shapes

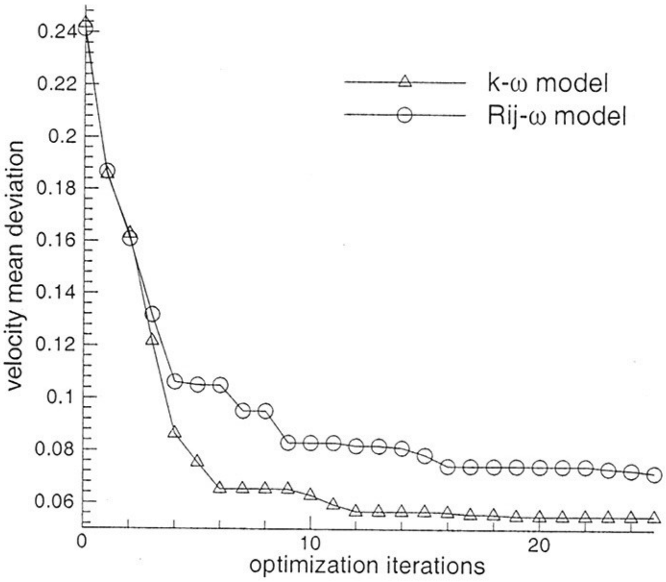

Figure 10: Evolution of the cost function

A NEW POTENTIAL / RANSE APPROACH FOR WATER WAVE DIFFRACTION

Pierre Ferrant, Lionel Gentaz, David Le Touzé

Division Hydrodynamique Navale, Laboratoire de Mécanique des Fluides,
Ecole Centrale de Nantes, 1, rue de la Noë, BP 92101, 44321 Nantes Cedex 03, France
e-mail : Pierre.Ferrant@ec-nantes.fr, Lionel.Gentaz@ec-nantes.fr, David.Letouze@ec-nantes.fr

Abstract

This paper is devoted to the numerical simulation of water diffraction in viscous flow. An original approach using a diffracted flow defined as the difference between total and incident flows is followed. The incident flow is defined explicitly using nonlinear potential flow theory; Navier-Stokes equations and nonlinear free surface boundary conditions are solved for the diffracted flow only. This procedure, which is very efficient in terms of computing time and accuracy, was primarily developed by Ferrant (1996) for 3D non linear wave-body interactions in potential theory.

INTRODUCTION

Today Numerical Wave Tanks (NWTs) have become efficient tools for coastal or ocean engineering problems. First NWTs were based on the potential flow theory, following the Mixed Euler-Lagrange Method introduced by Longuet-Higgins and Cokelet (1976). Potential flow nonlinear NWTs were developed by Cointe (1989) in 2D or Beck (1994) in 3D, among many others. Alternative models based on RANS (Reynolds-Averaged Navier-Stokes) Equations with finite difference or finite volume methods may be developed, allowing vorticity and viscous effects occurring in wave-body interaction problems to be modeled. In such methods, the interface can be updated by different manners : the free surface capturing principle has been used by Harlow & Welch (1965) or Miyata (1986) with the Marker and Cell (MAC) method or Hirt & Nichols (1981) and many others with the Volume of Fluid (VOF) method. Examples of interface tracking methods may be found in Daubert & Cahouet (1984) or Yeung & Ananthakrishnan (1994)

Wave generation and absorption are of course of primary importance in such numerical simulations. Wave generation is usually performed by the simulation of a wavemaker on the upstream boundary of the wave tank, which is equivalent to the prescription of a wave kinematics on this boundary. The generation of waves by a pressure patch (see Armenio and Favretto 1997) acting over a narrow area of the free surface is advantageous because the upstream boundary can be used for wave damping. This damping can be achieved by implementing an open boundary condition (Orlanski 1976) or by modifying free surface boundary conditions (see e.g. Clément (1996) for the absorption in potential NWT's). However wave generation and wave damping remain an issue in NWTs based on RANS equations.

In RANSE NWT's a fine grid (more than 50 nodes per wavelength) is necessary for a correct simulation of wave propagation, without damping or dispersive effect, leading to large CPU. Moreover wave reflections on the body or on the downstream boundary and consecutively on the upstream boundary are going to affect the incoming wave train: as a consequence, the useable duration of the simulation (for computation of hydrodynamic loads on the structure for example) is usually limited.

In this paper a new formulation is proposed which suppresses these limitations by modifying the initial problem in order to solve the diffracted flow only. This approach was previously used for potential flow model in 2D (Schønberg & Chaplin 2001) or 3D cases (Ferrant 1996). It consists in splitting all unknowns of the problem (potential and free surface elevation) in a sum of an incident term and a diffracted term. The incident terms are described explicitly. Here splitting of unknowns will be applied to a 2D viscous flow solver (Gentaz *et al.* 2000) whose main properties are described hereafter. The case of a regular wave train on a submerged square body is studied to demonstrate the viability of the proposed approach.

NUMERICAL PROCEDURE

The initial RANSE Solver

The fluid domain is discretized by a structured monoblock grid. A free surface tracking method is used to update the interface : at each time step the mesh is regridded following the new shape of the free surface. RANS Equations and fully nonlinear free surface boundary conditions are discretised by 2nd order finite difference schemes in space and time. A pressure equation is obtained by combining the equation of mass conservation with transport equations following the Rhie and Chow procedure : thus checkerboard oscillations classically associated with center 2nd order schemes are suppressed.

An original method called fully-coupled method (Alessandrini and Delhommeau, 1995) is used to solve the discretized problem : at each time step all equations (RANS Equations, pressure equation, free surface boundary conditions, no-slip conditions) are collected in a single large and sparse linear system which is solved by a bi-CGSTAB algorithm. With such a technique the velocity-pressure coupling and nonlinear convergence are improved compared to weak coupling algorithms as SIMPLER, which is very beneficial for the accurate simulation of unsteady flows.

Definition of the diffracted problem

To consider the single diffracted problem primitive unknowns (Cartesian components of velocity (u^α) with $\alpha \in \{1,2\}$, pressure p and free surface elevation h) are decomposed as follows :

$$\begin{cases} u^\alpha = u_I^\alpha + u_D^\alpha \\ p = p_I + p_D \\ h = h_I + h_D \end{cases} \qquad \alpha \in \{1,2\} \tag{1}$$

where variables with the underscripts I and D represent incident and diffracted variables respectively.

This decomposition is then introduced in the set of initial equations by assuming that the incident wave flow verifies RANS Equations :

- RANS equations :

$$\frac{\partial u_D^\alpha}{\partial t} + \left(u_I^j + u_D^j\right)\frac{\partial u_D^\alpha}{\partial x^j} + u_D^j \frac{\partial u_I^\alpha}{\partial x^j} = -\frac{\partial p_D}{\partial x^\alpha} + \left(\nu + \nu_t\right)\frac{\partial^2 u_D^\alpha}{\partial x^{j^2}} + \frac{\partial \nu_t}{\partial x^j}\left(\frac{\partial u_D^\alpha}{\partial x^j} + \frac{\partial u_D^j}{\partial x^\alpha}\right) \tag{2}$$

- Mass conservation : $$\frac{\partial u_D^j}{\partial x^j} = 0 \tag{3}$$

- Free surface boundary conditions :

(i) kinematic condition $$\frac{\partial h_D}{\partial t} + u_D^1 \frac{\partial h_I}{\partial x^1} + \left(u_I^1 + u_D^1\right)\frac{\partial h_D}{\partial x^1} = u_D^2 \tag{4}$$

(ii) normal dynamic condition $$p_D = \rho g h_D + 2\rho\left(\nu + \nu_t\right)\frac{\partial u_D^i}{\partial x^j} n_i n_j \tag{5}$$

(iii) tangential dynamic condition $$\left(n_j t_i + n_i t_j\right)\frac{\partial u_D^i}{\partial x^j} = 0 \tag{6}$$

In equations (2) to (6) terms with incident variables (velocities, velocity gradients, free surface elevations and free surface elevation gradients ...) are explicitly computed knowing kinematics and interface position of the incident flow.

Models of incident flows

For numerical results presented below a non linear regular wave train has been used for the incident field. An algorithm based on the stream function theory of Rienecker and Fenton (1981) has been implemented.

A non linear irregular wave train could be easily prescribed by a spectral formulation. This kind of procedure has been already developed by Ferrant & Le Touzé (2002) combining a spectral formulation and a Boundary Element Method (BEM) to simulate an irregular wave train interacting with a 3D body under potential flow theory.

It has been supposed hereafter that incident wave flows verifies RANS Equations in order to establish equations (2) to (6) for the diffracted problem. This not strictly exact because incident flow models used here are based on potential flow theory. However the error made with this assumption is negligible in practical applications.

Finally the combination of incident potential flow and RANS solvers for the diffracted problem can be summarized as follows : At each time step of the computation the geometry of the fluid domain is updated. The kinematics of the incident wave flow is calculated on this updated grid and then the diffracted problem defined by equations (2) to (6) is solved following principles of the viscous flow software described previously.

RESULTS

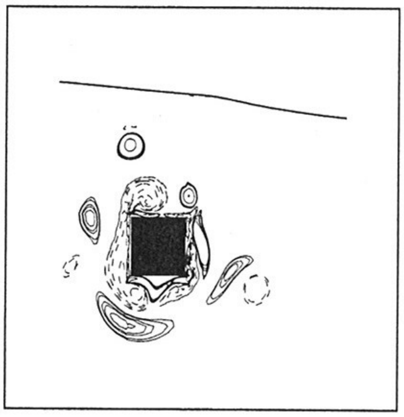

Fig. 1 : Vorticity field around the immersed structure

The interaction between regular waves and a fixed submerged square cylinder (figure 1) has been studied to validate the method. This case was studied experimentally by Araï (1995) and numerically by Armenio and Favretto (1997).

The water depth is H=0.78 m. The submerged square cylinder is 0.045 m in breadth and its center is 0.093 m below the mean water level. The wave period is T=1.05 s. Simulations were be carried out for wave steepnesses $2\xi_a / H$ varying from 1/191 to 1/24 (where ξ_a is the wave amplitude). Thus wavelength is about λ=1.735 m, depending on the amplitude. Corresponding Keulegan-Carpenter and Reynolds numbers range from 0.447 to 3.58 and 860 to 6900 respectively. Consequently numerical simulations were run with the assumption of laminar flow.

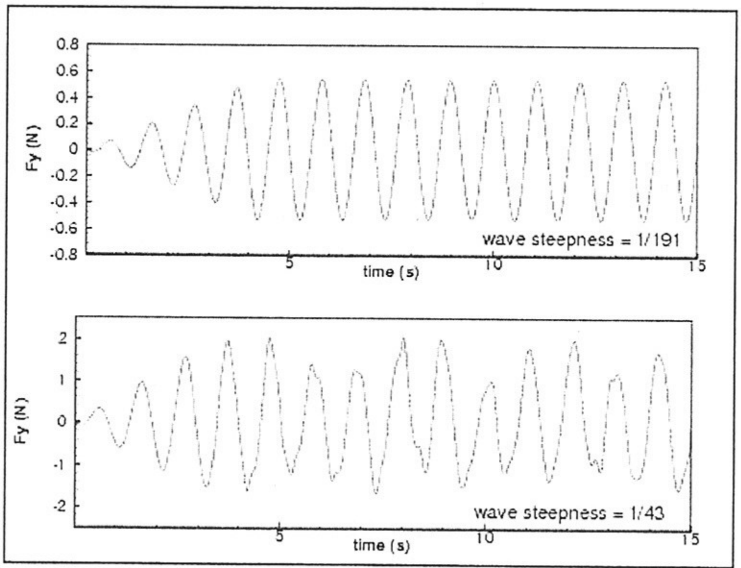

Fig. 2 : Variation of vertical hydrodynamic loads with time for $2\xi_a / H$ =1/191 (top) and $2\xi_a / H$ =1/43 (bottom)

A 39000- nodes grid is used for computations. Hydrodynamic loads are computed and compared with Armenio & Favretto's results for two steepnesses: 1/191 and 1/43. Figure 2 shows the time series of vertical hydrodynamic loads Fy acting on the immersed square section.

For the smaller amplitude a periodic regime is quickly obtained, owing to the small vortical component in the diffracted flow. On the contrary the shedding of vortices is very strong for the larger steepness of 1/43 and this shedding prevents the obtention of a periodic steady state.

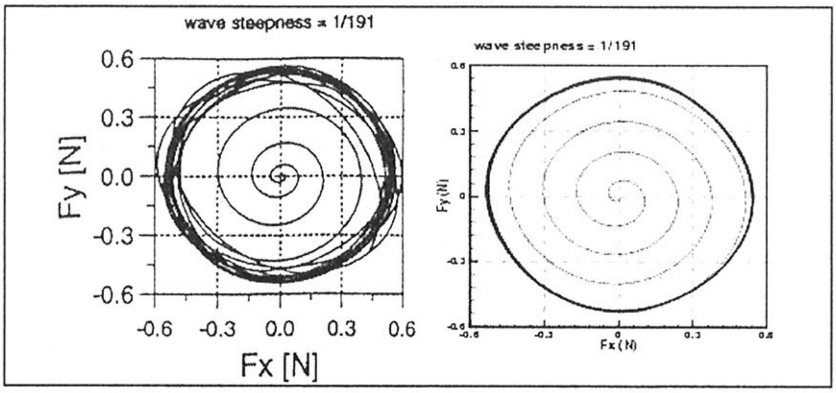

Fig. 3 : Rotating force for wave steepness $2\xi_a / H = 1/191$
Left : Armenio & Favretto's computations. Right : present computations.

Figures 3 and 4 show the rotating force (vertical component *Fy* versus horizontal component *Fx*) for steepnesses 1/191 and 1/43 respectively. On both figures present results are again compared with those of Armenio & Favretto (1997). The viscous NWT developed by these authors is based on an improved MAC method to calculate free surface elevation. Waves are generated by a periodic time variation of the pressure at the free surface. In this method the total unsteady flow is computed.

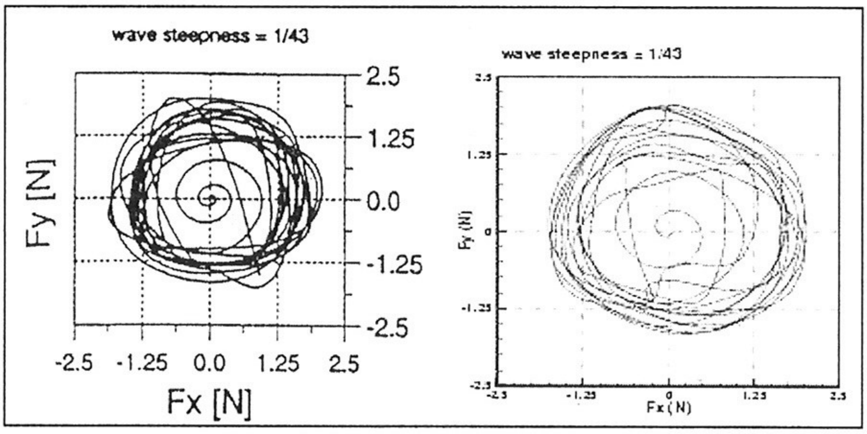

Fig. 4 : Rotating force for wave steepness $2\xi_a / H = 1/43$
Left : Armenio & Favretto computations. Right : present computations.

On the contrary in the present study RANS equations are solved for the diffracted flow only, and the total flow is obtained by summing the diffracted flow with the explicit incident flow. For both steepnesses the amplitude of horizontal and vertical forces given by present computations is in very good agreement with results of Armenio & Favretto (1997).

Finally hydrodynamic horizontal and vertical loads (per unit of length) have been decomposed following the Morisson equation (7).

$$\begin{cases} F_x(t) = \frac{1}{2}\rho D\left|u_I^1\right|\left(CD_x\right)u_I^1(t) + \rho D^2\left(CM_x\right)\dot{u}_I^1(t) \\ F_y(t) = \frac{1}{2}\rho D\left|u_I^2\right|\left(CD_y\right)u_I^2(t) + \rho D^2\left(CM_y\right)\dot{u}_I^2(t) \end{cases} \qquad (7)$$

D is the projected area of the body per unith length in both direction, ρ the water density, $u_l^1(t), u_l^2(t), \dot{u}_l^1(t)$ and $\dot{u}_l^2(t)$ velocity and acceleration components at the position of the body, $|u_l^1|$ and $|u_l^2|$ the amplitudes of horizontal and vertical velocity components, CM_x and CM_y the coefficients of the inertial forces in phase with acceleration, CD_x and CD_y the coefficients of drag forces in phase with the fluid velocity.

Practically these coefficients are computed by using a Fourier decomposition of time history of horizontal and vertical loads in a moving window. Coefficients of the Fourier decomposition in $cos(\omega t)$ and $sin(\omega t)$ lead to the determination of the inertial coefficients CM_x and CM_y. Terms of higher order are not reproduced here but could give higher-harmonic components of forces.

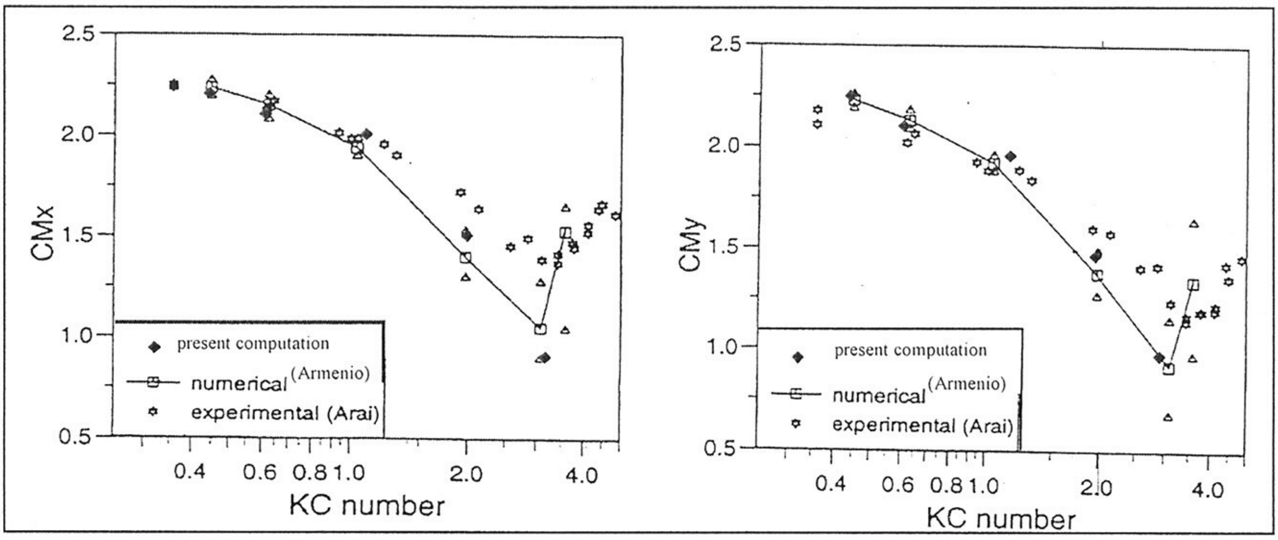

Fig. 5 : Inertial coefficients in horizontal direction (left) and vertical direction (right) versus KC number

Inertial coefficients CM_x and CM_y are compared with Armenio and Favretto computations and Araï experiments in figure 5. The agreement is quite good showing a decrease of coefficients with KC increase except for KC around 3 where present computations are comparable to Armenio & Favretto's results but underestimate experimental values.

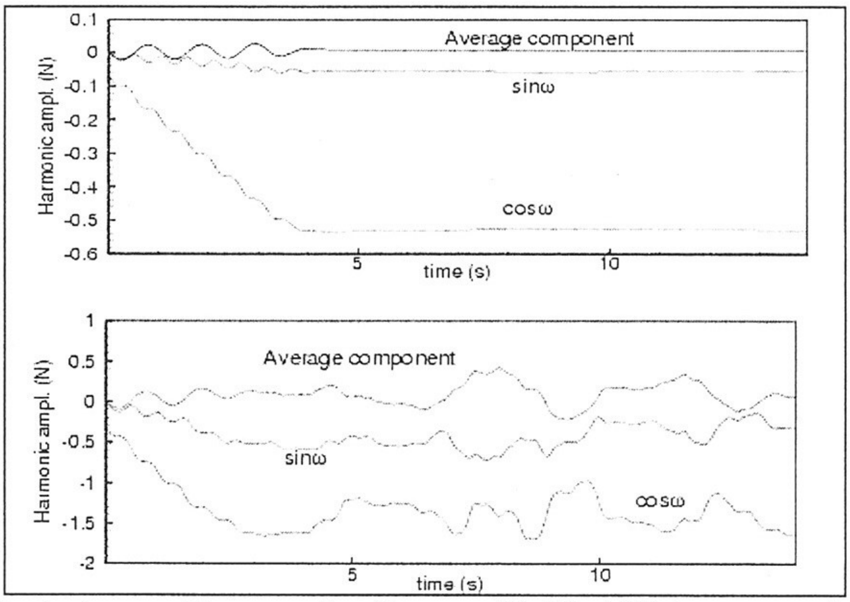

Fig. 6 : Terms of Fourier decomposition versus time. Top : case $2\xi_a / H$ =1/191, bottom : case $2\xi_a / H$ =1/43

In figure 6 the Fourier decomposition is shown for two steepnesses. The moving window is one wave period long. For the weaker steepness of 1/191, the average component or terms in $cos(\omega t)$ and $sin(\omega t)$ are sensibly constant after the first four seconds during which the incident wave field is gently introduced in the computation. This is due to small vortices which interact with the body at this steepness. On the contrary the signals are perturbed for the steepness of 1/43 that is coherent with the strong vortex shedding in this case. This conclusion is confirmed by Armenio &

Favretto's results in figure 5. The variance of results (shown by triangles for each *KC* number) increases indeed when KC becomes larger.

CONCLUSION

A new approach for wave-body interaction in viscous flow has been presented here. Instead of computating the whole velocity, pressure and free surface fields, the diffracted flow only is computed by solving RANS Equations. The incident wave field (which is nonlinear, either regular or irregular) is prescribed explicitly.

First results concerning the action of non linear regular wave field on a submerged square cylinder are encouraging and demonstrate the effectiveness of the method. With this approach classical problems of reflection of waves on bodies or boundaries that lead to a drastic reductions of useful time of calculation are avoided.

Besides non linear incident wave fields defined by domain spectral method will be considered to extend this approach to irregular wave diffraction (Ferrant *et al.*, 2001) and this approach will be developed for a three-dimensional RANS Equations solver.

REFERENCES

Alessandrini, B., Delhommeau, G. 1995. *"A multigrid velocity-pressure-free surface elevation fully coulpled solver for calculation of turbulent incompressible flow around a hull"*, 9th Int. Conf. On Numerical Methods In Laminar and Turbulent Flows, Atlanta, 1173-1184.

Araï, S. 1995. *"Forces and circulation of horizontal cylinders submerged in regular waves"*. Proc. Of 5th Int. Offs. and Polar Eng. Conf., The Hague, vol. 3, 348-355.

Armenio, V., Favretto, M. 1997. *"Development of a viscous numerical wave tank and numerical evaluation of dynamic loads on submerged bodies at small KC numbers"*, 7th Int. Offshore and Polar Eng. Conf., Honolulu, vol. 3, 98-105.

Beck, R.F. 1994. *"Time Domain Decomposition for Floating Bodies"*. J. of Applied Ocean Research, vol. 16, 267-282.

Clément, A. 1996. *"Coupling of Two Absorbing Boundary Conditions for 2D Time Domain Simulations of Free Surface Gravity Waves"*. J. of Comp. Phys., 126, 139-151.

Cointe, R. 1989. *"Nonlinear Simulation of Transient Free Surface Flows"*. 5th Int. Conf. Num. Ship Hydr, Hiroshima.

Daubert, O., Cahouet, J. 1984. *"Approche numérique de la houle par les equations de Navier-Stokes"*. Laboratoire National d'Hydraulique, EDF.

Ferrant, P. 1996. *"Simulation of Strongly nonlinear wave generation and wave-body interaction using a 3D MEL model"*. Proc. 21st ONR Symp. on Naval Hyd., Trondheim.

Ferrant, P., Le Touzé, D. 2002. *"Fully-Nonlinear Spectral/BEM Solution for Irregular Wave Interactions With a 3D Body"*. OMAE Conference, Oslo.

Ferrant, P., Le Touzé D., Pelletier K. 2001. *"Nonlinear time domain models for irregular wave diffraction about offshore structures"*, Proc. ECCOMAS Computational Fluid Dynamics Conference, Swansea.

Gentaz L., Maury C., Alessandrini B., Delhommeau G. 2000. *"Numerical Simulation of a Two-dimensional Wave Tank in Viscous Fluid"*. International Journal of Offshore and Polar Engineering (IJOPE), vol.. 10, No. 1, 1-9.

Harlow, F.H., Welch, J.E. 1965. *"Numerical calculation of Time-Dependant Viscous Incompressible Flow of Fluid with Free Surface"*. Phys. Fluids, vol. 8.

Hirt, C.W., Nichols, B.D. 1981. *"Volume of Fluid (VOF) Method for the Dynamics of Free Boundaries"*, J. of Comp. Phy., vol. 39, 201-225.

Longuet-Higgins, M.S., Cokelet, F.R.S. 1976. *"The Deformation of Steep Surface Waves on Water I:A Numerical Method of Computation"*. Proc. R. Soc. London A., 350 1.

Miyata, H. 1986. *"Finite-Difference Simulation of Breaking Waves"*. J. of Comp. Phys., vol. 65, 179-214.

Orlanski, I. 1976. *"A Simple Boundary Condition for Unbounded Hyperbolic Flows"*. J. Comp. Phy., vol. 21, 251-269.

Rienecker, M.M., Fenton, J.D. 1981. *"A Fourier approximation method for steady water waves"*, J. of Fluid Mechanics, vol. 104, 119-137.

Schønberg, T., Chaplin, J.R. 2001. *"Computation of Non-Linear Wave Reflections and Transmissions from a Submerged Horizontal Cylinder"*. Proc. of 11th Int. Offs. And Polar Eng. Conf., Stavanger, vol. III, 280-287.

Yeung, R.W., Ananthakrishnan P. 1994. *"Nonlinear Interaction of a Vortex Pair with Clean and Surfactant-Covered Free Surfaces"*. Wave Motion, vol. 19, 343-365.

Unstructured Multigrid Method for Ship Flows

Takanori HINO and Nobuyuki HIRATA *
National Maritime Research Institute, JAPAN

1. INTRODUCTION

Modern ships have a complex shape and the presence of propulsors and various appendages further increase their geometrical complexity. Therefore, hydrodynamic design tools for ship hull forms should be able to cope with bodies of complex geometry. Due to its flexibility of handling complex geometry, unstructured grid methods are expected to be one of the powerful CFD (Computational Fluid Dynamics) approaches for use of practical design applications. Flow solvers for ship design are also required to have capability of free surface flow simulations since a free surface has significant effects on the hydrodynamic performance of ships.

However, unstructured grid approaches generally require larger amounts of memory and CPU time than structured grid counterparts. Memory saving can be achieved to some extent by using an adaptive grid method, in which grid density distribution is optimized. Thus, CPU time reduction is essential for a practical use of an unstructured grid method. In the present study, a multigrid method which enables the fast convergence for steady state flow simulations is applied to an unstructured Navier-Stokes solver with a free surface capability.

In order to demonstrate the efficiency of the present approach, numerical simulations of flows around ship hulls are performed.

2. NUMERICAL PROCEDURE

2.1 Flow Solver

The flow solver used in this study is called SURF ("Solution algorithm for Unstructured RaNS with FVM") which is under development at National Maritime Research Institute[1, 2, 3]. The governing equations are the 3D Reynolds averaged Navier-Stokes equations for incompressible flows. Coupling between pressure and a velocity field is made by artificial compressibility approach. The final form can be written as follows:

$$\frac{\partial q}{\partial t} + \frac{\partial (e - e^v)}{\partial x} + \frac{\partial (f - f^v)}{\partial y} + \frac{\partial (g - g^v)}{\partial z} = 0 \tag{1}$$

and

$$q = [\ p \quad u \quad v \quad w\ ]^T$$

In the above, all variables are made dimensionless using the reference density ρ_0, velocity U_0 and length L_0. In case of free surface flows, pressure p is modified as

$$p = p^* + \frac{z}{F^2}$$

where p^* is the original pressure and F is the Froude number, $U_0/\sqrt{gL_0}$, with z being the vertical coordinate. The velocity components in the (x, y, z) direction is expressed as (u, v, w).

---

[*] *hino@nmri.go.jp* and *hirata@nmri.go.jp*

The inviscid fluxes e, f and g and the viscous fluxes e^v, f^v and g^v are defined as:

$$e = \begin{bmatrix} \beta u \\ u^2 + p \\ uv \\ uw \end{bmatrix}, \; f = \begin{bmatrix} \beta v \\ vu \\ v^2 + p \\ vw \end{bmatrix}, \; g = \begin{bmatrix} \beta w \\ wu \\ wv \\ w^2 + p \end{bmatrix}, \; e^v = \begin{bmatrix} 0 \\ \tau_{xx} \\ \tau_{xy} \\ \tau_{zx} \end{bmatrix}, \; f^v = \begin{bmatrix} 0 \\ \tau_{xy} \\ \tau_{yy} \\ \tau_{yz} \end{bmatrix}, \; g^v = \begin{bmatrix} 0 \\ \tau_{zx} \\ \tau_{yz} \\ \tau_{zz} \end{bmatrix}$$

where β is a parameter for artificial compressibility and $\tau_{ij} = \left(\frac{1}{R} + \nu_t\right)\left(\frac{\partial u_i}{\partial x_j} + \frac{\partial u_j}{\partial x_i}\right)$. R is the Reynolds number defined as $U_0 L_0/\nu$ where ν is the kinematic viscosity. ν_t is the non-dimensional kinematic eddy viscosity which is determined by the Splart-Allmaras one equation model[4] or its variant[5].

Since a basic numerical procedure for the Navier-Stokes equations are described in references[1, 2], only the brief outline is given here and the treatment of free surface and the multigrid method are described in the following sections.

Spatial discretization is based on a cell-centered finite-volume method. A computational domain is divided into unstructured polyhedral cells and flow variables (pressure, velocity and eddy viscosity) are stored in the center of each cell. Cells whose shape are hexahedra, tetrahedra, prisms or pyramids can be used and the combinations of these cells give greater flexibility for handling complex geometry.

For the inviscid fluxes (convection terms and pressure gradient terms), the second order upwind scheme based on the flux-differencing splitting of Roe[6] with the MUSCL approach is employed. The viscous fluxes are evaluated by the second order central scheme. Thus, the overall accuracy in space is the second order.

The backward Euler scheme is used for the time integration. Local time stepping method is used, in which time increment is determined for each cell in such a way that the CFL number is globally constant. The linear equations derived from the time linearization of the fluxes are solved by the Gauss-Seidel iteration.

2.2 Free Surface Treatment

Free surface is an interface between air and water in the present applications. Free surface conditions consist of kinematic and dynamic conditions and they are implemented in the interface capturing framework.

The kinematic condition is the condition that fluid particles on a free surface remain on an interface. This condition is implemented based on the localized level set method[7] which improves the efficiency of the original level set approach[8] used in the previous version of the present code[3].

Since most of ship hydrodynamics applications require a flow field of water region only, one-phase flow approach is used, i.e., the flow equations are solved only in a water region. Flow variables in an air region are, therefore, extrapolated from a water region in such a way that the dynamic condition on free surface boundary is satisfied. This method also has an advantage that it is not necessary to cope with large density difference between air and water. At this point, the present method differs from the original level set method[8] where two-phase flow approach is employed.

The dynamic free surface condition can be approximated by the following two conditions. 1) the velocity gradients normal to the free surface are zero. 2) the pressure on the free surface is equal to atmospheric pressure. In order to satisfy the first condition, the velocity components are extrapolated in the direction normal to the interface. Following the method introduced in [7], this is achieved by solving the following convection equation in an air region for the pseudo time τ.

$$\frac{\partial q}{\partial \tau} - \frac{\nabla \phi}{|\nabla \phi|} \cdot \nabla q = 0 \qquad (2)$$

Note that the quantity $-\nabla\phi/|\nabla\phi|$ is the unit vector normal to the interface whose direction is from water to air. In the region away from the interface where ϕ is constant, $-\nabla\phi/|\nabla\phi|$ is replaced by the vector $(0, 0, 1)^T$.

The pressure boundary condition is written as

$$p = \frac{h}{F^2} \text{ on the free surface} \tag{3}$$

where atmospheric pressure is assumed to be zero and h is the z-coordinate of the interface. For an air cell which is next to a water cell, pressure is extrapolated by computing the approximated location of free surface using the level set functions of both cells. See reference[3] for detail. In case that an air cell has several adjacent water cells, the pressure value is obtained by taking the average of the extrapolated values from each water cell. In the remaining air region, pressure is extrapolated using Eq.(2).

2.3 Multigrid

A multigrid method is known as the extremely efficient way to get fast convergence. The concept of a multigrid time stepping applied to the solution of hyperbolic equations is to compute corrections to the solution on a fine grid by the time-stepping on a coarser grid. This is called a geometric multigrid and successively coarser grids should be generated geometrically from an original grid.

The procedure of the multigrid method is as follows. Equations to be solved is written as

$$\frac{d\boldsymbol{q}}{dt} = -\boldsymbol{R}(\boldsymbol{q}) \tag{4}$$

and the subscript k denotes the grid index.

First,the solution $\boldsymbol{q}_k$ is obtained in the fine grid (k) by solving

$$\frac{d\boldsymbol{q}_k}{dt} = -\boldsymbol{R}_k(\boldsymbol{q}_k) \tag{5}$$

by the numerical scheme described above, i.e., the Euler-backward scheme and the Gauss-Seidel iteration. The solution is transferred from the fine grid (k) to the next coarser grid ($k+1$) by

$$\boldsymbol{q}_{k+1}^{(0)} = T_k^{k+1}\boldsymbol{q}_k \tag{6}$$

where T_k^{k+1} is a transfer (restriction) operator for a solution defined as

$$T_k^{k+1}\boldsymbol{q}_k = (\sum \boldsymbol{q}_k V_k)/V_{k+1} \tag{7}$$

where the sum is over cells to be fused to a coarser grid cell and V is a cell volume. The solution in the coarse grid is updated by solving the equation

$$\frac{d\boldsymbol{q}_{k+1}}{dt} = -\boldsymbol{R}_{k+1}(\boldsymbol{q}_{k+1}) - \boldsymbol{P}_{k+1} \tag{8}$$

with the same manner except that the spatial operator $\boldsymbol{R}_{k+1}$ adopts the first order scheme and $\boldsymbol{q}_{k+1}^{+}$ is obtained. $\boldsymbol{P}$ in the above equation is called the forcing terms in the coarse grid ($k+1$) defined as

$$\boldsymbol{P}_{k+1} = Q_k^{k+1}\boldsymbol{R}_k(\boldsymbol{q}_k) - \boldsymbol{R}_{k+1}(\boldsymbol{q}_{k+1}^{(0)}) \tag{9}$$

where Q_k^{k+1} is another transfer operator for a residual and is the sum of the residuals of cells to be merged into a coarser grid cell, i.e.,

$$Q_k^{k+1}\boldsymbol{R}_k(\boldsymbol{q}_k) = \sum(\boldsymbol{R}_k) \tag{10}$$

$\boldsymbol{q}_{k+1}^{+} - \boldsymbol{q}_{k+1}^{(0)}$ gives the correction of the solution at the grid ($k+1$) which reduces the residual in the finer grid k due to the forcing terms added in the coarse grid equation above. Finally, the correction is transferred back from the coarse grid ($k+1$) to the fine grid (k) by

$$\boldsymbol{q}_k^{+} = \boldsymbol{q}_k + I_{k+1}^{k}(\boldsymbol{q}_{k+1}^{+} - \boldsymbol{q}_{k+1}^{(0)}) \tag{11}$$

where I_{k+1}^{k} is an interpolation (prolongation) operator for a correction. Simple injection is used for I_{k+1}^{k} in the present scheme. A multigrid cycle employed here is V-cycle in which the equations are first solved at the finest grid and the solution moves down to the coarsest grid with an update of a solution at each grid and the interpolation is used in the transfer of correction from the coarsest grid to the finest one.

3. RESULTS

3.1 KVLCC2

The ship model used is called the KRISO VLCC2 (KVLCC2) which was one of the test cases in Gothenburg 2000 Workshop for Numerical Ship hydrodynamics[9]. In this case, a free surface is treated as a symmetric plane and the Froude number is set zero, while the Reynolds number is set 4.6×10^6 which corresponds to the model scale of $L_{pp} = 5.5172$m.

The grid used is based on the structured grid of O-O topology with $256 \times 48 \times 64$ hexahedral cells. Four level multigrid is used for this computation. The coarser grids are generated based on the information of the structured grid.

Shown in Fig. 1 is the comparison of convergence histories between a single grid computation and a multigrid one. Horizontal axes are the work unit which corresponds to the CPU time required for one multigrid cycle. It is obvious that the multigrid case accelerates the convergence significantly.

Hull surface pressure distribution is shown in Fig.2. The result appears to be reasonably well compared with other results presented in the Workshop[9].

3.2 KCS

The second case is for free surface flows around a container ship. The ship hull used is called the KRISO Container Ship (KCS) which was also one of the test cases for the Workshop at Gothenburg[9]. The computation is performed for the model scale in which $L_{pp} = 7.2786$m and the Froude number and the Reynolds number are set 0.26 and 1.4×10^7, respectively.

The computational grid is generated as a structured grid of O-O topology with $128 \times 24 \times 32$ cells and its data structure is converted into that of an unstructured grid. The three level multigrid is used in this case. Again, the coarser grids are generated based on the structured grid data.

Convergence histories are shown in Fig.3. Although the full convergence is difficult to achieve due to the nature of free surface capturing approaches, the total drag history shows reasonable convergence. The multigrid acceleration can be observed in this free surface flow simulation as well.

The computed wave contour around a ship hull, which is the iso-surface of $\phi = 0$, is compared with the data measured at KRISO[9] in Fig.4. The computation and the measurement agree well, although a finer grid is required to obtain a more accurate wave field away from a ship hull.

4. CONCLUDING REMARKS

An multigrid method for an unstructured Navier-Stokes solver has been developed. The acceleration of convergence is demonstrated both for a double model flow simulation and for a free surface flow simulation.

References

[1] Hino T.," A 3D Unstructured Grid Method for Incompressible Viscous Flows", J. of the Soc. Naval Archit. Japan, Vol.182, pp.9 -15, (1997).

[2] Hino T.," Navier-Stokes Computations of Ship Flows on Unstructured Grids", Proc. of the 22nd Symp. on Naval Hydro., (1998).

[3] Hino, T.," An Interface Capturing Method for Free Surface Flow Computations on Unstructured Grids", J. of the Soc. Naval Archit. Japan, Vol.186, pp.177 - 183, (1999).

[4] Spalart, P.R. et al., "A One-Equation Turbulence Model for Aerodynamic Flows", La Recherche Aérospatiale, No.1, pp.5 - 21, (1994).

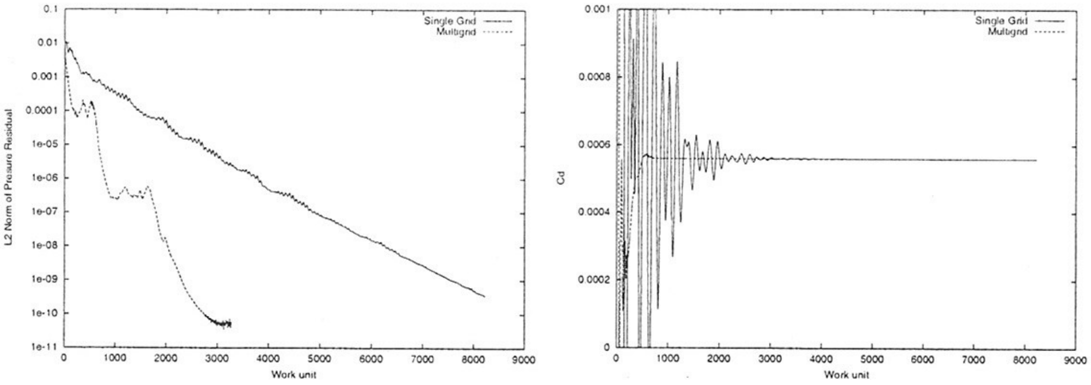

L2 Norm of Pressure Residual   Total Drag

Figure 1: Convergence Histories of KVLCC2 computation

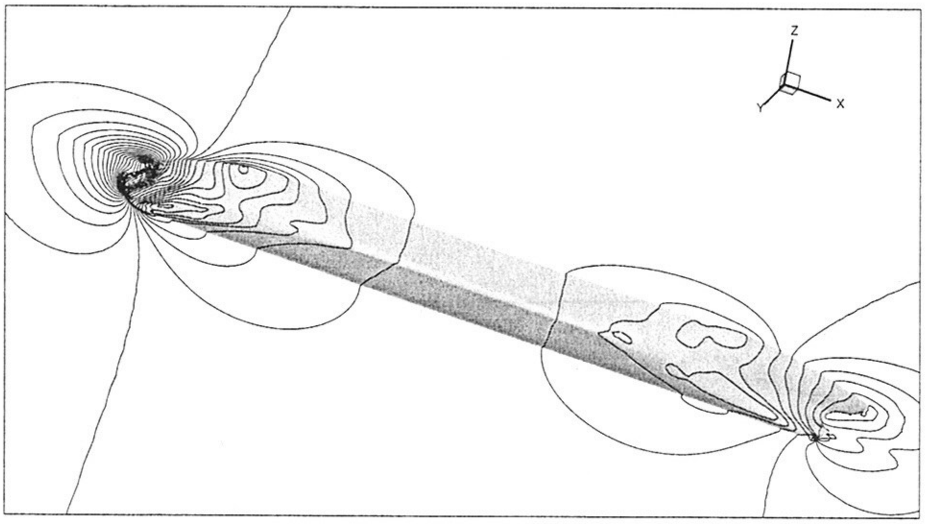

Figure 2: Computed Pressure Distribution around KVLCC2

[5] Rhee, S.H. et al., "Unstructured Grid Flow Solver for Practical Ship Hulls", Proc. Workshop in Numerical Ship Hydrodynamics, Gothenburg, Sweden, (2000).

[6] Roe, P.L., "Characteristic-Based Schemes for the Euler Equations", Ann. Rev. Fluid Mech., Vol. 18, pp.337 – 365, (1986).

[7] Peng, D. et al., " A PDE-Based Fast Localized Level Set Method", J. Comput. Phys., Vol.155, pp.410-438, (1999).

[8] Sussman, M. et al., " A Level Set Approach for Computing Solutions to Incompressible Two-Phase Flow", J. Comput. Phys., Vol.114, pp.146-159, (1994).

[9] Larsson, L., et al., V. (Ed.), Gothenburg 2000 2000 A Workshop in Numerical Ship Hydrodynamics Proc., Gothenburg, Sweden, (2000).

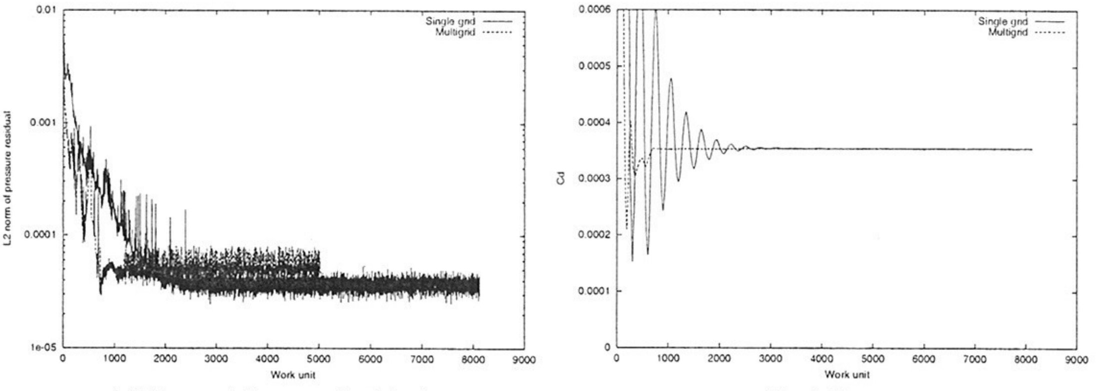

L2 Norm of Pressure Residual

Total Drag

Figure 3: Convergence Histories of KCS computation

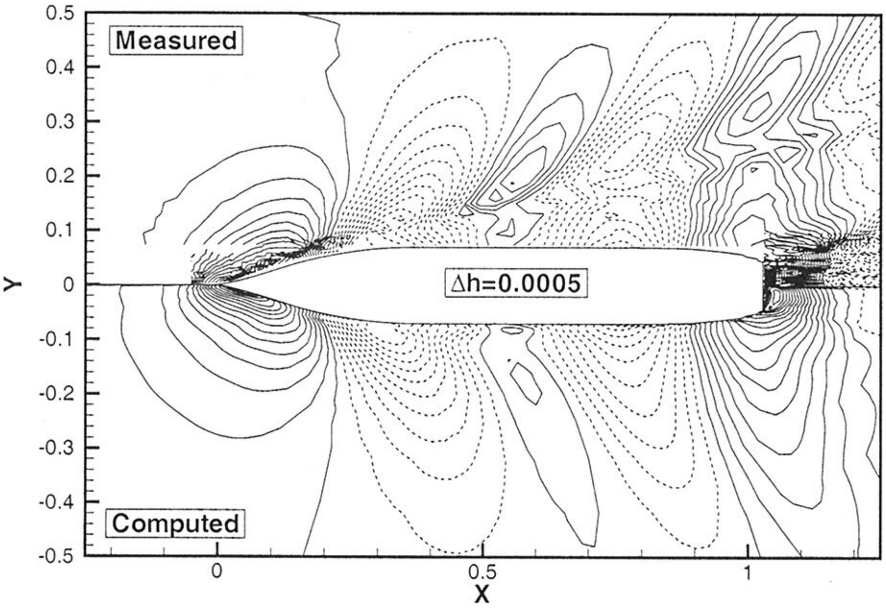

Figure 4: Measured and Computed Wave Contours around KCS

NUMERICAL SIMULATION OF PROPELLER-RUDDER INTERFACE

Jean-Marc Laurens and François Grosjean (Ensieta)
(laurenje@ensieta.fr)

A numerical method coupling a potential flow code and a RANS solver has been developed to compute the hydrodynamic coefficients of a rudder operating within a propeller slipstream. The obtained results are in good agreement with available experimental results. Moreover, the computational velocity allows a parametric analysis of the interaction (rudder position, propeller load, etc.) to be carried out and the method is extendable to other configurations or studies like contra-rotating propellers. In unsteady state mode, amplitudes of fluctuations of hydrodynamic forces on the rudder are far from negligible and, depending on the configuration, frequencies of the fluctuations are not only at blade rate but also at blade rate multiples (BR_2, BR_3, etc.) and at frequencies comprised between BR and RPM when the propeller is itself operating in an unsteady state mode. It has been verified that the averaged hydrodynamic coefficients of the rudder in unsteady mode are similar to the results obtained in steady state mode. Several configurations are simulated in unsteady state mode in order to assess the influence of geometric parameters on the hydrodynamic coefficients of a rudder operating within the propeller slipstream.

Experimental results obtained by Molland and Turnock (1994) show that, even when using a correction formula for wake constriction as proposed by Söding in Brix (1993), the actuator disk theory used to determine the flow acceleration downstream of the propeller leads to an overestimate of the hydrodynamic coefficients of the rudder when the propeller is heavily loaded. Nowadays, a full explicit Navier-Stokes simulation of the propeller rudder system still requires a lot of computational power as well as considerable preparation time which do not allow parametric studies to be carried out within a reasonable time scale.

Based on years of previous research and development, three methods coupling a potential flow code and a Navier-Stokes solver by way of induced velocities were developed in order to simulate steady and unsteady flows around complex systems such as the propeller / rudder interaction. The experimental data and results of the three different methods were compared and satisfactory results were obtained, see Figure 1. The third method (M3) was then selected for further development. Not only because the obtained results were closer to the experimental results but also because it seemed to be the most stable method. Furthermore, changing the set-up to simulate various configurations is not very time consuming and relatively few computational resources are needed.

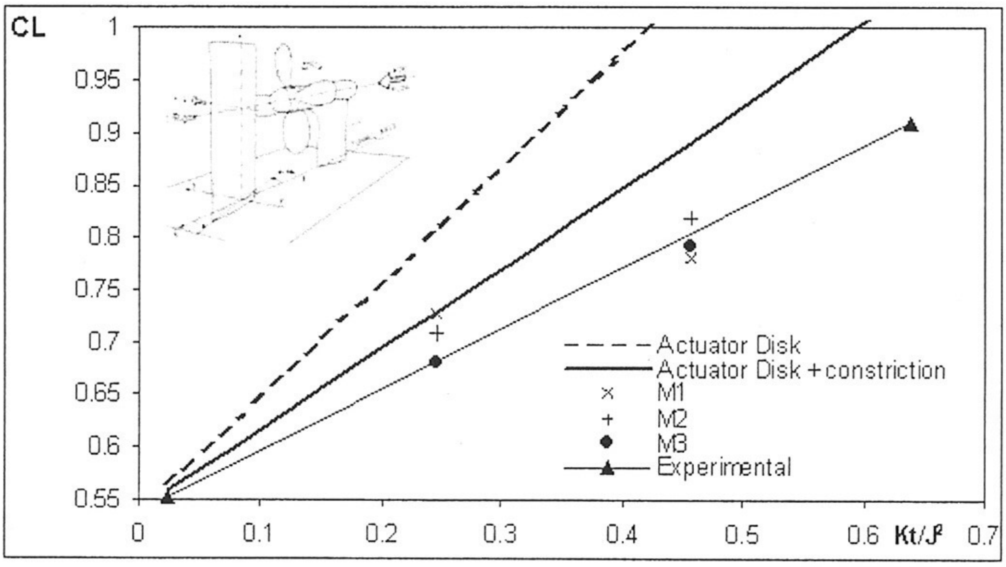

Figure 1. *Rudder lift coefficient (C_L) at 9.2° angle of attack versus propeller load coefficient (Kt/J^2).*

The retained method consists in a simulation of the propeller using the potential flow code. The propeller induced velocities are subsequently computed within a plane parallel to the propeller disk and situated immediately downstream. These velocities are then imposed as velocity inlet boundary conditions within the Navier-Stokes domain of computation where no obstacles are present. The velocities computed by the RANS solver are then interpolated at the control points of the surface mesh of the rudder which is simulated using the potential flow code. The opposite figure illustrates the method used for a standard rudder propeller configuration. The propeller induced velocity field can be either averaged in time to proceed to a steady state simulation or taken per time step in order to perform an unsteady state simulation, see Figure 2.

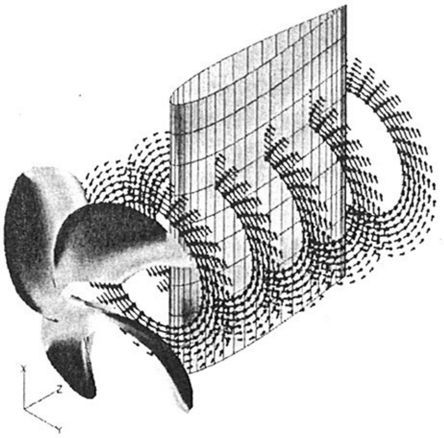

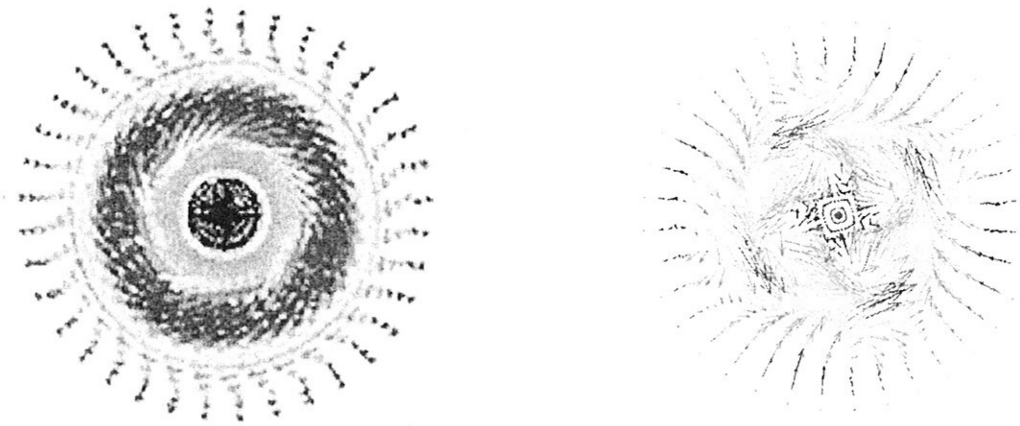

__Figure__ 2. Example of a propeller induced velocity field. Averaged (left) and instantaneous (right).

A large number of configurations were simulated in order to assess the importance of geometrical parameters such as the lateral and longitudinal position of the rudder. Simulation results have shown that the hydrodynamic coefficients of the rudder can be quite different when operating within the slipstream of various different propellers with the same load. The propeller load distribution influences the overall hydrodynamic coefficients of the rudder. The hub diameter effect was examined and was found to be of some importance but did not explain all the differences. The negative rudder drag which generates additional thrust and increases the propulsive efficiency can also be assessed.

The example of steady state simulation results presented at Figure 3 shows the influence of the lateral position of the rudder in terms of lift coefficient for a constant NACA0020 section rudder at zero degree of attack working within the propeller slipstream operating at a thrust coefficient of $C_{th}=2$.

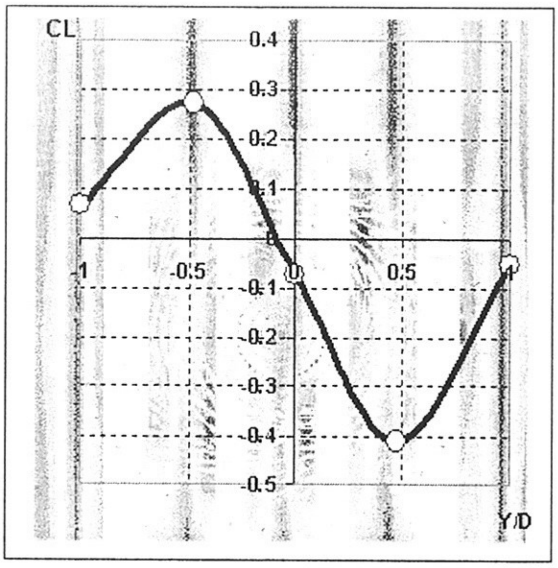

Figure 3. Rudder lift coefficient at a zero angle of attack operating in the propeller slipstream with a C_{th}*=2 load. The graph background shows the Cp distributions obtained for 5 lateral positions of the rudder as well as the velocity vectors induced by the propeller in the entry plane.*

The method is sufficiently flexible to be used for other types of configurations such as contra-rotating propellers or twisted rudders.

An example of pressure coefficients, Cp, distributions and wakes for a twisted rudder operating within the slipstream of a propeller is presented in Figure 4 together with the same results obtained for the conventional rudder. The propeller load is C_{th}=2, the rudders are at a zero degree angle and the configuration is standard. The hydrodynamic coefficients for the rudder in this case and the open water case are presented in *Table 1*. The propulsive efficiency of the twisted rudder increased and the lift decreased.

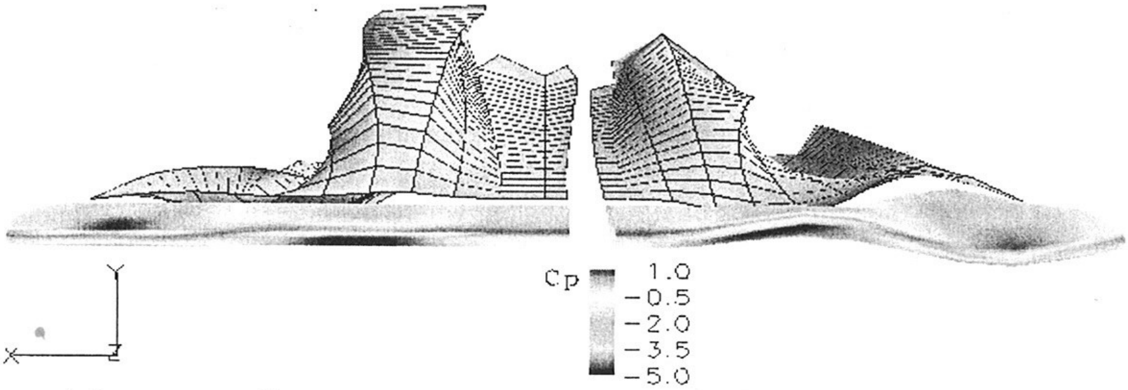

Figure 4*. Pressure coefficients, Cp, distributions and wake for a twisted propeller compared with the conventional rudder.*

Table 1. *Lift and Drag coefficients, C_L and C_d, obtained for the two rudders*

	Open water		With propeller	
	C_d	C_L	C_d	C_L
Conventional	5.800E-04	-3.500E-06	-2.058E-02	-2.112E-01
Twisted	4.430E-03	2.920E-02	-3.096E-02	-1.206E-01

Results of unsteady simulations such as the example presented on Figure 5, show that force fluctuations on the rudder operating within the propeller slipstream are far from negligible. In this particular example, non-negligible fluctuations occur from BR (Blade Rate) to BR_4 (Blade Rate time 4). Of course when the propeller is itself working in unsteady state mode, frequencies as high as the propeller rate are also obtained.

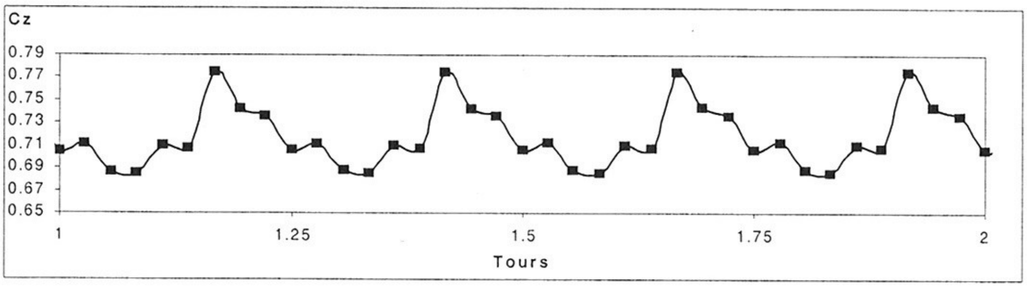

Figure 5. *Rudder lift coefficient fluctuations at a 10° angle of attack operating within the slipstream of a four blade propeller operating at $C_{th}=0.6$ during a complete rotation.*

When computing the average rudder lift coefficient from the results of the unsteady state simulation of Figure 5, the obtained values are almost identical to those obtained for the same case simulated in steady state mode, see *Table 2*.

Table 2. *Average CL and C_d obtained compared with steady state simulation results.*

	C_L	C_d
Unsteady state simulation	0.72	0.054
Steady state simulation	0.74	0.053

If this trial is repeated when the rudder is at a zero degree angle of attack and with a propeller Cth of 2, we obtain the results given in *Table 3* where the average lift coefficient is almost unchanged between the two modes of simulations but where the negative drag coefficient has significantly increased for the unsteady state simulation.

Table 3. *Average C_L and C_d compared with the steady state simulation where the propeller load is $C_{th}=2$ and the rudder is at a 0° angle of attack.*

Steady state		**Unsteady state**	
C_d	C_L	C_d	C_L
-2.058E-02	-2.112E-01	-4.27E-02	-2.14E-01

The computation time of the unsteady state simulations is reasonable enough to conduct parametric studies. For example, as common sense suggests, it has been found that increasing the number of blades decreases the amplitudes of the hydrodynamic coefficients fluctuations of the rudder.

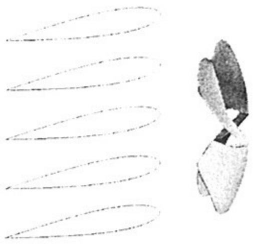

In the final example presented here we consider the test cases of Figure 3 where the lateral position of the rudder is modified. The rudder is at 10° angle of attack (see the opposite figure) and unsteady state simulations are performed. The hydrodynamic coefficient responses of the rudder are presented in Figure 6.

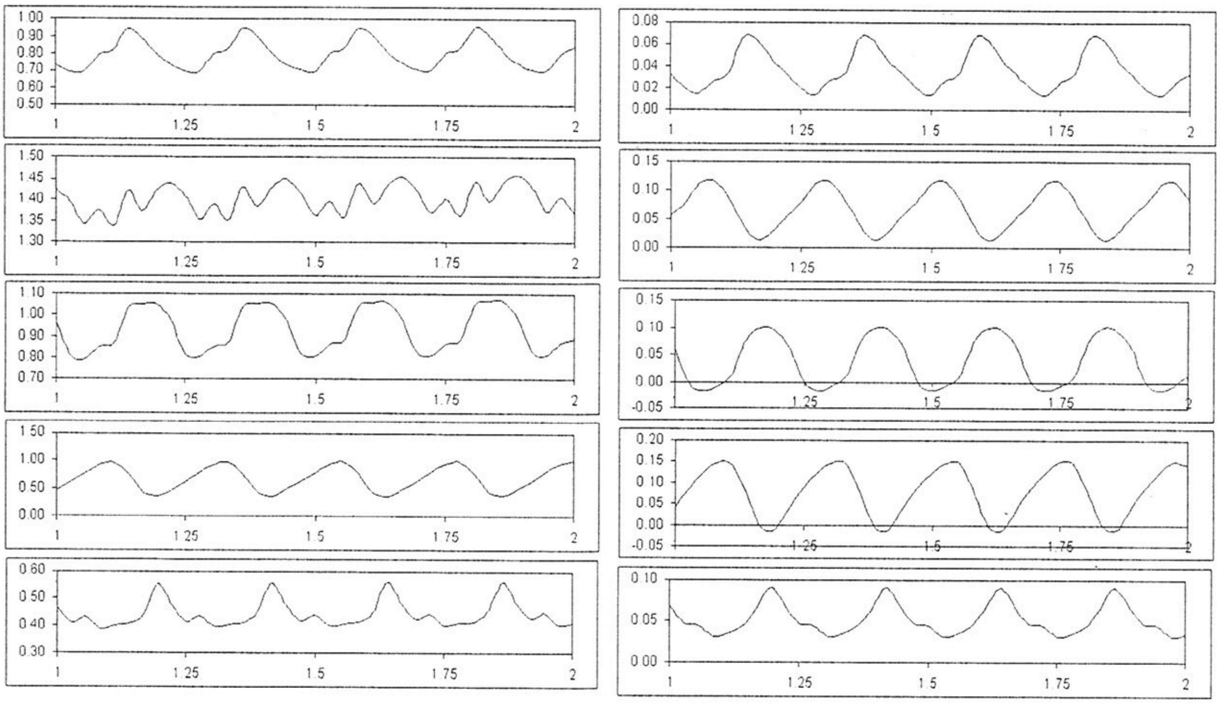

***Figure 6**. Fluctuations of rudder lift coefficients (left) and drag coefficient (right) for different lateral positions.*

This last example demonstrates the difficulty to predict the hydrodynamic coefficient fluctuation behaviour of the rudder without explicit simulations. The curves of Figure 6 could not have been predicted intuitively.

The simulation method briefly presented here together with various application examples can be used for many purposes such as the assessment of some of the numerous devices designed to improve propulsion efficiency. Furthermore, computed pressure fluctuations can be used as a boundary condition to estimate the vibrations generated by rudder propeller configurations.

This study has been partially funded by the Bassin d'essais des carènes.

BRIX J. (1993) (Ed.), *Manoeuvring Technical Manual,* Seehafen Verlag Gmbh, Hamburg.

MOLLAND, A.F.; TURNOCK S.R. (1994), Prediction of ship rudder-propeller interaction at low speed and in four quadrants of operation, Manoeuvring and Control of Marine Craft, Southampton, pp. 319-333.

RANSE Simulations for Cavitating Hydrofoils

Olaf Lindenau, Heinrich Streckwall,, HSVA, streckwall@hsva.de
Volker Bertram, ENSIETA, Volker.Bertram@ensieta.fr

RANSE methods have been applied to the analysis of ship propellers in open-water condition and behind ships for a good decade now. So far, these applications did not model cavitation. We present here first results of our attempts to include a practical cavitation model in the commercial finite-volume RANSE solver Comet. Before applying the cavitation model to propeller calculations we validate the model on 2-d and 3-d hydrofoils. The fundamental cavitation model follows largely Sauer (2000).

Comet is based on a finite-volume method and allows unstructured grids with cell-wise refinements. The equations for conservation of mass and momentum are solved in integral form using a second-order discretization in space, a first-order Euler implicit method for time discretization, and a segregated solution algorithm based on the SIMPLE method. The Reynolds stresses (due to turbulent fluctuations) were modeled using the RNG and the standard k-ε turbulence model.

At the inlet, velocity components, turbulent energy and its dissipation rate are prescribed. At the outlet, zero gradients in longitudinal direction are enforced. On solid surfaces, the no-slip condition is enforced using a wall function.

The main new feature in our simulations of flows is the cavitation model. The basic treatment for the two-phase flow is analogous to the treatment of free-surface flows using the interface capturing method in combination with a volume of fluid approach. Here an additional transport equation is solved for the volume percentage of air in each cell. The two-phase fluid is treated as one effective fluid with effective viscosity and density determined by a weighted sum of air and liquid in each cell. For the modeling of cavitation the transport equation is adapted, now having on the right hand side a source term. This source term based on classical bubble dynamics models the growth and collapse of vapor bubbles. The fluid is now an effective fluid consisting of vapor and liquid.

The cavitation model is built up in three steps:

- Seed distribution
  The different seed types are idealized by a single seed type micro-bubble, and the spectral seed distribution in a liquid is approximated by an average seed radius R_0 and an average number of seeds n_0. The parameter n_0 is a material constant defined as the number of cavitation seeds in a unit volume of liquid.

- Convection of vapor bubbles
  It is assumed that the vapor bubbles in a control volume have the same radius and a homogeneous distribution. This assumption allows us to describe the distribution of a bubbles by a single scalar field, namely the vapor volume fraction $C_v=V_v/V$. V_v is the volume occupied by the vapor, V the total volume of the control volume. Assuming that only one liquid and the corresponding vapor can occupy the control volume where cavitation takes place, we can express C_v as a function of the average vapor bubble radius R:

$$C_v = \frac{N_b 4\pi R^3/3}{V_l + V_v} = \frac{n_0 4\pi R^3/3}{1+n_0 4\pi R^3/3} \tag{1}$$

  V_l is the volume occupied by the liquid, N_b is the number of vapor bubbles in the control volume. The mixture of liquid and vapor is treated as an effective fluid, i.e. as a continuous single fluid with changing density and viscosity determined by a weighted sum of vapor and liquid in each cell.
  The vapor fraction inside a control volume can change due to convective transport and the bubble growth of collapse. The equation describing the transport of the vapor fraction C_v was derived by the

Lagrangian observation of a cloud of bubbles and exploiting that the vapor density is much smaller than water density:

$$\frac{D}{Dt}\int_V C_v\, dV + \int_S C_v(\vec{v}-\vec{v}_s)\cdot d\vec{s} = \int_V \frac{n_0}{1+n_0 4\pi R^3/3}\,\frac{D}{Dt}\left(\frac{4}{3}\pi R^3\right) dV \qquad (2)$$

$\vec{v}$ is the velocity vector of the fluid, $\vec{v}_s$ the velocity vector of the control volume surface, V the volume, S the surface of the control volume, and $d\vec{s}$ the outward surface vector on the control volume surface.

- Vapor bubble growth

The modeling of the rate of phase change, which appears on the r.h.s. of Eq.(2), is based on the conventional bubble dynamics (observation of a single bubble in an infinite stagnant liquid). The analysis results in the "extended Rayleigh-Plesset equation":

$$R\frac{D^2R}{Dt^2}+\frac{3}{2}\left(\frac{DR}{Dt}\right)^2 = \frac{p_B-p_\infty}{\rho_l}-\frac{2\sigma_s}{\rho_l R}-4\frac{\mu_l}{\rho_l R}\frac{DR}{Dt} \qquad (3)$$

p_B is the pressure of saturation which corresponds to the temperature at the bubble surface, p_∞ the pressure of the surrounding liquid, ρ_l the water density, μ_l the viscosity, and σ_s the surface tension coefficient. The inertia controlled growth model, derived by Rayleigh neglecting the inertia, viscous and surface tension terms in Eq.(3) is given by:

$$\left(\frac{DR}{Dt}\right)^2_{Ray} = \frac{2}{3}\frac{p_B-p_\infty}{\rho_l} \qquad (4)$$

Our first applications were for relatively thick 2-d and 3-d foils of low aspect ratios as found in rudders and stabilizing foils. The results were qualitatively as expected based on our experience from model tests and with inviscid flow codes. E.g. for the 2-d foil, a cyclic detachment of cavitation bubbles was observed in the time simulation. The fluctuation of the cavitation in 3-d simulations was less pronounced which corresponds again to our experience in model tests. Overall, Comet managed to reproduce the essential characteristics of real cavitation:

a) Unsteady character of sheet cavitation at foils
b) Relatively stable cavitation at sharp corners
c) Extended longitudinal cavitation areas at foil tips

After gaining experience with the initial test cases, we applied the cavitation model to a NACA 16-206 a=0.8 (mod) 2-d and 3-d hydrofoil. This thin foil represents a typical cross section of a propeller. For the 2-d foil we did some numerical tests varying for example the size of time step, the grid and the parameters in the cavitation model. Periodic supercavitation is observed for all cases. Finally a robust set of solver settings were found and applied to the 3-d problem. The results of the 3-d calculations are compared to the experiments of Ukon (1986). A reasonably good agreement between the visual observations in the experiments and the calculations is noted. Even the beginning of tip vortex cavitation is captured by the simulation. The visualization of the periodic three dimensional cavitation process is additionally done using the Virtual Reality Modeling Language (VRML97). Details on these calculations and the VRML model are presented in Lindenau (2002).

Although some numerical problems during these first tests were observed we are encouraged to apply this cavitation model to rudders and propellers.

References:

COMET, ICCM Institute of Computational Continuum Mechanics GmbH, Comet Version 2.004.A, Hamburg, now part of Computational Dynamics Ltd

LINDENAU, O. (2002), *Simulation einer kavitierenden Strömung mit einem RANSE-Löser und ihre Visualisierung durch Virtual Reality Techniken*, Diploma Thesis, Technical University of Hamburg-Harburg

SAUER, J. (2000), *Instationär kavitierende Strömungen – Ein neues Modell basierend auf Front Capturing (VoF) und Blasendynamik*, Ph.D. Thesis, University Karlsruhe (TH)

SAUER, J.; SCHNERR, G.H. (2000), *Unsteady cavitating flow – A new cavitation model based on a modified front capturing method and bubble dynamics,* ASME Fluids Eng. Summer Conf., Boston, FEDSM2000-11095

UKON, Y., *Cavitation characteristics of a finite swept wing and cavitation noise reduction due to air injection*, Proceedings of the International Symposium on Propeller and Cavitation, Wuxi, China

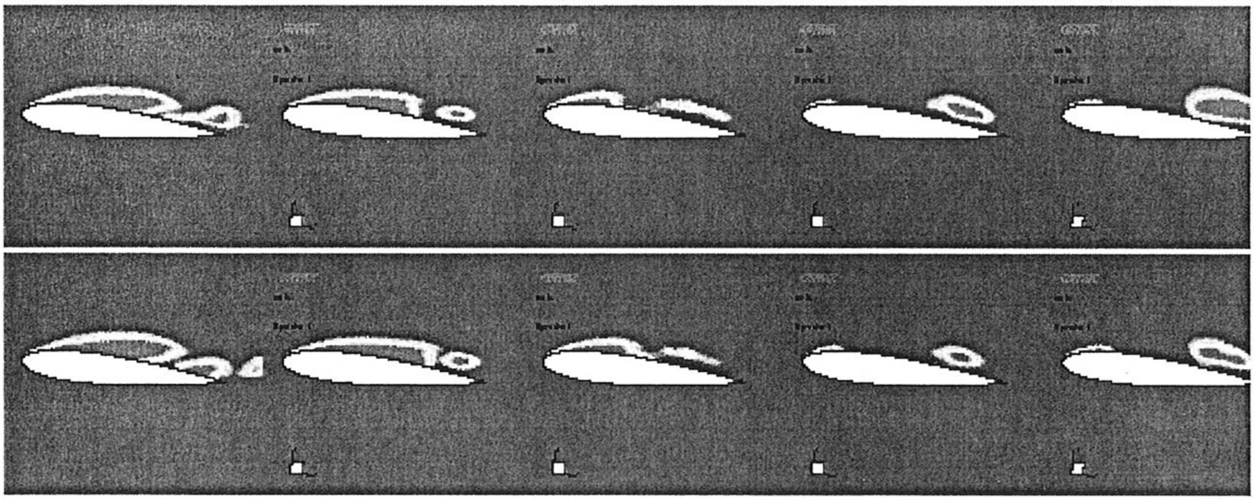

Fig.1: Fluctuating cavitation on NACA 0015 foil for two cycles with attached and detaching cavitation bubble, inflow velocity 12 m/s, angle of attack 6°, cavitation number σ=1.0

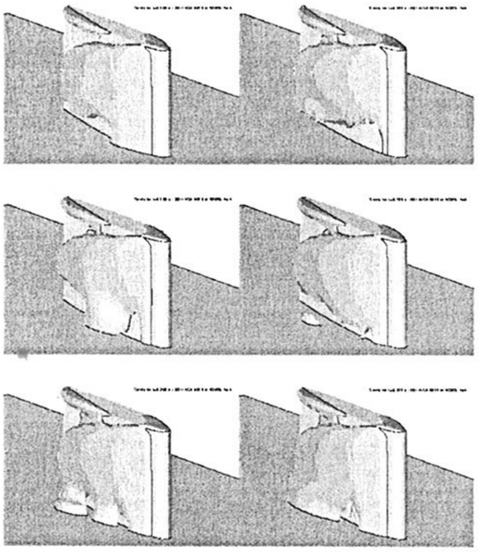

Fig.2: Cavitation on a rectangular NACA0015 foil of small span, inflow velocity 12m/s, angle of attack 6°, cavitation number σ=0.5, time steps=0.005 s from left to right, from top to bottom

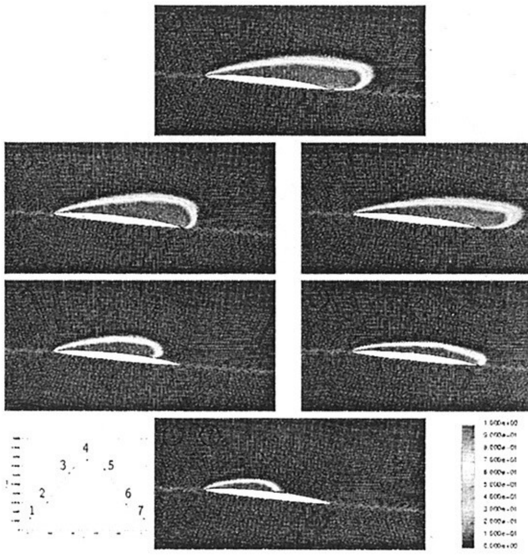

Fig.3: Periodic supercavitation on NACA 16-206 foil, inflow velocity 8m/s, angle of attack 6°, cavitation number σ=0.628

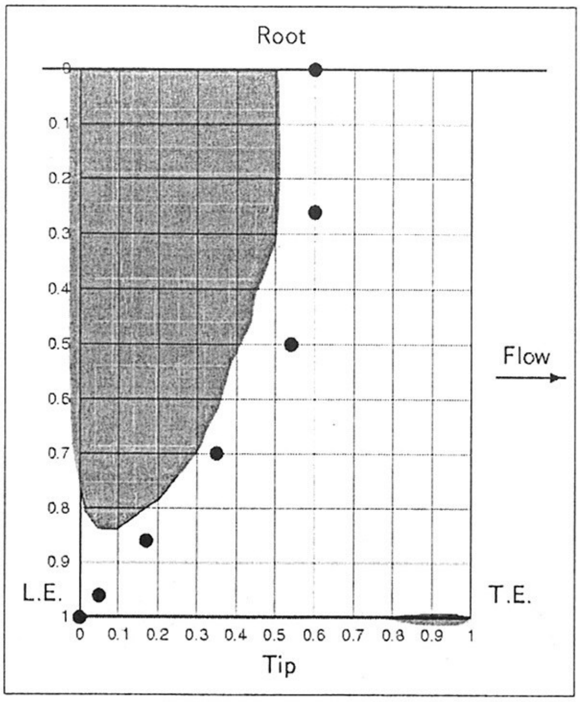

Fig.4: Isosurface $C_v = 0.05$ of simulated cavitation in comparison to mean cavity length in experiment on NACA 16-206 foil, inflow velocity 8m/s, angle of attack 6°, cavitation number σ=0.628

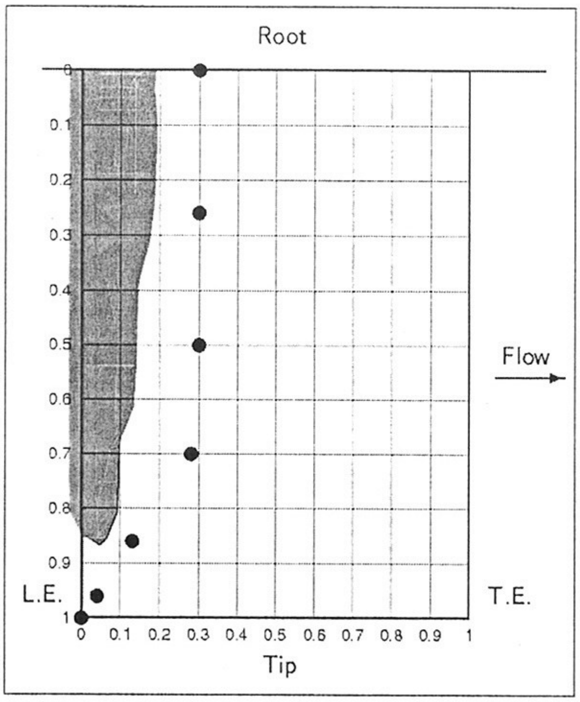

Fig.5: Isosurface $C_v = 0.05$ of simulated cavitation in comparison to mean cavity length in experiment on NACA 16-206 foil, inflow velocity 6m/s, angle of attack 10°, cavitation number σ=1.357

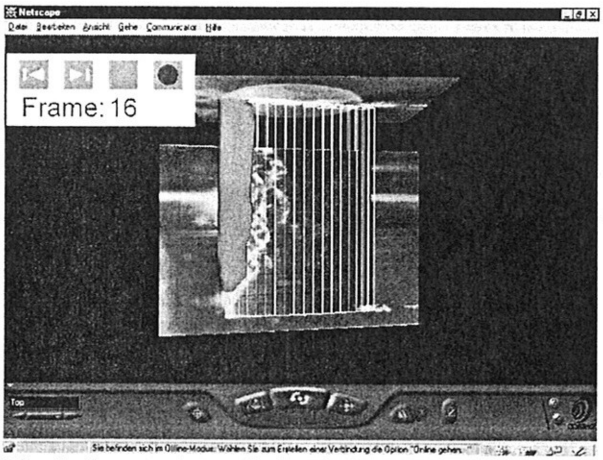

Sie befinden sich im Offline-Modus: Wählen Sie zum Erstellen einer Verbindung die Option "Online gehen."

Fig.6: Comparison of simulation and experiment employing a VRML model

Numerical Investigations of the Viscous Flow around Costa Bulbs

Lars Ole Lübke, Potsdam Model Basin,
e-mail: luebke@sva-potsdam.de

1 Introduction

The presented work is part of a research project dealing with the propeller rudder interaction and the design of a twisted rudder with bulb. All following results are used as a basis for proceeding design tasks and experiments.

The rudder operates in an accelerated flow with the inclination angles varying, due to the rotational energy imposed by the propeller into the fluid. The stagnation pressure of the rudder is decelerating the flow and thereby increasing the thrust loading of the propeller blades as a function of the angular position of the blades. This implies that both parts interact and influence their operation conditions.

The concept of the costa bulb is more than 70 years old but experiences an increasing interest in order to discover unrealized gains in ship design. Most applications of the CPB concept were realized for more moderate ship speeds in the range of 12 to 16 knots. Thus one aim of the work is also to investigated if the costa propulsion bulb (CPB) is applicable for high speed container vessels and if the approach via CFD is able to reveal more profound design criteria for such applications.

The idea behind the costa bulb concept is to recover vortex related energy and thus enhance efficiency. Each blade of an operating propeller induces a root vortex into the flow. Additionally, due to it's viscosity (no-slip condition), the water near the hub rotates with the speed of the propeller forming a hub vortex. These different vortex systems (blade root and hub vortex) can interact, combining their intensity in a single vortex behind the hub. The energy required to create and maintain the vortex system has to be imposed by the propeller and supplied via the propeller torque.

According to Maierform in [1], they achieved savings between 2 % and 5 % in motive power compared to a conventional rudder configuration in model scale. In general improvements in required power for a given speed can reach values up to 4% for model and 8 % for full-scale [3].

In the literature two main reasons for this gain can be identified.

- The costa bulb achieves this goal by preventing the vortex system to join, leading the vortices separately over the device, and thus decreasing the rotational component in the flow.
- According to Ebersolt [1] the costa bulb also generates a vortex-system which acts in the opposite direction than the sense of rotation of the propeller and thus reduces the hub vortex. It is considered that the diameter of the bulb is large enough in order to assume that the upper and lower rudder act independently in the flow. If it is further assumed that the inclination angle of the upper and lower rudder varies, causing the pressure to differ on the lower and the upper side of the rudder. This difference in pressure induces a flow in counter rotation to the propeller and thereby decreases the intensity of the hub vortex.

Numerical simulations were carried out to investigate different ruder - costa bulb - configurations under the aspect of hydrodynamic performance in propulsion conditions. The costa bulbs were investigated with a five bladed propeller in design conditions.

2 Computational method

The numerical calculations of the viscous flow were carried out using the commercial method CFX-TASCflow. The code solves the three dimensional Reynolds-averaged Navier-Stokes (RANS) equations. An adopted formulation for rotating coordinate systems is employed, which involves additional terms resulting from the transformation of the equations. The effects of turbulence on the flow are modeled by the SST model.
The approach to discretize the convective fluxes in the transport equations are based on the schemes developed by Raithby [4]. All calculations in this report were carried out employing the Linear-Profile-Skew-Upwind-Differencing-Scheme (LPS). Further a Physical-Advection-Correction (PAC) was employed. A multigrid solver is used to solve the coupled equation system.

3 Geometry

As geometry to start with the five bladed KP505 propeller employed for the KRISO container ship (as example of a fast container vessel) was chosen, with full-scale diameter $D = 7.9m$, area ratio $A_e/A_0 = 0.8$ and mean pitch ratio $P/D = 0.95$. Three different costa bulb geometries according to test made by Maierform (1984) were employed, with the costa bulb varieing mainly in length and diameter. In the following the different geometries are denoted Costa0 for the bare rudder and Costa1, Costa2 and Costa3 for the three different costa bulb variations. Whereas Costa2 is a variation of diameter and length and Costa3 being mainly a variation in diameter, compared to the design of type Costa1. See also Figs. 1. A rudder with lateral area $A = 82.6\,m^2$ was arranged behind the propeller with distance between propeller axis and rudder shaft of $l = 0.64D$, with D being the propeller diameter. The ship hull was not included in the calculations, hence the hub was prolonged 1.5 propeller diameters to the front and fitted with a conventional hub cap. It is considered, that the neglecting of the ship's wake and thus assuming a homogeneous inflow to the propeller is of minor effect regarding the CPB performance.

4 Boundary conditions

The solution domain was chosen to extent approximately 20 times the propeller diameter D to the front, downwards, to port and to starboard side, $80 \times D$ to the back and $1.5 \times D$ upwards. The origin corresponds to the bottom end of the leading edge of the rudder. At the inflow boundary the velocities, the length scale and the turbulence intensity are given.

At the outflow boundary the gradients of the velocity vector and of the turbulence values are set to zero. The rudder, the costa bulb, the hub, the shaft and the propeller are treated as smooth walls. For the outer boundaries no-slip walls were employed, with the upper boundary being located in the distance of the propeller clearing of the KC-ship.

Part of the investigations were carried out using a fully unsteady calculation with turning propeller. For these simulations the solution domain is divided into a stationary and a rotating part, with the rotating part confining a region around the propeller. See also Fig. 2, with the rotating frame being rendered in blue. Sliding interfaces separate both frames of reference, e.g. rotating and stationary part.

5 Computational mesh

In the solution domain a block-structured, body fitted and non-orthogonal grid was generated, consisting of hexahedral control volumes, using the commercial ICEM-CFD HEX mesher. The grid topology around the costa bulb rudder configuration is shown in fig. 2. In Fig. 3 and the numerical mesh is shown for configuration of type Costa2 .

For the stationary simulations the mesh around the costa-bulb-rudder configuration could be generated as a single multiblock domain, while for the unsteady calculations six multiblock domains were employed. One domain covers rudder with costa bulb and the outer solution domain, while the other five contain each one propeller blade. The propeller grids are periodic for the lower radii of the propeller, meaning that matching interfaces exist near the hub. Grid information is given in Tab. 1.

Part	No. of knots	
	with prop.	without prop.
Rudder	388000	408000
Rudder with CPB	497000	-
Propeller	493000	-

Table 1: Mesh size and quality

The overall number of grid cells for the case with bare rudder and turning propeller amounts to approximately 881000, while for the costa bulb calculations (all three cases) 990000 cells were used.

6 Results

All calculations were carried out for an advance speed of $V_a = 24$ kn in full-scale, under consideration of an wake coefficient of $w = 0.192$. For the simulations under propulsion conditions the rate of revolution was taken to be $n = 1.69$, leading to an advance speed of $J = 0.747$. The model scale data was derived for an scale ratio of $\lambda = 31.6$.

6.1 Rudder behind Propeller

The bare rudder in the wake of the hub was investigated in model and full-scale for the operation point given above. In Tab. 2 the resistance values for uniform inflow with inactive (first row for each coefficient) and in the slip stream of the propeller (second row for each coefficient) are given. The ratios between these values are given in the third row. The values are made dimensionless with the stagnation pressure and the lateral rudder area.

For both scales an resistance increase for the investigated configuration of approximately 55% can be established.

	model	full-scale	full/model
C_t	$1.895 \cdot e^{-2}$	$1.296 \cdot e^{-2}$	0.684
	$2.921 \cdot e^{-2}$	$2.034 \cdot e^{-2}$	0.696
ratio	1.541	1.569	

Table 2: Comparison of model to full-scale resistance of rudder with inactive (first row) and with active propeller (second row)

In Figs. 4 and 5 the axial and circumferential velocities for model scale are shown in two vertical plains with turning propeller. The first plane is located 0.3D behind the propeller, which corresponds to approximately 0.1D in front of the rudder, and 0.2D behind the trailing edge of the rudder at height of the propeller axis. The propeller diameter is refered to as D. Please note, that the leading and trailing edge of the rudder are not vertical.
In Fig. 4, showing the plane in front of the rudder, the wake of the hub and the deceleration of the flow due to the rudder (stagnation point) can be seen. The maximum thrust is produced roughly between radius 0.6 and 0.7.
Behind the rudder the angular momentum of the flow causes the propeller slip stream to move upwards on one side and downwards on the other. The rotational energy in the propeller slip stream is reduced behind the rudder, it is believed that a conversion towards the axial component in the flow occurs, which improves the propeller efficiency, by increasing the propeller thrust.

In Tab. 3 the generated thrust and torque coefficients are given for the propeller operating with or without rudder. The propeller in full-scale generates more thrust and requires less torque compared to model scale, due to relatively smaller viscous losses.

	model		full-scale	
	free	rudder	free	rudder
J	0.747	0.747	0.747	0.747
K_T	0.133	0.147	0.147	0.162
$10K_Q$	0.252	0.267	0.247	0.264
$K_T/10K_Q$	0.528	0.551	0.595	0.614
C_{Th}	0.607	0.669	0.668	0.739
η_0	0.627	0.651	0.705	0.728

Table 3: Thrust and torque coefficients for the propeller only and a propeller rudder configuration Costa0

It shows that the thrust loading of the propeller increases due to the interaction with the rudder. The reason is the deceleration of the flow near the leading edge of the rudder, increasing the pressure on the pressure side of the blades for the 180° degree and especially for the 360° degree position. And also for reasons of decreasing the rotational momentum. The rise in thrust amounts to about 10% for both scales and the rise in torque about 6% in model and 7% in full-scale compared to the free running propeller. This implies an increase in efficiency. Please note, that the calculations were carried out with a propeller mesh especially fine near the hub in order to resolve the flow around the hub and, in the following sections, the bulb most accurately. This implies that the blades at higher radii, were most thrust and torque is generated, was coarsened, due to limiting memory resources. Therefor the chosen approach accepted already less accurate values and the author ask to beer that circumstance in mind.

For the calculation rudder behind a propeller three main conclusions can be drawn.

- The rudder reduces the rotational momentum and therefor increases the propeller efficiency
- The interaction between rudder and propeller causes an increase in propeller thrust loading (the applied actuator disk calculations were not able to capture this interaction).
- The hub vortex is more pronounced in model scale

6.2 CPB behind Propeller

The obtained results for propeller with rudder (Costa0) are taken as reference to evaluate the costa bulb configurations. Since the aim of the study is to obtain data for full-scale in order to design a twisted rudder with bulb, the calculations were carried out for that scale. Also the model scale calculations were not fully completed by the time writing the paper. It is believed that the number of grid cells required to resolve especially the full-scale flow sufficiently is not reached, but that the approach to carry out a comparison of different configurations is feasible and gives the right tendency.

The costa bulb are designed such that the CPBs are placed in the hub vortex, reducing the separation zone. See also Figs 6 and 7. In Tab. 4 the friction, the pressure and the total resistance of the different CPB variations are given for turning propeller. The forces are normalized with the corresponding bare rudder resistances, thus for the configuration denoted Costa0 the values are one. See also Tab. 2. In the following all dimensionless coefficients with sub 0 refer to the bare rudder, configuration Costa0.

The configuration denoted Costa2 causes the smallest resistance compared to the other costa bulb configurations but produces an resistance increase of 13% compared to the bare rudder. The bulbs are exposed on the entire circumference to the propeller slip stream, while the rudder is only exposed on a smaller region at the leading edge.

	Costa0	Costa1	Costa2	Costa3
C_f/C_{0f}	1.0	1.013	1.000	1.005
C_p/C_{0p}	1.0	1.409	1.207	1.379
C_t/C_{0t}	1.0	1.261	1.130	1.240
C_p/C_t	0.628	0.702	0.671	0.699

Table 4: Rudder with CPB resistance under propulsion conditions

In Fig. 8 the thrust and the net thrust for the different configurations is plotted over two propeller revolutions. The net thrust is generated with the resistance of the entire configuration being subtracted from the propeller thrust. This approach takes the resistance into account and enables a better comparison of the CPB configurations.

In Figs. 9 to 11 the propeller efficiency is plotted for a single propeller blade, for all blades employing the propeller thrust only and with the net thrust of the entire configuration over the rate of revolution. A minor increase in efficiency amounting to approximately 1% for all types can be observed if the additional resistance of the bulb is not taken into account. In case of taking the net thrust the small benefits in efficiency for the investigate operation point and geometry is reducing to almost zero

In addition the propeller characteristics generated with the net thrust are given (torque does not change) in Tab. 5. The data is normalized with the corresponding values for the configuration denoted Costa0. It shows that the efficiency for all configurations is the same, with the gain in efficiency amounting to 0.2% for Costa1 and to 0.6% for Costa2 and Costa3.

	Costa0	Costa1	Costa2	Costa3
K_T/K_{0T}	1.0	1.032	1.020	1.020
K_Q/K_{0Q}	1.0	1.029	1.015	1.015
η_0/η_{00}	1.0	1.002	1.006	1.006

Table 5: Propeller characteristics set in relation to propeller in front of rudder (Costa0) for $J = 0.747$

It has to be considered that an increase in propeller thrust is observed for all three configurations. If the propeller is looked upon as a disk accelerating the flow and the thrust being the change in momentum ($T = \dot{m} \cdot \Delta v$), the axial component of the flow has to be increased by the CPB's and it is assumed that this increase is due to an conversion of vortex related energy to the axial component. For example the propeller in front of bulb type Costa1 produces 3% more thrust, but also extra effort has to be invested to lead the flow over the bulb. The concept may be therefor also applicable if more thrust is desired. To show the dependency of the obtained results to the ratio of bulb to hub diameter, Figs 12 and 13 are introduced. For the configuration of type Costa1 this ratio is $d_{bulb}/d_h = 2.0$, for Costa2 $d_{bulb}/d_h = 1.64$ and for Costa3 $d_{bulb}/d_h = 1.8$. It shows that an increase in thrust can be observed for the investigated range in case of increasing bulb to hub diameter ratio, which goes hand in hand with an corresponding rise in torque. Therefor no gain in efficiency is observed.

7 conclusion

Three different costa bulb configurations original designed for more moderate speeds were investigated for a speed of $V_s = 24$ kn with rotating propeller. The final comparison was carried out in full-scale. Beside all encountered uncertainties the following conclusions are drawn.

- The CPB's lead to an increase in generated thrust for reasons of converting rotational momentum to axial velocities. But due to a rise in required torque no efficiency increase was found for the investigated operation point.
- Bulbs designed for more moderate speeds are not directly applicable for higher velocities

Publications indicate that CPB's are sensitive to the Rn-number. Unfortunately model scale calculations were not finished on time.

References

[1] Ebersolt, M.: Reducing Propeller Hub Vortex, The Naval Architect, September 1999

[2] Yamano, T.; Yamashita, Y.; Iwasaki, Y.; Taguchi, K.: An Energy Saving Apparatus, J. Kansai Soc. N. A., Japan, No. 223, March 1995

[3] Greger, O.: Testing the Costa Propulsion Bulb with a view to its use on modern ships, Int. Shipbuilding Progress, Vol.8, No.77, January 1961

[4] Raithby, G. D.: Skew-Upstream Differencing Schemes for Nearly-Steady Problems Involving Fluid Flow, Comp. Meth. Appl. Mech. Eng., Vol. 9, pp 153-164, 1976

Figure 1: Comparison of costa bulb geometries

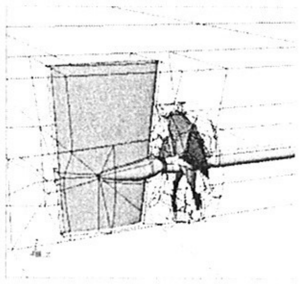

Figure 2: Grid topology

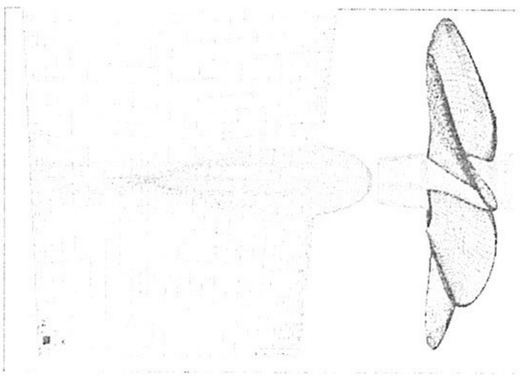

Figure 3: Grid for bulb of typ Costa2

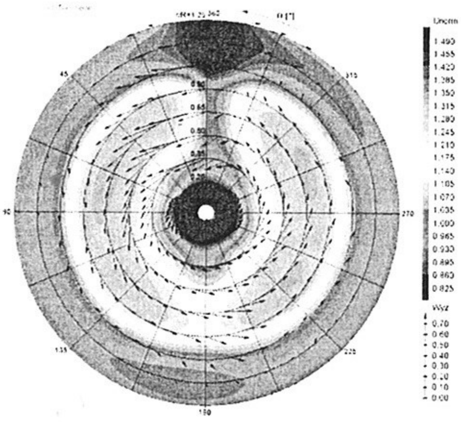

Figure 4: Velocity field in front of rudder, model scale, Costa0

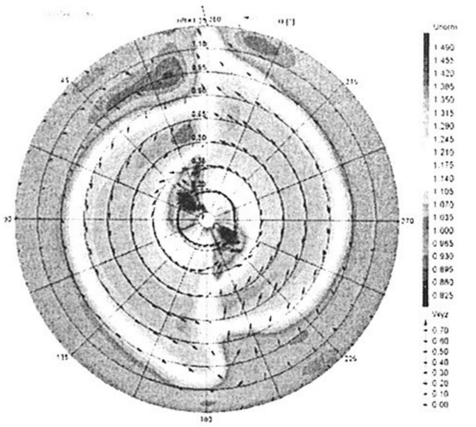

Figure 5: Velocity field behind rudder, model scale, Costa0

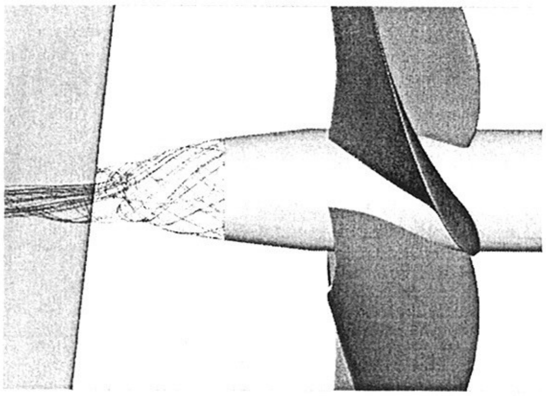

Figure 6: Hub vortex for bare rudder Costa0, full-scale

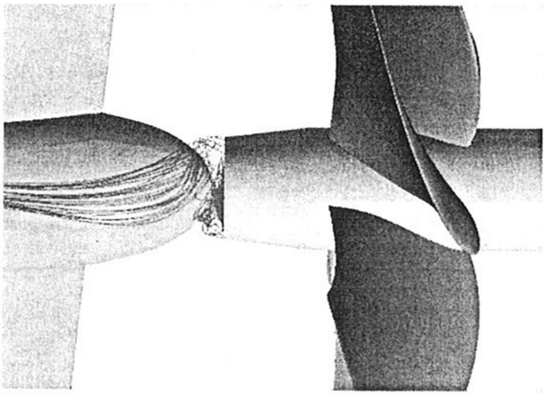

Figure 7: Hub vortex for bulb of typ Costa2, full-scale

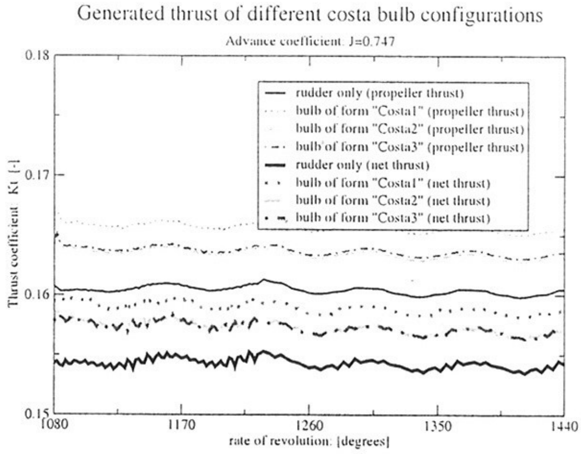

Figure 8: Comparison of the propeller thrust with the net thrust for the different configurations

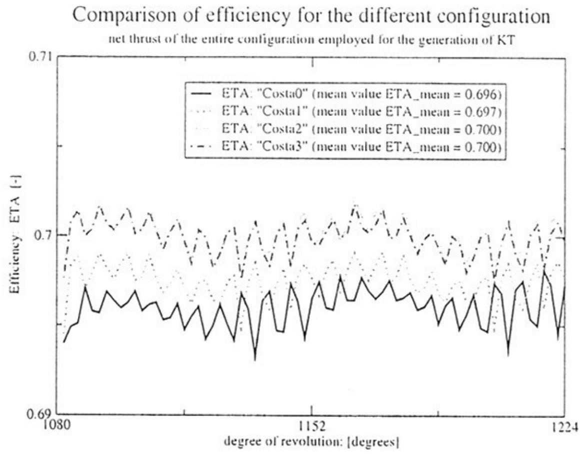

Figure 11: Comparison of efficiency values generated with the net thrust

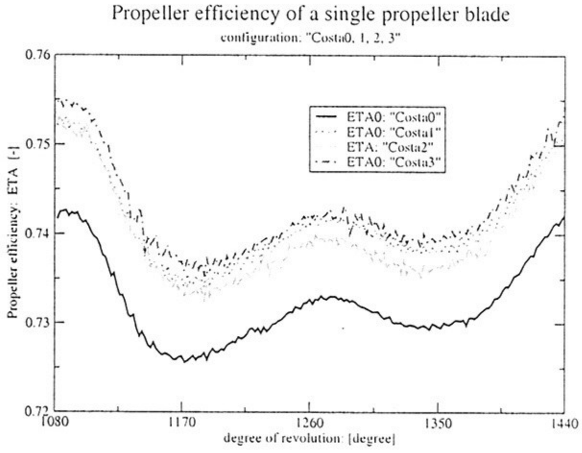

Figure 9: Comparison of efficiency values of a single propeller blade

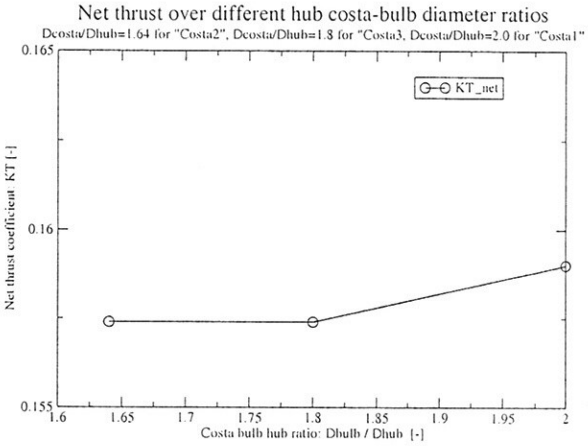

Figure 12: Comparison of net thrust coefficients for different costa bulb hub diameter ratios

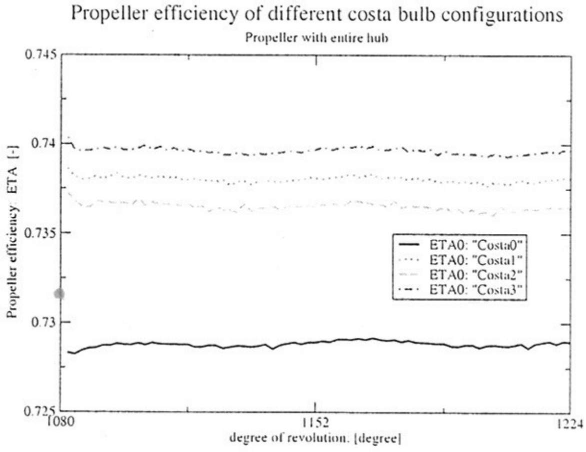

Figure 10: Comparison of efficiency values generated with the propeller thrust only

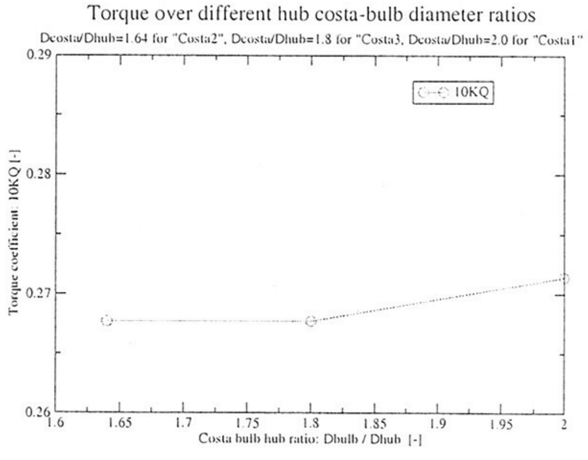

Figure 13: Comparison of torque coefficients for different costa bulb hub diameter ratios

TOWARDS SHIP PREFORMANCE IMPROVEMENT USING modeFRONTIER

J.J.Maisonneuve, SIREHNA
1, rue de la Noë, BP42105, 44321 Nantes cedex 3
Jean-Jacques.Maisonneuve@sirehna.ec-nantes.fr
www.sirehna.com

INTRODUCTION

Optimal design is an idea that is investigated for a very long time, but remained unused up to the recent years for different combined reasons. Sirehna has believed in this approach since 1990, and thus focused on solving the problems that prevent from an efficient use of it since this time.

The first investigations were performed in the field of ship forward resistance, with help of deterministic algorithms taken in mathematical libraries, with simplified deformation tools. This led to successful but limited demonstration of the applicability of such methods.

A decisive progress was made through the EC Brite Euram project called Optim, led by Sirehna and involving a number of European partner from various sectors. This project allowed a wide investigation of multi-disciplinary optimisation approaches, including aeronautic and maritime applications. It led to some tools applicable for general purpose applications, that were ready to be used in some consultancy work after the project. A number of maritime applications were performed, especially dedicated to ship bow shape optimisation for resistance purpose.

Despite the progress made in the tools, still some improvements were necessary to really jump to practical routine use of optimal design technologies. This first concerned the ease of connection of any external analysis software, the exploitation of best information technology to take advantage of multi-processing, distributed computing in heterogeneous environment, portability. But over all, these approaches were still oriented towards mono-objective, local deterministic optimisation, which are robust in their domain of validity, but which domain of validity only covers a small range of the variety of practically encountered problems. Efficient methods to deal with noisy functions, discrete or mixed problems, failures inherent to any complicated calculation, without preventing the method to give interesting results, were expected.

At the end of the 1990's, Sirehna got involved in numerous FP6 EC projects, especially with the role of promoting and investigating the possible applications of optimal design approaches in the maritime domain, in particular by solving the above described shortcoming of the current tools. The specifications in this sense were established, and it turned out that a lot of them were met by the tools developed during a previous project, *modeFRONTIER*.

This software is an outcome of an Esprit projects called Frontier, which took place between 1996 and 1999, and addressed multi-partner collaborative design optimisation, with a multi-sectorial partnership. The transfer of the knowledge acquired during this project into a successful commercial product (*modeFRONTIER*) was performed after the project by a new Italian company, ESTECO.

This software, in addition to an offer of different optimisation algorithms, provides and environment dedicated to the set up of design assessment chains and efficient investigation of the design space. In brief it includes

- intuitive tools for the integration of assessment calculation chains, allowing complicated logics, and thus able to address real life cases where conditional process must be ensured (eg stopping calculation as soon as some criteria are not satisfied, to avoid useless computing time...)
- exploitation of most recent technologies (java, xml...) in order to address remote calculations in heterogeneous environments, concurrent calculations, maintenance and readability of full design database, portability (only one version to maintain), etc...
- tools and algorithms for an efficient exploration and analysis of the design space, including:
    - design of experiments
    - response surfaces, from classical (like linear, quadratic approximations, local interpolation...) to advanced methods (gaussian processes, neural networks)
    - optimisation algorithms, from classical deterministic local algorithms (BFGS, SQP,...) to most recent technologies, including true multi-objective optimisation (genetic algorithms, MOGA...). This last point is still unique and of prime importance for practical design problems, which are very rarely naturally mono-objective ones.
    - multi-criteria decision making tools, that allow the designer to define his preferences through a limited number of choices within best designs (in the multi-objective sense), and help him to get the best trade-off solution.
    - graphical analysis tools for a quick and good understanding of the design space: scatter

plots, parallel plots, response surfaces visualisation,

- an harmonious possibility of combination of the above features. For example, it is possible to mix real calculations with response surface approximation within an optimisation, in order to minimise calculation time while keeping sufficient accuracy. This is very efficient in case of high computing demanding problems.

PRACTICAL APPLICATIONS IN THE MARITIME FIELD

After set up and first trials of *modeFRONTIER*, the number of identified applications where it could bring significant benefits , in the domain of maritime design, grew in an exponential way. Since this date, a number of such applications started to be investigated, either internally or through R&D projects, mainly related with ship design. Some of them are described below.

In addition, some investigations are led in the field of optimal distributed ship design. Such an application is also described in the wash minimisation example below.

Ship hull form. This problem is still of major importance in ship design, and has no straightforward solution. The advantages brought by optimal design are further investigated namely within the EC Growth project "Fantastic" which gathers most of the European leading shipyards, design and research centres, and software companies. The following key problems are addressed:

- ship hull parametric modelling, including classical CAD tools (*Napa*) but also innovative approaches (*Friendship*, TUB), or general purpose tools (*Catia*)
- improvement of accuracy, automation, speed and communication of ship assessment tools, focused on potential flow calculation methods, and entering viscous flow domain.
- investigation of design search and optimisation approaches applied to this problem,
- practical implementation in actual design environment and procedure assessment.

A ship hull model is built with relevant tools (*Napa* or *Friendship* or specific ones). The process flow is then built with *modeFRONTIER*, involving the defined parameters and specifying the calculation chain and the multi-objective optimisation problem, here minimising ship resistance while maximising displacement. The calculation chain can be set up in a multiple platform environment. The MOGA algorithm enables to detect the set of best designs for both objectives (Pareto frontier), then allowing the user to define within this set the trade off solution that best fits his needs. Some help is provided by *modeFRONTIER* to investigate this, like for example the parallel plot of all input/output values within their variation range, which enables to visualise and filter the solutions as wished. Then a set of alternative interesting solutions can be selected for further study.

Ship wave wash minimisation. The problem of ship wave wash minimisation has become crucial with the use of high speed craft, for environmental and safety reasons regarding the shore line and related activities. This problem is in particular addressed through an EC Growth project, "Flowmart", which aims at improving the involvement of wash criteria in design procedure.

The problem consists in minimising the ship wave wash together with its forward resistance with some constraints on its capabilities regarding cargo transportation (displacement), propulsion (transom stern area) and stability.

Figure 1 shows information on this case. The parametric modelling is performed by Chantiers de l'Atlantique with *Napa*, and consists in a set of 18 parameters ruling the shape of two sections (middle and aft) and of the bow.

The wave wash and resistance calculation are performed by SSPA with the *Shipflow* solver.

The whole process is thus distributed between three geographical areas: St Nazaire for the shape generation with *Napa*, Gothenburg for the hydrodynamic calculation with *Shipflow*, and Nantes for the calculations management and optimisation procedure with *modeFRONTIER*.

This is implemented by using a tool developed at Sirehna (*Asydas*) which ensures an asynchronous client-server based communication between the different nodes.

This procedure, using a mixing of genetic algorithms and response surfaces leads to some significant gains in both wash and resistance. Some *modeFRONTIER* tools (t-student) providing information on the sensitivities of outputs to design variables are used in intermediate steps, in order to better define the parametric modelling.

Ship stabilisation fin. This case was the occasion to set up a complete advanced flow calculation chain, including the following components:

- *GridGen*, high level grid generation tool fitted with automation and parametric capabilities through its command language Glyph.
- *Fluent*, the well known general purpose flow solver,
- *FieldView*, flow post-processing tool, including advanced capabilities for extraction of accurate information, and fitted with automation capabilities through its command language Fvx.

The problem concerns the optimisation of ship roll stabilisation fins, by modification of their profile. It consists in maximising the lift, while minimising the drag and risk of cavitation, at a given angle of incidence. The above calculation chain is easily set up with *modeFRONTIER*. The search strategy is chosen in order to minimise the computational effort. It consists in setting up response surfaces on an initial designs database, and performing multi-objective optimisation with a mix of real calculations (using the calculation chain) and of virtual calculations (using the response surfaces). This approach is very efficient, leading to an accurate detection of the pareto front while keeping short calculation time. The further step consists in investigating this pareto set, visualising designs, and establishing pair-wise preferences between them, according to criteria that can be subjective (guessed as difficult to manufacture, aesthetic,...). Then the multi-criteria decision making tool of *mode**FRONTIER*** establishes a ranking of the designs and produces utility functions that are then used in a unique global objective function. This function is then minimised to get the "best" trade-off.

Integration of ship appendage. The problem consists here in using 3D viscous flow calculations to assess the added drag due to the integration of an appendage on a hull, and try to minimise it (see figure 2).
The link between the hull and the appendage is made of a surface ruled by a number of nodes, which coordinates are the design variables of the problem. This is managed with ***Pro/Engineer***.
The grid generation is made by the ***GridGen*** software on the basis of an IGES file generated by ***Pro/Engineer***.
The flow is calculated with the ***Fluent*** solver, on the ***GridGen*** generated grid.
For saving computing time, advantage is taken of the local character of the perturbation to reduce the computational domain once an initial flow field is calculated on the whole domain.
The search strategy consists in setting up response surfaces approximation on an initial set of designs before running a genetic algorithm mixing real and virtual calculations. Once this is done, the response surfaces are updated with the new real calculated designs, and the global virtual optimum is search. The validity of the solution is then checked with a full real calculation. The total calculation is about 120h for a total of 75 real calculations, and some hundreds of virtual ones.
One major problem addressed in such a real life case is robustness. Many sources of error or failure exist: combination of parameters that cannot be handled by the CAD, geometry that cannot be meshed by the grid generator, grid quality insufficient for the flow solver, solver divergence, and even hardware/network temporary breakdowns. This highlights the importance to have an algorithm which supports such things and gives anyway useful information. The genetic algorithms in *mode**FRONTIER*** are quite successful in this sense.

Shape optimisation involving Ranse solvers. The progress in design search techniques now makes it possible to seriously envisage their use with high computing demanding flow analysis tools like Ranse solvers, on the whole ship. Some investigations are being performed at the moment in the EC "Fantastic" project. Another preliminary application is being performed in collaboration between Sirehna and the fluid mechanics laboratory of ECN, involving the **ICARE** RANSE solver (B.Alessandrini).
The problem consists, in a first step, in minimising the forward resistance of a ro-ro ship, which front shape is parametrically modelled with help of the Catia surfacic modeller. The flow around shape variations is calculated as a perturbation of the flow initially calculated on a reference ship, in order to save time. A combination of wide spread search genetic algorithm with more focused algorithms is used, which leads to some significant gains in term of ship resistance, in a reasonable time. This work is to be continued, namely taking advantage of response surface techniques, and addressing more global shape variations, which can normally be handled more accurately with such a method than with classical panel methods.

Ship wave pattern identification. This is another example of the use of *mode**FRONTIER*** for identification purpose.
The problem is here to predict wave height at a given long distance from the ship centreline, from model tests in a narrow towing tank which only allow measurements near the ship, thus including reflections on the walls.
The principle is to minimise the difference between wave heights measured on longitudinal cuts and wave heights calculated with a model of the ship ruled by a finite number of parameters, and then remove the walls in the model to predict wave heights in free water.

TRENDS FOR R&D WORK

The trends for future work in the domain of optimal design are multiple.

One aspect which must be worked on is parametric modelling. Indeed, this is a key area that is not yet solved in a satisfactory way. CAD tools theoretically offer parametric capabilities, but these are not robust enough when addressing complex problems like arbitrary surface modelling. In some specific cases, it can be relevant to develop specific modellers, dedicated to one domain (like ship shape modelling). The complex problem of multi-disciplinary design, which involves multiple sets of design parameters, is also to be considered carefully, as well as the multiple level parametric description of the product, corresponding to several stages of the design progress.

One specific aspects is producibility. Most of the assessment tools are able to predict product performances, and some simple geometric criteria. It is more difficult however to guarantee that the design will be producible at a cost that will ensure the overall viability of the product. Two ways are generally possible for this. The first one is to natively ensure good producibility with adapted parametric shape modellers (eg metal sheets developability). The second one is to assess producibility as post-processed criteria (eg curvatures), which are forced to satisfy given constraints through the optimisation process. No satisfactory solution exists yet, and some effort must be put on it.

The performance of product assessment tools have now reached a good level in many domains: finite element methods are robust, flow solvers are becoming more and more reliable, and most tools can now be run in an automated way, after a configuration stage. However, some work is still needed to improve capabilities, accuracy and computing performance of such tools especially in the domain of free surface complex flows.

Even if the present design search algorithms are now efficient and able to provide very relevant information on the design space, it is still worthwhile to improve them. This is in particular addressed by ESTECO. Several trends are investigated, among which the coupling of response surface and optimisation techniques, which must drastically decrease the number of real design evaluation for a given level of information. Robust design innovative techniques will also be provided, based on multi-objective approaches, enabling the user to optimally define the trade-off between optimal performance and stability of the solution (ie independence with respect to variations in the parameters).

Finally, one important area lies in the integration of such methods with on-going design methodologies and approaches, taking into account tools (CAD, PDM, innovative IT...) as well as physical or human design organisation, capacities and knowledge (distributed remote computing, concurrent or flexible design, knowledge management,...). This is also a great challenge for the optimal exploitation of design search tools.

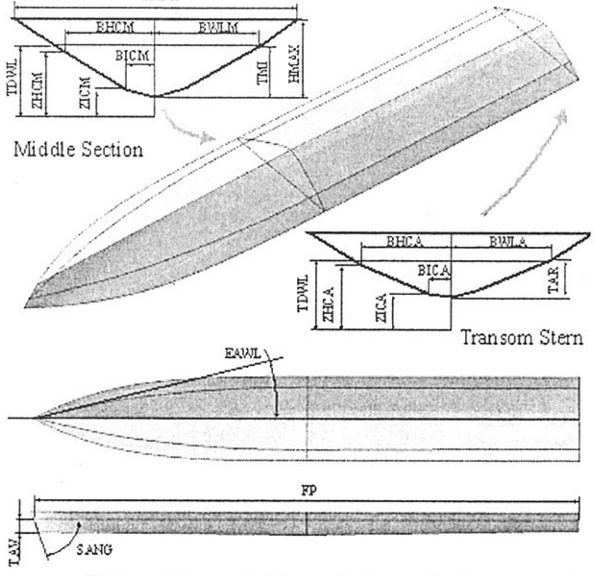

Parametric modelling of ship hull shape

Objectives :

- minimising generated wash wave
- minimising ship forward resistance

Constraints:
- displacement
- transom stern area
- stability criterion

Parameters: 18 parameters, middle ship and transom sections + bow parameters (see on the left)

Parametric modelling: NAPA (at CAT)

Analysis software: Shipflow (at SSPA)

Algorithms: Genetic algorithm mixed with response surfaces.

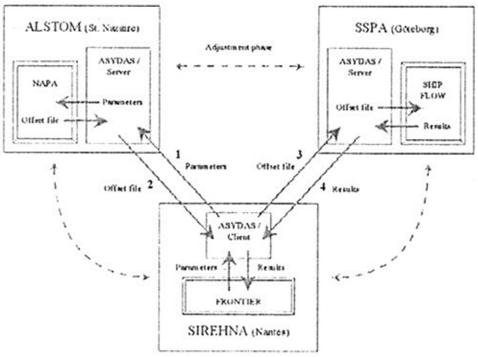

Distant applications managed by ***Asydas*** and *mode**FRONTIER***

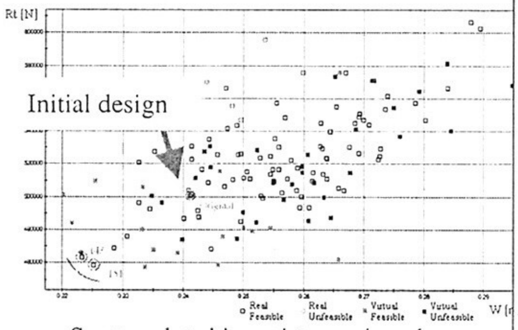

Scatter plot ship resistance / wash
Mixing real and virtual designs
Pareto frontier (bottom left) / inital design

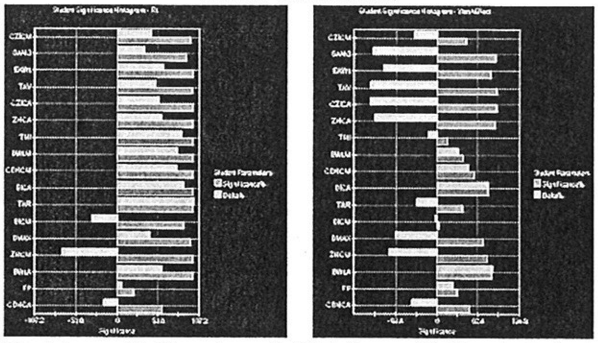

Resistance (left) and wash (right) sensitivity : t-student graphs figuring dependencies vs design variables (direction, magnitude, reliability)

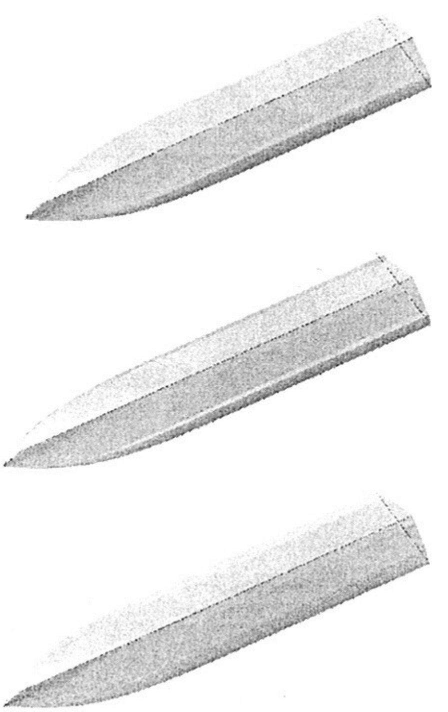

Original shape and 2 alternatives =>

<u>Figure 1</u>: Wave wash minimisation of a high speed craft *(2002)*

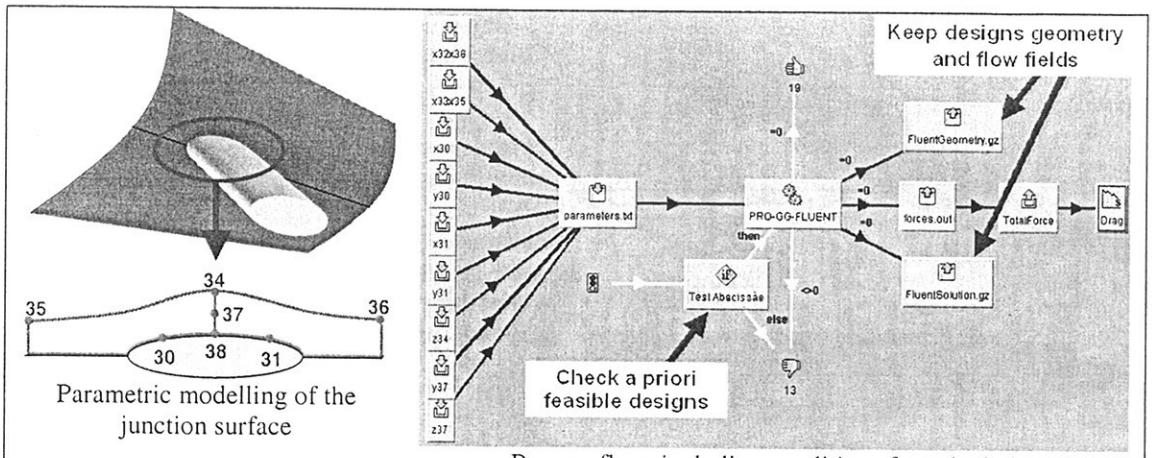

Parametric modelling of the junction surface

Process flow, including conditions for calculation of only relevant configurations

Objective: - minimise drag
Parameters: 9 coordinates of points on the junction surface
Model: - parametric modelling: ***Pro/Engineer***
- grid generation: ***GridGen***
- flow calculations: ***Fluent***

Search strategy:
- initial population (35 individuals, 52h calculation)
- response surfaces set up
- genetic algorithm 20% real / 80% virtual
- updating response surface
- search virtual optimum
- check with real calculation

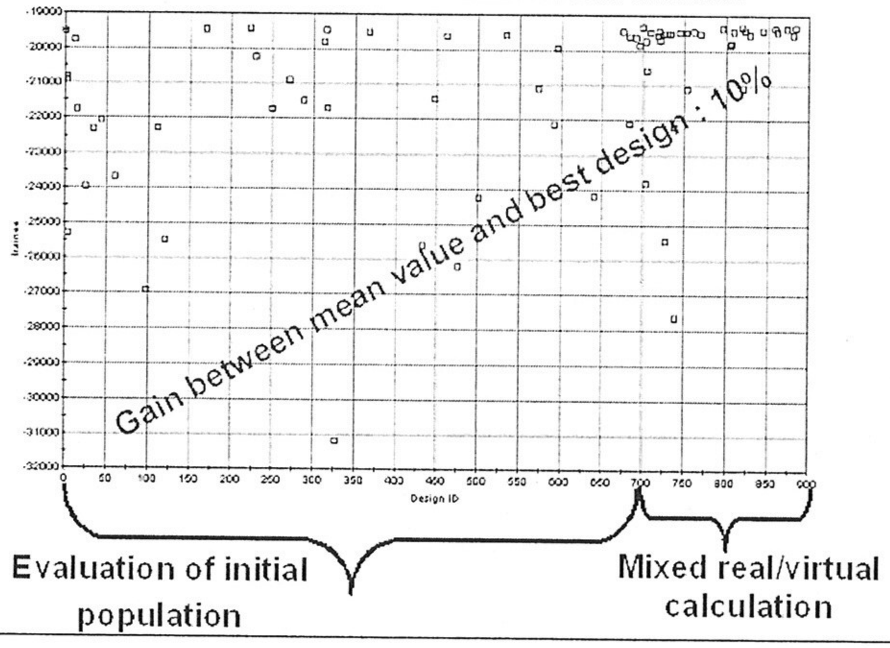

Figure 2: Ship appendage integration *(2002)*

Development of an Unstructured Pressure-Correction Solver Based on Triangle Meshes

*Tommi Mikkola**
Ship Laboratory, Helsinki University of Technology

1 Introduction

In the recent years a lot of effort has been put in the development of computational methods for viscous ship flow calculations. The methods used have almost exlusively been based on structured grids. However, within the field of computational fluid dynamics (CFD) in general, the interest in unstructured methods has been constantly increasing. The difference between these two alternatives is in the structure and indexing of the division of the computational domain into finite elements. In the case of a structured approach, the computational grid can be projected into a cartesian grid with a continous mapping, that preserves the structured ordering of the elements relative to each other. By knowing the index of an element we hence know the indeces of its neighbours as well. With unstructured grid, on the other hand, the ordering of the elements is arbitrary and thus the grid does not have any well-defined structure. It is therefore not possible to deduce the indeces of the neighbouring cells from the structure of the grid.

Both structured and unstructured grid based methods have their respective advantages and disadvantages. Due to the nature of the linear equation systems arising from the use of structured grids, the numerical solution methods for these are very efficient compared to the ones for unstructured grids. On the other hand, grid generation, especially for complex geometries, has become a bottle-neck in the solution process using structured methods. The drawbacks related to structured grids have been emphasized in case of complex hull forms with the deforming grid based surface tracking method used at Ship Laboratory for free surface problems. The advantage of the unstructured approach lies particularly in the flexibility of the grid generation and adaption. Hence, it has been seen as fruitful to also explore the alternative unstructured approach for the solution of free surface flows.

In the early stages, the work has concentrated on the development of the basic flow solver part. The result of this work is a finite volume solver using unstructured triangle meshes for laminar 2D flows. The mass conservation is satisfied with a SIMPLE-type pressure correction approach. A cell-centred collocated grid arrangement has been adopted with an explicit pressure damping term in the mass flux calculation in order to avoid velocity and pressure oscillations.

2 Governing equations

The flow is assumed to be incompressible, laminar and isothermal in 2D. The governing equations for the flow are the incompressible 2D continuity and momentum balance equations in the conservation form. For the finite volume method the domain of interest is divided into a finite number of nonoverlapping triangles, i.e. control volumes and the equations are applied for each volume separately. The conservation of mass for triangle l can be written as a sum over the three edges lm of the triangle:

$$\sum_m \dot{m}_{lm} = 0 \,, \tag{1}$$

where $\dot{m}_{lm}$ is the averaged mass flux through face lm. The balance of momentum can be written similarly as

$$\frac{\partial v_{i,l}}{\partial t} = -\frac{1}{\rho V_l} \sum_m \left(F^{iv}_{i,lm} - F^{v}_{i,lm} \right) \,, \tag{2}$$

where

$$F^{iv}_{i,lm} = \left(\rho v_{i,(lm)} \bar{v}_{(lm)} + p_{(lm)} n_{i,(lm)} \right) S_{(lm)} \tag{3}$$

and

$$F^{v}_{i,lm} = \mu \frac{\partial v_{i,(lm)}}{\partial n} S_{(lm)} \tag{4}$$

are the averaged inviscid and viscous fluxes on face lm respectively. Here $\bar{v}_{lm}$ is the convection velocity normal to face lm.

3 Pressure correction method for triangle meshes

The first intermediate goal of the development was a 2D, cell centred pressure correction solver for laminar flows based on unstructured triangle meshes, which would then act as a basis for further development. The pressure correction approach in the method is of SIMPLE [1] type. Boundary conditions are satisfied using ghost cells located outside the boundaries of the computational domain.

The solution process is based on a velocity-pressure decoupling, in which a new velocity field is first constructed from momentum balance Eq. (2) and corrected after this by altering the pressure according to the mass balance error in the continuity equation Eq. (1). This process is iterated until a steady state is reached. Each of these iterations can be divided into three parts: calculation of the change of velocities, the mass balance error and the pressure corrections.

3.1 Change of velocity

The changes of the velocity components in each triangle are calculated using the implicit Euler scheme for Eq. (2). By linearizing the fluxes with respect to the cell centre values from the old time level, the implicit scheme for Eq. (2) in triangle l can be written as

$$\sum_n \left(\frac{\rho V_l}{\Delta t} \delta_{ln} + a_{ln} \right) \Delta v_{i,n} = R_{i,l} \,, \tag{5}$$

where

$$a_{ln} = \sum_m \frac{\partial F_{i,lm}}{\partial v_{i,n}} \qquad R_{i,l} = -\sum_m F_{i,lm} \,. \tag{6}$$

Here $R_{i,l}$ and $F_{i,lm}$ are the explicit residual in cell l and the sum of the inviscid and viscous fluxes on face lm respectively.

3.1.1 Inviscid flux

The convection part of the inviscid flux in Eq. (3) is upwinded as

$$\frac{1}{2}\rho S_{(lm)} \left[\bar{v}_{(lm)} \left(v^r_{i,(lm)} + v^l_{i,(lm)} \right) + \right.$$
$$\left. - |\bar{v}_{(lm)}| \left(v^r_{i,(lm)} - v^l_{i,(lm)} \right) \right] \tag{7}$$

---

*Ship Laboratory, Helsinki University of Technology, Otakaari 4, FIN-02015 Espoo, Finland – E-Mail: Tommi.Mikkola@hut.fi

where $v^r_{i,lm}$ and $v^l_{i,lm}$ are the extrapolated values on the right and left hand sides of the face lm respectively. The convection velocity $\bar{v}_{lm}$ and the pressure p_{lm} on the face are calculated as averages of the cell centre values to the left and right of the face. Here, the outer normal of a cell face is assumed to point from left to right. The convected velocity components $v^{r/l}_{i,lm}$ are extrapolated onto the face based on a higher order construction by Frink [2]. This is illustrated in Fig. 1. The approximation can be written as

$$v_i^{r/l} = v_i^c + \frac{1}{3}\left(\frac{v_i^2 + v_i^3}{2} - v_i^1\right) . \tag{8}$$

The higher order extrapolation above is used in the calculation of the flux terms in the explicit residual (6). This extrapolation would, however, lead to a complicated and large stencil on the left hand side of the implicit stage Eq. (5). Therefore a simple, first order approximation is used for the fluxes appearing in the a_{ln} term of (6). Only the closest neighbours of a cell are therefore included into the stencil of the momentum matrix.

3.1.2 Viscous flux The normal derivatives for the calculation of the viscous part of the momentum fluxes (4) are resolved by using the Gauss theorem for an auxiliary volume surrounding the face (see Fig. 2). We get

$$\frac{\partial v_{i,lm}}{\partial x_j} = \frac{1}{V^a_{lm}} \sum_{n=1}^{4} v_{i,lmn} n^a_{j,lmn} S^a_{lmn} \tag{9}$$

for the velocity derivative on the face. Here, V^a_{lm} is the area of the auxiliary volume and $n^a_{j,lmn}$ and S^a_{lmn} are the components of the outer normal and size of face n of the auxiliary volume respectively. The velocity components $v_{i,lmn}$ at the centre of face n of the auxiliary volume are approximated by an average of the values at the corner points of this face. Form (9) is used for the calculation of the explicit residual (6) in the momentum equation. Similarly to the inviscid flux, a much simpler approximation is used for the fluxes on the left hand side of Eq. (5). For these the normal derivative is approximated as

$$\frac{\partial v_{i,lm}}{\partial n} = \frac{v_{i,m} - v_{i,l}}{(x_{j,m} - x_{j,l})\, n_{j,lm}} , \tag{10}$$

i.e. as the difference between velocities at cell centres on both sides of the face divided by the distance normal to the face between the cell centres. As before, this leads to a stencil including only the closest neighbours of a cell.

3.2 Calculation of the mass imbalance

As the velocities resulting from the momentum equations probably do not satisfy the continuity condition, mass imbalance in the continuity equation (1), driving the pressure correction, has to be calculated. The use of velocity interpolation scheme by Rhie and Chow [3] for the mass flux calculation is a common approach on collocated structured grids to avoid possible decoupling of neighbouring pressures and velocities. There has been modifications of this scheme for unstructured grids as well, eg. by Davidson [4] and Thomadakis and Leschziner [5]. As these effectively lead to fourth-order dissipation similar to the one commonly used with central differencing to stabilize the solution of the momentum equations [6], a simplified pressure diffusion term is used in the current approach. This term is added to the convection velocity taken as average of the values at the cell centres on both sides of the face leading to form

$$\dot{m}^*_{lm} = \rho S_{(lm)} \left[\bar{v}^*_{(lm)} + \frac{C S_{(lm)}}{4 A_{P,(lm)}} \left(p^n_{ml} - 3p_m + 3p_l - p^n_{lm}\right)\right] \tag{11}$$

for the mass flux in Fig. 3. Here C is a parameter controlling the overall amount of damping and $A_{P,lm}$ is the average of the diagonal terms on the left hand side of the momentum equations (5) for cells l and m to the left and right of the face.

3.3 Pressure correction

If the continuity condition is not satisfied and there is mass imblance, the velocity field has to be corrected accordingly. This is done by adjusting the pressure in the domain. The flow variables satisfying the continuity equations can be given as

$$v_i = v_i^* + v_i' \qquad p = p^* + p' , \tag{12}$$

where v_i' and p' are the unknown corrections. By substituting the velocities into the continuity equation (1) we get an equation for the mass flux corrections

$$\sum_m \dot{m}'_{lm} = -\sum_m \dot{m}^*_{lm} . \tag{13}$$

An equation for the pressure corrections is reached by giving the changes in mass flux on the left hand side of Eq. (13) in terms of changes in pressure. This is done by substituting the yet unknown values (12) for velocity components and pressure into the momentum equations (5) and by taking into account that the provisional values v_i^* and p^* satisfy these equations. This gives us a relation between the velocity and pressure changes in a cell and its neighbours. We follow the approach used in the SIMPLE method [1] and approximate the relation by neglecting the velocity corrections in the neighbouring cells, leaving relation

$$A_{P,(l)} v'_{i,(l)} = -\sum_n S_{ln} p'_{ln} n_{i,ln} . \tag{14}$$

Based on the Gauss theorem, the left hand side is equal to the volume integral of the pressure derivative in direction x_i over triangle l. The relation for convection velocity $\bar{v}_{lm}$ on face lm is reached by averaging the relations for cells l and m and by taking a dot product between Eq. (14) and the normal vector on face lm giving

$$\bar{v}'_{lm} = -\frac{V_{(lm)}}{A_{P,(lm)}} \left(\frac{\partial p'}{\partial n}\right)_{(lm)} . \tag{15}$$

Here, V_{lm} and $A_{P,lm}$ are taken as averages of the respective values in cells l and m. By approximating the normal derivative similarly to Eq. (10) and by substituting the relation (15) into Eq. (13), we get the pressure correction equation

$$\sum_m \alpha_{lm} p'_m = -\sum_m \dot{m}^*_{lm} , \tag{16}$$

where

$$\alpha_{lm} = -\frac{3}{2} \frac{\rho S^2_{lm}}{A_{P,l} + A_{P,m}} \qquad \alpha_{(l)(l)} = -\sum_{m \neq l} \alpha_{lm} \tag{17}$$

are the off-diagonal and diagonal elements respectively.

The velocity corrections are calculated from (14). After this, the velocities and pressures are updated. However, practice has shown, that for a stable calculation, pressure has to be under-relaxed at this point. This is a known feature of the SIMPLE-algorithm [7]. Pressures are thus updated from

$$p_l^{n+1} = p_l^n + \alpha_p p_l' \tag{18}$$

Parameter α_p is the under-relaxation factor for the corrections and a value between 0 and 1 should be given depending on the case.

3.4 Overall algorithm

Now, that the individual parts of the solver have been discussed, we can summarize the algorithm with the following sequence of steps.

1. Initialize the velocities and pressures in the computational domain.
2. Update the ghost cell values according to the boundary conditions.
3. Calculate the inviscid and viscous fluxes for v_1.
4. Calculate the explicit residuals of v_1.
5. Determine the matrix coefficients (6) for the implicit stage.
6. Solve the change of v_1 from the linear system (5).
7. Repeat steps 3–6 for velocity component v_2.
8. Update the velocity components.
9. Calculate the mass imbalance on the right hand side of Eq. (16) using Eq. (11).
10. Determine the coefficients (17) of the pressure correction equation.
11. Solve the pressure corrections from (16).
12. Update the pressures according to Eq. (18) with under-relaxation.
13. Calculate the velocity corrections from Eq. (14).
14. Repeat steps 2–13 until convergence.

4 Data structures

For unstructured solution methods the connections between different grid elements have to be explicitly defined. Thus the data structure is an integral part of any unstructured flow solver. It has influence on both the memory and CPU time requirements and the data structure is usually a compromise between these two.

4.1 Face based data structure

The data structure used to define the faces of the element grid is similar to the ones in e.g. [5] and [8]. These have four identification integers for each face in the grid, which define the two endpoints of the face and the triangles to the left and right of the face respectively. For our purposes, two additional integers are added for each face. These define, which subregion of the grid do the triangles on the left and right hand sides of the face belong to. For instance, the ghost cells of different boundary patches belong to different subregions. For face lm in Fig. 4 the entries in the face datastructure are

$$\begin{array}{ll} iface(lm,1) = n & iface(lm,2) = p \\ iface(lm,3) = l & iface(lm,4) = m \\ iface(lm,5) = \text{block}(l) & iface(lm,6) = \text{block}(m)\ , \end{array}$$

with the direction of the face from n to p, leaving element l on the left hand side and m on the right hand side of the face.

4.2 Element based data structure

The data structure for triangles is similarly an extension of the element data structure used in e.g. [5]. The original data structure has three entries for each triangle, giving the indeces of the faces forming the triangle. This leads to a hierarcial data structure, in which the element structure gives the faces of a triangle and face data structure gives the corner points. However, with this approach each corner point of a triangle is resolved twice and common corner points have to be eliminated separately. In this work, the problem is avoided by using an approach based on a reference triangle shown in Fig. 5. The first three entries for each element are the indeces of the sides of the triangle. These are collected in a counter clockwise direction starting from some arbitrary side of the triangle. In addition to these, there are three entries, which define the orientations of the sides relative to the reference triangle. These give a data structure

$$\begin{array}{ll} ielem(l,1) = lm & ielem(l,4) = \text{orient}(lm,l) \\ ielem(l,2) = ln & ielem(l,5) = \text{orient}(ln,l) \\ ielem(l,3) = lp & ielem(l,6) = \text{orient}(lp,l)\ , \end{array}$$

where

$$\text{orient}(lm,l) = \begin{cases} 0 & \text{if } l \text{ is to the left of } lm \\ 1 & \text{if } l \text{ is to the right of } lm \end{cases}$$

is the orientation marker for face lm relative to triangle l.

5 Numerical tests

Several test calculations for different types of flows have been carried out during the development of the solution method. These include e.g. fully developed channel flow, lid-driven flows in square and skewed cavities and flow around a 2D cylinder. Results for a lid-driven cavity flow are presented below. The linear systems arising from the momentum equations are solved using Gauss-Seidel iteration, whereas the pressure correction equation is solved using either Gauss-Seidel or conjugate gradient stabilized (CG-STAB) method.

An overview of the case is presented in Fig. 6. Cavity flows are standard benchmark cases for testing solution methods for Navier-Stokes equations with a great deal of reference data available in the literature. The geometry is simple, yet the recirculating flow is quite complex associated with a balanced presence of both diffusive and convective processes. [5]

The dimension L of the cavity and the velocity u of the lid are 1.0 m and 1.0 m/s respectively with Reynolds number set to 1000. The angle β of the cavity for the tested case is 30 degrees. The no-slip boundary condition was applied on all walls. Computational grid shown in Fig. 7 was generated by dividing the quadrilaterals of the corresponding structured uniform 40×40 grid into two triangles. The resulting mesh has 1681 nodes, 4880 sides and 3200 triangles. A constant time step of 0.6 s was used for the momentum equations and the resulting linear systems were solved using 24 Gauss-Seidel iterations. The mass flux damping parameter C was set to 0.5. The Gauss-Seidel solver was used for the solution of the pressure correction equation with 6 iterations. The under-relaxation factors for pressure and velocity were $\alpha_p = 0.2$ and $\alpha_v = 1.0$ respectively. The convergence of the residuals is presented in Fig. 8. As can be seen, the residuals do not change anymore after around 380 global iterations. By this time, the L_2-norms of the momentum residuals have dropped by over 5 decades and the norm for the pressure corrections by 3 decades.

The velocities in the cavity are compared to the numerical reference data by Demirdžić et al. [9]. The comparison is based on the v_1 and v_2 velocity components along the centre lines of the cavity from left to right and from bottom to top. This is shown in Fig. 9. As the cell centres of the computational grid do not coincide with the exact centre lines of the cavity, points closest to these lines below and above or to the left and right have been used. As can be seen from these figures, the computations agree rather well with the reference solutions. The minimum of v_2 velocity is, however, overestimated by 7.4 per cent. Additionally the difference between the computed solutions above and below the horizontal centre line is quite large at the right hand wall of the cavity. This is due to the fact, that in this case the end of the centre line is located very close to the point, where the flows from above and below converge. It is likely, that the grid resolution is somewhat insufficient and the accuracy of the results could be improved by making the grid finer at certain locations. In fact, in the grid dependence studies by Demirdžić et al. [9] the locations most sensitive to changes in grid spacing were the ones mentioned above.

6 Conclusions and future work

An unstructured, pressure correction based flow solver for laminar flows on triangle meshes has been developed and tested with several different test cases. Results for a lid-driven skewed cavity flow have been presented. The accuracy of the method for the cases tested has been comparable to similar methods found in the literature. However, all of the grids used for testing were featured with a smoothly varying cell size. Some validation using grids with considerable differences in the sizes of the neighbouring cells should therefore be done in the future.

The development is still in an early stage, but a solid base for further development has already been established. The long term goal of this work is the application of the solver for free surface flows using surface tracking grid reconstruction, in which new cells are introduced and old ones destroyed, as necessary, following the movement of the free surface. For this a method for the surface deformation computation as well as a grid reconstruction algorithm have to implemented.

Acknowledgements

The financial support for this work by the Academy of Finland is greatly appreciated.

References

[1] L. S. Caretto, A. D. Gosman, S. V. Patankar, and D. B. Spalding. Two calculation procedures for steady, three-dimensional flows with recirculation. In *Proc. Third Int. Conf. Numer. Methods Fluid Dyn.*, Paris, 1972.

[2] Neal T. Frink. Recent Progress Towards a Three-Dimensional Unstructured Navier-Stokes Flow Solver. *AIAA 94-0061*, 1994.

[3] C. M. Rhie and W. L. Chow. A numerical study of the turbulent flow past an isolated airfoil with trailing edge separation. *AIAA Journal*, 21:1525–1532, 1983.

[4] Lars Davidson. A pressure correction method for unstructured meshes with arbitrary control volumes. *International Journal for Numerical Methods in Fluids*, 22:265–281, 1996.

[5] Michael Thomadakis and Michael Leschziner. A pressure-correction method for the solution of incompressible viscous flows on unstructured grids. *International Journal for Numerical Methods in Fluids*, 22:581–601, 1996.

[6] A. Jameson, W. Schmidt, and E. Turkel. Numerical solutions of the Euler equations by finite volume methods with Runge-Kutta time stepping schemes. *AIAA 81-1259*, 1981.

[7] S. V. Patankar. *Numerical heat transfer and fluid flow.* McGraw-Hill, 1980.

[8] D. J. Mavriplis. Multigrid Solution of the Two-Dimensional Euler Equations on Unstructured Triangluar Meshes. *AIAA Journal*, 26(7):824–831, 1988.

[9] I. Demirdžić, Ž. Lilek, and M. Perić. Fluid Flow and Heat Transfer Test Problems for Non-Orthogonal Grids: Benchmark Solutions. *International Journal for Numerical Methods in Fluids*, 15:329–354, 1992.

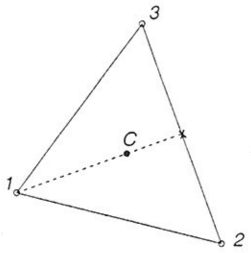

Figure 1: Higher order extrapolation of the face values.

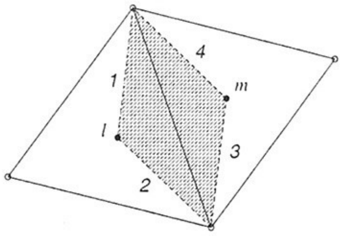

Figure 2: Auxiliary volume for the calculation of normal derivatives on a face.

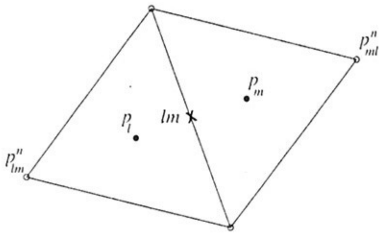

Figure 3: Calculation of the damping term for the mass flux.

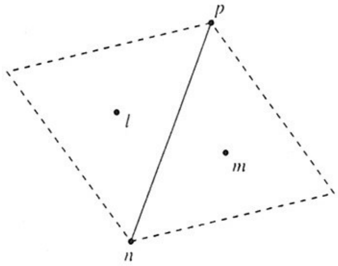

Figure 4: The data structure for element faces.

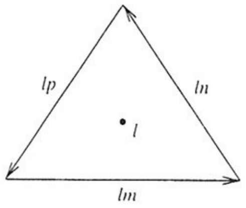

Figure 5: Reference triangle approach for the element datastructure.

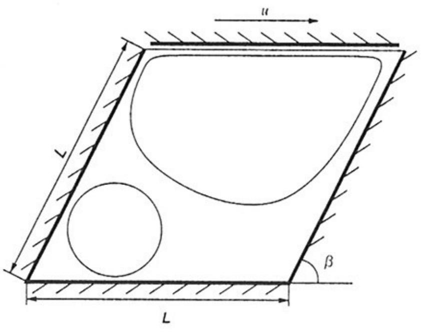

Figure 6: Lid-driven cavity flow.

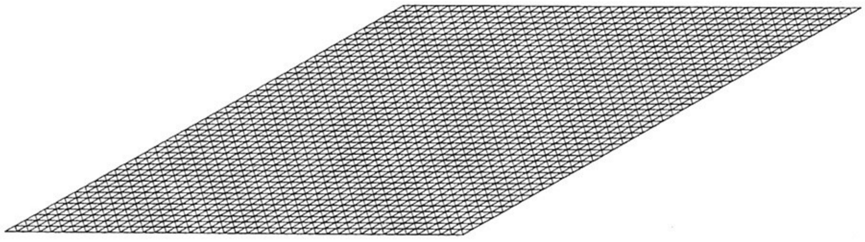

Figure 7: Computational grid for the 30 degrees skewed cavity.

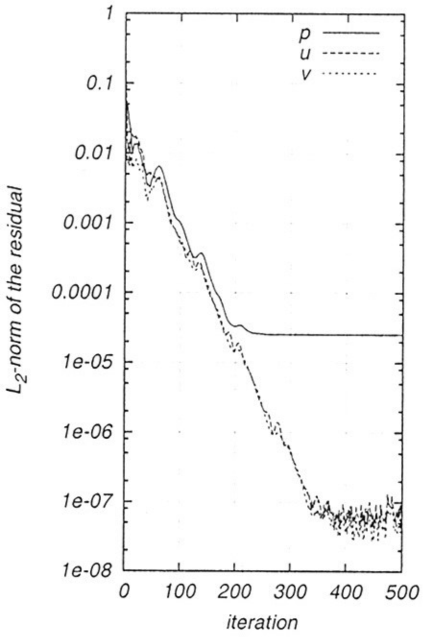

Figure 8: Convergence histories for the lid-driven cavity flow.

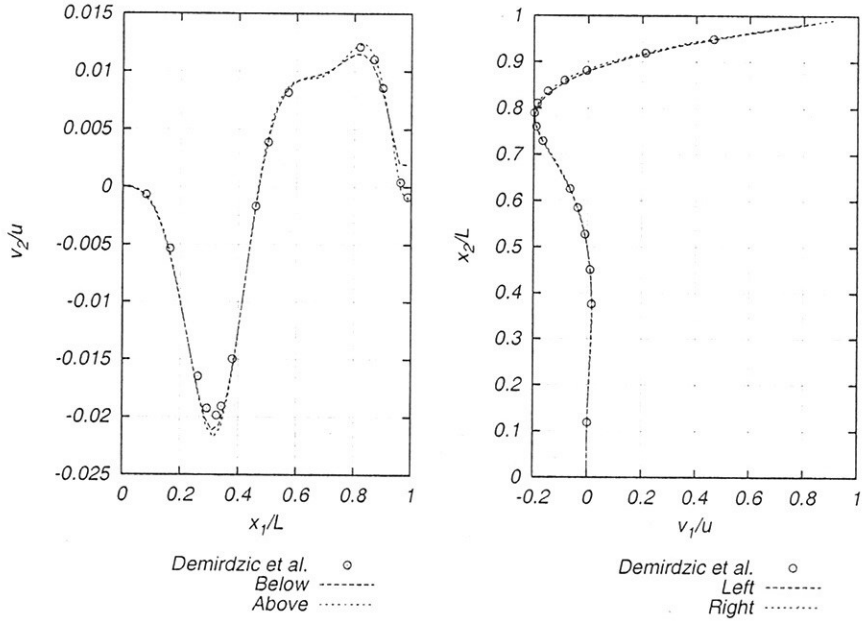

Figure 9: Velocity components on the centre lines for the 30 degrees cavity with $Re = 1000$: Left, v_2 velocity on the horizontal centre line; right, v_1 velocity on the centre line from bottom to top.

Farfield dispersive waves and the radiation condition

Francis Noblesse[1] and Chi Yang[2]

[1] NSWC-CD, 9500 MacArthur Blvd, West Bethesda, MD 20817-5700

[2] School of Computational Sciences, George Mason University, Fairfax, VA 22030-4444

1. Introduction

The important fundamental problem of defining the farfield waves generated by a ship advancing in calm water or in regular waves (or an offshore structure in waves) is considered for deep water and uniform finite water depth. A classical Fourier representation defines the farfield time-harmonic (or steady) waves generated by a ship or an offshore structure in terms of one-dimensional Fourier superpositions of elementary waves that satisfy the Laplace equation and the boundary conditions at the sea floor and the free surface. This classical Fourier representation of farfield waves does not satisfy the radiation condition (and thus does not preclude, for instance, waves ahead of a ship advancing in calm water). Another Fourier representation of farfield dispersive waves, given in *Noblesse and Chen (1995)* and *Noblesse (2001)*, does satisfy the radiation condition, as well as the boundary conditions at the free surface and the sea floor. However, this representation (which involves the sign function) does not satisfy the Laplace equation exactly.

Thus, neither the classical Fourier representation of farfield waves nor the representation given in *Noblesse and Chen (1995)* satisfy all the equations and conditions that define the farfield waves generated by a ship or an offshore structure. These two known Fourier representations of farfield waves are reconsidered and extended here. A representation — which exactly satisfies the Laplace equation, the radiation condition, and the sea-floor and free-surface boundary conditions — is given. Thus, this new farfield representation satisfies all the equations and conditions that define the farfield waves generated by a ship or an offshore structure, except the nearfield boundary condition at the wetted hull of the ship or structure (the nearfield boundary condition determines the amplitude of the farfield waves). The new farfield representation can be useful (i) to couple a nearfield flow calculation method and a farfield linear potential flow representation, as in *Yang et al. (2000)*, (ii) for numerical methods based on a spectral approach, and (iii) to define *practical Green functions* based on Rankine sources and Fourier superpositions of elementary waves, as will be shown elsewhere.

Although farfield waves generated by a ship advancing in calm water or in regular waves, or an offshore structure in regular waves, are primarily considered here, the approach and the analysis expounded in the study are valid more generally and in fact can easily be applied to a broad class of dispersive waves.

2. Problem statement

A ship advances in regular (time-harmonic) waves along a straight path, with constant speed $\mathcal{U}$, at the free surface of a large body of water of uniform depth D. The X axis is chosen along the path of the ship, and points toward the ship bow. Thus, the ship advances in the direction of the positive X axis. The Z axis is vertical and points upward, and the mean free surface is taken as the plane $Z=0$. The sea floor $Z=-D$ is assumed to be a rigid wall. The flow is observed from a Cartesian system of coordinates moving with speed $\mathcal{U}$ along the X axis, and is expressed as the sum of a steady component, which represents the flow due to the ship advancing in calm water, and a time-harmonic component associated with the ambient waves, the waves diffracted by the ship, and the radiated waves due to the motions of the ship about a mean position. g and ω represent the gravitational acceleration and the frequency of the waves encountered by the advancing ship, respectively. The steady and time-harmonic components of the flow due to the ship are expressed in nondimensional form in terms of the water density and a reference length L and velocity U, which can be taken as the length and the speed $\mathcal{U}$ of the ship, respectively. Thus, nondimensional coordinates $\vec{\xi} = (\xi, \eta, \zeta) = \vec{X}/L$ and velocity potential $\phi = \Phi/(UL)$ are used here. The nondimensional water depth is $d = D/L$.

Farfield waves generated by a ship may be analyzed within the framework of linear potential-flow theory. Thus, farfield ship waves are defined in terms of a velocity potential ϕ that satisfies the Laplace equation

$$\phi_{\xi\xi} + \phi_{\eta\eta} + \phi_{\zeta\zeta} = 0 \tag{1}$$

In addition, the potential ϕ satisfies either the deep-water boundary condition

$$\phi \to 0 \quad \text{as} \quad \zeta \to -\infty \tag{2a}$$

or the (rigid) sea-floor boundary condition

$$\phi_\zeta = 0 \quad \text{at} \quad \zeta = -d \tag{2b}$$

The potential of farfield time-harmonic ship waves also satisfies the free-surface boundary condition

$$\phi_\zeta - f^2\,\phi + F^2\,\phi_{\xi\xi} + i\,2\tau\,\phi_\xi - i\,\varepsilon\,(\,f\,\phi - i\,F\,\phi_\xi\,) = 0 \quad \text{at } \zeta = 0 \tag{3a}$$

where $f = \omega\,\sqrt{L/g}$, $F = \mathcal{U}\,/\sqrt{gL}$, $\tau = F f$ and $0 < \varepsilon \ll 1$. The potential of farfield steady ship waves satisfies the free-surface condition

$$\phi_\zeta + F^2\,\phi_{\xi\xi} - \varepsilon\,F\,\phi_\xi = 0 \quad \text{at } \zeta = 0 \tag{3b}$$

This condition corresponds to the special case $f = 0 = \tau$ of the condition (3a) associated with diffraction-radiation of time-harmonic waves with forward speed. The parameter $0 < \varepsilon \ll 1$ in the free-surface boundary conditions (3) is associated with initial conditions that correspond to a flow starting from rest at time $T = -\infty$; e.g. see *Lighthill (1978)* or *Noblesse (2001)*. These initial conditions and the related parameter ε in the free-surface boundary conditions (3) ensure that the radiation condition is satisfied. Finally, the potential ϕ satisfies boundary conditions at the ship hull that specify the derivative $\partial\phi/\partial n$ of ϕ along the normal to the hull surface. However, these nearfield boundary conditions are not required for the present analysis of farfield ship waves.

3. Elementary waves and dispersion functions

Consider the elementary wave functions

$$W(\,\xi\,,\eta\,,\zeta\,) = e^{-\,i\,(\,\alpha\,\xi\,+\,\beta\,\eta\,)\,+\,k\,\zeta} \tag{4a}$$

$$W(\,\xi\,,\eta\,,\zeta\,) = e^{-\,i\,(\,\alpha\,\xi\,+\,\beta\,\eta\,)}\,\cosh\left[\,k\,(\,\zeta + d\,)\,\right]/\cosh(\,k\,d\,) \tag{4b}$$

where k is the wavenumber defined as

$$k = \sqrt{\alpha^2 + \beta^2} \tag{5}$$

The elementary wave (4b) is identical to (4a) in the deep-water limit $k\,d \to \infty$. At the mean free-surface plane $\zeta = 0$, the wave functions (4a) and (4b) become

$$W(\,\xi\,,\eta\,,\zeta = 0\,) = e^{-\,i\,(\,\alpha\,\xi\,+\,\beta\,\eta\,)}$$

The elementary wave functions (4) satisfy the Laplace equation (1). In addition, the elementary wave (4a) satisfies the deep-water boundary condition (2a) and the elementary wave (4b) satisfies the sea-floor boundary condition (2b). The elementary wave functions (4) also satisfy the free-surface boundary condition (3a) if the Fourier variables α and β satisfy the dispersion relation

$$D + i\,\varepsilon\,D_1 = 0 \tag{6}$$

with the dispersion functions D and D_1 given by

$$D = (f - F\alpha)^2 - k \qquad\qquad D_1 = f - F\alpha \tag{7a}$$

$$D = (f - F\alpha)^2 - k\,\tanh(k\,d) \qquad\qquad D_1 = f - F\alpha \tag{7b}$$

for the wave functions (4a) and (4b), respectively. The dispersion function D defined by (7b) is identical to the deep-water dispersion function (7a) in the limit $k\,d \to \infty$.

Thus, the elementary waves (4) — where k , α and β satisfy (5) and (6) with (7) — satisfy the Laplace equation and the boundary conditions at both the free surface $\zeta = 0$ and the sea floor $\zeta = -d$ or $\zeta = -\infty$. These wave functions therefore are elementary farfield solutions. Accordingly, the farfield waves generated by a ship or an offshore structure can be represented by a Fourier superposition of the elementary waves defined by (4a) in deep water or (4b) in water of uniform finite depth d . This Fourier representation of farfield waves is examined below for generic dispersive waves of the form (4a) and (4b) associated with a dispersion relation of the form (6). Farfield waves corresponding to the dispersion relation (6) with $\varepsilon = 0$ are considered first, and the dispersion relation (6) with $0 < \varepsilon \ll 1$ is examined subsequently.

4. Classical representation of farfield ship waves

In the limit $\varepsilon = 0$, the dispersion relation (6) becomes

$$D = 0 \tag{8}$$

For instance, consider the dispersion function D defined by (7a) in the special case $F = 0$, which corresponds to wave diffraction-radiation without forward speed (e.g. by an offshore structure) in deep water. The dispersion function D in this special case is $D = f^2 - k$ and the dispersion relation (8) yields $k = f^2$. Thus, the dispersion relation for this special case shows that the Fourier variables α and β in (4a) lie on a circle with radius f^2 centered at the origin $k = 0$ of the Fourier plane $(\alpha\,,\beta)$. More generally, the dispersion relation $D(\alpha\,,\beta) = 0$ associated with generic dispersive waves typically defines several curves, called dispersion curves, in the Fourier plane.

Thus, farfield waves can be represented by one-dimensional Fourier superpositions of the form

$$\sum_{D=0} \int_{D=0} ds\, A\, W \tag{9}$$

where the Fourier variables $(\alpha\,,\beta)$ lie on the dispersion curves defined by the dispersion relation (8). In (9), summation is performed over all the dispersion curves defined by (8), ds represents the differential element of arc length of a dispersion curve, W is the elementary wave function given by (4a) or (4b), and A stands for an amplitude function (that is determined by the nearfield boundary condition at the ship hull surface). The classical Fourier representation (9) of farfield waves is associated with the dispersion relation (8), which corresponds to (6) with $\varepsilon = 0$. Thus, the farfield waves defined by the classical Fourier representation (9) do not satisfy the radiation condition. For instance, the representation (9) does not preclude steady ship waves ahead of a ship advancing in calm water. Farfield waves associated with the dispersion relation (6) with $0 < \varepsilon \ll 1$, which accounts for the radiation condition, are now considered.

5. Elementary waves that satisfy the radiation condition

The dispersion relation (6) with $0 < \varepsilon \ll 1$ defines complex Fourier variables of the form

$$\alpha + i\,\varepsilon\,\alpha_1 \qquad \beta + i\,\varepsilon\,\beta_1 \qquad k + i\,\varepsilon\,k_1 \tag{10a}$$

and requires

$$D(\alpha + i\,\varepsilon\,\alpha_1\,,\beta + i\,\varepsilon\,\beta_1) + i\,\varepsilon\,D_1(\alpha + i\,\varepsilon\,\alpha_1\,,\beta + i\,\varepsilon\,\beta_1) = 0$$

In the limit $\varepsilon \to 0$, this dispersion relation yields

$$D(\alpha\,,\beta) + i\,\varepsilon\,[\,\alpha_1 D_\alpha + \beta_1 D_\beta + D_1\,] + O(\varepsilon^2) = 0$$

where D_α and D_β are the derivatives of the dispersion function D with respect to the Fourier variables α and β. The foregoing equation and the relation $D(\alpha\,,\beta) = 0$ yield

$$\alpha_1 D_\alpha + \beta_1 D_\beta = -D_1 \tag{10b}$$

Furthermore, the Laplace equation requires

$$k + i\,\varepsilon\,k_1 = \sqrt{(\alpha + i\,\varepsilon\,\alpha_1)^2 + (\beta + i\,\varepsilon\,\beta_1)^2}$$

In the limit $\varepsilon \to 0$, this relation and (5) yield

$$k_1 = (\,\alpha\,\alpha_1 + \beta\,\beta_1)/k \tag{10c}$$

Using the Fourier variables (10a) in (4a) yields elementary waves of the form

$$e^{-i\,(\,\alpha\,\xi + \beta\,\eta - \varepsilon\,k_1\,\zeta\,) + k\,\zeta + \varepsilon\,(\,\alpha_1\,\xi + \beta_1\,\eta\,)} \tag{11a}$$

For $\varepsilon > 0$, the elementary wave function (11a) is unbounded in the limit $\xi^2 + \eta^2 \to \infty$ if $\alpha_1\,\xi + \beta_1\,\eta > 0$. Elementary waves of the form

$$\Theta\; e^{-i\,(\,\alpha\,\xi + \beta\,\eta - \varepsilon\,k_1\,\zeta\,) + k\,\zeta + \varepsilon\,(\,\alpha_1\,\xi + \beta_1\,\eta\,)} \tag{11b}$$

are bounded everywhere if the function Θ is null in the farfield for $\alpha_1\,\xi + \beta_1\,\eta > 0$. For instance, the function Θ

$$\Theta = [\,1 - \mathrm{sign}(\alpha_1\,\xi + \beta_1\,\eta)\,]\,/\,2 \tag{11c}$$

satisfies this requirement. The limit $\varepsilon \to 0$ of the bounded wave function (11b) may then be taken and yields

$$\Theta\; e^{-i\,(\,\alpha\,\xi + \beta\,\eta\,) + k\,\zeta} \tag{11d}$$

The elementary wave function defined by (11d) and (11c) does not satisfy Laplace's equation. Thus, the function Θ is now modified so that the elementary wave (11d) satisfies Laplace's equation.

Consider the function

$$\Theta(\frac{\alpha_1\,\xi+\beta_1\,\eta+i\,k_1\,\zeta}{\sigma_*}) \tag{12a}$$

where σ_* is a positive real function of the Fourier variables α and β. The function defined by (11d) and (12a) satisfies Laplace's equation if

$$k^2=\alpha^2+\beta^2 \qquad k_1^2=\alpha_1^2+\beta_1^2 \qquad k\,k_1=\alpha\,\alpha_1+\beta\,\beta_1$$

The first and last of these three conditions are satisfied by virtue of (5) and (10c), and the second condition requires $\alpha_1/\alpha=\beta_1/\beta$. Thus, the wave function (11d) satisfies Laplace's equation if

$$(\alpha_1\,,\beta_1\,,k_1)=\Gamma\,(\alpha\,,\beta\,,k) \tag{12b}$$

Expression (10b) defines the proportionality factor Γ as

$$\Gamma=\frac{-D_1}{\alpha D_\alpha+\beta D_\beta}=\frac{-D_1}{kD_k}=-\mu\,\frac{|\,D_1\,|}{k\,|\,D_k\,|} \tag{12c}$$

where $D_k=D_\alpha\,\alpha/k+D_\beta\,\beta/k$ is the derivative of the dispersion function D in the radial direction $(\alpha\,,\beta)/k$ and μ is defined as

$$\mu=\text{sign}D_1\ \text{sign}D_k \tag{12d}$$

Expressions (12a)–(12c) then yield

$$\Theta(-\mu\,\frac{\alpha\,\xi+\beta\,\eta+i\,k\,\zeta}{\sigma}) \tag{12e}$$

where $\sigma=\sigma_*\,k\,|\,D_k/D_1\,|$ is a positive real function of α and β.

A simple function of the form (12e) that satisfies the farfield condition associated with (11) is

$$\Theta=1/\,[\,1+\exp(-\mu\,\frac{\alpha\,\xi+\beta\,\eta+i\,k\,\zeta}{\sigma})\,] \tag{13a}$$

Indeed, (13a) yields $\Theta\to 0$ as $\mu\,(\alpha\,\xi+\beta\,\eta)/\sigma\to-\infty$ and $\Theta\to 1$ as $\mu\,(\alpha\,\xi+\beta\,\eta)/\sigma\to\infty$. Furthermore, (12d) yields

$$\Theta\sim\frac{1+\text{sign}D_1\ \text{sign}D_k\ \text{sign}(\alpha\,\xi+\beta\,\eta)}{2} \qquad \text{as} \qquad \frac{|\,\alpha\xi+\beta\eta\,|}{\sigma}\to\infty \tag{13b}$$

in accordance with (11c).

Thus, the elementary wave function

$$e^{-\,i\,(\alpha\,\xi+\beta\,\eta)+k\,\zeta}/\,[\,1+\exp(-\mu\,\frac{\alpha\,\xi+\beta\,\eta+i\,k\,\zeta}{\sigma})\,] \tag{14a}$$

where μ is given by (12d), satisfies the Laplace equation (1), the deep-water condition (2a), and the free-surface boundary condition (3a), which accounts for the radiation condition. The elementary wave (14a), related to the deep-water elementary wave (4a), can be extended to uniform finite water depth by substituting the function

$$e^{\,k\,\zeta}\,\Theta(-\mu\,\frac{\alpha\,\xi+\beta\,\eta+i\,k\,\zeta}{\sigma})$$

by the function

$$e^{\,k\,(\zeta+d)}\,\Theta(-\mu\,\frac{\alpha\,\xi+\beta\,\eta+i\,k\,(\zeta+d)}{\sigma})+e^{-k\,(\zeta+d)}\,\Theta(-\mu\,\frac{\alpha\,\xi+\beta\,\eta-i\,k\,(\zeta+d)}{\sigma})$$

which satisfies the boundary condition (2b) at the sea floor $\zeta=-d$. The elementary wave function

$$e^{-\,i\,(\alpha\,\xi+\beta\,\eta)}\left(\frac{\exp[\,k\,(\zeta+d)\,]}{1+\exp[-\mu^*\{\alpha\,\xi+\beta\,\eta+i\,k\,(\zeta+d)\}\,]}+\frac{\exp[-k\,(\zeta+d)\,]}{1+\exp[-\mu^*\{\alpha\,\xi+\beta\,\eta-i\,k\,(\zeta+d)\}\,]}\right) \tag{14b}$$

where $\mu^*=\mu/\sigma$, satisfies the Laplace equation, the sea-floor and free-surface boundary conditions, and the radiation condition.

6. Fourier representation of farfield ship waves

The foregoing analysis shows that farfield ship waves can be expressed in terms of one-dimensional Fourier superpositions of the elementary wave functions defined by (14) and (12d), which satisfy every farfield condition (Laplace equation, sea-floor and free-surface boundary conditions, and radiation condition). This Fourier representation of farfield ship waves is now given. The Fourier variables α and β and the horizontal coordinates ξ and η are expressed in the polar forms

$$\begin{Bmatrix} \alpha \\ \beta \end{Bmatrix} = k \begin{Bmatrix} \cos\gamma \\ \sin\gamma \end{Bmatrix} \quad \text{with} \quad k = \sqrt{\alpha^2+\beta^2} \quad \text{and} \quad -\pi \le \gamma \le \pi \tag{15a}$$

$$\begin{Bmatrix} \xi \\ \eta \end{Bmatrix} = h \begin{Bmatrix} \cos\theta \\ \sin\theta \end{Bmatrix} \quad \text{with} \quad h = \sqrt{\xi^2+\eta^2} \quad \text{and} \quad -\pi \le \theta \le \pi \tag{15b}$$

These polar representations and expressions (14) show that the potential ϕ of farfield (steady or time-harmonic) waves generated by a ship (or an offshore structure) can be expressed as

$$\phi \sim \sum_{i\ge 1} \int_{\gamma_i^L}^{\gamma_i^U} d\gamma\, A_i\, \Theta\, \Delta\, (\cos H - i\, \sin H) \tag{16a}$$

Here, H is defined as

$$H = \alpha\,\xi + \beta\,\eta = k\,h\, \cos(\gamma - \theta) \tag{16b}$$

and the function Δ is given by

$$\Delta = \exp(k\,\zeta) \qquad \Delta = \cosh[\,k\,(\zeta + d)\,]\,/\cosh(k\,d) \tag{16c}$$

in deep water and in uniform finite water depth d, respectively. Summation in (16a) is performed over all the dispersion curves defined by the dispersion relation $D=0$. The wavenumber k in (16a)–(16c) is a function of γ that is given by

$$k = k_i(\gamma) \qquad \text{with} \qquad \gamma_i^L \le \gamma \le \gamma_i^U$$

where $k_i(\gamma)$ are the roots of the dispersion relation $D=0$, and γ_i^L and γ_i^U are the lower and upper limits of the corresponding range of the polar angle γ. The function Θ in (16a) is given by

$$\Theta = \frac{\exp H_* + \cos V_* + i\,T \sin V_*}{\exp H_* + 1/\exp H_* + 2\cos V_*} = \frac{\exp H_* + \cos V_* + i\,T \sin V_*}{2\,(\cosh H_* + \cos V_*)} \tag{17a}$$

where the functions H_* and V_* are defined as

$$H_* = \mu\, H/\sigma \qquad V_* = \mu\, V/\sigma \qquad \text{with} \quad \mu = \text{sign} D_1\ \text{sign} D_k \tag{17b}$$

and $D_k = D_\alpha \cos\gamma + D_\beta \sin\gamma$. The functions T and V in (17a) and (17b) are given by

$$T = \begin{Bmatrix} 1 \\ \tanh V \end{Bmatrix} \qquad V = \begin{Bmatrix} k\,\zeta \\ k\,(\zeta + d) \end{Bmatrix} \tag{17c}$$

in deep water and in uniform finite water depth d, respectively. The variation of the function H_* that corresponds to a period of the trigonometric function $\exp(-i\,H)$ is given by $2\pi/\sigma$. Thus, the choice $\sigma = 1$ in (17b) ensures that the function Θ defined by (17a) becomes practically identical to 0 or 1, more precisely to the farfield approximation given below by (18), within one period (wavelength) of the function $\exp(-i\,H)$. The amplitude function $A_i = A_i(\gamma)$ in the Fourier representation (16a) is determined by nearfield boundary conditions, not considered in the farfield approximation (16a).

7. Comparison of alternative farfield representations

The farfield waves defined by the Fourier representation (16), with Θ given by (17) and the dispersion functions D and D_1 given by (7), satisfy the Laplace equation, the free-surface boundary condition (3a) with $0 < \varepsilon \ll 1$, and the boundary conditions (2a) or (2b) at the sea floor. The potential ϕ defined by the Fourier representation (16) with $\Theta = 1$ satisfies the Laplace equation, the free-surface boundary condition with $\varepsilon = 0$, and the sea-floor boundary condition. The function Θ in the Fourier representation (16a) of farfield waves corresponds to the dispersion relation (6) with $0 < \varepsilon \ll 1$, and introduces restrictions that do not exist in the classical representation associated with $\Theta = 1$, $\varepsilon = 0$, and the dispersion relation (8). The restrictions introduced by the function Θ account for the information that is included in the dispersion relation (6) but is ignored in the dispersion relation (8). Specifically, the dispersion relation (6) assumes a flow that starts from rest at time $T = -\infty$, whereas the dispersion relation (8) includes no information about initial conditions. Accordingly, the dispersion relation (8) does not yield uniquely-defined time-harmonic flows. If this dispersion relation is used, a unique time-harmonic flow can be defined by invoking an additional consideration, called radiation condition, that specifies that wave energy is radiated away from the flow disturbance that generates the waves. This additional consideration, required to supplement the dispersion relation (8), is automatically satisfied if the dispersion relation (6) is used instead of (8).

The farfield approximation (13b) yields

$$\Theta = [\,1+ \mathrm{sign}D_1\, \mathrm{sign}D_k\, \mathrm{sign}(\alpha\,\xi+\beta\,\eta)\,]/2 \tag{18}$$

in the farfield limit $|\,\alpha\xi + \beta\eta\,|/\sigma \to \infty$. The representation (16) with Θ given by (18) satisfies the boundary conditions at the sea floor and the free surface, and the radiation condition. However, this representation does not satisfy the Laplace equation. The main contribution to the Fourier integral (16a) in the farfield limit $h \to \infty$ stems from points where the phase H of the trigonometric functions $\cos H$ and $\sin H$ is stationary. Expressions (16b) and (15) show that a point $(\alpha\,,\beta)$ of a dispersion curve $D(\alpha\,,\beta) = 0$ where the phase $H = \alpha\,\xi + \beta\,\eta$ is stationary is determined by the relation

$$dH/ds = \xi\, d\alpha/ds + \eta\, d\beta/ds = 0$$

Here, ds is the differential element of arc length of a dispersion curve, as already noted. The vectors $(\,d\alpha/ds\,, d\beta/ds\,)$ and $\nabla D = (\,D_\alpha\,, D_\beta\,)$ are tangent and normal, respectively, to a dispersion curve, and therefore are orthogonal. Thus, the vector $(\xi\,,\eta)$ is normal to a dispersion curve at a point $(\alpha\,,\beta)$ where $dH/ds = 0$, i.e. at a point of stationary phase, and the relation

$$(\,\xi\,,\eta\,)/\sqrt{\xi^2+\eta^2} = \nu\,(\,D_\alpha\,, D_\beta\,)/\sqrt{D_\alpha^2+D_\beta^2} \quad \text{with} \quad \nu = \pm 1$$

holds at such a point. This relation yields

$$\mathrm{sign}(\,\alpha\,\xi + \beta\,\eta\,) = \nu\, \mathrm{sign}(\,\alpha\, D_\alpha + \beta\, D_\beta\,) = \nu\, \mathrm{sign}(\,D_k\,)$$

It follows that we have

$$1+ \mathrm{sign}D_1\, \mathrm{sign}D_k\, \mathrm{sign}(\alpha\,\xi+\beta\,\eta) = 1+ \nu\, \mathrm{sign}D_1$$

at a point of stationary phase. This expression is null if $\nu = -\mathrm{sign}D_1$. Thus, a point of stationary phase yields a non-zero contribution to the Fourier integral (16a) if the relation

$$\frac{(\,\xi\,,\eta\,)}{\sqrt{\xi^2+\eta^2}} = (\,\cos\theta\,, \sin\theta\,) = \mathrm{sign}D_1\, \frac{(\,D_\alpha\,, D_\beta\,)}{\sqrt{D_\alpha^2+D_\beta^2}} = \mathrm{sign}D_1\, \frac{\nabla D}{\|\nabla D\|} \tag{19}$$

is satisfied. The relation (19) shows that a point $(\alpha\,,\beta)$ of a dispersion curve (in the Fourier plane) mostly generates waves (in the physical space) along an angle $\eta/\xi = \tan\theta$ that is orthogonal to the dispersion curve and in the direction $(\mathrm{sign}D_1)\,\nabla D$. Conversely, farfield waves observed along a direction θ stem mostly from the point(s) of the dispersion curve(s) where the condition (19) holds. This well-known result, e.g. see *Lighthill (1978)* and *Chen and Noblesse (1997)*, provides a verification of the Fourier representations given by (16) with (17) or (18), and also shows that these farfield approximations are asymptotically equivalent to the approximation (16) with Θ defined as

$$\Theta = [\,\mathrm{sign}D_1 + \mathrm{sign}(\xi D_\alpha+\eta\, D_\beta)\,]/2 \tag{20}$$

given in *Noblesse and Chen (1995)* and *Noblesse (2001)*.

8. References

Chen, X.B., Noblesse, F. (1997) *Dispersion relation and farfield waves*, 12th Itl Workshop on Water Waves and Floating Bodies, Carry-le-Rouet, France, 31-34

Lighthill, J. (1978) *Waves in Fluids*, Cambridge Univ. Press 504 pp.

Noblesse, F. (2001) *Analytical representation of ship waves*, Ship Technology Research 48:23-48

Noblesse, F. and Chen, X.B. (1995) *Decomposition of free-surface effects into wave and near-field components*, Ship Technology Research 42:167-185

Yang, C., Löhner, R., Noblesse, F. (2000) *Farfield Extension of Nearfield Steady Ship Waves*, Ship Technology Research 47:22-34

Numerical Simulation of Ship Flows under Self-Propulsion Condition with Contrarotating Propellers

Kunihide Ohashi, Nobuyuki Hirata, Takanori Hino
National Maritime Research Institute, Japan
e-mail: k-ohashi@nmri.go.jp

1.Introduction

In recent years, efficient propulsion systems are in demand for reducing emission of greenhouse effect gas. Among many such systems proposed so far, contrarotating propellers (CRP) are one of the most efficient propulsors. A great deal of efforts have been made on performance predictions of CRP, mainly based on a vortex theory or a lifting line theory[1].

On the other hand, CFD methods based on Navier-Stokes solvers are being widely used for hydrodynamic performance analysis of ship hull forms in a design process. For a prediction of propulsive efficiency by CFD methods, propeller effects should be taken into account in Navier-Stokes simulations. The most simplified way to do this is the use of a body force distribution representing propeller effects. This approach has been applied to analysis of ship flows with a propeller effect[2,3] and generally showed good agreements with measured data. However, all the above body force models are concerned only with a conventional single propeller(CP) and the applications to CRP have not been carried out.

The purpose of the present paper is to examine the applicability of two body force models for Navier-Stokes solvers to CRP. One is the prescribed body force model[2] which determines a bodyforce distribution based on the given values of thrust and torque and the geometrical information. This model cannot take into account considered of the interaction between two propellers(fore and aft propellers of CRP). Another body force model can cope with the interaction of two propellers of CRP. In this model, the body force distributions are calculated by a simplified propeller theory[4] in which a propeller thrust and torque are determined from the informations of propeller inflow and operating conditions.

At first the numerical simulation of propeller open water characteristics of CRP is performed, then the numerical simulation of ship flows under self-propulsion condition is carried out. Through the above numerical simulations, the applicability of the present model is examined.

2.Numerical Method

The basic flow solver used is *NEPTUNE* [5] which solves the three-dimensional incompressible Navier-Stokes equations with artificial compressibility. In this work, the propeller effects are taken into account in the body force term of the governing equations as

$$\frac{\partial \mathrm{q}}{\partial t} + \frac{\partial(\mathrm{e}+\mathrm{e}_v)}{\partial x} + \frac{\partial(\mathrm{f}+\mathrm{f}_v)}{\partial y} + \frac{\partial(\mathrm{g}+\mathrm{g}_v)}{\partial z} + \mathbf{H} = 0 \tag{1}$$

where x, y and z are the Cartesian coordinates. In Eq.(1), $\mathbf{q}$ is the dependent variables $[p, u, v, w]^T$, $(\mathbf{e}, \mathbf{f}, \mathbf{g})$ and $(\mathbf{e}_v, \mathbf{g}_v, \mathbf{f}_v)$ are the inviscid fluxes and the viscous fluxes and $\mathbf{H}$ is the body force vectors $[0, -fbx, -fby, -fbz]^T$.

The propeller effects are represented using the body force distributions. In the present work, two body force models are used. One is the prescribed body force distributions proposed by Hough and Ordway[2](this is called as Model1 hereafter) and the other is the body force distributions which are calculated by a simplified propeller theory[4](this is called as Model2.

3.Results and Discussions

3.1 Results for Propeller Open Water Characteristics

The numerical simulations of propeller affects in open water are carried out. Table 1 shows the principal particulars of CRP(MP258[fore] /259[aft]).

Table 1 Principal Particulars

	CRP	
MP.No.	MP258	MP259
Diameter(m)	0.250	0.2399
Boss Ratio	0.220	0.229
Pitch Ratio(0.7Rp)	1.274	1.366
Expanded Area Ratio	0.482	0.518
Blade Thickness Ratio	0.053	0.047
Number of Blades	4	5
Direction of Turning	Right	Left
Blade Section	NACA66,a=0.8	NACA66,a=0.8

Fig.1 is the distributions of the axial and circumferential velocity of CRP case. The computed results show a good agreement in the axial velocity. The both models can simulate the large decrease of circumferential velocity and Model2 can simulate the flow field slightly better than the prescribed body force model(Model1), although the velocity amplitudes are under-predicted compared with the measured data. One of the reason for this under-prediction is considered to the fact that the propeller boss effect is neglected in the computations.

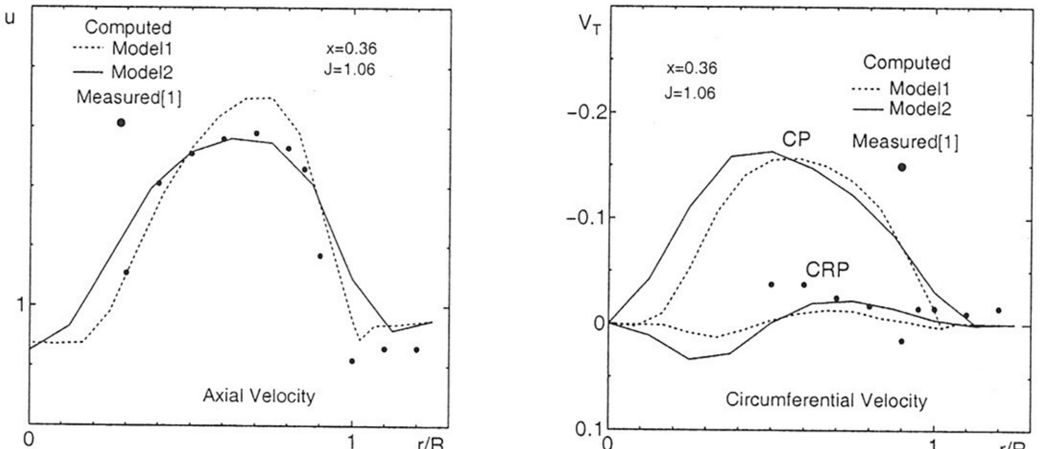

Fig.1 Velocity Distributions in the Propeller Race of CRP(x=0.36,MP258/259)

3.2 Results of Self-propulsion Condition

In this section, the numerical simulation of ship flows under self-propulsion condition is carried out with the prescribed body force model(Model1). Model2 results will be discussed at the meeting.

For simplicity, free surface effect is not considered and a rudder is not adopted. Computed results are compared with measured results[1] in terms of thrust deduction coefficient in particular because the prescribed body force model is not able to obtain other self-propulsion factors. Also the flows behind CP and CRP are compared and CRP effects on the wake flows are discussed.

The ship type is a container ship. The solution domain is set

$$-1.5 < x < 3.0, -2.0 < y < 2.0, -2.0 < z < 0.0$$

where (x,y,z) are non-dimensionalized by L_{pp}. The origin of the coordinate is located at FP on the waterplane. Fig.2 depicts the computational grid. The grid consists of 145 × 65 × 81 grids points and the minimum spacing is $1.0 \times 10^{-2}, 2.4 \times 10^{-3}$ and 2.8×10^{-6} in streamwise, girth and normal directions, respectively. The grids points are clustered in the boundary layer of a ship hull and near the propeller section. The Spalart-Allmaras model is adopted as a turbulence model.

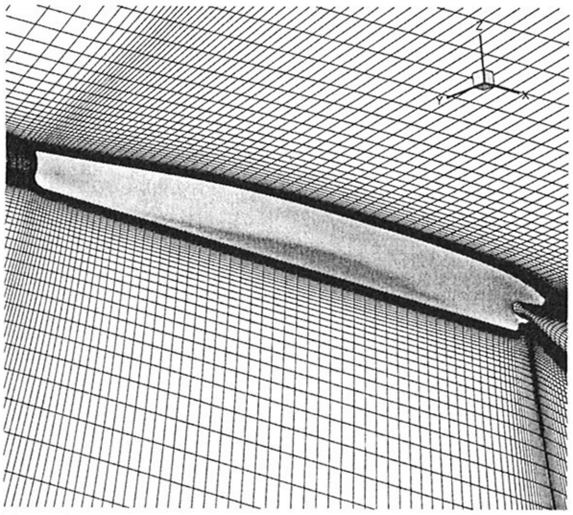

Fig.2 Computational Grid(Only a half side is shown)

Table 2 shows the principal particulars of the model propellers MP145(CP) and MP258/259(CRP) used in this computation.

Table 2 Principal Particulars of MP145 and MP258/259

	CP	CRP	
MP.No.	MP145	MP258	MP259
Diameter(m)	0.256	0.250	0.240
Boss Ratio	0.180	0.220	0.229
Direction of Turning	Right	Right	Left

In the present work, self-propulsion condition is determined by thrust-identity method which changes the propeller thrust value until the self-propulsion condition is satisfied. The propeller thrust and torque are interpolated by the polynominal approximation of the measured results.

Fig.3 shows the flows behind the propeller at x=1.0(AP) and Fig.4 depicts pressure distributions on the aft hull surface. Comparison of the flows of CRP case with those of CP case shows the cross flows behind CRP decrease drastically and the axial velocity distributions of CRP case are almost y-symmetric. In Fig.4, the high pressure area with CRP is much smaller than that without propeller because of the propeller suction effects. This area is larger than that with CP, since the longitudinal distance between the propeller and the ship stern is larger in CRP than in CP. This leads to decrease of the viscous pressure resistance C_{vp} and rise in thrust deduction coefficient 1-t in CRP case(see Table 3). The values of 1-t obtained by the numerical simulations are larger than the measured results.

This is due to the fact that the computed thrusts are smaller than the measured ones since the wave making resistance is not taken into account in the numerical simulation.

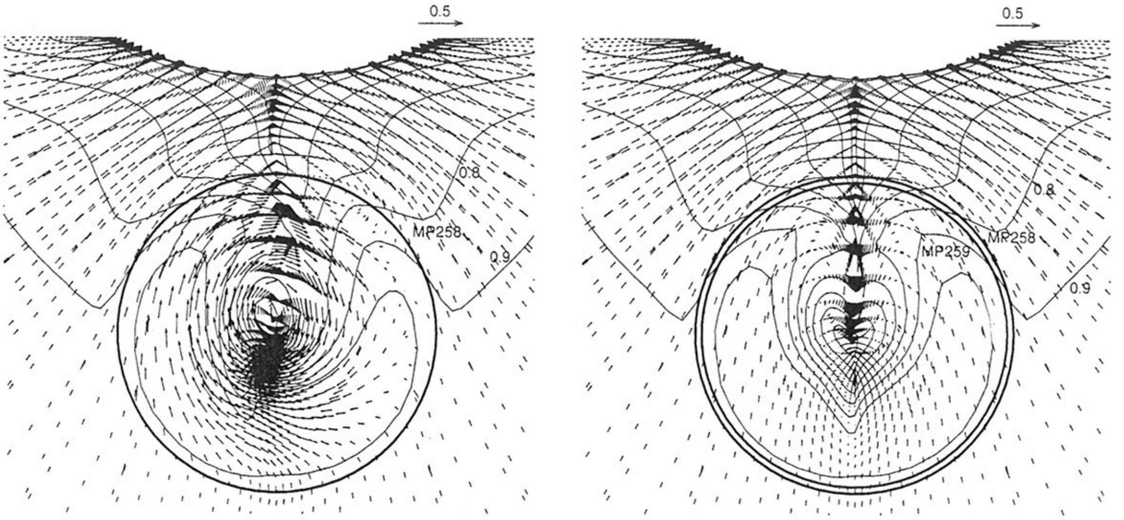

CP CRP

Fig.3 Comparison of Axial and Tangential Velocity Distribution($\Delta u=0.1$, $x=1.0$)

Table 3 Comparison of Resistance Coefficient and 1-t

	w.o.prop.	CRP	CP
$C_v \times 10^3$	3.200	3.440	3.496
$C_{vp} \times 10^3$	0.327	0.660	0.717
1-t(Computed)	—	0.868	0.844
1-t(Measured[1])	—	0.836	0.800

4.Conclusion

The applicability of the body force models of CRP has been examined for a Navier-Stokes solver. At first, the numerical simulation of propeller open water characteristics of CRP is performed. The present body force models can simulate the large decrease of the cross flow velocities, although the values are under-predicted compared with the measured data. One of the reason for this under-prediction is considered to the fact that the propeller boss effect is neglected in the computations. In the future, the propeller boss effect must be considered to improve accuracy.

Next the numerical simulation of ship flows under self-propulsion condition with CRP is carried out. The self-propulsion factor, thrust deduction coefficient in particular, is compared with the measured results. The computed results show a similar tendency as the measured results that the thrust deduction coefficient of CRP case is larger than that of CP case.

References

[1]Ukon, Y., Kurobe, Y., Kawakami, Y., Yanagihara, T., Kadoi, H., Kudo, T. : On the Design of Contrarotating Propellers y Application to High Speed Container Ship , (in Japanese), Trans. of the West-Japan Society of Naval Architects, Vol.75 (1988), pp.52-64

[2]Stern, F., HT, Kim., VC, Patel., HC, Chen : Viscous-Flow Approach to the Computation of Propeller-Hull Interaction, Journal of Ship Research, Vol.32 No4 (1988), pp.246-262

[3]Hinatsu, M., Kodama, Y., Fujisawa, J., Ando, J : Numerical Simulation of Flow around a Ship Hull

Including a Propeller Effect , (in Japanese), Trans. of the West-Japan Society of Naval Architects, Vol.88 (1994), pp.1-11

[4]Moriyama, F. : On an Approximate Numerical Method for Estimating the Performance of Marine Propellers, (in Japanese), Papers of Ship Research Institute, Vol.16 No.6 (1979), pp.361-376

[5]Hirata, N., Hino, T. : An Efficient Algorithm for Simulating Free Surface Turbulent Flows around Advancing Ship, Journal of the Society of Naval Architects of Japan, Vol.185 (1999), pp.1-8

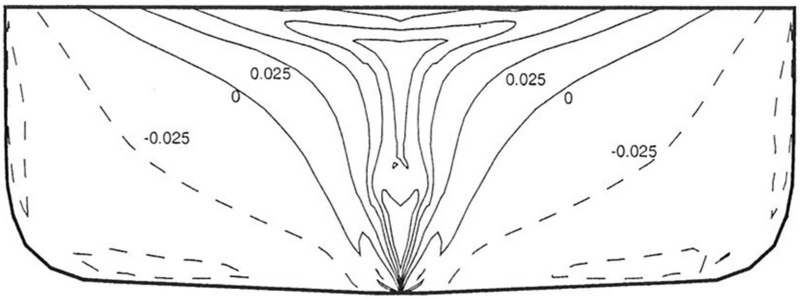

Without Propeller

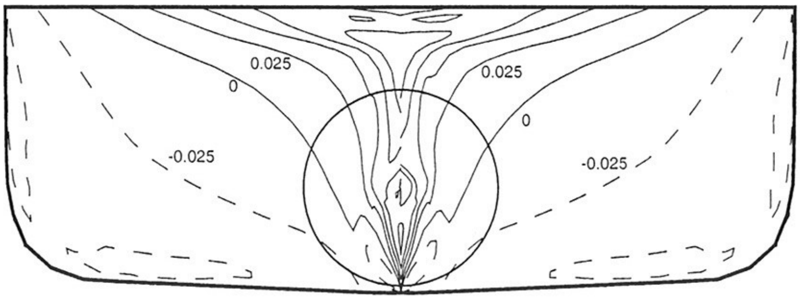

CP

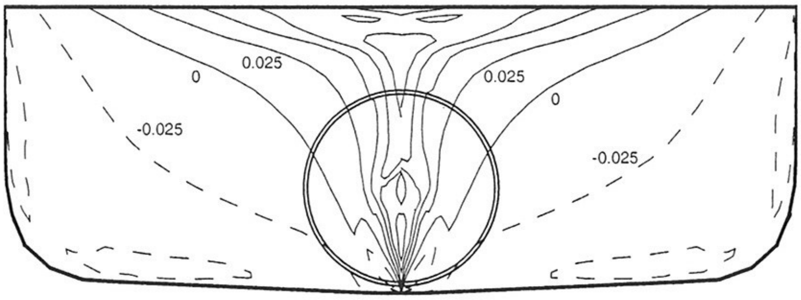

CRP

Fig.4 Comparison of Pressure Distribution($\Delta p=0.025$)

THE ROLE OF TRANSITION ON THE PERFORMANCE CHARACTERISTICS OF HYDROFOILS

by

V.Papakonstantinou, G.Tzabiras, S.Voutsinas

Department of Naval Architecture and Marine Engineering, National Technical University of Athens,
Heroon Polytechniou 9, Zografos 157 73, Athens, Greece (Tel. +30 1 7721038 , Fax. +30 1 7721032)
(e-mail : vkpapnav@central.ntua.gr , tzab@fluid.mech.ntua.gr , spyros@fluid.mech.ntua.gr)

ABSTRACT

The prediction of the lift and drag characteristics of hydrofoils at high incidence angles is examined, when transition occurs. Two turbulence models are examined i.e. the Spalart-Almaras one-equation model and the k-ω – SST two-equation model in conjunction with empirical and theoretical calculations of the laminar flow regimes. Computations are compared to measurements.

INTRODUCTION

In their majority, complex turbulent flow-fields are calculated by RANS solvers by employing suitable turbulence models. Such methods have been applied with success for the calculation of lift and drag characteristics of airfoils when the flow is fully turbulent. However, if transition from laminar to turbulent flow occurs, there are special difficulties to model accurately the extension of laminar zones especially at high angles of incidence. Since the existence of transition affects drastically the overall coefficients, the prediction of transition points remains one of the crucial problems for this type of flows.

In many cases there are experimental data providing information about the location of transition and the corresponding calculations are made to compare numerical predictions to measured quantities for this kind of flows. Needless to say that there is no need, then, to adopt a transition model. However this is not the case for required 2D and 3D applications where the transition zones must be calculated implicitly by the numerical method. Since this problem is still open, empirical physical models are often applied to determine transition and their success depends, as for the turbulence models, on the geometry and the situations considered. The purpose of the present study is to examine the influence of such models on the prediction of flows past airfoils, mainly near stall.

Two methods are examined to predict the transition point. The first one (T1) is based on experimental data from airfoils according to the empirical proposal of Schlichting-Granville [1]. This approach involves the integral boundary layer parameters that are calculated by the Polhhausen method, in order to compute the location of the point of instability and the point of transition. The second transition model (T2) is the theoretical "n-factor" based on Falker-Skan two parametric velocity distributions. In both cases, the external velocity at the edge of the boundary layer is calculated implicitly through the pressure distribution along the foil that is derived from the overall solution of the RANS equations.

In order to investigate also the significant role of the turbulence modeling two turbulence models have been employed, i.e. the Spalart-Almaras (SA) [2] one equation model and the k-ω SST two-equation model (SST) [3]. In all tests, a RANS solver developed at the School of NAME, NTUA has been applied.

Two test cases were examined. In case A (typical wind generator section, Table 1) the lift and drag coefficients were calculated using both turbulence models in low and high angles of attack, with fixed transition. Since the k-ω SST showed better behavior in case A, this model was exclusively used in case B (NACA 63-415) for fully turbulent or with-transition calculations, employing both transition models. The numerical results are compared with experimental data.

2-D RANS SOLVER

The governing RANS equations and the turbulence model equations are expressed in orthogonal curvilinear coordinates. They are solved according to finite volume approach using a staggered grid. The fluid domain was covered by an orthogonal C-type mesh, which was extended 6 chords downstream and 5 chords in the transverse direction [Fig.1]. The grid was produced by the conformal mapping technique [4] and had a density of 1200x150 points (NI x NJ) where the first number shows the nodes along the foil contour.

The code uses the hybrid, first-order scheme for the convection terms and a pressure correction, SIMLE-like procedure [5] to calculate the pressure field together with the velocity components. To be able to include transition predictions, the method also includes a boundary layer prediction in order to estimate the momentum thickness, which is necessary to apply methods T1 and T2.

With regard to the turbulence modeling, the one equation SA model was used in test case A with specific treatment of diffusion terms according to [2], which, however, did not show any remarkable differences in the results. The model requires an initial value of the employed variable, which was introduced by a k-ε solution for the first iterations of the convergence procedure. The k-ω SST two-equation model was applied in its standard form or in conjunction with the one-equation k-model for eddy viscosity calculation close to the wall. In this approximation, the mixing length is determined by the simple Van-Driest formula.

BOUNDARY CONDITIONS

The employed 2-D RANS solver leads to an elliptic form of non-linear algebraic equations, so it requires boundary conditions on every boundary. The velocity components on the external boundary of the C-mesh are computed assuming the flow undisturbed (Dirichlet conditions) while for all other variables Neummann conditions are applied. At the exit plane non-reflecting conditions have been employed and the pressure is calculated by linear extrapolation

On the wall the velocity components are set equal to zero, the pressure is calculated assuming zero normal gradient, while, as mentioned above, two kinds of boundary conditions are imposed when the SST model is used. According to the first condition, the ω value on the wall is computed through:

$$\omega \rightarrow \frac{6\nu}{\beta_1 y^2} \quad \text{as} \quad y \rightarrow 0 \tag{1}$$

whereas, in the second approach, this value is implicitly approximated by finding the corresponding value of the eddy viscosity according to the one-equation k-model.

TRANSITION MODELS

The empirical method T1 uses the Schlichting-Ulrich diagram to define, first the instability point and, then, the Granville experimental results on airfoils to find the distance between the instability and the transition to fully turbulent flow The method requires the calculation of the momentum thickness which is calculated according to the Pohlhausen laminar-boundary layer method, where the potential velocity is calculated from the pressure field.

The theoretical "n-factor" method T2 is based on Falker-Scan two-parametrical velocity profiles. The transition occurs when the Tollmien-Schlichting wave in the boundary layer increases with a factor of $e^n = e^9 = 8100$. The Falker-Skan profiles define "n" as the solution of the differential equation:

$$\frac{dn}{ds} = \frac{dn}{d\,Re_\theta} \cdot \frac{d\,Re_\theta}{ds} \tag{2}$$

where,

$$Re_\theta = \frac{\rho u \theta}{\mu_l} = \frac{u\theta}{\nu}$$ is the critical Reynolds number

θ is the momentum thickness and

s is the curvilinear direction tangential to the wall

The integration of equation (2) provides the n-factor in each s-location on the wall. The gradient dRe_θ/ds is calculated by the velocity distribution and the gradient dn/dRe_θ is approximated by the empirical equation:

$$\frac{dn}{d\,Re_\theta} = 0.01[(2.4H - 3.7 + 2.5\tanh(1.5H - 4.65))^2 + 0.25]^{1/2} \tag{3}$$

with $H = \delta/\theta$, where
δ is the thickness of boundary layer

RESULTS AND CONCLUSIONS

To assess the selected turbulence models the code has been applied firstly to airfoil A in a wide range of incidence angles. The results for the lift and drag coefficients are compared in this case with the obtained by well documented potential-boundary layer methods (FOIL2W [6]), Figs. 2 and 3. In both cases the transition was fixed according to the FOIL2W results with the n-factor. While the SA model gives practically equal results with the SST and FOIL2W up to 10 deg. incidence, the two-equation model produces better results near the stall region, i.e. 15-20 deg. incidence. Besides, calculations with the RANS solver show that solutions can be obtained at very high angles of attack. .e.g. at 40 deg. With the SA model, while FOIL2W gives convergent solutions up to 22 deg., roughly.

Next, the k-ω SST turbulence model with the two empirical transition models was tested on airfoil B for which experimental data are available. When the flow-field is treated as fully turbulent, the lift coefficient is over-predicted by, about, 20% in the range of stall incidence angles of 10-20 degrees, Figs. 4 and 5. When transition is taken into account, the n-factor method gives almost the same results with the fully turbulent computations, while the application of the Schlichting's proposal produces substantially better results at 14 and 16 deg. incidence. It should be noted here that the fulfillment of the transition criterion is made independently of the appearance of the leading edge separation.

It is remarkable that the leading edge separation, due to the existence of the laminar flow region, leads to quite different pressure distributions on the foil, as shown in Fig. 6. The predicted pressure values with the transition model show a surprisingly close agreement with the measured values at 16 deg. incidence. No matter how the transition point has been calculated, it is obvious that the leading edge laminar separation affects the whole suction region, which can be also established by comparing the different sizes of the separation area, Figs. 7 and 8. The Schlichting – Granville empirical method with Pohlhausen calculations for the momentum thickness predict better the lift coefficient at 16 deg angle of attack where the transition occurs towards the stagnation point. Also the calculated with transition model pressure coefficient corresponds to the experimental results in the same angle of attack (fig 6).

Consequently, the present investigation demonstrates that the correct estimation of transition is of major importance and it is necessary for obtaining reliable results for the integrated coefficients. The work is continued for predicting unsteady and 3D flows past wings.

ACKNOWLEDGMENT

The present work is a part of the European program entitled "WIND TURBINE BLADE AERODYNAMICS AND AEROELASTICITY" (KNOW-BLADE WP1). The authors would like to express their deepest gratitude for the significant support by the Commission.

REFERENCES

1.Schlichting H., *"Boundary layer theory"* McGraw Hill, 6th edition 1968.
2.Spalart P.R. and Almaras S.R.,*"A one equation turbulence model for aerodynamic flows"*, AIAA 92-0439, 30th Aerospace Sciences Meeting & Exhibit, Reno NV, 1992.
3.Menter F.R.,*"Zonal two equation k-ω turbulence models for aerodynamic flows"*, AIAA 93-2906, 24th fluid Dynamics Conference, Orlando Florida, 1993.
4.Tzabiras G., Dimas A., Loukakis T.,*"A numerical method for the calculation of incompressible, steady, separated flows around airfoils"*, Int. J. for Numerical Methods in Fluids, 6, 1986,
5.Tzabiras G.D., "A *numerical investigation of the Reynolds scale effect on the resistance of bodies of revolution"*, Ship Technology Research, 39, 1992.

Table I
Test cases definition

	Airfoil	Re
Case A	1	3×10^6
Case B	NACA 63-415	1.6×10^6

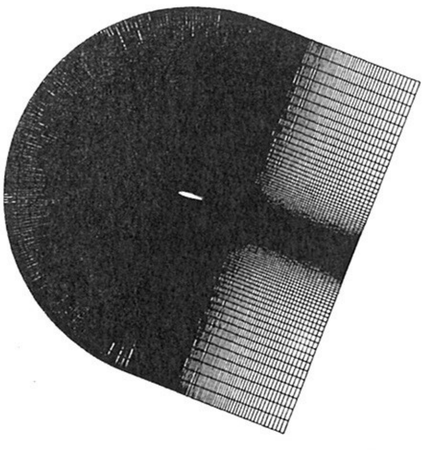

Fig. 1: Computational Grid.

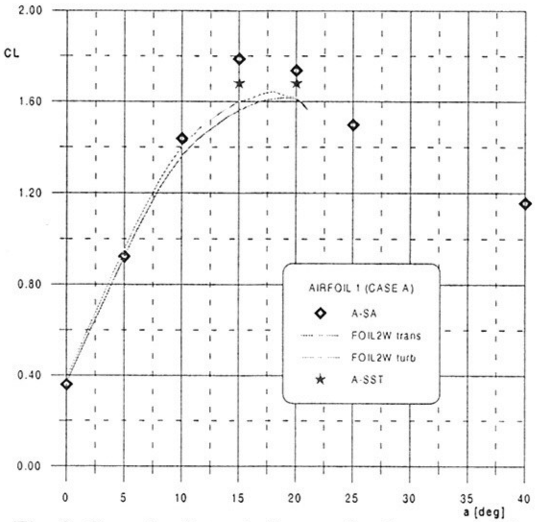

Fig. 2: C_l-angle of attack diagram for the test case A

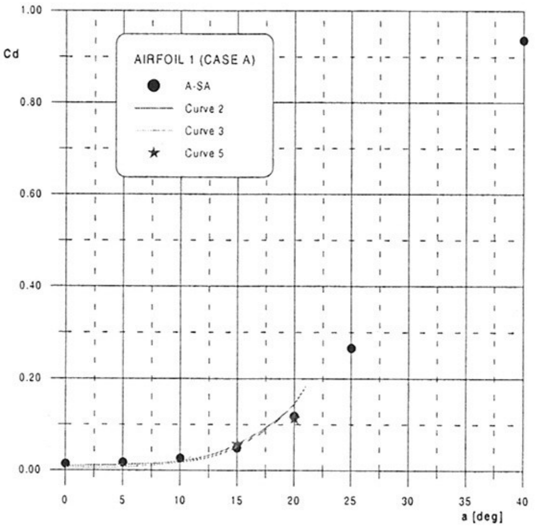

Fig. 3: C_d-angle of attack diagram for the test case A.

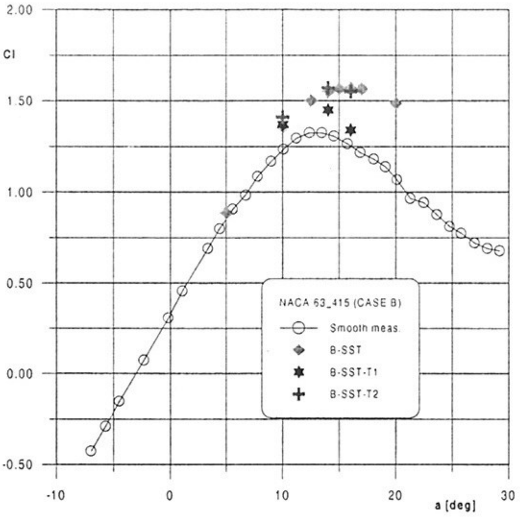

Fig. 4: C_l-angle of attack diagram for the test case B.

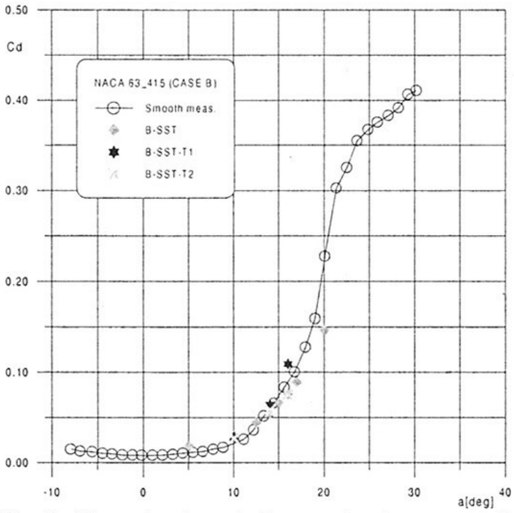

Fig. 5 : C_d-angle of attack diagram for the test case B.

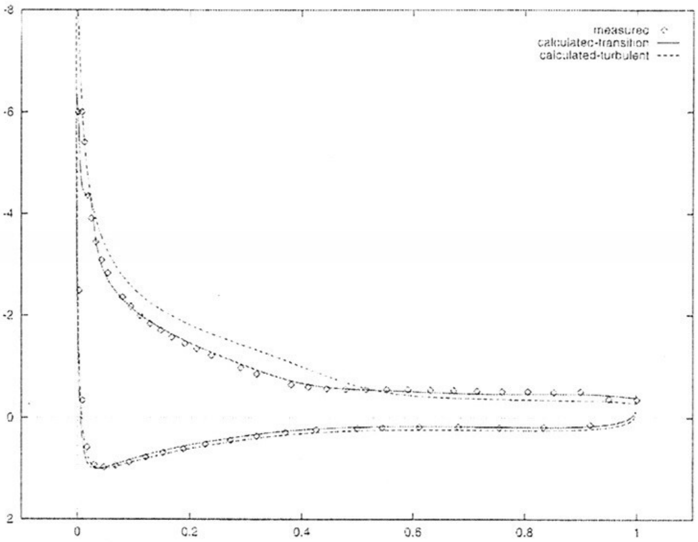

Figure 6: Cp measured and calculated turb. And trans for Case B, a = 16 deg

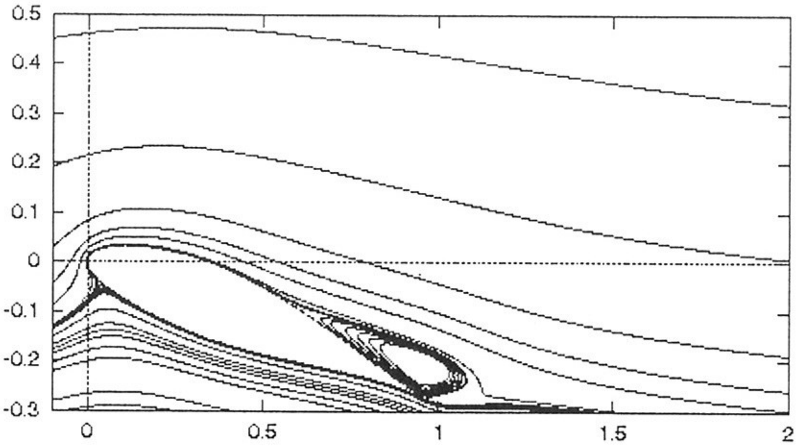

Figure 7: Streamlines for fully turbulent calc. a =16 deg.

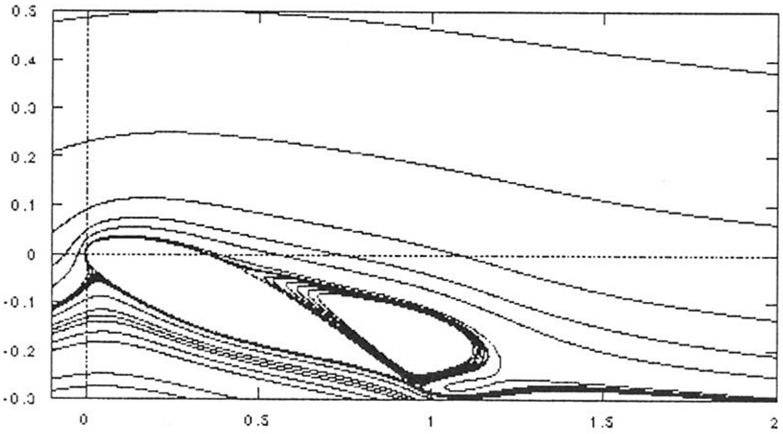

Figure 8: Streamlines for the calc. with transition point from empirical model a =16 deg.

An Adaptive Quadtree Surface Marker Method for Fully Non-linear Wave Simulations

Authors: **C M P Santos**, Dept of Architecture and Civil Engineering, University of Bath, Bath, BA1 7AY, UK, abpcmpds@bath.ac.uk
D M Greaves, Dept of Architecture and Civil Engineering, University of Bath, Bath, BA1 7AY, UK, abpcmpds@bath.ac.uk

SUMMARY

This article describes a finite difference method for numerical modelling of non-linear waves in two dimensions. It uses explicit free surface tracking and adaptive hierarchical Cartesian grids. Massless particles called surface markers are used to define the surface profile. Attention is focused on the calculation of velocities at the surface for which a novel approach is presented using tangential and normal velocities. A multigrid scheme is applied to improve the speed of convergence of the solution. Preliminary results are presented for waves of moderate amplitude.

1. INTRODUCTION.

Potential flow theory may be used in the description of free surface wave flow provided the principal dimensions of the marine structure are comparable with the wavelength, in which case the forces on the structure are dominated by inertia effects and the viscous drag component may be neglected. Simulation of large amplitude wave motions requires a fully non-linear approach, in which the calculation grid deforms throughout the simulation to fit the moving free surface.

The principal difficulty in calculating such a flow resides in the accurate advection of the free surface after each time step. The shape and position of the interface are not known prior to the solution of the governing equations and must be determined as part of the solution. Surface capturing techniques view the free surface as the interface of a two-phase flow, but are prone to numerical diffusion that results in the sharpness of the advancing phase front being blurred. Examples of surface capturing methods include volume-of-fluid (Hirt and Nichols (1981)) and level-set (Osher and Sethian (1988)) approaches.

By contrast, front tracking methods (Glimm *et al.* (1981)) use a calculation grid that is attached to the free surface and deforms with it throughout the simulation, as is the case in this work. This provides two main advantages: a) the interface remains sharp throughout the solution in time; and b) the governing equations need only be solved in the fluid part of the domain. This gain in computer storage can then be used to refine the grid to provide increased accuracy in areas where the velocity potential has a higher gradient.

This paper describes a moving boundary finite difference solver for two-dimensional fully non-linear time-dependent wave flows. The velocity potential is found by solving Laplace's equation as a boundary value problem with a non-linear free surface boundary condition. The grid is automatically regenerated at each time step once the surface has been moved. A Cartesian quadtree grid is chosen to provide variable refinement since its inherent structure lends itself to fast automatic grid generation and adaptation.

2. FINITE DIFFERENCE FORMULATION.

The numerical problem is to solve Laplace's equation for the velocity potential in the fluid domain at each time step using Neumann boundary conditions on rigid boundaries and a Dirichlet condition at the free surface. A two-dimensional Cartesian system, O-*xy*, is used with *y* pointing vertically upwards and the origin being placed at the bottom left hand corner of the domain. Additionally, the surface elevation, η, is defined as the distance in the *y*-direction between a point on the surface and the mean water level, *h*. The problem is hence defined by,

$$\nabla^2\phi = 0\,, \tag{1}$$

where ϕ denotes the velocity potential. At rigid stationary boundaries, Neumann conditions are used,

$$\frac{\partial\phi}{\partial n} = 0\,, \tag{2}$$

where n is the direction normal to the rigid boundaries pointing out of the fluid domain. At the free surface, $y = b + \eta$, the dynamic and kinematic boundary conditions written in Lagrangian form are, respectively,

$$\frac{\mathrm{d}\phi}{\mathrm{d}t} = -g\eta + \frac{1}{2}\nabla\phi\cdot\nabla\phi\,, \tag{3}$$

$$\frac{\mathrm{d}x}{\mathrm{d}t} = \frac{\partial\phi}{\partial x} = u\,; \quad \frac{\mathrm{d}y}{\mathrm{d}t} = \frac{\partial\phi}{\partial y} = v\,. \tag{4}$$

At time $t = 0$, the initial conditions are given as,

$$\phi(x, y = h + \xi, t = 0) = -g\xi\,; \quad \eta(x, t = 0) = \xi(x)\,, \tag{5}$$

where $\xi(x)$ is a function describing the initial shape of the surface in terms of surface elevation. Once equation (1) has been solved at $t = 0$, the velocities of the surface markers are calculated from equation (4) and the surface is advected using, for example, a first-order forward differencing scheme,

$$\begin{aligned} x\big|_{t+\Delta t} &= x\big|_t + \left.\frac{\mathrm{d}x}{\mathrm{d}t}\right|_t \Delta t \\ y\big|_{t+\Delta t} &= y\big|_t + \left.\frac{\mathrm{d}y}{\mathrm{d}t}\right|_t \Delta t \end{aligned} \;. \tag{6}$$

The velocities at the surface are also used in equation (3) to obtain the time derivative of ϕ which is subsequently updated using,

$$\phi\big|_{t+\Delta t} = \phi\big|_t + \left.\frac{\mathrm{d}\phi}{\mathrm{d}t}\right|_t \Delta t\,. \tag{7}$$

Alternatively higher order schemes may be used to increase accuracy, such as the second order Adams-Bashforth method (used in the results herein) or the fourth order Runge-Kutta technique.

3. QUADTREE GRID GENERATION

Having initially been developed in the field of image processing (Samet (1990)), quadtree grids have found their way into studies of a variety of physical phenomena. Due to their ability to produce variable refinement across the domain whilst preserving an inherent tree structure, quadtree grids have often been employed in the field of computational fluid dynamics (Yiu *et al.* (1996) and Yang *et al.* (2000) for example)

In this work, the surface is defined by a series of massless particles, called surface markers, whose positions at $t = 0$ are defined by function $\xi(x)$. The surface markers are used as seeding points of the quadtree grid, together with additional seeding points placed on the rigid boundaries. The quadtree grid is generated by recursive subdivision of cells containing seeding points until a prescribed maximum division level (*LM*) has been reached (a minimum division level, *LB*, is also set). Samet (1990) provides details on the generation of quadtree grids. As a result higher grid refinement is achieved along all boundaries of the fluid domain. The fluid part of the domain is identified from the position and shape of the free surface and cells empty of fluid are disregarded for the purposes of computation. Figure 1 is an example of a quadtree grid, *LM*=6 and *LB*=4, for a rectangular tank containing water with a sinusoidal free surface elevation.

Laplace's equation is discretised for each of the twelve different neighbour arrangements possible in quadtree grids plus additional configurations at rigid boundaries. Additionally, for certain cells near the surface it is necessary to use surface markers in the discretisation of equation (1). As the markers are allowed to move arbitrarily during the solution, a general discretisation method is required for these cells. This is achieved using the method of unknown coefficients as detailed in Fletcher (1988).

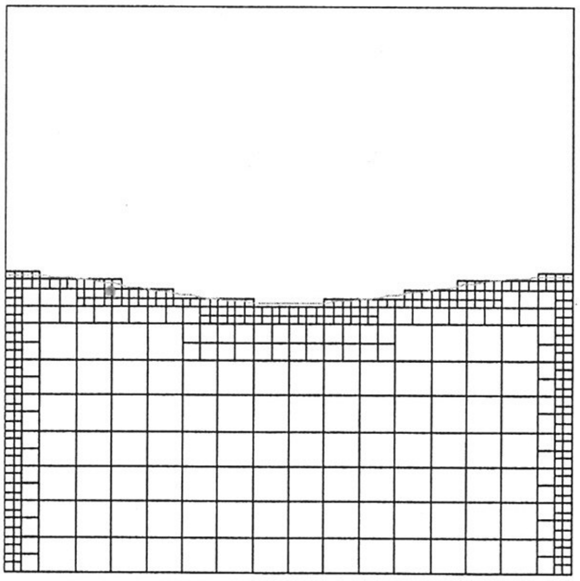

Figure 1. Quadtree grid

4. FREE SURFACE VELOCITY CALCULATION

Preliminary attempts to model the motion of quasi-linear and non-linear waves show that the accuracy of this method is strongly dependent on the method employed for calculating velocities at the free surface, in particular the vertical velocity, v. Several techniques were attempted as described in the following.

4.1 CALCULATION OF v AT CONSTANT x

This technique, presented by Turnbull (1999), requires that the surface markers be kept at known values of x throughout the solution. After each time step, once the surface marker positions and potential values have been updated, the markers are returned to their original x values and new values of y and ϕ are assigned using linear interpolation on the updated solution. This ensures that each surface marker will have a grid node vertically beneath it with the same x co-ordinate. For example, in Figure 2 surface marker, SM_1, has the same x co-ordinate as node, N_1, and surface marker, SM_2, has the same x co-ordinate as node, N_2. This allows a first-order approximation to v to be available from the nodal value of ϕ_N, using

$$v = \frac{\partial\phi}{\partial y} \approx \frac{\phi_{SM} - \phi_N}{y_{SM} - y_N}. \tag{8}$$

The technique can be extended by imposing conditions on the grid generation algorithm to enforce that a second grid node lies underneath the marker, allowing for the use of a second-order accurate approximation.

4.2 LEAST-SQUARES APPROXIMATION

An alternative method of calculating velocities at the surface, also discussed by Turnbull (1999) consists of using a least squares approximation to velocities u and v from the neighbouring nodal values of ϕ. This is

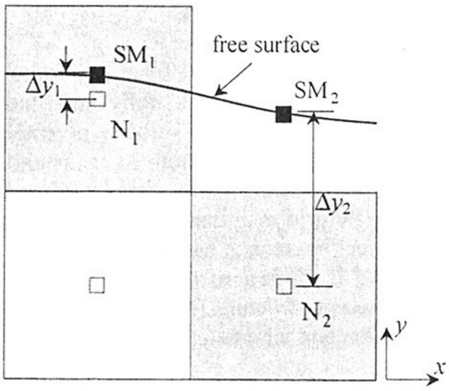

Figure 2: Velocity calculation at constant x. Surface markers, SM_i, and grid nodes, N_i.

achieved by minimising the expression,

$$\sum_{i=1}^{I}\left(u l_x^i + v l_y^i - \frac{\partial \phi}{\partial l^i}\right)^2 \qquad (9)$$

where l^i is the position vector of neighbouring node i with respect to the surface marker, the x and y subscripts denote the horizontal and vertical components of l^i, and I is the total number of nodes used in the approximation.

4.3 NORMAL AND TANGENTIAL VELOCITY CALCULATION

The techniques described above both suffer from severe inaccuracy under certain configurations of the free surface and underlying quadtree grid. This occurs when there is a marked difference in Δy for consecutive markers, as shown in Figure 2 where $\Delta y_1 << \Delta y_2$. This causes a discontinuity in the v-velocity field at the surface and a consequent step in the surface profile once the surface is advected. The error accumulates and soon leads to the calculation breaking down.

A solution to this problem is to calculate the velocities using an approximation with a constant distance throughout the surface profile. This is achieved by first finding velocities normal and tangential to the surface. At a surface marker SM_i the tangential direction to the surface profile is estimated by using central differencing between markers SM_{i-1} and SM_{i+1}. A normal vector $\vec{n}$ is then used to locate a submerged point P, located at a distance from SM_i equal to the edge length of the smallest cells in the grid, as shown in Figure 3.

The value of the velocity potential is calculated at P by discretising equation (1) using the method of unknown coefficients with the surrounding nodal values of ϕ. Because P always lies inside a polygon formed by known values of ϕ this calculation is much less susceptible to the distances between P and each of the surrounding nodes. The normal velocity, q_n, is then estimated using a first-order differencing expression,

$$q_n \approx \frac{\phi_P - \phi_{SM_i}}{\|\vec{n}\|}, \qquad (10)$$

positive in the direction of the fluid. The tangential velocity, q_t, is calculated along the free surface using the values of ϕ at the adjacent markers. This results in the expression,

$$q_t \approx \frac{\phi_{SM_{i+1}} - \phi_{SM_{i-1}}}{\|\vec{t}\|}, \qquad (11)$$

where $\vec{t}$ is the vector connecting surface markers SM_{i-1} and SM_{i+1} used to estimate the tangent to the surface at SM_i. The u- and v-velocities are then given by,

$$\begin{aligned} u &= -q_n \cos\alpha + q_t \sin\alpha \\ v &= -q_n \sin\alpha + q_t \cos\alpha \end{aligned}. \qquad (12)$$

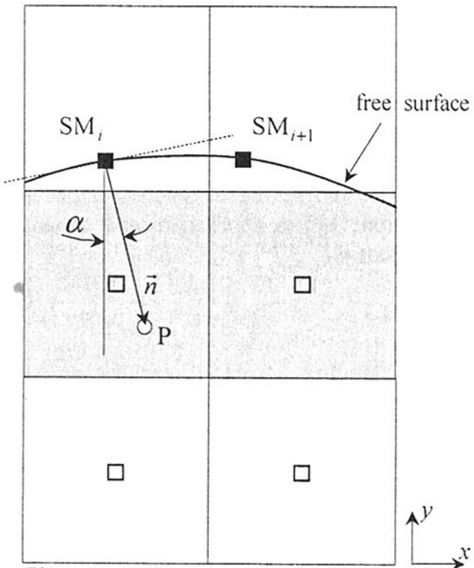

Figure 3: Calculation of normal and tangential velocities

5. MULTIGRID ITERATIONS

To improve the speed of convergence of the solver, a multigrid solving scheme is implemented. Quadtree grids are specially suited to the implementation of the multigrid strategy since all cells have already been created during the grid generation process. Using the generated quadtree as the finest grid in the multigrid cycle, the coarser grids are automatically obtained by replacing the smallest cells with their larger ancestors. As an example, the coarser grid to that of Figure 1 is shown in Figure 4. The process is repeated for each of the desired multigrid levels. It follows that there is no need to create new grid cells, as they already exist in the overall quadtree. The algorithm simply changes which of the existing grid cells are selected for computation at each multigrid level. Furthermore, the numbering system used to reference quadtree cells (see Samet (1990)) already provides a link between each of the grids and, as a result, additional storage is not required.

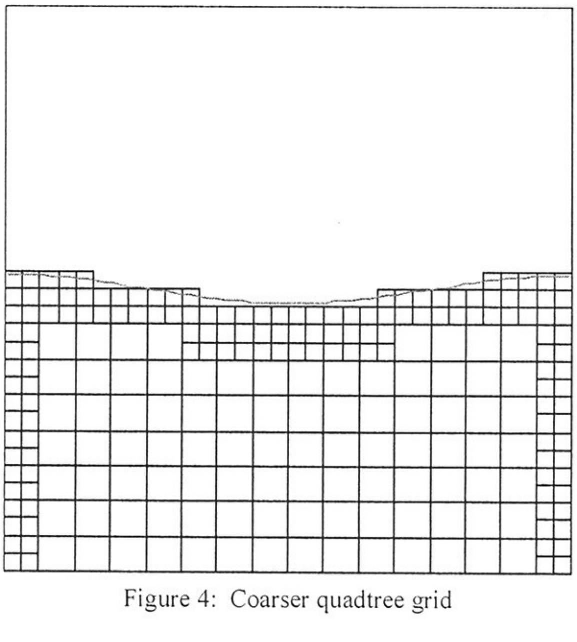

Figure 4: Coarser quadtree grid

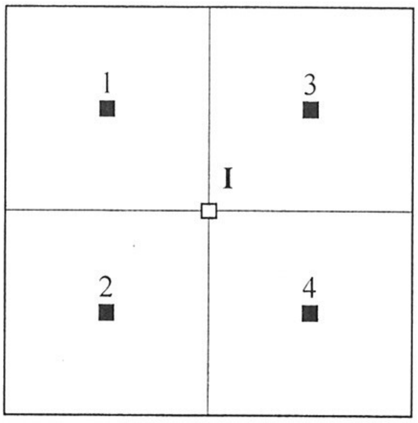

Figure 5: Solution transfer from fine (black squares) to coarse grid cell (white square)

There are two approaches to the multigrid strategy. The first involves solving the system of discretisation expressions for a number of iterations, *n*, on the coarsest grid to obtain a rough solution to f and transferring this to increasingly refined grids iterating *n* times at each grid until the finest grid is reached (ϕ correction). This provides a good initial guess and reduces the number of iterations required to reach convergence on the finest grid. The second consists of solving the residual equation on the coarser grids, to take advantage of the more oscillatory nature of the error when transferred to larger cells (error correction). The error is then prolonged to the finer grids and added to the existing solution of the potential.

The discretised version of (1) in matrix form is

$$\mathbf{A}\boldsymbol{\Phi} = \mathbf{0}, \qquad (13)$$

where $\mathbf{A}$ contains the coefficients of discretisation expressions and $\boldsymbol{\Phi}$ is the vector with the numerical solution of the velocity potential. The residual is then obtained from,

$$\boldsymbol{\rho} = \mathbf{0} - \mathbf{A}\boldsymbol{\Phi}, \qquad (14)$$

where $\boldsymbol{\rho}$ is a vector with values of the residual error at each grid node. The convergence error can then be obtained from

$$\mathbf{A}\mathbf{e} = \boldsymbol{\rho}, \qquad (15)$$

where $\mathbf{e}$ is a vector of nodal values of the convergence error.

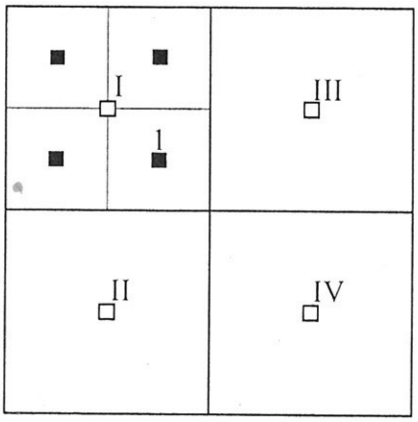

Figure 6: Solution transfer from coarse (white squares) to fine grid cells (black squares)

5.1. RESTRICTION

The residual is transferred from fine to coarse cells using the following restriction operator,

$$\rho_I = \frac{\rho_1 + \rho_2 + \rho_3 + \rho_4}{4}, \qquad (16)$$

where ρ_i are the nodal values of the residual, the roman numeral denotes the coarse cell, and Arabic digits represent the fine grid cells as illustrated in Figure 5. Equation (16) is equivalent to a bilinear interpolation of the fine grid values of the residual calculated at the centre of the coarse grid cell.

Alternative interpolation schemes are used when one or more of the fine cells contained in the coarse cell are not submerged under the free surface and hence do not hold a value of the potential at their centre nodes.

5.2. PROLONGATION

Conversely, the solution of the residual equation is transferred from coarse to finer grids using the following prolongation operator,

$$e_1 = \frac{9e_I + 3e_{II} + 3e_{III} + e_{IV}}{16}, \qquad (17)$$

where e_i are the nodal values of the convergence error, and the subscripts refer to the cell arrangement of Figure 6. The convergence error is then added to the existing solution of ϕ on the fine grid. Equation (17) is obtained by discretising Laplace's equation at node 1 for the distribution of coarse grid cells shown.

Alternative expressions are used if one or more of the surrounding coarse grid cells are not computational cells because they contain an insufficient amount of fluid.

To provide an initial guess to the solution at each time step, the multigrid strategy is used in a different way. A reduced number of iterations (usually 3) are perfect at each multigrid level starting at the coarsest grid and prolonging the coarse grid solution to the more refined grids until the top multigrid level is achieved. In this case, equation (17) is applied instead to values of the velocity potential.

6. RESULTS

Sinusoidal standing waves of varying amplitude in a square container are used to compare the numerical results with first and second order analytical predictions. The second-order analytical solution is obtained using a Stokes perturbation expansion of the velocity potential as detailed by Wu and Eatock Taylor (1994).

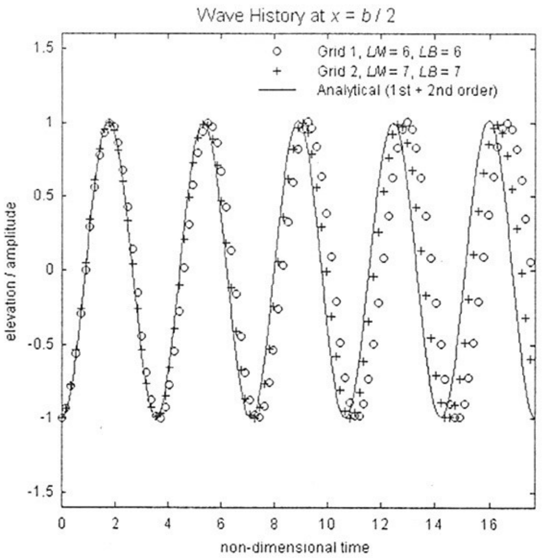

Figure 7: Grid Convergence (spatial)

Simulations are produced for a wave length, λ', equal to the unit length of the container, b'. The mean water level, h', is equal to 0.5. Results are non-dimensionalized as follows,

$$L = L'/h'$$
$$t = t'\sqrt{g'/h'} \quad , \qquad (18)$$
$$\omega = \omega'\sqrt{h'/g'}$$

where L is any length, g is the acceleration due to gravity, t is time and ω is the wave frequency. The prime denotes dimensional values.

The spatial grid convergence of the numerical scheme is investigated by simulating a wave of dimensionless amplitude $a = 0.005$ on two grids of uniform size ($LM = LB$). Grid one contains 2048 cells and grid two contains 8192 cells and the elevation history at the centre of the tank for each is illustrated in Figure 7. The theoretical wave period for this wave is $T = 3.55$; the numerical wave period calculated using grid 1, $T = 3.70$ and using grid 2, $T = 3.62$. It is clear that the numerical solution is closer to the analytical solution as the grid is refined, and so the method is grid convergent.

A finer grid would improve the accuracy of the simulation presented in Figure 7; however using a refined uniform grid is expensive in terms of grid storage and CPU time. Quadtree grids have high resolution where required combined with a low overall number of grid cells. Figure 8 shows the results obtained on a quadtree grid, $LM = 6$ and $LB = 4$ (shown in Fig. 1) which contains 602 cells, plotted together with the results obtained on the uniform grid, $LM = LB = 6$ which contains 2048 cells, for comparison. The results show excellent agreement and the calculation time on the quadtree grid is approximately half of that on the uniform grid. Thus, by using a quadtree grid, savings in computing costs are achieved whilst the same numerical accuracy is accomplished.

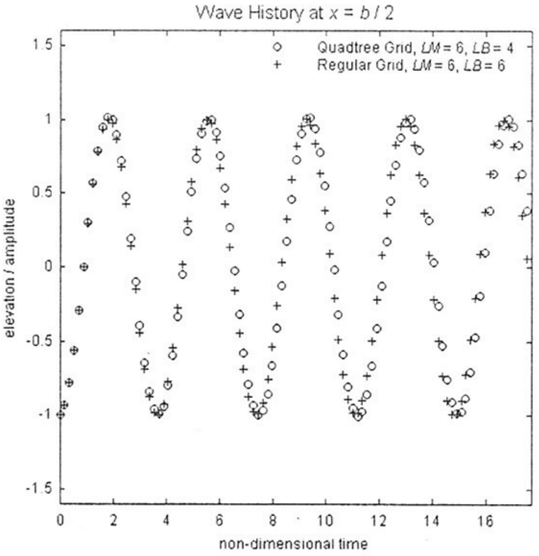

Figure 8: Comparison between quadtree and uniform grids

In Figure 9, preliminary results for a wave of moderate amplitude, $a = 0.04$, are shown. This case is investigated to test the ability of the method to model non-linear behaviour. A relatively coarse grid of $LM = LB = 5$ is used. As would be expected, the non-linear numerical solution agrees with the first plus second order analytical solution more closely than the linear analytical solution. However, a finer grid at the free surface is required to simulate the wave more accurately.

The effect of using multigrid to obtain an initial guess on the fully refined grid is illustrated by the following

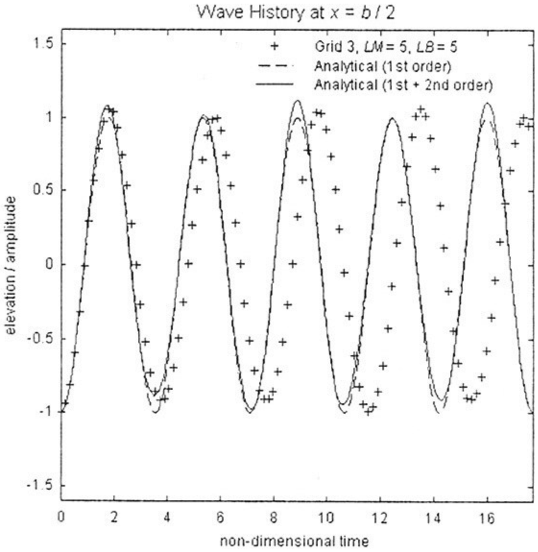

Figure 9: Elevation history of wave $a = 0.04$

values. For the quadtree solution of Figure 8 ($LM = 6$, $LB = 4$), each time step typically requires around 450 iterations and a CPU time of 3.5s on a 450MHz PC processor. The use of the multigrid method to obtain an accurate initial guess (ϕ correction), using $LM = 6$, $LB = 4$ at the top multigrid level and $LM = LB = 2$ at the bottom multigrid level reduces the number of iterations to 250 and the corresponding CPU time to 2.45s, a reduction of 30%.

7. CONCLUSIONS

In this paper, a method for the simulation of fully non-linear waves using adaptive quadtree grids has been described. A novel technique of calculating the free surface velocities and results for simulations of standing waves of small and moderate amplitudes have been presented. Preliminary values on the effect of the multigrid method in obtaining a good initial guess to the solution have been shown that quadtree grids are ideal targets for a multigrid strategy.

Planned improvements to the method also include a second-order approximation to the normal velocities at the surface and a higher order time-stepping scheme, such as the fourth order Runge-Kutta method. Work is under way to investigate the effect of applying the multigrid scheme to the residual equation and consequent error correction.

ACKNOWLEDGEMENTS

This work was carried out with the support of an EPSRC studentship grant.

References

Fletcher, C. A. J., (1988), *Computational Techniques for Fluid Dynamics – Volume I*, p. 53, Springer-Verlag, Berlin

Glimm, J., Marchesin, D., McBryan, O. (1981), A Numerical Method for Two-Phase Flow with an Unstable Interface, *J. Comp. Phys.*, **39**, 179-201

Hirt, C. W.; Nichols, B. D. (1981), Volume of Fluid (VOF) Method for the Dynamics of Free Boundaries, *J. Comp. Phys.*, **39**, 201-225

Osher, S.; Sethian, J. A. (1988), Fronts Propagating with Curvature-Dependent Speed Algorithms Based on Hamilton-Jacobi Formulations, *J. Comp. Phys.*, **79**, 12-49

Samet, H. (1990), *The Design and Analysis of Spatial Data Structures*, Addison-Wesley, New York

Turnbull, M. S., (1999), The Numerical Modelling of Steep Waves Interacting with Structures, DPhil Thesis, University of Oxford

Wu, G. X., Eatock Taylor, R. (1994) Finite Element Analysis of Two-dimensional Non-linear Transient Water Waves, *Applied Ocean Res.*, **16**, 363-372

Yang, G.; Causon, D. M.; Ingram, D. M. (2000) Calculation of Compressible Flows About Complex Moving Geometries Using a Three-Dimensional Cartesian Cut Cell Method, *Int. J. Numer. Methods Fluids*, **33**, 1121-1151

Yiu, K. F. C.; Greaves, D. M.; Cruz, S.; Saalehi, A.; Borthwick, A. G. L. (1996), Quadtree Grid Generation: Information Handling, Boundary Fitting and CFD Applications, *Computers & Fluids*, **25**, 8, 759-769

Investigation of Two-Dimensional Transom Waves Using Inviscid and Viscous Free-Surface Boundary Conditions at Model- and Full-Scale Ship Reynolds Numbers

Juha Schweighofer[1]

Ship Laboratory, Helsinki University of Technology, Espoo, Finland

1 Introduction

A ship moving in water always creates a wave system. When computing such a wave system, the kinematic and the dynamic boundary conditions are applied on the free surface. Usually, several simplifications are introduced in viscous flow simulations leading to the same free-surface boundary conditions as for potential flow. However, there is vorticity at the free surface, *Choi and Stern (1993), Dabiri and Gharib (1997), Longuet-Higgins (1997), Lundgren and Koumoutsakos (1999), Ohkusu (1996).* In consequence, the velocity gradients are non-zero. Also, the pressure is non-zero due to the viscous terms appearing in the dynamic boundary condition in the normal direction to the free surface. The error associated with the application of the inviscid free-surface boundary conditions may be unacceptable, *Stern et al. (1996).* The application of the physically correct viscous free-surface boundary conditions seems to be desirable. Even for identical analytical formulation of the free-surface boundary conditions, computed wave profiles differ depending on the numerical scheme used. Publications usually give the analytical formulation, but unfortunately often not the numerical scheme employed.

Detached transom flows over a large range of Reynolds numbers up to full scale have not been treated so far using the viscous free-surface boundary conditions including the influence of turbulence. Most ships have a transom, and the stern induced resistance is significant, *Saisto (2000). Vanden-Broek (1980)* and *Saisto (1995,2000)* investigated 2-d detached transom flows as potential flow past a semi-infinite flat-bottomed body. Respective viscous flow evaluations are given in *Tahara and Iwasaki (1998), Funeno and Yamano (2001)* and *Yamano et al. (2000,2001).* In transom flows, the boundary layer of the hull is convected into the transom waves. There, the velocity gradients and vorticity become stronger compared with the case where the boundary layer is not existing. Therefore, the application of the viscous free-surface boundary conditions seems to be appropriate in such cases.

The investigation is performed in two dimensions to keep CPU times reasonably short. This simplifies the problem, allowing to evaluate the pure influence of the free-surface boundary conditions on the computed transom waves. The conclusions should be valid also for three dimensions. A more detailed description of the investigation is given in *Schweighofer (2001a,2001b).*

2 Numerical Method

The computations used the RANSE solver FINFLO. The Reynolds-averaged Navier-Stokes (RANS) equations are iteratively solved by a cell-centered finite-volume method until the steady state is reached. Incompressibility of the flow is considered by an artificial compressibility approach. An

---

[1] Correspondence to: Ship Laboratory, Helsinki University of Technology, Otakaari 4, FIN 02015 Espoo, Finland, e-mail: juhaschw@nefer.hut.fi, phone: +358 9 451 3503, fax: +358 9 451 4173

upwind-type spatial discretization of third-order accuracy without flux limitation is applied to the approximation of the convective terms. Incompressible flux-difference splitting is used as flux-splitting method. The viscous fluxes are evaluated according to a thin-layer approximation which is activated in all coordinate directions. Here, the central differencing scheme is used for the calculation of the velocities at the cell surfaces. The solution of the discretized equations is obtained using a diagonally dominant alternating direction implicit (DDADI) time integration method with time stepping adjusted depending on a parameter based on local velocities and cell sizes. Chien's low-Reynolds number k-ϵ turbulence model is applied. No wall functions are used. The boundary layer is resolved till the wall. The free surface is evaluated by a moving-grid technique.

2.1 Free Surface

The kinematic boundary condition is given by

$$\frac{d\beta}{dt} = w = \frac{\partial \beta}{\partial t} + u\frac{\partial \beta}{\partial x} + v\frac{\partial \beta}{\partial y} \ . \tag{1}$$

$\beta(x, y, t)$ is the local wave elevation. u, v and w are the components of the velocity vector $\vec{V}$ in the x-, y- and z-directions of a right-handed Cartesian coordinate system, respectively. The z-axis is directed upwards from the free surface. t is the time. The kinematic boundary condition does not contain any approximations. Integration of Eq. (1) with respect to time gives the shape of the free surface. Having reached the steady state, $\partial\beta/\partial t$ will be zero.

The dynamic boundary condition states that the normal and tangential stresses must be equal on both sides of the free surface. Neglecting surface tension and shear stresses of the air, the dynamic boundary condition in tensor notation is, *Ferziger and Perić (1999)*:

$$(T_{ij}n_j)n_i = 0, \quad (T_{ij}n_j)t_i = 0, \qquad T_{ij} = -p\delta_{ij} + \mu\left(\frac{\partial u_i}{\partial x_j} + \frac{\partial u_j}{\partial x_i}\right) - \rho\overline{u_i^{'}u_j^{'}} \ . \tag{2}$$

T_{ij} is the stress tensor, $\vec{n} = (n_1, n_2, n_3)^T$ the outward unit normal vector on the free surface, $\vec{t} = (t_1, t_2, t_3)^T$ is the unit tangential vector on the free surface, p the pressure, and μ is the molecular viscosity. δ_{ij} the Kronecker symbol. Using the Boussinesq approximation, *Anderson et al. (1984)*, the Reynolds stresses are:

$$-\rho\overline{u_i^{'}u_j^{'}} = \mu_T\left(\frac{\partial u_i}{\partial x_j} + \frac{\partial u_j}{\partial x_i}\right) - \frac{2}{3}\rho k\delta_{ij} \ . \tag{3}$$

μ_T is the turbulent viscosity, derived from Chien's low-Reynolds number k-ϵ turbulence model. ρ is the density, k the turbulent kinetic energy, and ϵ its dissipation rate. Eq. (3) applied to Eq. (2) yields

$$T_{ij} = -p\delta_{ij} + (\mu + \mu_T)\left(\frac{\partial u_i}{\partial x_j} + \frac{\partial u_j}{\partial x_i}\right) - \frac{2}{3}\rho k\delta_{ij} \ . \tag{4}$$

2.1.1 Inviscid Free-Surface Boundary Conditions

For inviscid flow, the molecular viscosity μ and the Reynolds stresses vanish. The dynamic boundary condition becomes simply

$$p = p_{air} = 0, \quad \psi = \rho g\beta \ . \tag{5}$$

ψ is the corresponding piezometric pressure, and $g = 9.81\ \text{m/s}^2$. For the calculation of the velocities on the free surface and in the ghost cells, a zero-gradient condition is applied

$$\frac{\partial u}{\partial n} = \frac{\partial v}{\partial n} = \frac{\partial w}{\partial n} = 0 \ . \tag{6}$$

For viscous flow, it is common to use the same free-surface boundary conditions as for inviscid flow. Additional conditions for the turbulence quantities must be introduced:

$$\frac{\partial k}{\partial n} = \frac{\partial \varepsilon}{\partial n} = 0 \ . \tag{7}$$

Eqs. (1), (5) to (7) are the "inviscid free-surface boundary conditions".

2.1.2 Viscous Free-Surface Boundary Conditions

The investigation described in this work is carried out for a 2-d case, Fig.1. All quantities in y vanish. The kinematic boundary condition is given by Eq. (1). On the free surface, the flat-surface approximation is applied.

The tangential-stress free-surface boundary conditions are obtained from Eqs. (2), and (4) with tangential stresses set to zero:

$$\frac{\partial u}{\partial z} = -\frac{\partial w}{\partial x} \ . \tag{8}$$

The continuity equation yields

$$\frac{\partial w}{\partial z} = -\frac{\partial u}{\partial x} \ . \tag{9}$$

The pressure p and the piezometric pressure ψ are obtained from Eq. (5). Eq. (7) is applied to the turbulence quantities. Eqs. (1), (5), (7) to (9) are the "tangential-stress free-surface boundary conditions".

The Reynolds-stress free-surface boundary conditions are obtained from Eqs. (2) and (4). The tangential and normal stresses are set to zero. The velocity derivatives in z-direction are calculated from Eqs. (8) and (9). The pressure on the free surface is not equal to zero anymore. It contains a contribution resulting from the molecular viscosity and the Reynolds stresses. The order of magnitude of the appearing Reynolds numbers is 10^6 and 10^9. Therefore, the influence of the molecular viscosity in the dynamic boundary condition is negligible, yielding:

$$p = 2\mu_T \frac{\partial w}{\partial z} - \frac{2}{3}\rho k = -2\mu_T \frac{\partial u}{\partial x} - \frac{2}{3}\rho k \ , \qquad \psi = p + \rho g \beta = -2\mu_T \frac{\partial u}{\partial x} - \frac{2}{3}\rho k + \rho g \beta \ . \tag{10}$$

Eqs. (1), (7) to (10) are the "Reynolds-stress free-surface boundary conditions".

2.1.3 Alternative Inviscid Free-Surface Boundary Conditions

Appart from the inviscid mirror free-surface boundary conditions, three alternative approaches regarding the inviscid free-surface boundary conditions were implemented and investigated.

For irrotational flow, the vorticity vector $\vec{\gamma}$ is zero giving

$$\vec{\gamma} = \nabla \times \vec{V} = \vec{0} \quad \Rightarrow \quad \frac{\partial u}{\partial z} = \frac{\partial w}{\partial x} \ . \tag{11}$$

∇ is the nabla operator.

In this work, Eqs. (1), (5), (7), (9), and (11) are the "inviscid irrotational free-surface boundary conditions".

Using a flat free-surface approximation and the assumption that the normal and tangential gradients of the normal velocity are negligible, the inviscid flat free-surface boundary conditions are obtained, *Choi and Stern (1993)*:

$$\frac{\partial u}{\partial z} = \frac{\partial w}{\partial z} = 0 \ . \tag{12}$$

Eqs. (1), (5), (7), and (12) are the "inviscid flat free-surface boundary conditions".

Taking the continuity equation into consideration, a physically more correct relation for the inviscid flat free-surface boundary conditions may be obtained, *Stern et al. (1996)*:

$$\frac{\partial u}{\partial z} = 0 \ , \qquad \frac{\partial w}{\partial z} = -\frac{\partial u}{\partial x} \ . \tag{13}$$

Eqs. (1), (5), (7) and (13) are the "inviscid flat-continuity free-surface boundary conditions".

2.1.4 Realization of the Dynamic Free-Surface Boundary Conditions

In the two ghost-cell rows, the pressure is obtained by a linear extrapolation of the respective values on the free surface and the ones of the first cell row below the free surface. The flow quantities in the ghost cells are needed for the bulk-flow solution.

Similar to the realization of Eq. (7), using the inviscid mirror free-surface boundary conditions, the velocities on the free surface are obtained by a second-order extrapolation setting the velocity gradients to zero. The velocities in the two ghost-cell rows are equal to the ones of the first two cell rows below the free surface, respectively.

In all other cases, a liner extrapolation is applied to the evaluation of the velocities on the free-surface and in the ghost cells using the respective values of the first cell row below the free surface.

In the cases where the velocity gradients in the z-direction are calculated from the ones in the x-direction, the gradients in the x-direction are calculated from the velocities in the cell centres of the first cell row below the free surface using a two-point upwind scheme of first-order accuracy.

3 Computations

The model is assumed to be infinitely wide in the y-direction (Fig. 1). The shape of the bow is a circle segment with radius R and the bottom is flat. The transom is located at the origin of the global Cartesian coordinate system. At the bow, the formation of the bow wave is suppressed. At the transom, the wave height of the free surface is set equal to the draught T. Behind the transom, the free surface may be deformed arbitrarily. The geometrical dimensions of the investigated model are length overall $L = 2.000$ m, length between perpendiculars $L_{pp} = 1.529$ m, $R = 1.450$ m, $T = 0.100$ m. The geometrical dimensions are scaled to full scale using the scaling 40.

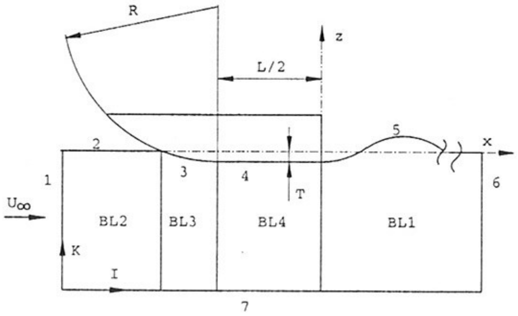

Fig.1: Computed case, subdivision of domain.

The computations are carried out at $F_{nT} = U_\infty/(\sqrt{gT}) = 2.1$, 2.2, 2.3 and 2.8. The Reynolds numbers, $R_n = U_\infty \cdot L_{pp}/\nu_\infty$ are 2.8×10^6, 2.933×10^6, 3.066×10^6 and 3.732×10^6, respectively. The full scale computations are carried out for $F_{nT} = 2.8$ and $R_n = 9.442 \times 10^8$. U_∞ is the free stream velocity, and ν_∞ is the free-stream kinematic viscosity.

At model scale, the grid consists of four blocks, Fig.1. The blocks are composed of $64 \cdot 64$, $48 \cdot 64$, $48 \cdot 64$ and $384 \cdot 64$ cells. Side 1 is located 20 m upstream from the origin. The grid height from the still water level is $5L = 10$ m. The expected wave length is about $2.5L$. Side 6 is located at 40 m downstream from the origin. The waves are resolved by at least 45 equally distributed cells per wave length. The resolution of the boundary layer is continued in BL2 and BL1, but becomes coarser in BL1 farther downstream. The grid is very fine at the bow and at the transom. The nondimensional distance of the first node from the wall remains always $y^+ < 4$. Almost everywhere at the wall, $y^+ \approx 0.7$. The blocks are connected with matching interfaces.

At full scale, the grid and its geometrical dimensions are similar to the ones at model scale. It is composed of $64 \cdot 96$, $48 \cdot 96$, $48 \cdot 96$ and $384 \cdot 96$ cells. Almost everywhere at the wall, $y^+ \approx 2$.

At model scale, the initial values of the turbulence level and the nondimensional turbulence coefficient are set to 0.02 and 10.00 in the computational domain and to 0.001 and 0.01 at the outer boundaries (sides 1 and 6). At full scale, the same values are applied but the nondimensional turbulence coefficient is set to 16.5 at the outer boundaries. The turbulence coefficients are made nondimensional with the free-stream molecular viscosity.

Side 1 is the inflow boundary, side 6 the outflow boundary. Here the flow quantities are simply set to their free-stream values. Sides 2 and 7 are defined as symmetry planes. Sides 3 and 4 are defined as solid walls. The no-slip condition on the wall is fulfilled by setting the velocities to zero instead of the use of wall-functions. Side 5 is defined as free surface.

4 Results

In Fig. 2, the significant effect of the numerical realization of the free-surface boundary conditions on the computed transom waves is shown. The different inviscid free-surface boundary conditions give a more or less dampened wave profile. The damping is due to numerical damping and the modification of the flow field close to the free surface caused by the respective boundary conditions. The assumption of $\partial w / \partial z = 0$ should be avoided, and, instead, the continuity equation should be used. The viscous and inviscid irrotational free-surface boundary conditions give almost no difference at model and full scale. Therefore, in this case, the influence of the turbulence on the free surface through the dynamic free-surface boundary conditions may be neglected at model and full scale, although the turbulent viscosity and the velocity gradients are very high close to the transom at full scale. At model scale, the application of the Boussinesq approximation to the free-surface boundary conditions gives a correct result with respect to the wave profile.

In Fig. 3, with decreasing Froude numbers and Reynolds numbers, the waves become steeper and the curvature is increased. Their shape approaches the one of an overturning wave for the lower Froude numbers. With decreasing Froude numbers, the viscosity effects are increased and, at the lower ones, it makes already a difference whether the inviscid or viscous free-surface boundary conditions are applied, although the Reynolds numbers are still rather high (about 3×10^6).

References

ANDERSON, D.A., TANNEHILL, J.C., PLETCHER, R.H. 1984. Computational Fluid Dynamics and Heat Transfer, Hemisphere Publishing Corporation, McGraw-Hill Book Company.

CHOI, J.E. AND STERN, F. 1993. Solid-Fluid Juncture Boundary Layer and Wake with Waves, *Proceedings of the 6th International Conference on Numerical Ship Hydrodynamics*, Iowa City, Iowa.

DABIRI, D. AND GHARIB, M. 1997. Generation Mechanisms and Sources of Vorticity Within a Spilling Breaking Wave, *21st Symposium on Naval Hydrodynamics*, pp. 520-533.

FERZIGER, J.H. AND PERIĆ, M. 1999. Computational Methods for Fluid Dynamics, Second Edition, Springer-Verlag, Berlin, Heidelberg.

FUNENO, I. AND YAMANO, T. 2001. On Free Surface Flows behind a Two-Dimensional Transom Stern, Journal of the Kansai Society of Naval Architects of Japan, No. 235, pp. 23-30.

LONGUET-HIGGINS, M.S. 1997. Progress Toward Understanding How Waves Break, *21st Symposium on Naval Hydrodynamics*, pp. 7-28.

LUNDGREN, T. AND KOUMOUTSAKOS, P. 1999. On the Generation of Vorticity at a Free Surface, *J. of Fluid Mech.*, Volume 382, pp. 351-366.

OHKUSU, M. 1996. Advances in Marine Hydrodynamics, Computational Mechanics Publications, Southampton, Boston, pp. 59.

SAISTO, I. 1995. Laivan perän muodostaman aallon laskenta kaksidimensioisella reunaelementtimenetelmällä, Report M-193, Ship Laboratory, Helsinki University of Technology.

SAISTO, I. 2000. Computation of two-dimensional stern wave using the boundary element method, Licentiate Thesis, Department of Mechanical Engineering, Helsinki University of Technology.

SCHWEIGHOFER, J. 2001a. Computations of Two-Dimensional Transom Waves Using Inviscid and Viscous Free-Surface Boundary Conditions, Report M-258, Ship Laboratory, Helsinki University of Technology.

SCHWEIGHOFER, J. 2001b. Computations of Two-Dimensional Transom Waves Using Inviscid and Viscous Free-Surface Boundary Conditions, Ship Technology Research - Schiffstechnik, Vol. 48, No. 2, pp. 68-78.

STERN, F., PATERSON, E.G. AND TAHARA, Y. 1996. CFDSHIP-IOWA: Computational Fluid Dynamics Method for Surface-Ship Boundary Layers, Wakes and Wave Fields, IIHR Report 381, Iowa Institute of Hydraulic Research, College of Engineering, The University of Iowa, pp. 11.

TAHARA, Y. AND IWASAKI, Y. 1998. A Study of Transom-Stern Free-Surface Flows by 2-D Computational and Experimental models, New Ship & Marine Technology into the 21st Century, Conference Proceedings, Osaka Prefecture University, Japan, pp. 83-92.

VANDEN-BROECK, J.-M. 1980. Nonlinear Stern Waves, *J. Fluid. Mech.*, part 3, pp. 603-611.

YAMANO, T., IKEBUCHI, T. AND FUNENO, I. 2000. On Forward-Oriented Wave Breaking just behind a Transom Stern, Journal of the Society of Naval Architects of Japan, Nr. 187, pp. 25-32.

YAMANO, T., IKEBUCHI, T. AND FUNENO, I. 2001. Stern Waves consisting of Forward-Oriented Breaking Waves and the Remaining Following Waves, Journal of Marine Science and Technology, Nr. 6, pp. 13-22.

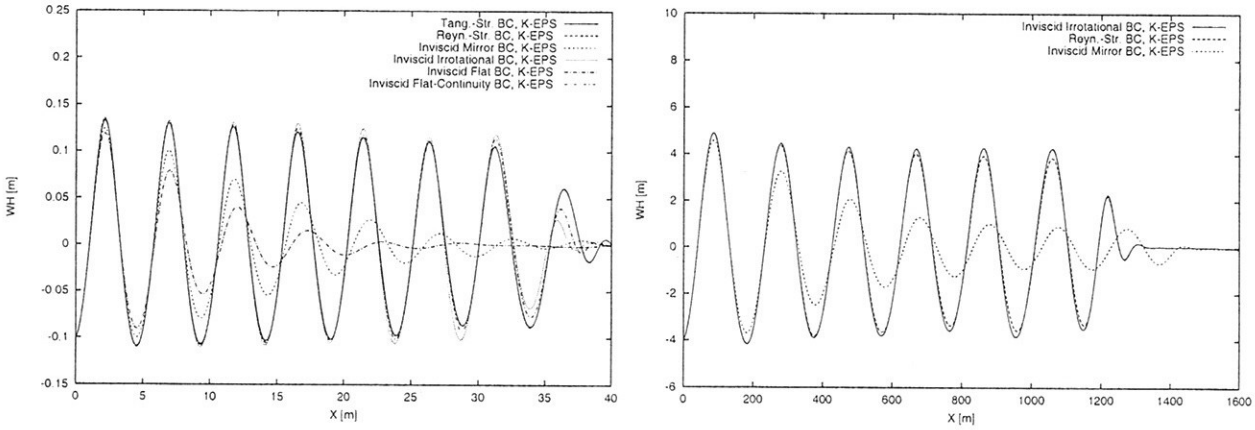

Fig.2: Computed wave profiles behind the transom. $F_{nT} = 2.8$. **Left:** $R_n = 3.732 \times 10^6$. **Right:** $R_n = 9.442 \times 10^8$.

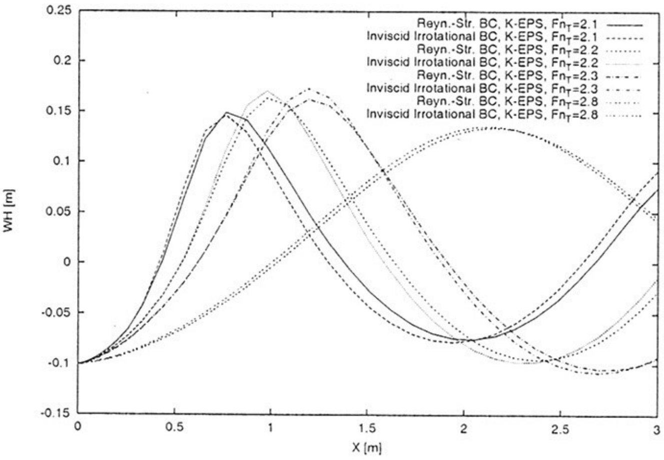

Fig.3: Computed wave profiles behind the transom. Model scale. F_{nT}= 2.1, 2.2, 2.3 and 2.8.

Study of three RANS body force propeller models

Claus D. Simonsen, John Cross-Whiter
FORCE/DMI, cds@force.dk

Introduction

When RANS is used to study rudder, propeller and hull interaction in connection with manoeuvring it is important to use a propeller model which both gives the right amount of suction on the hull upstream of the propeller and the right velocity distribution over the rudder located downstream of the propeller. The most complex model includes the propeller geometry directly in the RANS model. This model of course gives very detailed information about the flow, but it also complicates the grid generation considerably and increases the size of the model and the computational time. For some applications it is not required to get the detailed information about the flow over the propeller itself, so a more simple approach is to replace the real propeller by a body force field that reflects the time-averaged influence of the propeller on the flow field in the propeller region. However, in order for the method to work it is essential to use a body force distribution which reflects the local loading on the propeller and therefore gives a good description of the flow field upstream and downstream of the propeller. Several methods with different levels of complexity can be used, but the more details that are required the more effort needs to be put into model. The methods range from simple prescribed models to lifting line type models, to panel models in which the propeller is represented by its real geometry. The first type of method works on the nominal wake field, whereas the other two take the effective wake field into account, by running interactively with the RANS solver.

Depending on the type of applied propeller model the involved work will vary, so it is important to know how each model performs in order to select an appropriate model for the flow problem. The present paper focuses on a comparison between three different body force propeller models to gain knowledge about their performance. The present study is carried out for the Series 60 ship without any appendages.

Numerical method

The computations are performed with the Reynolds Averaged Navier-Stokes (RANS) solver CFDSHIP-IOWA developed at IIHR, [1]. The code solves the RANS equations on a regular grid by means of finite differencing. For the steady state calculations performed in this context the temporal discretization is based on a first order backward Euler difference. The spatial discretization is performed by a second order upwind scheme for the convective terms, while all other first derivatives and viscous terms are discretized by a standard second order central difference scheme. The pressure and the velocities are coupled by means of the PISO method. Closure of the Reynolds stress problem is achieved by means of the one-equation Baldwin Lomax turbulence model, which does not apply wall functions. The propeller effect is implemented in the CFD-code by additional body force terms included in the source terms of the momentum equations.

Three different propeller models are considered. The first model is based on a radial varying body force field, which follows the variation of a theoretically derived circulation, [2]. It is prescribed by means of the ship speed based advance coefficient J_V and the propeller coefficients C_{Th} and K_Q. The model is integrated in the CFD-code, where the axial and tangential force components are given by

$$fb_X = A_X r^* \sqrt{1-r^*} \quad , \quad fb_\theta = A_\theta \frac{r^* \sqrt{1-r^*}}{(1-r_h)r^* + r_h} \tag{1}$$

Here the non-dimensional propeller and hub radii are defined by $r^* = (r - r_h)/(1 - r_h)$ and $r_h = R_h / R_p$. Finally, with Δxbeing the longitudinal extension of the disk divided by the ship length, the coefficients A_x and A_θ are defined by

$$A_x = \frac{C_{Th}}{\Delta x} \frac{105}{16(4+3r_h)(1-r_h)} \tag{2}$$

$$A_\theta = \frac{K_Q}{\Delta x J_V^2} \frac{105}{\pi(4+3r_h)(1-r_h)} \tag{3}$$

The second model is suggested by Yamasaki [3] and has later been used for potential based rudder-propeller-hull calculations in [4]. The method, referred to as the simplified propeller model, represents the propeller by a thin disk, in which the finite number of propeller blades is neglected. It is based on a potential theory formulation, in which the propeller is represented by bound vortex sheets on the propeller disk and free vortices shed from them downstream of the propeller. Unlike the first model this model calculates the body forces based on the effective wake field, which means that the propeller solver, which is implemented in the CFD-code, is run interactively with the RANS solver. The body forces are calculated from

$$fb_x = \frac{A}{\Delta x}\Big[\ \rho V\Gamma(r,\theta)\,V_\theta(r,\theta) - \frac{1}{4\pi}C_{PD}Nc(r)\sqrt{1+(h/r)^2}\,V_{0x}(r)V_{0\theta}(r)\ \Big] \tag{4}$$

$$fb_\theta = \frac{A}{\Delta x}\Big[\ \rho V\Gamma(r,\theta)\,Vx(r,\theta) - \frac{1}{4\pi}C_{PD}Nc(r)\sqrt{1+(h/r)^2}\,V_{0\theta}^2(r)\ \Big] \tag{5}$$

where ρ, V, C_{PD}, N and $c(r)$ are water density, ship speed, blade section drag coefficient, number of propeller blades and radial cord length distribution, respectively. The constant A is used for bringing the forces into CFD-code format

$$A = \frac{1}{1/2\,\rho V^2 R_P\,(1-r_h)} \tag{6}$$

$V_x(r,\theta)$ and $V_\theta(r,\theta)$ are the axial and tangential propeller inflow velocities, respectively, and $V_{0x}(r)$ and $V_{0\theta}(r)$ are the axial and tangential circumferentially averaged inflow velocities. All 4 velocity components are total velocities interpolated from the RANS solution, so before using them for the propeller solution, the propeller induced velocities are subtracted. Γ is the strength of the vortices on the disk and h is the effective propeller pitch, which is defined by

$$h = \frac{1}{2}\left[a(r) + \frac{r\int_0^{2\pi} V_x(r,\theta)\,d\theta}{\int_0^{2\pi}\big(\Omega r + V_\theta(r,\theta)\big)d\theta}\right] \tag{7}$$

where Ω is the angular velocity and $2\pi\, a(r)$ is the effective pitch ratio.

$$\left[\left\{\frac{2\sqrt{r^2+a(r)}}{k_1 rNc(r)} + \frac{r^2+h^2}{2hr^2\kappa(r,h)}\right\}V(r,\theta) + (u_p - \frac{h}{r}v_{\theta P}) + (V_x(r,\theta) - \Omega a(r) - \frac{a(r)}{r}V_\theta(r,\theta)\right]_{(SP)} = 0 \tag{8}$$

The vortex strength Γ is found from (8), which can be solved for $\Gamma(r,\theta)$ when the propeller inflow field and the number of propeller revolutions are known. Finally, $\kappa(r,h)$ represents Prandtl's tip correction factor and k_1 is a correction for the finite width of the propeller blade. Both factors are defined in [4].

Finally, the third propeller model is based upon the external propeller code ProPulse. This is an unsteady, potential-based surface panel code, similar to that described in [5]. The surface of the key blade on the propeller is represented by quadrilateral panels. At each time step, the potential at each panel i is given by the solution of the linear system:

$$\sum_{j=1}^{M\cdot N} a_{i,j}\phi_j = \sum_{k=1}^{Z}\ \sum_{j=1}^{M\cdot N} b_{i,j,k}\sigma_{j,k} - \sum_{k=2}^{Z}\ \sum_{j=1}^{M\cdot N} a_{i,j,k}\phi_{j,k} - \sum_{k=1}^{Z}\ \sum_{m=1}^{M}\ \sum_{l=1}^{Nw} W_{i,m,l,k}\Delta\phi_{m,l,k} \tag{9}$$

where Z is the number of blades, M and N are the spanwise and chordwise number of panels on the blade, respectively, N_w is the chordwise number of panels in the trailing wake, a is the panel-panel dipole influence function, b is the panel-panel source influence function, W is the wake-panel dipole influence function, ϕ is the local potential and σ is the local source strength.

The local source strength σ is dictated by the local onset velocity, which is derived from the input axial, radial and tangential harmonic wake components.

The potential and source strengths are assumed to be constant over each panel, but the panels are not assumed to be flat. The near-field dipole and source potential influence functions are given by the hyperboloid panel functions detailed in [5]. The far-field influence functions are given by point singularity influence functions. The wake is assumed to have constant geometry, with $\Delta\phi$ given either by the Kutta condition at the current time step or the circulation at previous time steps, as appropriate.

On the propeller blade the tangential velocities are derived from the numerical differentiation of the panel potentials in the spanwise and chordwise directions. For field points outside of the blade the velocities are derived from the analytic differentiation of the potential influence functions.

The propeller force is the summation of the unsteady inviscid pressure forces, acting normal to the panel centroids, and the viscous friction forces, acting parallel to the local flow at each panel.

To convert the panel forces into body forces for the RANS calculations, a polar disk grid is defined, with radial panel distribution given by the radial distribution of panels in the propeller blade grid, and circumferential distribution given by equal angular increments corresponding to the number of time steps in the unsteady propeller calculation. At each time step, the centroid of each blade panel is located in a unique $\Delta r\Delta\theta$ sector at $\theta(t)$, to which the total force vector on that panel is assigned. The sector forces are then time averaged, divided by the sector volumes $\Delta r \Delta \theta \Delta x$ and interpolated onto the RANS cell locations to derive the body forces.

The propeller-induced velocities are computed at field points on a polar grid, with equal angular increments and radial distribution given by the radial distribution of control points on the propeller blade grid to minimize the singular influence at panel edges. These velocities are then interpolated onto the RANS cell locations.

The procedures for running the models are as follows. First a converged solution is calculated for the hull alone and then the propeller is turned on. If the prescribed model is used, the solver is run to convergence and the resulting solution is the with-propeller solution. If one of the two interactive models are used, wake information is extracted from the RANS solution and the propeller model is used to calculate the body forces. The body forces are then applied to the RANS model, which again is run, until a converged solution has been obtained. Then a new set of wake data is extracted and the procedure is repeated once more. When the propeller coefficients show convergence the calculation is stopped and the with-propeller solution is found.

Ship condition and computational grids

The study is carried out for a 4.0 m model of the Series 60 ship without any appendages. The model speed is 1.0 m/s, which corresponds to a Froude number equal to 0.16 and a model Reynolds number equal to Re=3.96 million. However, since the free surface is neglected, the Froude number is set to zero and a mirror image is applied instead of the free surface. Ship and propeller data can be seen in Table (1) and more data can be found in [6]. Concerning the grid, the computations are performed with a block-structured O-H grid consisting of approximately 0.64 million points including both sides of the ship. The grid is shown in Figure (1). Finally, since no wall functions are applied, the near wall spacing of the grid on the no-slip hull surface satisfies $y^+ \approx 1$. Concerning verification and validation it will not be carried out in this context, since the study only is based on a qualitative comparison. Though, in [7] it is shown that systematic grid refinement with the present grid results in grid convergence.

Model		Propeller	
L_{pp} [m]	4.0	R_p [m]	0.14564
B [m]	0.5333	R_h [%R$_p$]	0.2
T [m]	0.2133	N [blades]	5
S [m^2]	2.7189	n [rps]	7.8
C_b [-]	0.6	Δx [m]	0.03

Table (1). *Hull and propeller data.*

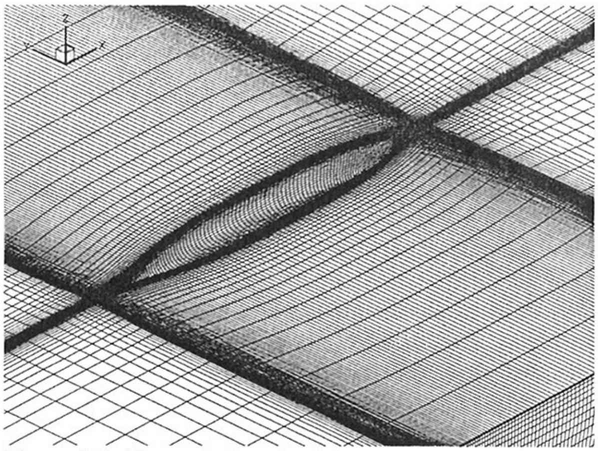

Figure (1). *Computational grid.*

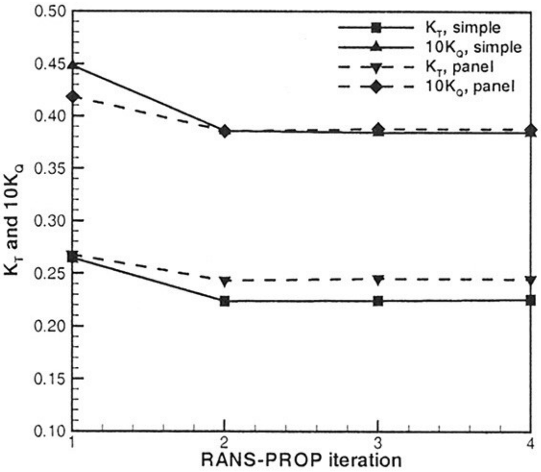

Figure (2). *Convergence history of propeller solution.*

Convergence history

Since two of the propeller models work based on the effective wake field, it is necessary to find the solution by means of an iterative procedure, as described above. Figure (2) shows the convergence history of the two interactive solutions. For both propeller models it is seen that both thrust and torque converge. It appears that K_T and K_Q decrease between the nominal wake solution (iteration 1) and the first effective wake solution (iteration 2) and that convergence is obtained relatively quickly during the next one or two iterations. According to [8] the decrease in thrust and torque is explained by the fact that the propeller works harder in the undisturbed nominal wake field than in the effective wake field, where the magnitude of the inflow velocities are higher.

Results for propeller quantities

The propeller quantities calculated with the three propeller models are shown in Table (2) together with experimental data from [6]. It should be noted that it has not been attempted to estimate the self-propulsion point of the model, but rather to calculate the propeller characteristics for fixed propeller settings that are equivalent to the settings used in the experiment. From the table it is seen that K_T and K_Q from the prescribed model match the experimental values. However, this will always be the case since the model is based on the two quantities. For the two interactive methods the agreement between calculation and experiment is fair. The simplified method predicts the thrust within 3.4% of the measured value, while the torque is predicted within 6.6%. Both quantities are predicted lower than in the experiment. The panel method predicts the thrust and torque within 4.7% and 5.6% of the measured values, respectively. The thrust is over predicted, while the torque is under predicted.

Two other quantities that are relevant to consider in connection with the hull-propeller configuration are the wake fraction, w and the thrust deduction factor, t defined by

$$(1-w)=\frac{J_a}{J_V} \qquad (1-t)=\frac{X_{wo}}{X_w} \tag{10}$$

where J_a and J_V are the advance coefficients based on advance and ship speeds, respectively. X_{wo} and X_w are the ship resistance for the without and with propeller conditions, respectively. J_a is estimated on the basis of a thrust identity on the open water curve.

	K_T	$10\,K_Q$	(1-w)	(1-t)
Exp.	0.234	0.411	0.75	0.86-0.87
Prescribed	0.234	0.411	---	0.865
Simplified	0.226	0.384	0.760	0.869
Panel	0.245	0.388	0.717	0.860

Table (2). *Measured and calculated propeller quantities.*

Concerning (1-w) the results in Table (2) show that the agreement between experiment and calculation is fair for both interactive models. The simplified model seems to over predict (1-w), but this is expected since the thrust is under predicted. The panel method under predicts (1-w), which is in agreement with fact that the loading is over predicted. With respect to the thrust deduction, (1-t), the agreement for all three models seems good when the results are compared with the experiment. This indicates, that all models do give the right amount of suction on the hull upstream of the propeller.

Results for flow field

Ship rudders are usually located in the slipstream of the propeller, so it is important to predict the right flow features downstream of the propeller when calculating rudder forces. Therefore, to investigate the quality of the computed flow field in the slipstream, the U, V and W velocity components obtained with the three propeller models are studied at AP, $X = L_{pp}$ and the results are compared with experimental data, [6]. Figures (3) and (4) on the last page of the paper show the measured U-contours and cross flow vectors in the propeller slipstream, and, with reference to the four numbered quadrants shown in Figure (3), the slipstream flow can be described as follows. In the lower part of 1 and 4 and in the top of 2 and 3 the wake deficit is strongest, which means that the inflow velocity to the propeller is low. This leads to relatively large local angles of attack, which means that the local propeller loading is high in these regions. Consequently the flow is accelerated, which explains the high axial velocity in the considered regions. Moving to the outer positions of 3, 4 and 1, 2, the axial inflow is higher, which should decrease the loading, but then the cross flow components of the inflow field start to play a role. With a right-handed propeller as used in this case, the propeller blades move towards the surface in quadrant 3 and 4, while they move towards the bottom in 1 and 2. If this is put in relation to the fact that the wake flow consists of two inboard and counter rotating bilge vortices, it is found that the cross flow components of the inflow field in 3 and 4 have the same direction as the propeller rotation, whereas they have the opposite direction of the rotation in 1 and 2. The result is that the angle of attack decreases in 3 and 4, while it increases in 1 and 2. Again this influences the local propeller loading, which leads to less acceleration of the flow in 3 and 4 compared to 1 and 2. Returning to the computations, the velocities calculated by means of the prescribed model are shown in Figures (5) and (6). Comparison of the calculated U velocities with the experiment shows that the numerical model gives U velocities of the same magnitude as the measurement, but that the shape of the contours are different. The reason is that the prescribed model applies constant body forces for fixed radii in the disk and therefore just accelerates the fluid in the propeller region without taking the local loading on the propeller into account. The asymmetry is caused by the swirl in the flow, which rotates the flow field in the same direction as the propeller rotates. With respect to the cross flow field in Figure (6), the overall features of the vectors appear to be in agreement with the experiment, but a closer study of the magnitude of the vectors shows that the computation and the experiment differs for the same reasons as described above. Moving to the simplified, but interactive model, the picture is different, since the overall features of the U-contours in Figure (7) are in better agreement with the experiment in Figure (3). In the outer part of quadrant 3 and 4 the axial velocity appears to be in fair agreement, but at the top and bottom of the slipstream, the computation under predicts the velocity. This is also the case in the outer part of 1 and 2. With respect to the cross flow vectors in Figure (8) the computation again gives overall flow features that are in agreement with the experiment in Figure (4). The cross flow seem to be a little weaker than for the prescribed model, which makes it agree better with the experiment. With respect to the panel model results, they are shown in Figures (9) and (10). When compared with the experiment in Figure (3), the computed axial velocity contours are in closer agreement than was the case for the other two models. Except for the regions in the top and bottom of the slipstream, the distribution and magnitude of the axial velocity shows fair agreement with the experiment. Concerning the cross flow vectors in Figure (10), they show the same characteristics as was found in the experiment and the other two propeller models. With respect to the magnitudes, they are approximately the same as for the prescribed model.

It must be noted that for both of the interactive models, the solutions are sensitive to the positions where the induced propeller velocities and total velocities are evaluated. Work is still ongoing to study this further.

Concluding remarks

Three different body forces propellers were applied to a hull-propeller configuration and the results were compared with experimental data. With respect to the effect of the propeller on the hull, it appears that all three models give approximately the right amount of suction on the hull in order to determine the thrust deduction. Concerning the propeller thrust and torque, the two interactive models were able to capture the thrust within 5% and the torque within 7% of the experimental data. With respect to prediction of the flow field down stream of the propeller it can be concluded that the axial slipstream velocity obtained with the prescribed model has approximately the right magnitude, but the distribution is different from the experiment. If a more accurate prediction is required it is necessary use interactive calculations. The simplified method gives an axial velocity distribution that reflects the local propeller loading, which means that it gets closer to the real flow field. However, it tends to slightly under predict the velocities when compared with experiments. Finally, the panel model gives an axial slipstream velocity distribution that agrees better with the experiment than for the simplified model. The magnitudes of the velocities agree with the experiment and that the distributions agree except for the regions in the top and bottom of the slipstream. Concerning the swirl in the propeller slipstream, all three methods seem to capture the flow features, though the magnitudes vary slightly.

Future activities

More work is put into a closer study of the positions for evaluation of the total and propeller induced velocities. Afterwards, the propeller models are to be applied to the appended tanker hull configuration described in [9]. The goal is to study the effect of the different propeller models on the quality of the calculated rudder forces and to study the interaction between the hull, rudder and propeller.

Acknowledgements

This research is sponsored by The Danish Ministry of Trade and Industry and the Office of Naval Research grant N00014-00-1-0589 under the Naval International Cooperative Opportunities in Science and Technology Program (NICOP). Jun Ando, Kyushu University, Japan is acknowledged for providing the propeller code based on Yamasaki's method.

References

[1] Wilson, R., Paterson, E. and Stern F.
Unsteady RANS CFD Methods for Naval Combatants in Waves, Twenty Second Symposium on Naval Hydrodynamics, August 9-14, Preprints, Washington, D.C., 1998, pp. 198-213.

[2] Stern, F., Kim, H. T., Patel, V. C. and Chen, H. C. A Viscous-Flow Approach to the computation of Propeller-Hull Interaction, Journal of Ship Research, Vol. 32, No. 4, Dec. 1988, pp. 246-262.

[3] Yamasaki, R.
On the propulsion Theory of Ships on Still Water-Introduction-Memoirs of the Faculty of Engineering, Kyushu University, Vol. 27 No. 4, 1968

[4] Nakatake, K.
A Practical Method to Calculate Propulsive Performance of Ships. Memoirs of the Faculty of Engineering, Kyushu University, Vol. 41 No. 1, 1981

[5] Hsin, C-Y, Development and Analysis of Panel methods for Propellers in Unsteady Flow, Report 91-1, Massachusetts Institute of Technology, 1991.

[6] Toda, Y. Stern, F., Tanaka, I. and Patel, V. C.
Mean-flow measurements in the boundary layer an wake of a Series 60 C_B=.6 model ship with and without propeller. IIHR Report No. 326.

[7] Stern, F., Wilson, R. W., Coleman, H. W. and Paterson E. G.
Verification and Validation of CFD Simulations, Proceedings of the 3rd ASME/JSME Joint Fluids Engineering Conference, July 18-23, 1999, San Fransico, California.

[8] Stern, F., Kim, H. T., Zhang, D. H., Toda, Y., Kerwin, J. and Jessup S.
Computation of Viscous Flow Around Propeller-Body Configurations: Series 60 C_B =0.6 Ship Model, Journal of Ship Research, Vol. 38, No. 2, June. 1994, pp. 137-157.

[9] Simonsen C. D. and Cross-Whiter J.
RANS Simulation of the Flow around a Manoeuvering Tanker, NuTTS'01, Hamburg.

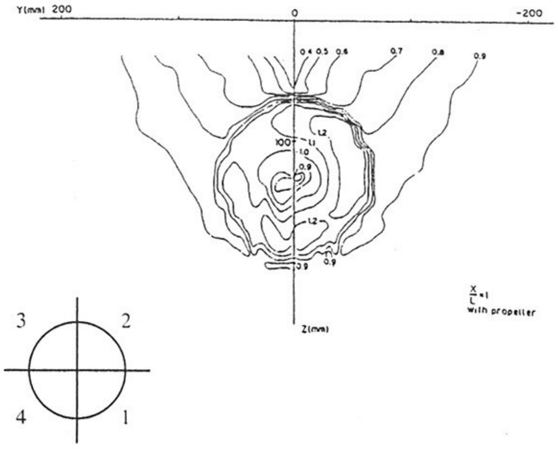

Figure 3. *Measured U-contours.*

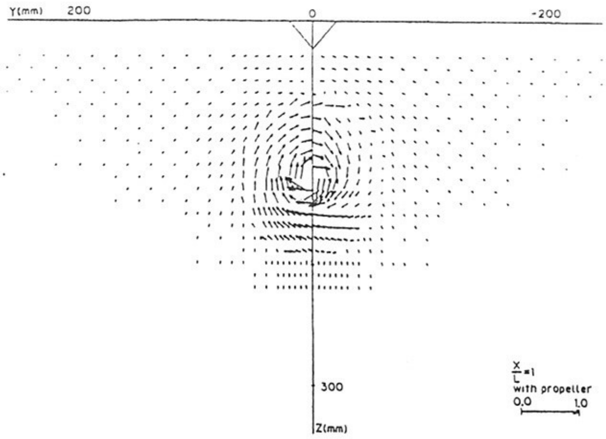

Figure 4. *Measured cross flow vectors.*

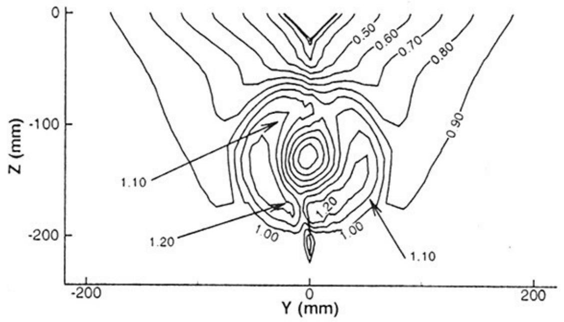

Figure 5. *U-contours, prescribed model.*

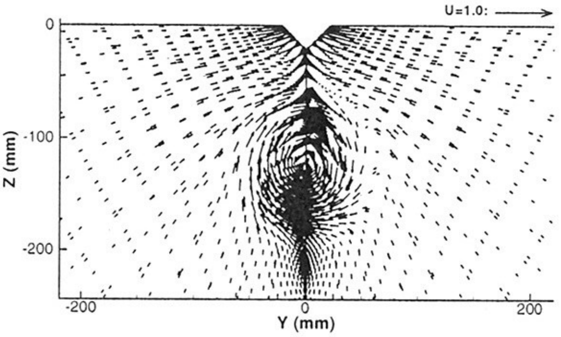

Figure 6. *Cross flow, prescribed model.*

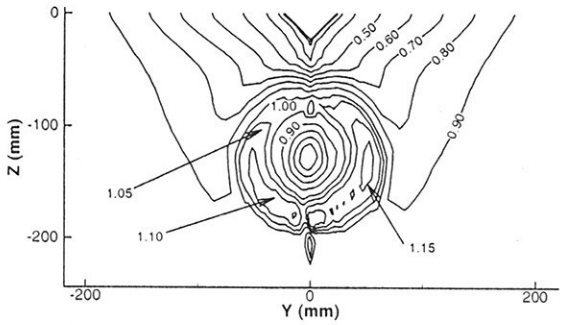

Figure 7. *U-contours, simplified model.*

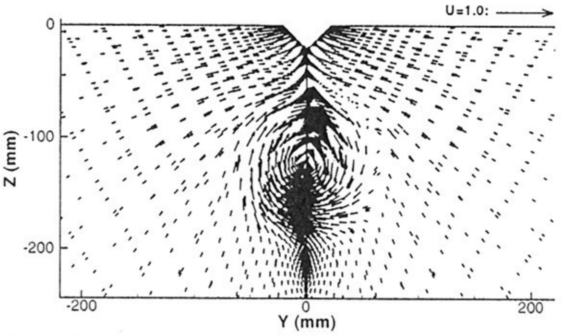

Figure 8. *Cross flow, simplified mode..*

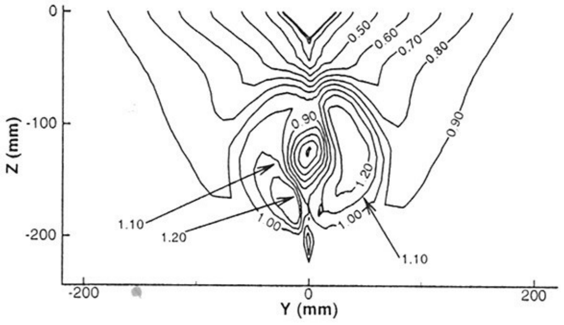

Figure 9. *U-contours, panel model.*

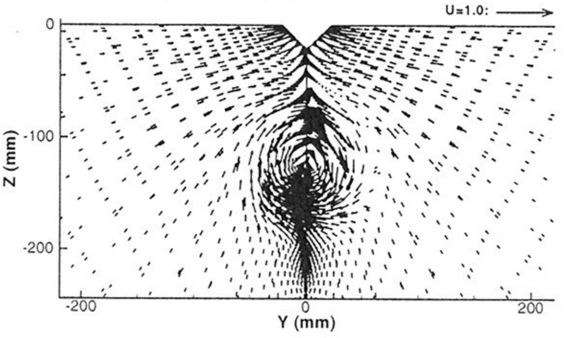

Figure 10. *Cross flow, panel model.*

Planing Boats in Waves

Heinrich Söding, TU Hamburg-Harburg
Lämmersieth 90, D 22305 Hamburg, h.soeding@tu-harburg.de

1 Method

The motions of high-speed planing boats in head waves are computed by applying a modified *Wagner (1932)* method to simulate the hydrodynamic forces F_x and F_z and the pitch moment M_y. Details about the hydrodynamics in still water were given by *Shigunov et al. (2001)*. However, the method can be simplified for planing boats:

1. corrections for blunt bodies are not required;
2. substantial negative pressures which could cause cavitation and/or ventilation were not observed.

The motion integration was performed by an implicit Euler method, with a time step of 1ms except for a few tests using smaller time steps. The added mass matrix was determined and updated by the method of *Söding (2001)*. Regular waves were modeled as 3rd order Stokes waves; however, for the small wave steepness of the following examples linear wave theory would have been sufficient.

2 Test case

Here I compare own simulations with measurements by *Katayama et al. (2000)*. The shape of their small model (Table 1, Fig. 1) is described for the simulation by offsets at 100 sections (Δx = 6.25mm) and 150 waterlines (Δz = 0.667mm), which was proved to be sufficiently fine.

Table 1. Model data

length L_{OA}	0.625m	breadth B	0.250m
length L_{pp}	0.600m		
depth D	0.106m	draft d	0.059m
deadrise β	22°	mass m	4.28kg
KG	0.111m	LCG–transom	0.285m

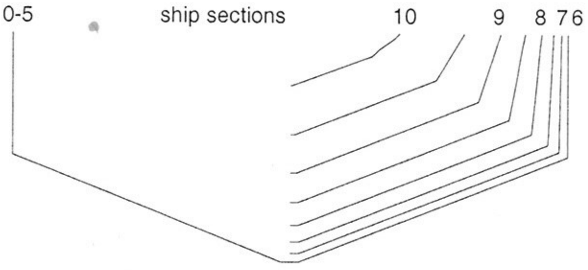

Fig. 1. Body plan of model

The model was towed with constant speed U at the centre of gravity G; thus at G the surge motion was suppressed. The same applies to the simulations. The heave motion refers to G. Whereas in the experiments the model, floating initially in equilibrium, was accelerated within a very short time to the test speed, in the simulations the model was dropped from slightly above the water with its final forward speed; drop height and initial trim angle were varied.

3 Results

Fig. 2 compares the natural pitch period T_n in still water after the acceleration phase (experiments) or the drop phase (simulations) depending on F_n. The coincidence appears reasonable. Not shown is the damping which seems to be higher in the simulations than in the experiment.

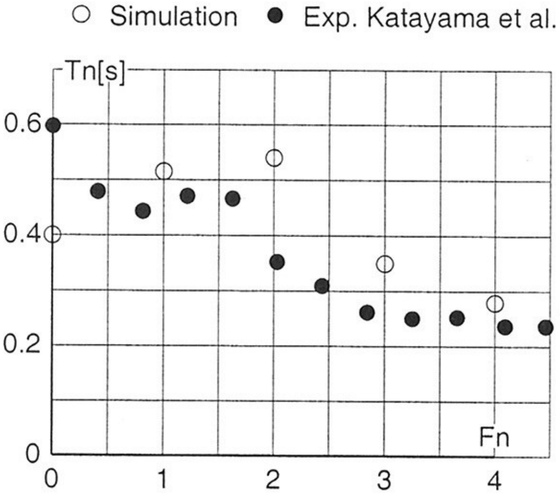

Fig. 2. Natural pitch period over $F_n = U/\sqrt{gL_{OA}}$

Fig. 3 shows nondimensional heave (maximum − minimum heave $Z(t)$ over wave height H_w = 2 · wave amplitude) for a regular wave of length λ = 1.556m at the moderate model speed 3m/s over wave height made non-dimensional by dividing it by draft at rest d = .059m. For the same case Fig. 4 gives nondimensional pitch = maximum − minimum pitch angle T_h divided by the (linear) wave slope $KH_w/2$ where K is wave number. The results apply to the stationary oscillation

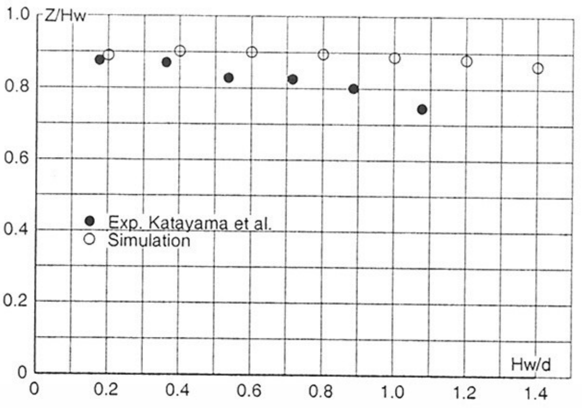

Fig. 3. Nondimensional heave over wave height; $\lambda/L_{OA} = 2.49$, $F_n = 1.21$.

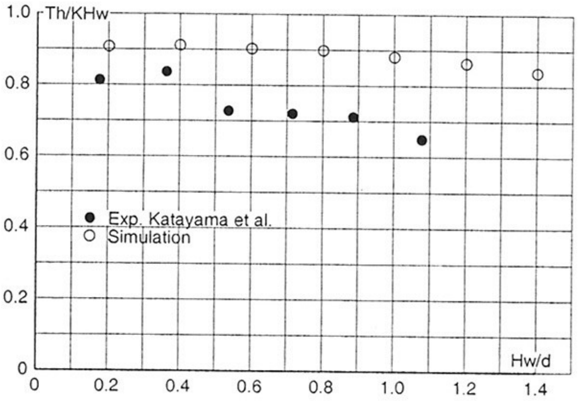

Fig. 4. Nondimensional pitch over wave height; $\lambda/L_{OA} = 2.49$, $F_n = 1.21$.

(limit cycle) of wave encounter period after the transients have died-out.

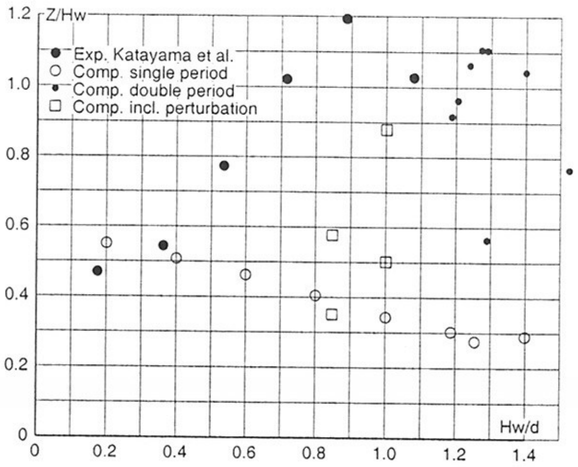

Fig. 5. Nondimensional heave over wave height; $\lambda/L_{OA} = 2.49$, $F_n = 3.93$.

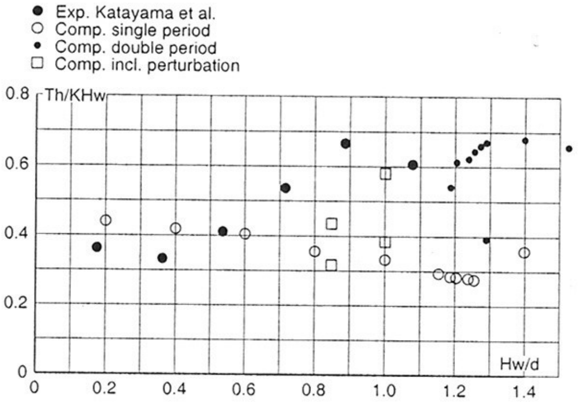

Fig. 6. Nondimensional pitch over wave height; $\lambda/L_{OA} = 2.49$, $F_n = 3.63$.

Corresponding results for the same wave length 1.556m but much higher speed $U = 9\text{m/s}$ are shown in Figs. 5 and 6. Here the ship motions converge to a stationary oscillation of wave encounter frequency only for low wave height. For somewhat larger wave height the motion repeats after twice the encounter period. According to the experiments the transition from single- to double-period motions seems to occur below $H_w/d = 1$, whereas in the simulations single-period motions were found until about $H_w/d = 1.4$ but not beyond. Between $H_w/d = 1.2$ and 1.4 both single-period and double-period responses were found as limit cycles, depending on the initial drop conditions of the model. According to the simulations there is no smooth increase of the nondimensional motion transfer functions with wave height; instead, if two-period motions occur as the limit cycle, they have much larger amplitudes than the single-period responses. Occasionally also two different two-period limit cycles are found for the same wave and speed conditions but different initial conditions. Further, the distinction between one-period and two-period limit cycles is not always clear: sometimes even and odd cycles of wave encounter period differ only slightly from each other. Further, the transition from an initial near-periodic response to the limit cycle may appear after long times and may be too long for the experiments (Fig. 7).

For the experiments Katayama et al. reported irregular motions for $H_w/d > 0.7$. That could be understood as chaotic motions. In the simulations, however, two-period responses were found up to about $H_w/d = 1.35$, and chaotic motions appeared only for $H_w/d > 1.63$. Because in some experiments the wave tracks shown by the authors are far from sinusoidal, I investigated also a slight perturbation of the regular wave by superimposing a wave of 0.283m length (avoiding a simple length ratio) and 1/6 of the height of the main wave (Fig. 8). This small irregularity, which

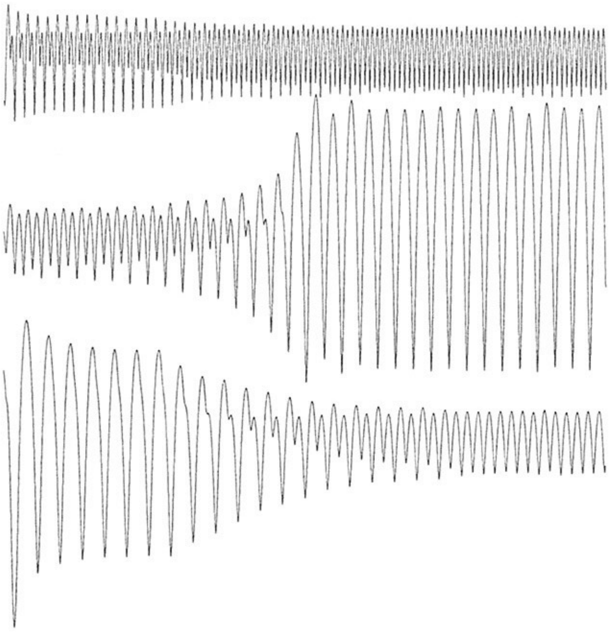

Fig. 7. Simulated heave motions in regular waves of 1.556m length for wave heights of 7.1cm (bottom), 7.55cm (middle) and 8.25cm (top). Different time scales (abszissa).

appears much smaller than that shown in the experiments, produced, e.g. at $H_w/d = 1$ (Figs. 5, 6), dramatic changes in the responses, and it lowered the range were double-period responses were found. Thus the irregular measured motions are probably influenced by irregularities of the very flat waves.

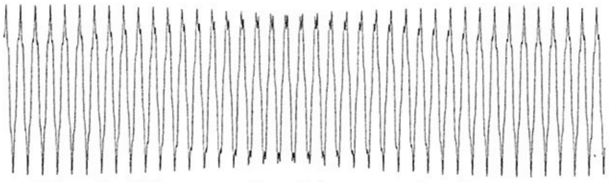

Fig. 8. Wave track with perturbation

All the above referred to waves of a single length $\lambda = 2.49 L_{OA}$. Figs. 9 and 10, on the other hand, show measured and simulated nondimensional heave and pitch for variable (greater) wave length for a single wave height of 2cm. The large measured responses near $\lambda/L_{OA} = 5.5$) occur for an encounter period $T_e = 0.30$s which is not far from the natural pitch period measured for the same $F_n = 3.63$ (Fig. 2). In the simulations no sharp peak response was found, neither with regular nor with the disturbed waves. For 4cm wave height the experiments showed a peak at a shorter wavelengh $\lambda/L_{OA} = 3$; also that peak was not found in the simulations (Figs. 11, 12). In all the simulations of Figs. 9-12 the responses were periodic with the wave encounter period.

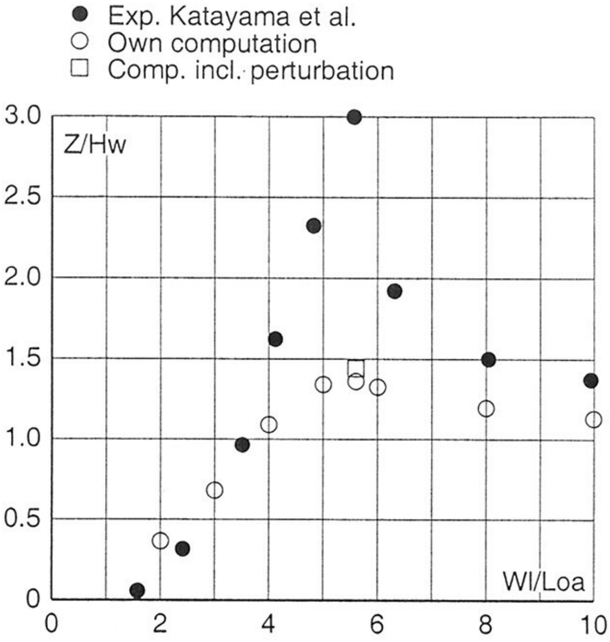

Fig. 9. Non-dimensional heave over nondimensional wave length for H_w = 2cm and U = 9m/s

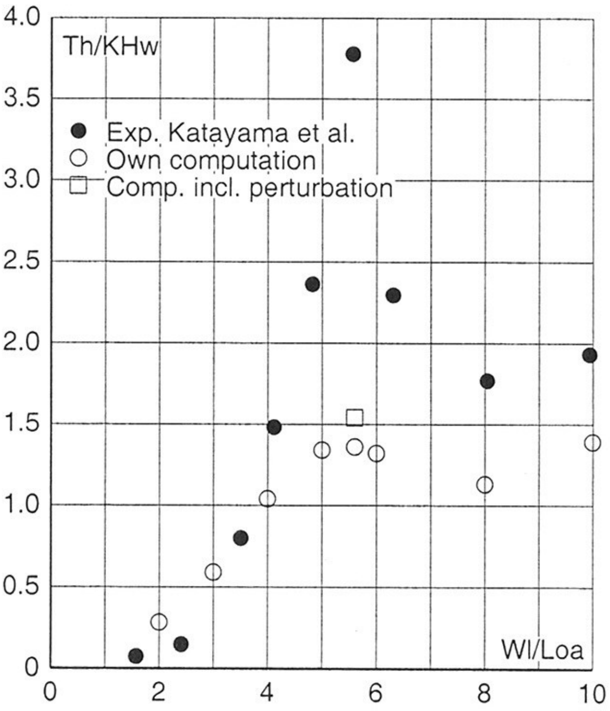

Fig. 10. Non-dimensional pitch over nondimensional wave length for H_w = 2cm and $U = 9$m/s

Fig. 13 shows average trim angle and standard deviation of pitch angle in natural longcrested head seaways containing wavelengths between about 0.95m and 2.3m, with maximum energy at about 1.6m wavelength. Here both the average trim and the standard deviation of pitch change continuously with significant wave height.

4 Conclusions

1. A simple Wagner-type method for forces on planing boats in head waves results in motion responses which compare moderately well to experiments by *Katayama et al. (2000)*.

2. Panel methods, and even more Ranse methods, would have been too slow to detect many of the interesting details of the strongly nonlinear responses. Thus fast methods are required besides more accurate, slow-running methods.

3. Due to the sensitivity of the responses to wave irregularities, and due to the many oscillations which are required frequently until the limit cycle is attained, reliable measurements in regular waves appear unusually difficult.

4. Different limit cycles for the same model and wave conditions make both measurements and simulations, to a certain degree, a matter of random.

5. The difficulties 3 and 4 are avoided if tests and simulations are performed in natural irregular seaways.

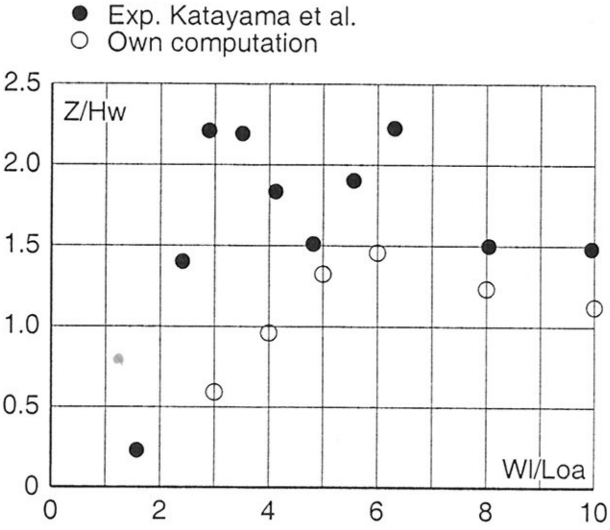

Fig. 11. Non-dimensional heave over nondimensional wave length for H_w = 4cm and U = 9m/s

5 References

KATAYAMA, T., HINAMI, T. and IKEDA, Y. (2000), *Longitudinal motion of a super high-speed planing craft in regular head waves*, Proc. 4th Osaka Colloquium on Seakeeping Performance of Ships

SHIGUNOV, V., SÖDING, H. and ZHOU, Y.-Z. (2001), *Numerical simulation of emergency landing of aircraft on a plane water surface*, HIPER, 419-430

SÖDING, H. (2001), *How to integrate free motions of solids in fluids*, NuTTS 01.

WAGNER, H. (1932), *Über Stoß und Gleitvorgänge an der Oberfläche von Flüssigkeiten*, ZAMM 12(4), 193-215

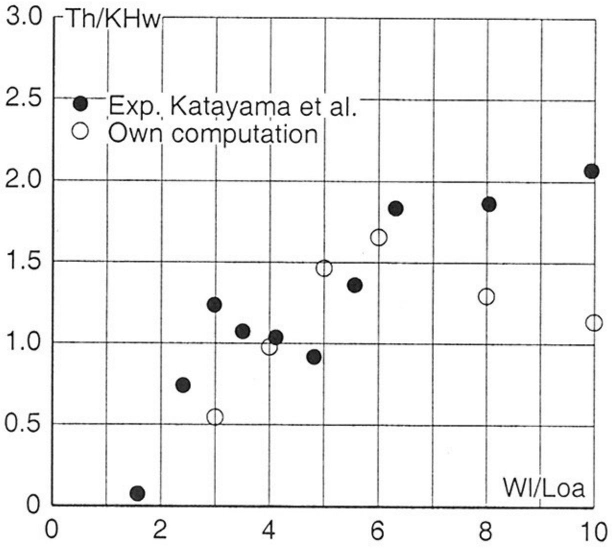

Fig. 12. Non-dimensional pitch over nondimensional wave length for H_w = 4cm and U = 9m/s

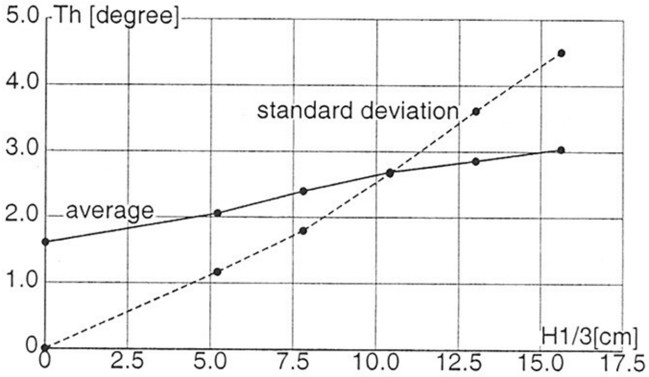

Fig. 13. Average trim and pitch standard deviation for U = 9m/s over significant wave height $H_{1/3}$.

Resistance and self-propulsion factors prediction for practical ship hulls by CFD

Noritaka Takada, noritaka_takata@nsmw.mhi.co.jp
Tetsuji Hoshino, hoshino@ngsrdc.mhi.co.jp
Satoru Ishikawa, ishikawa@ngsrdc.mhi.co.jp
Shoichi Higaki, higaki@ngsrdc.mhi.co.jp
(Mitsubishi Heavy Industries, LTD. ,JAPAN)

1.Introduction

For designing a lower delivered horse power ship, it is necessary not only to reduce hull resistance, but also good performance in self-propulsion factors. Self-propulsion factors represent propeller-hull interaction which are closely related with stern hull form. In the past, the designer optimized the hull form by iterating the model test in basin and redesign the hull form. In the present, CFD is used as a numerical tank and it contributes to saving costs and time.

The progressive study on predicting the self-propulsion factors was taken by Hinatsu et al [1, 2]. It is called NICE method. This method solves RANS equation around hull and rudder for zero Fn, and propeller effects are incorporated by the body force approach and propeller performance computation are based on infinitely-bladed propeller theory. This method can predict propeller-hull interaction and self-propulsion factors for low speed ship. In this method, free-surface effects are not considered. Then application of this method is restricted to low speed ship.

For free surface effects with propeller, Tahara et al [3] show good agreements in flow field with propeller for container ship without rudder using infinitely-bladed propeller theory. Real propeller geometry is not considered in infinitely-bladed propeller theory.

A study to generate grid considering real propeller geometry and solve directly flow field around hull and rotating propeller by using RANS-Solver has been taken. Abdel-Maksoud,M. et al [4] applied this method to container ship for zero Fn. However it takes much time for computation and grid generation. And it is difficult to use this method in the design procedure.

In the present study, for solving above problems, the simulation method of free surface viscous flow around practical hull and rudder with propeller effects has been developed.

For propeller performance computation, UQCM(Unsteady Quasi-Continuous Method) [5] based on lifting surface theory is used. And propeller effects are included in RANS-Solver by body force approach.

In the following, an overview is given of present numerical method, and the results for applied to container ship are discussed through comparison with measurements about flow field around ship. Finally the present method is applied to a modern full ship with rudder. The computed self-propulsion factors are verified by experiments.

2.Computational Method

In the present study, FS-MINTS is used as RANS-Solver. It has been developed by one of the authors, Takada [6]. For application to complex hull form, multi-block grid technique is used. And "BJ-SGS" [7] which is the method of updating boundary conditions on block interfaces is incorporated in the present code. The numerical algorithm to solve RANS equations at each block is adopted the similar method of "NEPTUNE" developed by Hirata et al [8] shown as follows. The artificial compressibility form of the three-dimensional incompressible Navier-Stokes equations is solved using an approximate Newton relaxation approach. A cell-centered finite volume approach is used for spatial discretization. The nonlinear free-surface condition are implemented and the re-gridding technique is used to treat the free-surface deformation. The multi-grid scheme and local time stepping method are applied to accelerate the convergence of the solutions. See [6] for more details. For turbulence model, modified Baldwin-Lomax model [9, 10] presented by SR222 Research Committee is used.

For propeller performance calculation, Unsteady Quasi-Continuous Method (UQCM) is used. UQCM is based on QCM that is a kind of lifting surface theory in incompressible potential flow. QCM is extended to UQCM for unsteady propeller lifting surface problems by one of the authors, Hoshino [5]. UQCM is able to consider propeller geometry (mean chamber surface). UQCM can reproduce propeller performance well in quantity. Then it is expected that flow field with propeller is well predicted. Additionally, there is the possibility to optimize not only hull form but also propeller geometry suited for the hull form.

Propeller effects are included in RANS equations by body force approach. In the present method, we do not solve unsteady flow, but mean flow during one revolution. It is enough to predict self-propulsion factors.

3.Comparison of calculation and experimental results in flow field

3.1 Model ship and calculation condition

At first, The validation of flow field around stern region with and without propeller conditions is carried out. Model ship is KRISO container ship (KCS). This model ship is tested on KRISO and NMRI[11]. See Table 1 for dimensions of model and calculation condition. In this section, computations are taken for hull without rudder and without/with propeller conditions.

3.2 Results

Fig.1,2 compare the present results for axial velocity and cross plane vectors with those for the measurements for without/with propeller conditions at x/L=0.4911. In both cases, axial velocity contours and cross plane vectors agree well with the measurements.

Fig.3 compares the velocity components for the computations and measurements at x/L=0.4911 along z/L=-0.03 for without/with propeller conditions. For without propeller conditions, the computations and measurements are in good agreement. For with propeller condition the present results are somehow over or under predicted near the center line. The reason is that hub rotating effects is not considered in the computations. Then near the hub, cross flow vectors on propeller plane are under predicted, see Fig.2.

Fig.4 shows contours of surface pressure differences between with and without propeller. These contours are given by subtracting surface pressure with propeller from that without propeller. Pressure decrease on stern region is well reproduced in quantity. The computations show pressure differences are positive(pressure increased by propeller acting) on above propeller region. Measurements are not taken on this region. Though we don't know it is true or not, the positive pressure on this region decreases thrust deduction factor. It is interesting to investigate the relationship between slope of hull on this region and thrust deduction factor. This phenomenon is due to a decreased flow caused by propeller suction. See Fig.5, this figure shows computed velocity field contours and vectors on center plane. Actually, on above propeller region, flow is decreased.

4.Validation of self-propulsion factors on full ship with rudder

In the present study, experimental data for full ship is used for validation. Because self-propulsion factors have a high influence on delivered horse power especially for full ship. This experimental data is measured on Nagasaki R&D Center in Mitsubishi Heavy Industries, LTD. Model ship length is 7.3 m.

4.1 Conditions of computation

Computations are on 4 ship speed (Froude number= 0.16, 0.18, 0.20, 0.22). In order to make comparison exactly of computed results with the experimental data, the Reynords number in the computations is set the same as the experiments, and propeller revolution is set the same, too. See Fig.14 for reference grid of full ship. In this grid, multi-block grid technique is used. This grid is divided into 2 part. One is under-water part and another is upper part. Upper part includes free surface, and the re-griding technique is used on this upper part. The under-water part includes Bottom, Propeller and Rudder block (See Fig.6). Even if it is possible to compute these three blocks as 1 block, Propeller block is made including propeller . Because smaller block is advantageous to computational time for interpolating inflow velocity and body force . Then this grid includes 6 blocks and 0.4 million points. In this topology, there are two restricts on geometry for free surface computation.

- There is no gap between hull and rudder.
- Connection point of rudder leading edge and hull must be under free surface.

4.2 Results

Fig.7 compares the residual resistance coefficient between measurements and computations on towing condition. The computations agree well with the measurements and are well reproduced the influence of ship speed.

Fig.8 to 10 shows the comparison of self-propulsion factors(t: thrust deduction, w_m: wake fraction, η_r: relative rotative efficiency). For analyzing w_m and η_r, propeller open characteristics predicted by UQCM and thrust identify method is used.

Each self-propulsion factors are in good agreement. An error in prediction is less than 10 % in each cases. In measurements, wake fraction is decreasing slightly with ship speed increasing. Such tendency appears in computations, too.

5.Conclusions

In the present method, CFD code which is able to estimate hull form resistance and self-propulsion factors for various kind of ship through full ship to fine ship has been developed.For applying present method to container ship, flow field near propeller and hull surface pressure on stern region which are closely related to self-propulsion factors are well predicted in quantity. Moreover, it is applied to calculate the flow around modern full ship hull and rudder without/with propeller. Consequently, its resistance and self-propulsion factors are accurately predicted.

Future works include adding the function to adjust the propeller revolution to ship point automatically and expanding to multi-screw ship and pod propulsion system.

Acknowledgment

The authors would like to express sincere gratitude to Ms Osumi of Mitsubishi Heavy Industries, LTD. for modification of UQCM program.

References

1) Hinatsu M., Kodama Y., Fujisawa J. and Ando J. *"Numerical Simulation of Flow around s Ship Hull Including a Propeller Effect"*, Trans. of the West-Japan Soc. of Naval Archit.,Vol. 88, Japan 1994.

2) Hinatsu M., Hino Y., Kodama Y., Fujisawa J. and Ando J. *"Numerical Simulation of Flow around s Ship Hull with Rudder in Self Propulsion Condition"*, Trans. of the West-Japan Soc. of Naval Archit.,Vol. 90, Japan 1995.

3) Tahara, Y. and Ando, J., *"Comparison of CFD and EFD for KCS Container Ship in Without/With-Propeller Conditions"*, A Workshop on Numerical Ship Hydrodynamics, Preprints, Gothenburg, Sweden, 2000.

4) Abdel-Maksoud, M., Rieck, K. and Menter, F., R., *"Unsteady Numerical Investigation of the Turbulent Flow Around the Container Ship Model (KCS) with and without Propeller"*, A Workshop on Numerical Ship Hydrodynamics, Preprints, Gothenburg, Sweden, 2000.

5) Hoshino T., *"Application of Quasi-Continuous Method to Unsteady Propeller Lifting-Surface Problems"*, J. of the Soc. Naval Archit. Japan, Vol. 158, pp.51-70, 1985

6) Takada N., *"Computation of ship transom stern flow using a multi block grid method"*, J. of the Soc. Naval Archit. Japan, Vol. 190, 2001.

7) Beddhu M., Pankajakshan R., Jiang M., Remotigue M., Sheng C., Taylor L.K., Briley W. and Whitfield D.L., *"Computation of Nonlinear Turbulent Free Surface Flows Using the Parallel Uncle Code"*, 23rd Symposium on Naval Hydrodynamics,Preprints, 2000.

8) Hirata N. and Hino T., *"An Efficient Algorithm for Simulating Free-Surface Turbulent Flows around an Advancing Ship"*, J. of the Soc. Naval Archit. Japan, Vol. 185, pp. 1-8, 1999.

9) Japan Ship Research Association, *"Progress in estimation of stern flows of large full hull forms"*, Report of SR222 Research Committee, 1996.

10) Kodama Y., *"Scope of CFD for Computing Ship Flows"*, Third Osaka Colloquium on Advanced CFD Application to Ship Flow and Hull Form Design, Japan, 1998.

11) Kume, K., Ukon, Y. and Takeshi, H., *"Measurements of Surface Pressure and Local Velocity Field around a KCS Model and Uncertainty Analysis"*, A Workshop on Numerical Ship Hydrodynamics, Preprints, Gothenburg, Sweden, 2000.

Table 1 Condition of computation

Model : KCS			
$L_{PP}(m)$	7.2786	Fn	0.26
Re	1.4×10^7	$np(rps)$	9.5

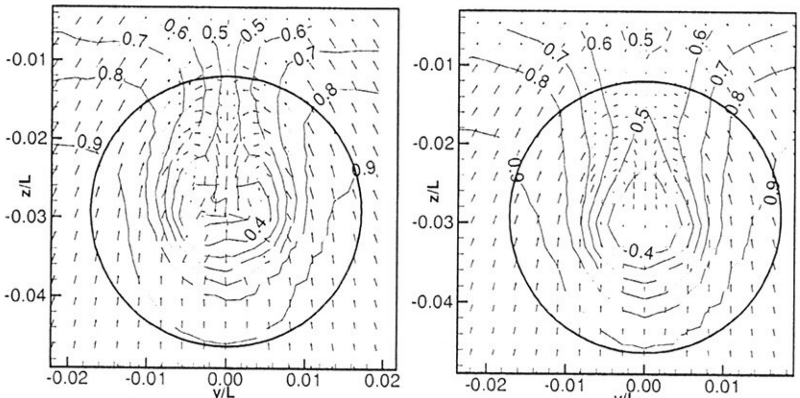

(Exp.) (Cal.)

Fig. 1 Axial-velocity contours and cross plane vectors at x/L =0.4911, without propeller, Fn=0.26, Re=1.4×10^7

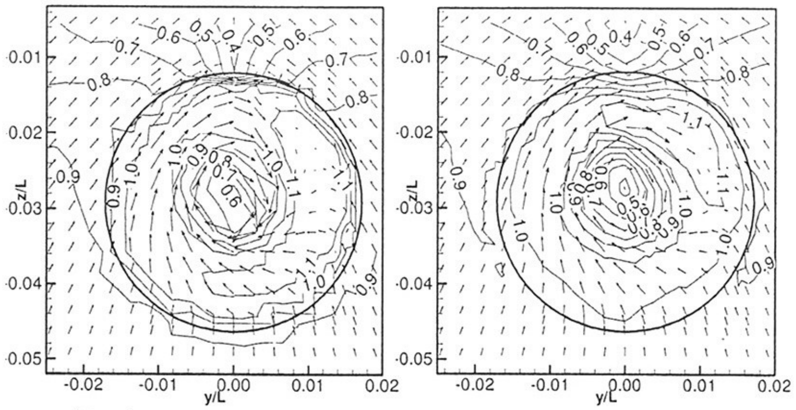

(Exp.) (Cal.)

Fig. 2 Axial-velocity contours and cross plane vectors at x/L=0.4911, with propeller, Fn=0.26, Re=1.4×10^7

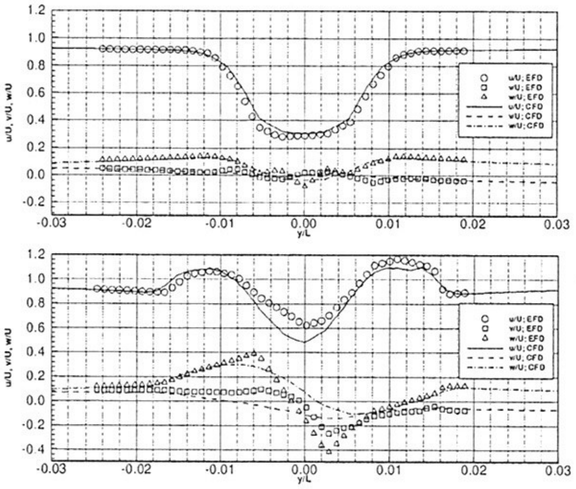

Fig. 3 Comparison of velocity components for the computations and measurements at x/L =0.4911 along z/L =-0.03, without (above) and with (below) propeller , Fn=0.26, Re=1.4×10^7.

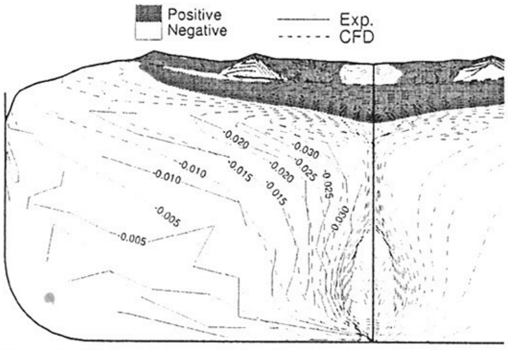

Fig. 4 Contours of hull surface pressure difference between with and without propeller for measured (solid line) and computed (dotted line), Fn=0.26, Re=1.4×10^7

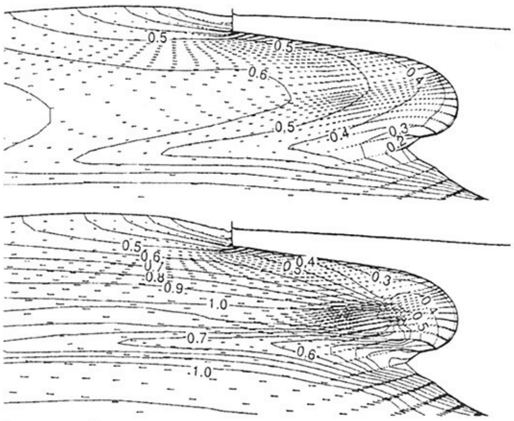

Fig. 5 Comparison of computed velocity field contours and vectors on center plane between without propeller (above) and with propeller (below), Fn=0.26 ,Re=1.4×10^7

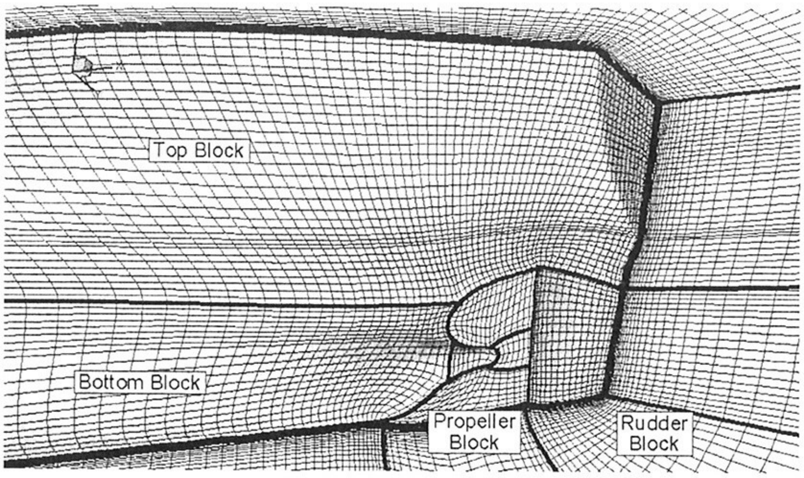

Fig. 6 Reference grid for full ship

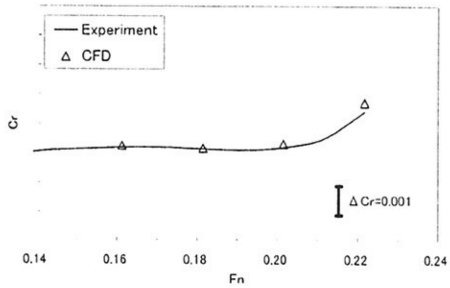

Fig. 7 Comparison of measured and computed residual resistance coefficient

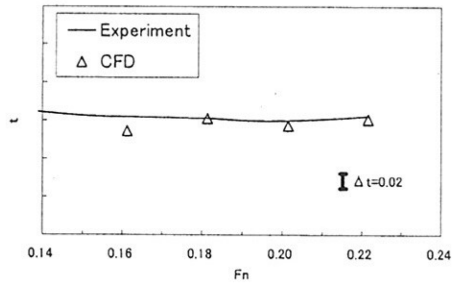

Fig. 8 Comparison of measured and computed thrust deduction factor

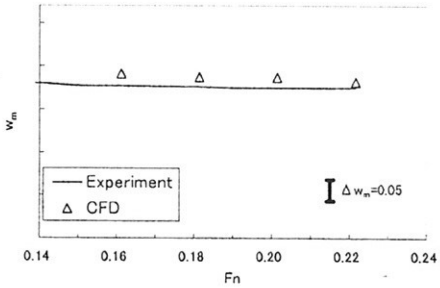

Fig. 9 Comparison of measured and computed wake fraction coefficient

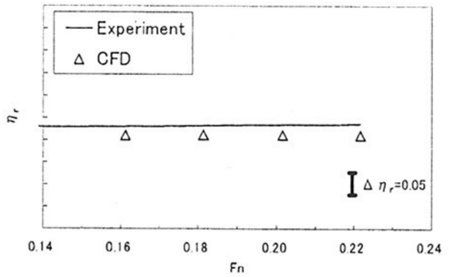

Fig. 10 Comparison of measured and computed relative rotative efficiency

Domain decomposition with implicit coupling and non-matching grids

A. van der Ploeg (Maritime Research Institute, Netherlands)
P. O. Box 28, 6700 AA Wageningen, the Netherlands
A.v.d.Ploeg@marin.nl.

1 Introduction

MARIN has developed the PARNASSOS code to analyse the viscous flow around a ship. If the geometry permits, the flow domain is covered with a single-block, boundary-fitted grid of H-O topology. However, for some ship forms the partitioning of the domain into two or more grid blocks makes grid generation a lot easier. An example is the class of so-called twin-skeg or twin-gondola ships. Maintaining the H-O grid lay-out, we can operate for those ships with a two-block grid, one on either side of the skeg, possibly further subdivided as in Fig. 1, which shows a velocity field in a cross-section of a 4-block grid.

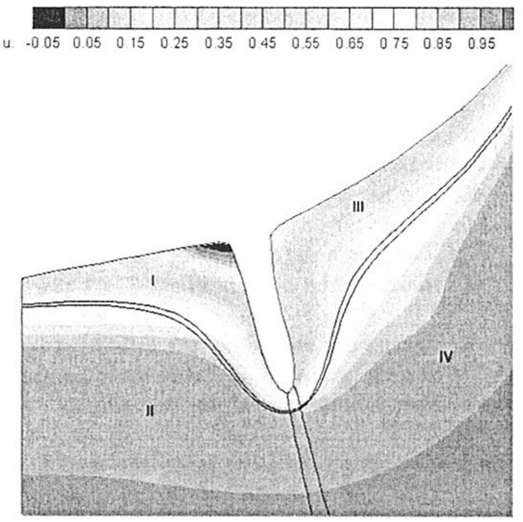

Figure 1: longitudinal velocity around a skeg computed by PARNASSOS, showing a partitioning in 4 domains with a small overlap.

The aim of this paper is to report some of our experiences with domain decomposition and its effects on the solution and on the solution process. The main features of the numerical method are briefly described in Section 2. Section 3 deals with the twin-skeg hull problem, while Section 4 concentrates on the flow around an 8 degrees inclined shaft protruding from a flat plate. The latter case has been chosen because the block interface is at the same time a symmetry plane so that we can compare the results of the multi-domain code with those of a single-block computation that uses the symmetry explicitly as a boundary condition. Also the convergence speed can be compared.

2 Numerical method

PARNASSOS [1] is a RANS-code that is currently in use at MARIN as a tool for quality assessment of hull designs on request of shipyards, navies and other customers. It solves the discretised partial differential equations that describe the viscous flow near a ship. The equations considered are the Reynolds-averaged Navier-Stokes equations for a steady, incompressible flow in three dimensions. PARNASSOS solves the fully coupled steady momentum and continuity equations in their original form, without resorting to pressure corrections or artificial compressibility. The grids are assumed to be regular and body-fitted, but may be generally non-orthogonal. They are stretched towards the hull in order to resolve the gradients in the boundary layer.

At the solid walls, the no-slip condition is applied. The boundary conditions imposed on the external and inlet boundaries are derived from a potential flow solution. Symmetry boundary conditions are applied at the water surface, and at the outlet boundary, the streamwise pressure gradient is set to zero. The governing equations are integrated down to the wall (no wall functions used) even for full-scale Reynolds numbers. The inherently very high aspect ratio of the cells near the hull puts high demands on the solver for the linear systems, which is one of the reasons to maintain the coupling between the equations in the iterative solution.

For the grid metric terms and for the diffusive terms we use second-order, central difference schemes. For the continuity equation and the gradients of the pressure we use a third-order four-point scheme. For stability reasons, the bias of the latter has to be opposite to that of the 'corresponding' derivative in the continuity equation. For the derivatives of the velocities in the convective terms a second-order upwind scheme in longitudinal direction is used, and a third-order upwind scheme for the normal and girth-wise direction. A detailed description of the mathematical model, the computational grid and the PDEs in curvilinear coordinates is given in [1].

The solution procedure in PARNASSOS has been set up in such a way that memory requirements can be very low. Reduction of the size of the equation system is obtained by dividing the computation domain into regions that consist of several stations ('planes' with constant streamwise coordinate). It is possible to choose these regions in the range from one station to even the complete domain. In a downwind sweep the eddy viscosity, the velocities and the pressure in one region are updated, before going to the next region. We use preconditioned GMRES [3] to compute a correction for the pressure and the velocities in each region. More details about the solution strategy and preconditioning technique can be found in [4].

2.1 Coupling of the domains

The current multi-domain version of PARNASSOS can deal with non-matching grids at the domain interfaces. Over the domain interfaces, bi-linear interpolation has been used. This is illustrated by Fig. 2, which shows two non-matching grids near an interface between two boundaries, together with the computed pressure distribution.

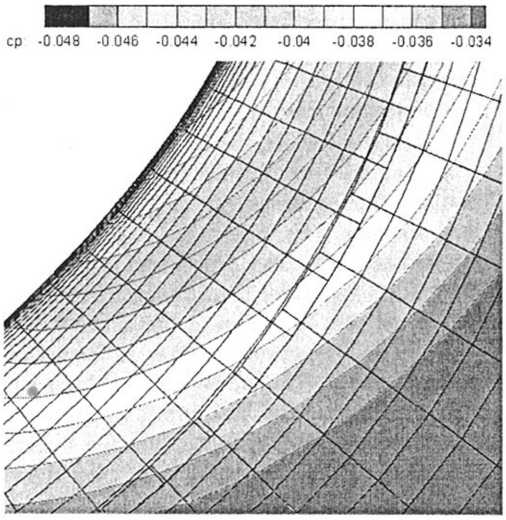

Figure 2: Computed pressure distribution in the neighbourhood of an interface between non-matching grids.

As mentioned above, PARNASSOS solves the fully coupled steady momentum and continuity equations. Therefore, we have chosen to make the coupling between the domains also fully implicit: the system of linear equations that is solved by preconditioned GMRES includes the discretised and linearized RANS-equations of all domains. The matrix includes the weights corresponding to the bi-linear interpolation. Every time a matrix-vector multiplication is performed, communication is required to obtain data from all neighbouring domains.

As a result of the implicit coupling, the splitting of the computational domain hardly influences the convergence behavior of the 'global' iteration that is required to make the coupling between the separate regions and to deal with the non-linearity. From numerical experiments it appears that also the number of iterations of GMRES increases only slightly when the number of domains is not larger than 8. If the number of domains becomes significantly more, it is likely that the preconditioning technique for GMRES has to be adapted.

3 A twinskeg geometry

An example of a geometry in which the structured grid requires domain decomposition is shown in Fig. 3. It displays a single plane of the grid around one symmetric half of a twin-skeg afterbody. One station further downstream the skeg disappears. As a result, the extensions of the inner and outer side of the skeg (both having a wall-normal coordinate $j = 1$) now coincide and form a sort of near-vertical plane, as illustrated in Fig. 4. It shows that there is still a strong refinement in wall-normal direction towards this $j = 1$-plane. The grid has several features that are not present in a grid without such a plane.

1. There is a singularity in the middle of the domain, at the bottom of the $j = 1$-plane.
2. Quite near this plane the cells have a very high aspect ratio. Usually, such cells are only located near a boundary of the domain.
3. The direction along both the wall-normal and girthwise direction is reversed when passing this plane.

These features severely complicate the computation of the flow around a twin skeg. To deal with these complications, the domain is split into two parts, such that the plane extending aft of the skeg is the block interface: both domains share the $j = 1$-plane right behind the skeg, in addition to a plane with constant girthwise coordinate k. A schematic view of the grid transformed to the computational domain together with the required communication is shown in Fig. 5.

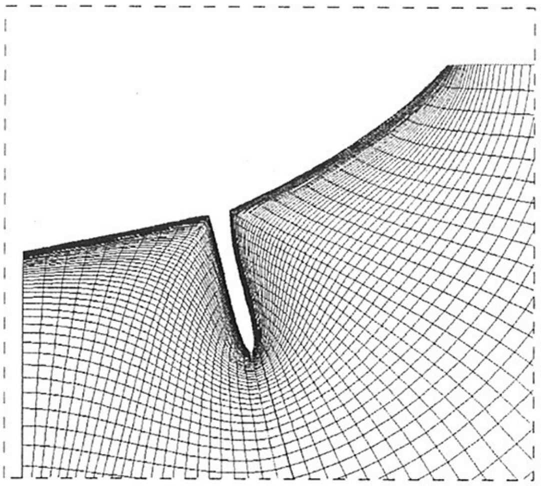

Figure 3: Grid around a skeg. Last station ('plane' with constant streamwise coordinate) containing the skeg.

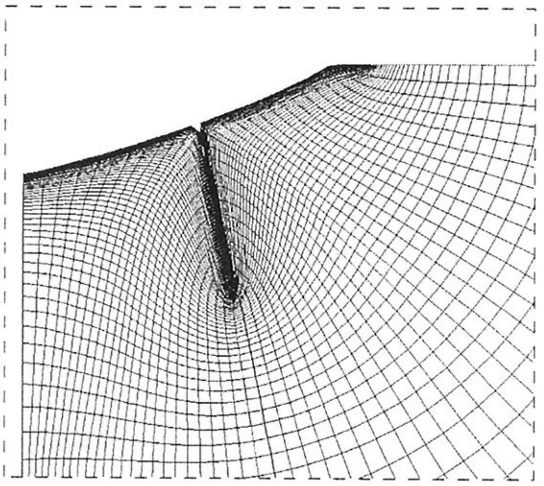

Figure 4: Grid in a station behind the skeg.

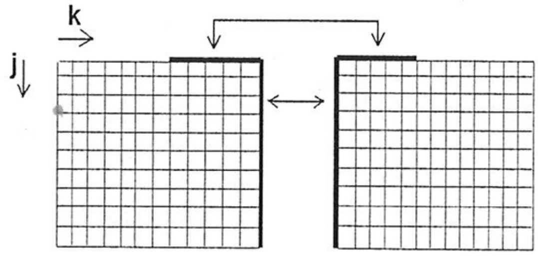

Figure 5: Schematic two-domain grid in computation domain.

3.1 Continuity of velocity, pressure and eddy viscosity

Across the common $j = 1$ plane, the Cartesian velocity components and pressure should be continuous. Mathematically, however, we can impose only three boundary conditions. From several numerical experiments it appeared that, in order to obtain a pressure that is continuous, the velocity component in normal (normal to the common plane)-direction has to follow from a linear combination of both momentum equations in normal direction. Therefore, we impose both momentum equations in this direction, and hence also any linear combination of both. The continuity equation is replaced by the momentum equation in normal direction from the other domain. The longitudinal and girthwise velocity components can follow from the momentum equations in longitudinal and girthwise direction. However, the convergence is extremely slow in that case, and from numerical experiments it appeared that it is not possible to obtain a fully converged solution.

Several possibilities have been studied to improve the convergence behavior. Adaptation of the grid behind the twin skeg by using a uniform mesh size in a small region instead of reducing the mesh size in normal direction towards the common plane (in the wake of the skeg a strong mesh refinement is not required) led to a slight improvement. The following combination of measures improved the convergence much more:

- Both momentum equations in normal direction mentioned above are applied fully implicitly instead of explicitly: the linear system solver GMRES takes care of the communication between both domains.

- Obtain the velocity components in longitudinal and girthwise direction on the common plane from an interpolation that uses points which are located symmetrically about this plane. From numerical experiments it appeared that this interpolation has to be at least third order accurate to obtain a converged solution. This is implemented using Newton divided differences.

- The speed of convergence is strongly influenced by the distance between the points in the abovementioned interpolation and the common plane. If these points are chosen too close to this plane, convergence is extremely slow. Therefore, these points are located at a distance h_{loc}, $2h_{loc}$, $3h_{loc}$,... from the common plane, in which h_{loc} is approximately 10% of the meshsize in girthwise direction.

- Not only velocity components in points of the common plane itself, but also the velocity components in longitudinal and girthwise direction

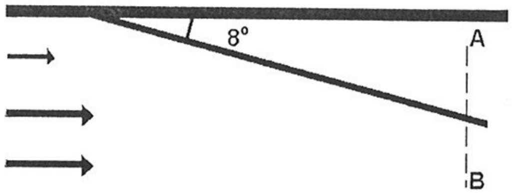

Figure 6: Side view of shaft protruding from a flat plate.

in points in the direct neighbourhood of this plane are obtained from the above-mentioned interpolation.

- The quantities on the common plane that are solved in the transport equations of the turbulence model are obtained from a linear interpolation using points in the direct neighbourhood ($j = 0$ and $j = 2$). From numerical experiments it appears to be necessary to implement this interpolation fully implicitly, otherwise the convergence of the global iteration stagnates.

4 Flow around a shaft

In order to study the effect of domain decomposition on the numerical solution and the convergence behavior, we compute the flow around a shaft inclined with respect to a flat plate from which it protrudes at an inclination angle of 8^o (Fig. 6). We compute the flow on two grids. The first, relatively coarse grid consists of $73 \times 81 \times 113$ nodes and the second grid consists of $145 \times 161 \times 225$ nodes in longitudinal, wall-normal and girthwise direction, respectively. Even for the coarse grid, the nodes closest to solid walls has y^+ values less than 0.7.

For one of the last stations containing the shaft, denoted by AB in Fig. 6, part of the first grid is shown in Fig. 7. Below the flat plate, and above the shaft there is again a common j = 1-boundary as described in the previous section. The Reynolds number based on the shaft diameter is 1.8×10^5. Menters one-equation turbulence model is used [2]. Fig. 8 shows that the computed solution is continuous over the interface boundary. Since the discretisation of derivatives in the direction normal to the common plane is not symmetric, we can expect deviations from a symmetric solution of the order of the discretisation error. From the results of Fig. 8 it appears that the deviations from symmetry become indeed smaller with grid refinement.

In this special case, the block interface is also a symmetry plane. Hence we can also compute the flow in only half of the domain and impose the symmetry directly as a boundary condition.

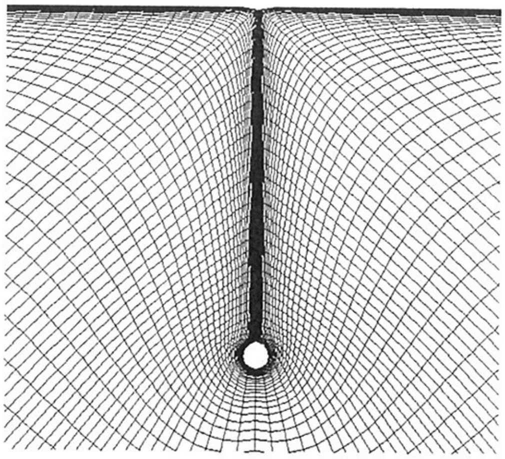

Figure 7: Detail of the grid around the shaft.

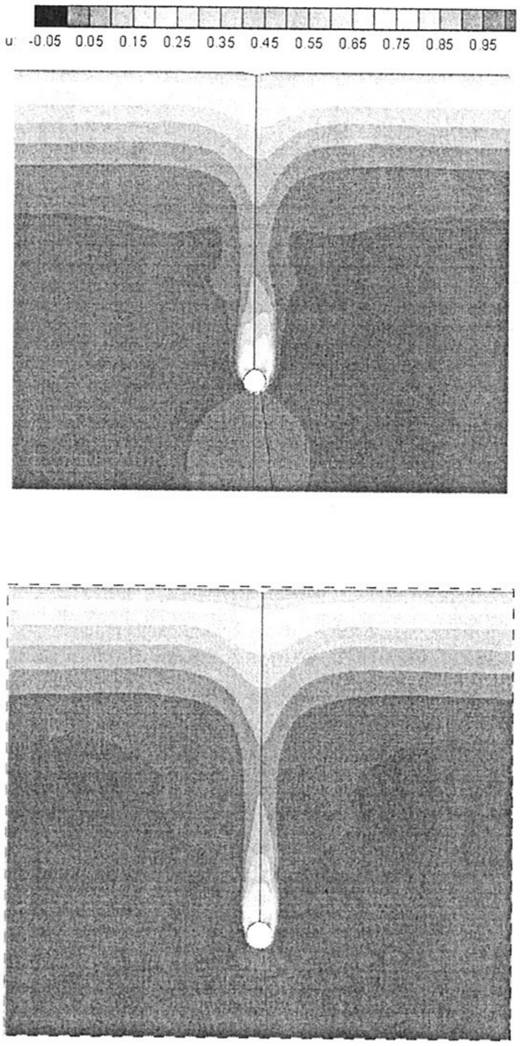

Figure 8: Computed longitudinal velocity on a relatively coarse grid (above) and a fine grid (below) for the same part of the domain as shown in Fig. 7.

4.1 Influence on the convergence behavior

In the single-domain computation we require GMRES to reduce the 2-norm of the residual with a factor of 0.05. When this same stopping criterion is also used in the 2-domain computation, the convergence behavior of the global iteration is much worse than in the single-domain computation. The systems of linear equations are twice as large, and GMRES has to compute the coupling between both domains. Therefore, in the 2-domain computation we use a more strict stopping criterion for the inner iteration: GMRES has to reduce the 2-norm of the residual with a factor 0.005. As a result, in each step of the global iteration, the number of GMRES iterations is approximately twice as much as in the single-domain computation. For the 2-domain computation on the relatively coarse grid, the wallclock time required on two SGI MIPS R12000 processors, working on 400 Mhz, for one step of the global iteration is 100 seconds. The single-domain computation requires 60 seconds for one step of the global iteration, using only one processor.

The convergence behavior of the global iteration for the relatively coarse grid is shown in Fig. 9. These pictures show the maximum (L_∞)-norm of the change in the pressure, eddy viscosity and longitudinal velocity between two consecutive steps of the global iteration. The other velocity components show a similar convergence behavior. Although the convergence behavior of the 2-domain computation is more irregular, the number of global iterations in both computations is comparable. The largest changes in the solution occur at the singularity behind the shaft and below the common $j = 1$-plane. In the rest of the computational domain, the changes between two consecutive iteration steps are significantly smaller. We like to point out that the more common L_2-norm of the residual would have suggested a much smoother convergence behavior, and that in most practical cases it is sufficient to get the maximum differences below 10^{-4}.

4.2 Influence on the computed solution

As mentioned before, we can expect deviations from a symmetric solution of the order of the discretisation error. Other differences between the two-domain computation and the single-domain computations are caused by the fact that in the neighbourhood of the common $j = 1$-plane not all discretised PDE's can be imposed. For example, only the momentum equation in normal direction is imposed. However, from numerical experiments it appears that at the first stations the computed results of the multi-domain version of PARNASSOS and

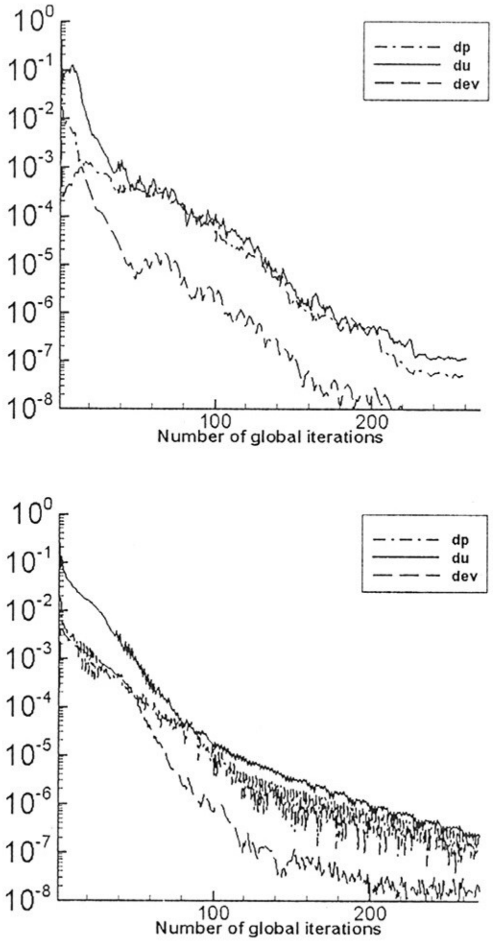

Figure 9: Maximum differences between two successive sweeps of the pressure, longitudinal velocity and eddy viscosity. Above: single domain. Below: two domains.

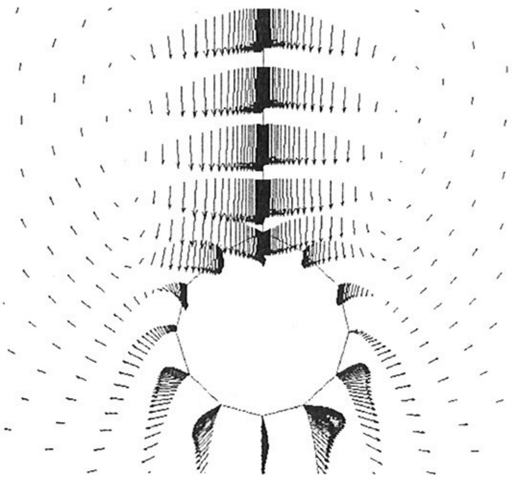

Figure 10: Transverse velocity vectors in the neighbourhood of the shaft. Left: multi-domain. Right: single-domain.

the single-domain version are very similar. Further downstream and near the shaft the deviations from symmetry tend to increase, which is illustrated by the results shown in Fig. 8.

Fig. 10 shows the transverse velocity vectors in the neighbourhood of the shaft, computed on the relatively coarse grid. These results are again shown for the station denoted by AB in Fig. 6. The left side is the solution of the left-most domain from the multi-domain version, the right-hand side the solution of the single-domain version of PARNASSOS. The differences become smaller when the grid is refined. This is demonstrated by Fig. 11, which shows the contour lines of the longitudinal velocity component from both the 2-domain and single-domain computations on both the relatively coarse grid and fine grid.

Acknowledgements

Part of the work presented in this paper has been performed within the EC funded Project FANTASTIC, G3RD-CT 2000-00096, a R&D project on 'Functional Design and Optimisation of Ship Hull Forms'. The Project Partners are FINCANTIERI, SIREHNA, FSG, IZAR, HSVA, TUB, NAPA, MARIN, FLOWTECH, SSPA, CHALMERS, CIMNE, SINTEF and CETENA.

The author wishes to thank M. Hoekstra and H.C. Raven for many stimulating discussions and numerous suggestions for improving the presentation of the paper.

References

[1] M. Hoekstra. *Numerical Simulation of Ship Stern Flows with a Space-Marching Navier-Stokes Method.* PhD thesis, Delft University, 1999.

[2] F.R. Menter. Eddy viscosity transport equations and their relation to the $k-\epsilon$ model. *J. of Fluids Eng.*, 119:876–884, 1997.

[3] Y. Saad and M.H. Schultz. A generalized minimal residual algorithm for solving nonsymmetric linear systems. *SIAM J. Sci. Statist. Comput.*, 7:856–869, 1986.

[4] A. van der Ploeg, L. Eça, and M. Hoekstra. Combining Accuracy and Efficiency with Robustness in Ship Stern Flow Computation. In *23rd Symposium on Naval Hydrodynamics*, september 2000.

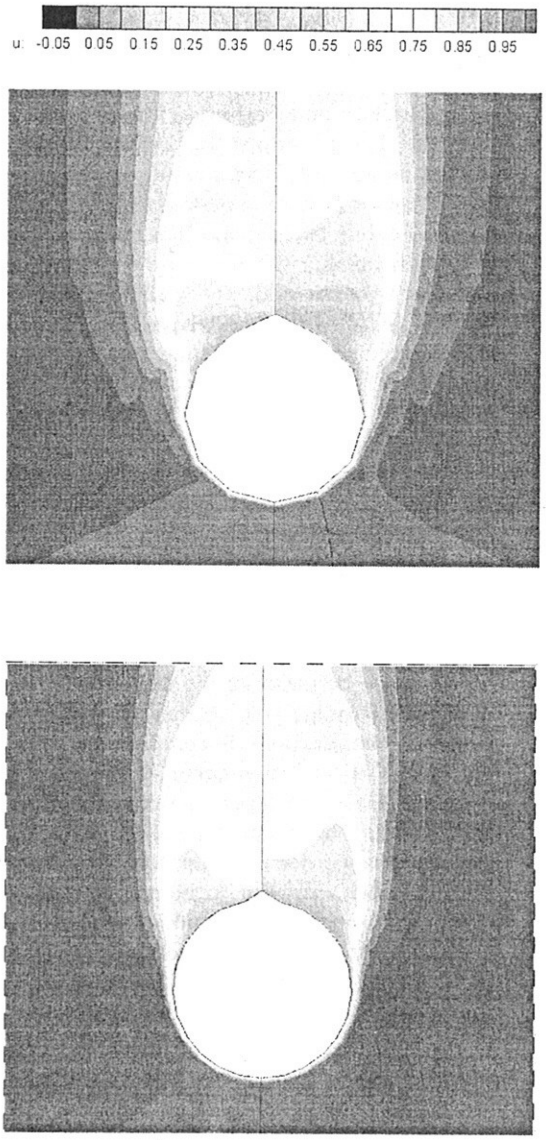

Figure 11: Contour lines of longitudinal velocity in the neighbourhood of the shaft. Left: multi-domain. Right: single-domain. Above: relatively coarse grid. Below: grid has been refined in all directions.

Verification of Navier-Stokes solutions - a study based on an analytical test case

Sofia Werner[1], Björn Regnström[2], Lars Larsson[3]

[1] Graduate Student, Dept. of Naval Architecture, Chalmers University of Technology, Sweden, sw@na.chalmers.se
[2] Flowtech International AB, Sweden
[3] Professor, Dept. of Naval Architecture, Chalmers University of Technology, Sweden

Abstract

Methods for numerical verification of CFD results are discussed and evaluated. The Richardson Extrapolation, the generalised RE described in the ITTC Quality Manual and a curve fitting approach are considered. The methods are applied to the results from an analytical test case. Conclusions about the suitability of the methods and their valid range are drawn.

1 Introduction

The use of CFD in practice requires methods for quantifying the error and uncertainty of the results. We distinguish between *verification* of the result (or the code), which concerns estimation of the numerical errors (iteration-, truncation- and round off errors), and *validation* of the same, which also deals with the modeling errors. This work investigates methods for verification of Navier-Stokes solutions.

In practice, the verification procedure may be carried out in different ways. Several alternative methods have been described and discussed in the literature over the last few years. The ITTC Resistance and Flow Committee has recently produced a Quality Manual [1] in order to establish a standard error quantification procedure for ship hydrodynamics. Those guidelines are based on an advanced version of the Richardson Extrapolation (RE) [6], as described by Stern.et.al. in [8]. There has been some discussion about the suitability of this method for verification work, for example by Eca and Hoekstra in [4]. In [5] and [2] they suggest an alternative approach based on a curve fitting method. The purpose of the current work is to study the mentioned verification methods by using an analytical test case: the flow field of a laminar flat plate boundary layer. The Navier-Stokes equations are applied to the flow field and the resulting residuals are compared with analytical results. The residuals are computed on a set of geometrically similar, uniform Cartesian grids with varying cell density. This approach enables us to isolate the spatial truncation errors from other possible numerical or modeling errors.

The investigated verification methods are based on the assumption that the analysed results are in the vicinity of this asymptotic range, where the higher order terms in the truncated series are negligible. By using the analytical test case we want to investigate the valid range and how the size of the higher order terms influence on the verification result.

2 Verification methods

Suppose that we have a number of results $\phi_{i,i=1..N}$ from numerical solutions of the Navier-Stokes equations on grids with grid sizes $h_{i,i=1..N}$. By replacing the continuous equations with discrete difference equations we have introduced an error corresponding to the truncated terms in the Taylor series. For a numerical method of formal order p_{th} this error equals

$$\delta_i = \phi_i - \phi_e = \sum_{j=p_{th}}^{\infty} \alpha_j h_i^j, \tag{1}$$

where ăϕ_e is the exact solution and α_i are real constants that are independent of h.

If all the terms in the sum (1) of higher order than p_{th} are negligible compared to the first term the solution is said to belong to the *asymptotic range*. The error can then be approximated as

$$\delta_i = \phi_i - \phi_e = \alpha h_i^p. \tag{2}$$

A verification procedure normally involves establishing of the order of accuracy p. As the grid size h decreases p should approach the theoretical order of accuracy p_{th} of the numerical method. The order of accuracy is used to compute an estimate of the numerical error, δ^*. The exact solution can be then assumed to belong to the interval

$$I = [\phi_1 - \delta^* + U_k; \phi_1 - \delta^* - U_k], \tag{3}$$

where U_k is the uncertainty of the error estimation and ϕ_1 is the solution from the finest grid.

Richardson Extrapolation

With the Richardson Extrapolation [6] the order of accuracy and the error estimate are found from the solutions from three grids with increasing cell sizes. From equation (2) the following expression can be derived:

$$\left(\frac{h_2}{h_1}\right)^p = \frac{\phi_3 - \phi_2}{\phi_2 - \phi_1} \cdot \frac{\left(\frac{h_2}{h_1}\right)^p - 1}{\left(\frac{h_3}{h_2}\right)^p - 1}. \tag{4}$$

The order of accuracy p is found by solving this equation iteratively. If the grid refinement ratios h_1/h_2 and h_2/h_3 are equal the explicit expression

$$p = \frac{\ln\left(\frac{\phi_3 - \phi_2}{\phi_2 - \phi_1}\right)}{\ln \frac{h_2}{h_1}} \tag{5}$$

may be used. The solution from the finest grid ϕ_1 can be corrected with the error estimate δ^* to receive the *extrapolated solution*,

$$\phi_0 = \phi_1 - \delta^*_{RE} \tag{6}$$

with

$$\delta^*_{RE} = \frac{\phi_2 - \phi_1}{\left(\frac{h_2}{h_1}\right)^p - 1}. \tag{7}$$

Roach [7] suggests the error estimation to be connected to a safety factor, so that the uncertainty of the error estimation is

$$U_k = F_s|\delta^*|. \tag{8}$$

Values between 1.25 and 3 are suggested for the safety factor.

The ITTC Quality Manual

For grids outside the asymptotic range, the higher order terms in (2) will affect the result of the Richardson Extrapolation. In the ITTC guidelines it is suggested that the higher order terms are accounted for by correcting the error estimate δ^*_{RE} with a correction factor C_k, such that the corrected error estimate is

$$\delta^*_c = C_k \cdot \delta^*_{RE} \tag{9}$$

with

$$C_k = \frac{\left(\frac{h_2}{h_1}\right)^p - 1}{\left(\frac{h_2}{h_1}\right)^{p_{th}} - 1}. \tag{10}$$

The extrapolated solution and the uncertainty is then

$$\phi_0 = \phi_1 - \delta^*_c \tag{11}$$

and

$$U_k = |(1 - C_k)||\delta^*_{RE}|. \tag{12}$$

If C_k is "sufficiently" close to 1 it has confidence, and δ^* , ϕ_0 and U_k can be estimated. Otherwise, only the uncertainty is estimated.

The ITTC guidelines recommend the explicit expression (5) for calculation of p. This expression requires that the grid refinement ratios h_1/h_2 and h_2/h_3 are equal. Ideally, a refinement ratio of 2 is recommended. For most applications this is not achievable, and therefore a refinement ratio of $\sqrt{2}$ can, according to the guidelines, be chosen instead.

The Curve Fit Method

Eca and Hoekstra deviate from the traditional use of Richardson Extrapolation for grid convergence studies. Instead, they calculate ϕ_0 and p by fitting the curve

$$\phi = \phi_0 + \alpha h^p \tag{13}$$

to the solutions $[h_i, \phi_i]_{i=1...N}$ by using the Least Square technique. This requires at least three grids, but it works with any number of grids $N \geq 3$. An advantage of this method over the ITTC method is that it does not put any restraints to the choice of grids. (Another advantage is that the method can average out any scatter originating from modeling errors, geometrically non-similar grids etc. Even though this is important for marine CFD application, it is irrelevant for the present test case and will not be considered here.) Eca and Hoekstra also approve of using a safety factor, similar to the one used by Roache, so that

$$\delta^* = \phi_1 - \phi_0 \tag{14}$$

and

$$U_k = F_s|\delta^*|. \tag{15}$$

The safety factor should be based on experience and common sense.

3 Discretisation and test case

For the evaluation of the described verification methods we use the results from a simple test case, the laminar boundary layer of a 2D flat plate. The flow field in the boundary layer can be described by Blasius equation

$$f'''(\eta) + \frac{1}{2}f(\eta)f''(\eta) = 0 \tag{16}$$

with $\eta = y\sqrt{\frac{U_0}{\nu x}}$. U_0 is the free stream velocity and ν the kinematic viscosity. This flow field is divergence free. Under the assumption that

$$\frac{\partial^2 u}{\partial x^2} << \nu\frac{\partial^2 u}{\partial y^2} \tag{17}$$

and the pressure is constant over x, it also satisfies the incompressible Navier-Stokes equations. If assumption (17) is *not* fulfilled, an application of the Navier-Stokes equations to the flow field will result in a residual:

$$u\frac{\partial u}{\partial x} + v\frac{\partial u}{\partial y} - \nu\left(\frac{\partial^2 u}{\partial y^2} + \frac{\partial^2 u}{\partial x^2}\right) = r. \tag{18}$$

By rewriting Blasius equation on x-y form,

$$u\frac{\partial u}{\partial x} + v\frac{\partial u}{\partial y} = \nu\frac{\partial^2 u}{\partial y^2}, \tag{19}$$

it is clear by inspection that the exact residual equals

$$r_e = \nu\frac{\partial^2 u}{\partial x^2}. \tag{20}$$

The difference between the computed residual r and the exact residual r_e constitutes the total numerical error:

$$E = r - r_e. \tag{21}$$

This error is evaluated at a point in the flow field that is a common grid point for all grids. The computational domain is l by l and it starts at a distance $20 * l$ behind the leading edge. The grids are rectangular, uniform Cartesian with cell sizes h reaching from $l/5$ to $l/100$. The test case is run for five different Reynolds numbers

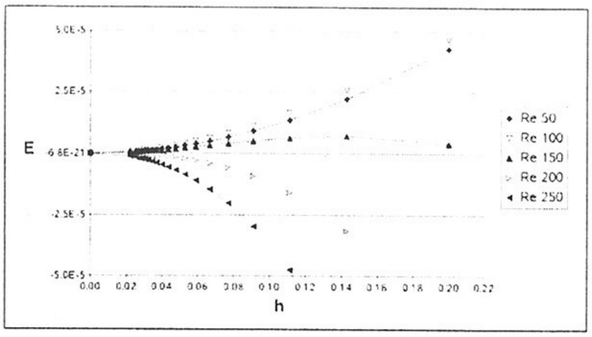

Figure 1: Test case results.

$Re = \frac{U_0 * l}{\nu}$.
The diffusive terms in the Navier-Stokes equations are discretised by a second order central difference scheme. The convective terms are interpolated by a third order upwind QUICK scheme. The resulting differences are second order. The total order of accuracy for both terms is hence second order.
Blasius equation is solved numerically with linear interpolation, where the steps size is smaller than 1/2000 of the smallest cell size. The results are shown in Figure 1.

4 Results

Order of accuracy with the ITTC method

In order to evaluate the verification method recommended by the ITTC Quality Manual the order of accuracy p was calculated for a number of grid triplets $[(h_1, \phi_1); (h_2, \phi_2); (h_3, \phi_3)]$. p was calculated with the recommended explicit expression (5). This expression requires that the two grid refinement ratios h_1/h_2 and h_2/h_3 are equal. Therefore, only the triplets that fulfilled

$$0.9 < \frac{h_1/h_2}{h_2/h_3} < 1.1 \tag{22}$$

were considered. Figure 2.a shows the resulting p for Re 250 plotted against the average cell size $h = (h_1 + h_2 + h_3)/3$ for each triplet. The plot for C_k has a similar appearance, since C_k depends on p. p is expected to approach 2 as the grid is refined. This is clearly not the case. Eca and Hoekstra found a similar unsystematic scatter in the prediction of p and C_k when they tested the ITTC method. This was one of the main reasons why they dismissed the method in [3].

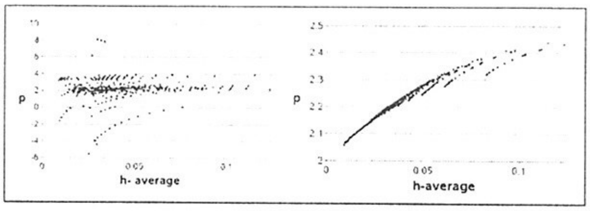

Figure 2: a) p by equation (5). b) p by equation (4)

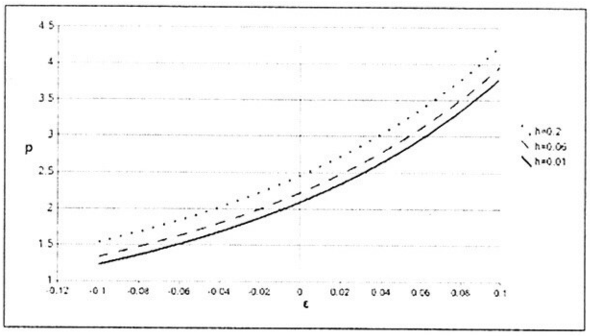

Figure 3: Influence of the disturbance ϵ on p.

On closer inspection we found that the scatter is caused by the violation of the requirement of equal grid refinement ratios. To clarify the importance of this requirement a sensitivity analysis was carried out. A typical convergence curve was represented by a polynomial $P = P(h)$ with known coefficients. The convergence data from the result of Re 250 was used as a template. In this way, the triplet members could be chosen arbitrarily. Three triplets with increasing average cell sizes were picked out. In each triplet, the finest grid was changed slightly so that the ratio between the refinement ratios were disturbed by a given amount ϵ:

$$\frac{h_1/h_2}{h_2/h_3} = 1 + \epsilon. \tag{23}$$

The polynomial was evaluated at the new values of $h_{1,2,3}$ and p was calculated. The result presented in Figure 3 shows that even a small deviation from the requirement results in a significant error in the predicted p .
We observe that for $\epsilon = 0$, i.e. when the refinement ratios are equal, p approach its theoretical value for decreasing average cell size h.
The initial refinement ratios h_1/h_2 and h_2/h_3 in this test were $1/\sqrt{2}$. For a larger refinement ratio the disturbance gets less significant and the sensitivity curves will flatten out. This explains the scatter in the observed p (Figure 2.a) and the results by Eca and Hoekstra. In both cases the analysed triplets had both varying amount of ϵ and varying refinement ratios. (Eca and Hoekstra also analysed triplets with refinement ratio ratio $\frac{h_1/h_2}{h_2/h_3}$ reaching from 0.9 to 1.1.)
The results show that care has to be taken when using this form of Richardson Extrapolation. For large complicated grids it might be difficult and time consuming to make sure that the requirement of equal refinement ratios is fulfilled in all directions. For small grids it might even be impossible. Take for example a grid of 20 cells and refine it twice with a ratio of $\sqrt{2}$. The necessity of an integer number of cells implies that the ratio $\frac{h_1/h_2}{h_2/h_3}$ equals 0.98, which can give a significant error in p.
It is worth mentioning that the general expression for p (equation 4) does not put any restraints to the grid refinement ratio. Figure 2.b shows p calculated with

this expression for the same triplets that gave the very scattered result in Figure 2.a. p smoothly approaches its theoretical value. However, this expression is never mentioned in the ITTC guidelines.

The ITTC correction factor

As described earlier, the ITTC guidelines suggest that the error estimate from the Richardson Extrapolation δ^*_{RE} (7) can be corrected by the correction factor C_k (10) to obtain an improved prediction of the extrapolated solution ϕ_0 (11). By introducing this correction the error estimate δ^*_c becomes a function of the two finest solutions and the theoretical order of accuracy only, (as was also pointed out in [5]). For a second order method, this corresponds to fitting the curve $\phi = \phi_0 + ah^2$ to the two finest data points, while using the original Richard Extrapolation is equivalent to fitting the curve $\phi = \phi_0 + ah^p$ to the three finest points. (The result of a traditional Richardson Extrapolation is always identical to the result of the Curve Fit method for 3 grids, provided that the iterative expression for p is used in the Richardson Extrapolation.) Naturally, the suggested correction approach works out if the observed order of accuracy p equals the theoretical one. If p deviates from p_{th} the higher order terms of the error equation cannot be neglected. Knowing that the data points then follow the curve $\phi = \phi_0 + a_2h^2 + a_3h^3 + a_4h^4 + ...$, and the higher order terms are not negligible, it is easy to realise that $\phi = \phi_0 + ah^p$ is a better approximation to this curve than $\phi = \phi_0 + ah^2$. The suggested correction approach is not in our opinion justified unless $p = p_{th}$. Figure 4 shows an example where the method fails. The residual error from the test case with Re 250 for three grids is analysed. By using the Richardson Extrapolation to estimate the extrapolated solution ϕ_0 we have improved the prediction compared to the result from the finest grid. (The exact result equals 0.) With the correction method the prediction is further away from the exact result than with the uncorrected method.

The correction factor C_k is also used to calculate the uncertainty U_k (12). In the given example the uncertainty interval for the corrected method is not acceptable.

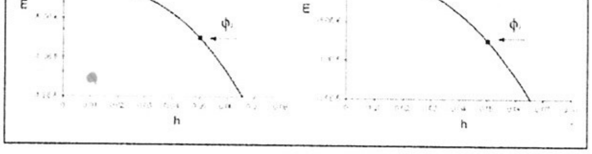

Figure 4: a) RE. B) corrected RE. (ITTC)

The effect of the higher order terms

All verification methods described here relate their valid range of grid sizes to the asymptotic range, which is normally defined as the range of cell sizes where the higher order terms in the error series (1) are negligible. In practice the size of the higher order terms is not known. It seems to be common practice to assume that the value of the observed p then indicates whether a set of solutions are close to the asymptotic range or not (e.g. [4], [8]). The following results seek to clarify the relation between the higher order terms and the observed order of accuracy p.

The described methods are based on the approximation of the entire error series (1) by the simple error equation (2). This is equivalent to approximating the curve $\varphi = \phi_e + ah^{p_{th}} + HOT$ with the curve $\phi = \phi_o + \alpha h^p$. If the higher order terms are significant p must deviate from p_{th} in order to approximate the original function φ. We suspect that there is a specific relationship between p and the relative size of HOT. In order to investigate this relationship a 6th degree polynomial was fitted to the simulation results. The 3rd order term was clearly dominant over the other higher order terms. To include 6 terms was therefore assumed to be sufficient for representing the full error series. Figure 5 shows the observed order of accuracy p plotted against the ratio between the higher order terms and the second order term. p is calculated by the Curve Fit method based on 3 grids close to each other. The terms in the polynomial are evaluated at the finest of those three. Each point in the graph represents one curve fit calculation. (Note that the Curve Fit method for three grids is equivalent to the normal Richardson Extrapolation. The behavior of the calculated p and ϕ_0 can be seen as an effect of assumption (2), and will be general for all methods based on this assumption.)

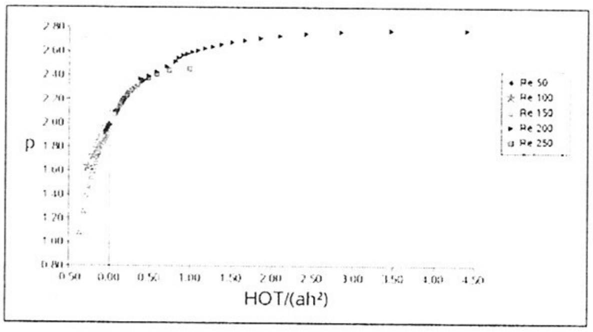

Figure 5: The effect of higher order terms on p.

The plot indicates that:

1. As the higher order terms approach zero the observe order of accuracy p approaches 2, as expected.
2. The higher order terms can be rather large. Even for a simple flow problem as the present test case the higher order terms can be in the same magnitude as the second order terms and even larger, even though the grids seem to be well resolved.
3. The influence of the higher order terms on p is not

symmetric about p_{th}

The next question is how those higher order terms influence the extrapolated solution ϕ_0. To help answering that we define the exact error factor C_e as the ratio between the exact error and the estimated error:

$$C_e = \frac{\delta_e}{\delta^*} = \frac{\phi_1 - \phi_e}{\phi_1 - \phi_0}, \tag{24}$$

where ϕ_1 is the solution from the finest grid. Figure 6 shows the calculated C_e plotted against p. Form this plot we can see that

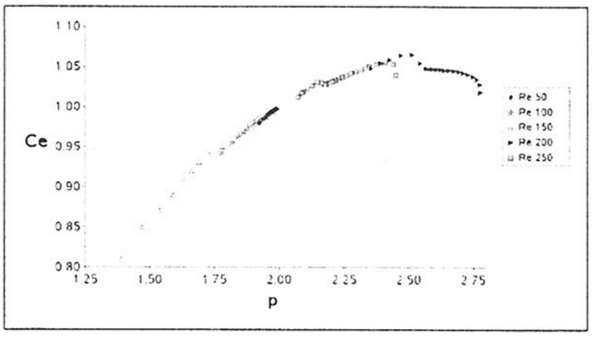

Figure 6: Exact error factor as function of p for results of the test case

1. The asymmetric behaviour is still present. When $p < p_{th}$ ϕ_0 is more sensitive to the higher order terms than when $p > p_{th}$.
2. The method is able to estimate the error well even when p deviates from p_{th}, especially for $p > p_{th}$. This indicates that the method, by adjusting p, take the higher order terms into account in an appropriate way.

The third-order-dominance range

In a certain range of grid sizes the $(p_{th}+1)^{th}$ order term in the error series (1) will dominate the higher order terms. We will denote this range the third-order-dominance range, since we in the current test case use a second order method. (The correct name would be the $(p_{th}+1)^{th}$-order-dominance range). In this range the analysed results can be assumed to lay on the curve $\varphi = \phi_e + ah^{p_{th}} + bh^{p_{th}+1}$. By using the normal Richardson extrapolation or the Curve Fit method, we try to approximate this curve with the curve $\phi = \phi_0 + \alpha h^p$. It can be shown that the resulting verification parameters depend on the sign of the coefficients a and b according to Table 1. Notice that the results from the test case presented in the Figure 5 and 6 display the same relations between the sign of $\frac{HOT}{(ah^{p_{th}})}$, p and C_e as the model polynomial φ does.

By using the information in Table 1 it is possible to formulate an uncertainty interval, to which the exact solution belongs for all 4 cases:

$$\phi_e \in [\phi_0 .. \phi_0 + (1 - C_s)\delta^*], \tag{25}$$

provided that

a	b	$\frac{HOT}{(ah^{p_{th}})}$	ϕ_0	ϕ_e	p	C_e
> 0	< 0	< 0	$< \phi_e$	$< \phi_1$	$< p_{th}$	< 1
< 0	< 0	> 0	$< \phi_e$	$> \phi_1$	$> p_{th}$	> 1
< 0	> 0	< 0	$> \phi_e$	$> \phi_1$	$< p_{th}$	< 1
> 0	> 0	> 0	$> \phi_e$	$< \phi_1$	$> p_{th}$	> 1

Table 1: Influence of a and b on verification parameters.

$$C_s < C_e \text{ when } p < p_{th},$$
$$C_s > C_e \text{ when } p > p_{th}.$$

(The factor C_s here plays the role of a safety factor. What value of C_s, fixed or variable, that should be chosen is not considered here.)

The direct implication of this is that we can make the uncertainty interval one sided and hence reduce the width of the interval by one half, provided that we know two things:

1. That the analysed solutions belong to the third-order-dominance range.
2. The value of p.

Beyond the valid range

Figure 7 illustrates what happens when the cell size h is increased beyond the range where the third order term is dominant. The polynomials representing the test data of Re 250, Re 200 and Re 100 have been evaluated for a wider range of cell sizes. We recognise the shape of the first part of the curves from Figure 6. At some point the third order term loses its dominance and the error factor C_e deteriorates rapidly. (The same behaviour has been observed for other test cases but those results will not be included here.) It is important to notice that the curve for each Reynolds number passes $p = 2$ twice. There is hence a risk that a calculation of p gives the value 2 and make us believe that the estimated error is zero, when it actually is large.

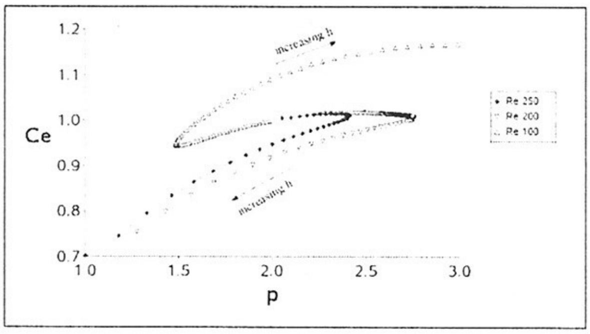

Figure 7: Exact error factor beyond the third-order-dominance range. Data from polynomial representing test data.

This demands a way of determining whether a set of solutions belong to third-order-dominance range or not. We can here use the fact that in this range, p is approaching monotonically p_{th} as the grid is refined, as shown in Figure 8. Each point in the graph represents one calculation involving three solutions. With two such calculations available, a linear extrapolation to $h = 0$ can indicate whether the solutions are inside the range or not. This would require at least 4 solutions. A larger number of solutions would of course increase the confidence in the ourcome.

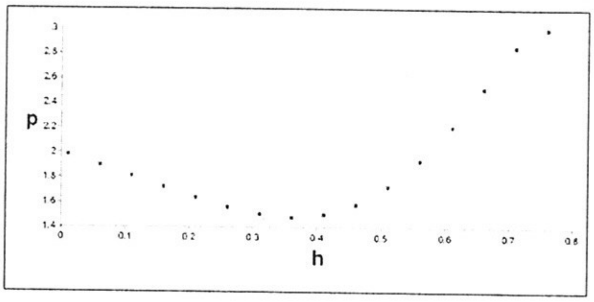

Figure 8: Order of accuracy p for polynomial representation of test data Re 250.

The ITTC uncertainty interval

We will now use the exact error factor C_e plotted in Figure 6 as a tool for considerations about the uncertainty interval recommended by the ITTC Quality Manual:

$$I = [\phi_0 + |(1 - C_k)||\delta^*|; \phi_0 - |(1 - C_k)||\delta^*|] . \quad (26)$$

The factor C_k depends on p as well as on the fraction h_2/h_1. Considering the observed relation between C_e and p, it seems appropriate to let the safety factor depend on p. In this way the interval can be more narrow than if a fixed safety factor is used. According to the results of the previous section, the exact solution ϕ_e belongs to the interval I if

$$\begin{array}{l} C_k < C_e \text{ when } p < p_{th} \\ C_k > C_e \text{ when } p > p_{th} \end{array}$$

provided that the grids are within the third-order-dominance range. Figure 9 shows an example where this is fulfilled. The polynomials representing the test data from Re 150 and Re 250 are evaluated with the Curve Fit method for three grids with equal refinement ratio $r = h_2/h_1 = h_3/h_2 = 1.3$. It can be seen that C_k varies with p in the same manner as the exact error factor C_e. However, C_k is also a function of the refinement ratio r. Figure 10 shows that the slope of the C_k curve increases with increasing r. As a comparison the exact error factor C_e is shown for the same refinements ratios r in Figure 11. Here the dependency of r goes the opposite way: the larger the r the smaller is the slope.

It is interesting to notice that if the fraction h_2/h_1 is inverted in the expression for C_k, the effect of increasing r will be more correctly modeled compared to the exact error factor C_e, at least for this test case. Figure 9 indicates that the uncertainty interval with the inverted r in C_k still would be safe, and that the interval would be more narrow.

Whether an uncertainty interval based on the factor C_k will always include the exact solution is still not proved. Before this has been validated, it seems to be safest to use a fixed safety factor set conservatively from experience and common sense, as recommended by Eca and Hoekstra in [4] and by Roach in [7].

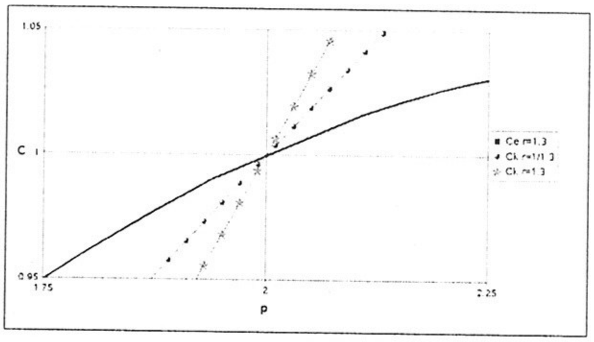

Figure 9: C_k and C_e for Re 150 and Re 250, $r = h_2/h_1 = 1.3$.

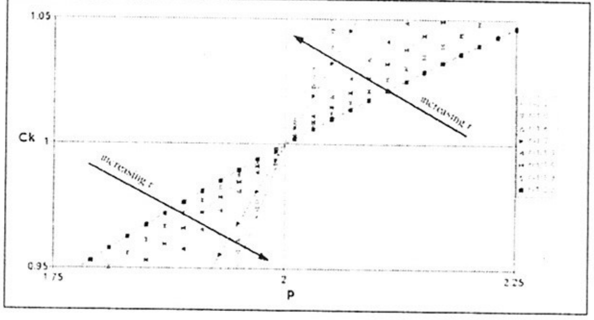

Figure 10: Influence of $r = h_2/h_1$ on C_k.

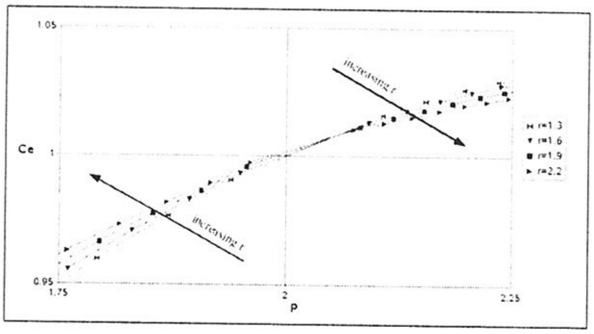

Figure 11: Influence of $r = h_2/h_1$ on C_e.

5 Conclusions

Three verification methods have been tested: the traditional Richardson Extrapolation, the generalised Richardson Extrapolation recommended in the ITTC Quality Manual and the Curve Fit method by Eca and Hoekstra. The three methods are based on the same approximation of the truncation errors.

The following conclusions can be drawn about the ITTC method:

- If the order of accuracy p is calculated the way the Quality Manual recommend, the two grid refinement ratios must be equal. In practice it can be troublesome or even impossible to fulfill this requirement to such an extent that is does not influence on the result.
- By using an implicit expression for the calculation of p the requirement of the grid refinement ratios is removed. There is no reasons not to use this expressions instead of the presently recommended one.
- The proposed use of a correction factor to improve the estimation of the extrapolated solution can not be justified from a theoretical point of view. The method has been shown to deteriorate the error estimate in a practical example.
- The recommended uncertainty interval depends on the grid refinement ratio in a way that does not model the error behaviour of the current test case well. By inverting the grid refinement ratio included in the expression for C_k a better model is obtained. Whether this the interval will always embrace the exact solution has not been verified.

The valid range of the tested verification methods is normaly related to the so called *asymptotic range.* With the present results three ranges that relate to the validity of the methods can be formulated:

The asymptotic range, where
- all higher order terms are negligible.
- p equals (or are very close to) p_{th}.
- ϕ_0 equals (or are very close to) the exact solution

The third-order-dominance range, where
- the $(p_{th}+1)^{th}$ order term (third order terms for a second order method) dominates the higher order terms.
- p approaches monotonically p_{th} as the grid size is decreased.
- $C_e > 1$ when $p > p_{th}$ and $C_e < 1$ when $p < p_{th}$.

Beyond the valid range, where
- the $(p_{th}+1)^{th}$ order term does not dominate the other higher order terms.
- p may approach or equal p_{th} even though the error estimate is incorrect.

We further conclude that
- For the current test case the influence of the higher order terms on the error estimate is smaller for $p > p_{th}$ than for $p < p_{th}$, provided that the third order term dominates the higher order terms. The implication of this is that a smaller safety factor can be used for $p > p_{th}$ than for $p < p_{th}$. Whether this is generally true still needs to be confirmed.
- A set of solutions can be believed to belong to the third-order-dominance range if it can be verified that p approaches p_{th} as the grid size h tends to zero. This requires **at least four grids**.
- If a set of solutions can be verified to belong to the third-order-dominance range the uncertainty interval can be halved, compared to the interval that is normally related to the described verification methods.

6 Discussion

The conclusions above are based on a simple, well behaved model problem. Whether the conclusions will have relevance for practical verification problems still needs to be investigated. With reservation for this, some words can be said about the suitability of the investigated verification methods.

The ITTC Quality Manual need to be revised.

The original Richardson Extrapolation is identical to the Curve Fit approach, when the latter is applied on three grids only. Including extra (coarser) grids will only serve to decrease the accuracy of the extrapolated solution. For a simple flow problem there is hence no reason to favour one of them to the other. They both seem to manage the task in an appropriate way.

For complicated flow problems the convergence curve may be afflicted with a large amount of scatter originating from turbulence models, flow limiters, boundary conditions, non-similar grids etc. In those cases the Curve Fit method might be favourable, since it is able to find the convergence parameters from an "average convergence curve". However, nothing prevents us from fitting a curve, with any kind of curve fitting method, to the simulation data and perform the Richardson Extrapolation *on* the fitted curve. In case of scatter it would also be appropriate to use a extra safety factor based on the amount of scatter and the number of simulations included. How these two methods and the new safety factor would work in practice will be an issue of future research.

References

[1] 22nd International Towing Tank Conference. *ITTC - Quality Manual*, 1999.

[2] Hoekstra M. Eca L. On the numerical verification of ship stern flow. In *1st MARNET-CFD Workshop Barcelona*, 1999.

[3] Hoekstra M Eca L. *An Evaluation of Verification Procedures for Computational Fluid Dynamics*. IST Report D72-7, 2000.

[4] Eca L. Hoekstra M. An example of error qualification of ship-related cfd results. In *7th Numerical Ship Hydrodynamic Conference Nantes*, 1999.

[5] Eca L. Hoekstra M. On the application of verification procedures in computational fluid dynamics. In *2nd MARNET-CFD Meeting Copenhagen*, 2000.

[6] Richardson LF. The deferred approach to the limit. *Trans. R. Soc. London*, 226:229–361, 1927.

[7] Roache P.J. Quantification of uncertainty in computational fluid dynamics. *Annu. Rev. Fluid. Mech.*, 29:123–160, 1997.

[8] Coleman H.W. Stern F., Wilson R.V. *Verification and Validation of CFD Simulations*. Iowa Institute of Hydraulic Research, College of Engingeering, The University of Iowa, Iowa city, Iowa, USA, 1999.

NuTTS'02
Fifth Numerical Towing Tank Symposium
1 September - 1 October, Pornichet, France

An Approach to Ship Maneuvering by Simultaneous Computation of Viscous Flow and Ship Motion

Yan Xing and Gerhard Jensen
Fluid Dynamics and Ship Theory Section
Technical University of Hamburg-Harburg
Lämmersieth 90, D-22305 Hamburg, Germany
email: yan.xing@tu-harburg.de, g.jensen@tu-harburg.de

Ibrahim Hadžić and Milovan Perić
Computational Dynamics, CD adapco Group
Dürrenhofstraße 4, D-90402 Nürnberg, Germany
email: i.hadzic@cd-germany.de, m.peric@cd-germany.de

keyword: floating body, viscous flow, ship maneuvering

Abstract

A finite-volume method for simultaneous computation of viscous free-surface flows and flow-induced motion of rigid bodies is presented. The RANS equations of fluid flow are solved using a commercial CFD package "Comet", which can employ moving grids made of arbitrary polyhedral cells and allows sliding interfaces between fixed and moving grid blocks. The computation of the six degrees of freedom of the floating body motion is coupled to the CFD code via its user-coding interface. The method is used to compute the motion of floating bodies in two dimensional cases as well as three dimensional applications and the results are compared to available experimental data, showing favorable agreement. Simulation of the flow-induced motion of a self-propelled ship during maneuvering operations is intended using the present method. The rudder is modeled geometrically and arbitrary rudder angles can be set up using the technique of sliding interfaces; the propeller is simulated by applying a body force distributed to a layer of finite-volume cells in the propeller plane. The preliminary results of this on-going work are presented.

1 Introduction

In ship and ocean engineering interaction between fluid flow and solid bodies is of crucial importance in many branches of applications, such as ship seakeeping and maneuvering. For ship maneuvering, the interaction plays a vital role concerning safety and functionality.

Numerical methods for fluid flow are well developed. The surface forces acting on the solid bodies can be easily integrated from solid boundaries of the fluid domain; it is true even if the boundaries are changing their shapes and positions in time as long as they are prescribed at each time step. On the other hand, the motion of the rigid bodies can be easily computed by solving its governing equations of motion when the forces acting on them are known.

To couple these two procedures is not so simple since such a computation has to allow the travel of information in both directions (the flow-induced forces control the body position and the body position affects the flow reversely). The computational grid has to be automatically adapted to the body motion since the body surfaces are part of the fluid domain boundaries. The time step has to be small not only for predicting the motion in time accurately but also for the stability and convergence of the coupled algorithm. Underrelaxation is usually necessary for both fluid flow and motion of rigid bodies.

For application in ship maneuvers, these issues are undoubtedly important because the geometry of a ship with its appendices becomes rather complicated and also attention has to be paid to automatic adaptation of the grid and simultaneous maintenance of the grid quality. In this paper, we present one approach which is suitable for this purpose. The numerical method for the free-surface flow simulation and a description for the computation of the body motion will be briefly introduced together with the coupled scheme. The method for adaptation of the grids to the body motion will be explained. The method is intended to be applied to the simulation of ship maneuvering in the future. Some results of elementary steps will be presented here. First, computations with a RoRo vessel with forward speed in head waves are compared to experimental data, showing satisfactory agreement (for computation of motion of two dimensional bodies subjected to large waves, see [4]). Then, the simulation of rudder and propeller is briefly discussed.

2 Coupled Computation of Fluid Flow and Body Motion

The finite volume method incorporated in the "Comet" code is used here to simulate incompressible viscous flows with free surface. The conservation equations for mass, momentum, and scalar quantities (e.g. energy or chemical species) are solved in their integral from. When the grid is moving, the so-called *space conservation law* (SCL) has to be satisfied. Interface-capturing method and High-Resolution Interface Capturing (HRIC) [1] scheme have been used to simulate the free-surface effects. In addition to the conservation equations for mass and momentum, a transport equation for void fraction of the liquid phase c has been introduced. Due to the limit of space, these basic equations will not be introduced here; for more detail, see [1-3].

The motion of rigid body is computed using standard rigid body dynamics, which will not be repeated here. As described before, the forces and moments acting on a floating body are obtained from the flow. However, the flow itself is influenced by body motion and both problems have to be considered simultaneously. For the prediction of body motion, a predictor-corrector method which can be easily coupled with the iterative procedure for flow prediction (SIMPLE-algorithm) has been used here.

Each of the body velocity components can be written in the following form:

$$\frac{\mathrm{dv}}{\mathrm{d}t} = \frac{f}{\mathrm{m}_B}, \quad \mathrm{v}_n = \mathrm{v}_{n-1} + \frac{1}{\mathrm{m}_B} \int_t f \, \mathrm{d}t \, . \tag{1}$$

This equation is integrated in time using the trapezoidal rule (corresponding to the second-order Crank-Nicolson scheme for flow computation), so that an estimate of the solution at time t_n is computed as:

$$\mathrm{v}_n = \mathrm{v}_{n-1} + \frac{1}{\mathrm{m}_B} \frac{\mathrm{f}_{n-1} + \mathrm{f}_n}{2} \Delta t = \mathrm{v}_{n-1} + \frac{1}{\mathrm{m}_B} [\mathrm{f}_{n-1} + \frac{\mathrm{f}_n - \mathrm{f}_{n-1}}{2}] \Delta t \, . \tag{2}$$

Note that f_n in Eq. (2) depends on the flow solution; so it is not known a priori. In the iterative solution method used here, at the m^{th} outer iteration on the new time level, the value from the previous outer iteration is used. The displacements of the body are computed in a similar manner:

$$\mathrm{r}_n = \mathrm{r}_{n-1} + \mathrm{v}_{n-1}\Delta t + \frac{\mathrm{f}_{n-1}}{\mathrm{m}_B}\frac{\Delta t^2}{2} + \frac{\mathrm{f}_n - \mathrm{f}_{n-1}}{\mathrm{m}_B}\frac{\Delta t^2}{6} \ . \tag{3}$$

The analogous procedure is also applied to compute the angular motion.
The above approach has been found appropriate and easy to implement. Also it is of the same order as the method used to compute the fluid flow and fits well within the overall iteration scheme.

The coupled computation of flow and body motion consists of the following steps:

1. Provide the initial values for the dependent variables (at the time t_0).
2. Advance the time by Δt and, if the grid moves due to the prescribed motion of the boundary, determine the location of CV vertices at time $\mathrm{t}_m+\Delta t$.
3. Assemble and solve by an iterative solver the linearized algebraic equations for the velocity components in turn, employing the currently available other dependent variables.
4. Assemble and solve the algebraic equations for the pressure correction and correct mass fluxes, velocity components, and pressure.
5. Assemble and solve the algebraic equations for volume fraction c and use the calculated values to update the properties of the effective fluid, such as density and viscosity etc.
6. Assemble and solve the algebraic equations for turbulent kinetic energy k and its dissipation rate ϵ and obtain turbulent diffusion coefficients.
7. Integrate the pressure and shear forces over body surface, solve the equations of motion for the floating body (velocity and displacement) using the predictor-corrector method described above, and adapt the grid to the new position of the body if moving-grid is used.
8. Calculate the current estimate of volumes ΔV_j swept by each face over the last time step. This completes one outer iteration.
9. Return to Step 3 and repeat until the sum of the absolute residuals for all equations has fallen by a prescribed number of orders of magnitude.
10. Return to step 2 and repeat until the prescribed number of time steps is completed.

3 Grid Adaptation to Body Motion

Two techniques have been used to adapt the grid to the body motion:

1. The part of grid around the body is moved with it, the distant grid is kept fixed, and the grid between these two regions is deformed, while keeping its topology the same. An example is shown in Fig. 1 (a). This method is suitable when the body motion is not so large that the grid in the deformed region gets too distorted.
2. The grid around the body is overlapped with the background grid, where the overlapping grid is moved together with the body and neither block of grid is deformed, as shown in Fig. 1 (b). Interpolation of the variables is required between these two blocks to ensure that the solution in the overlapping region is consistent on both grids. This approach is suitable for arbitrary motion and geometry of the body, but it is also expensive since it demands high computational effort.

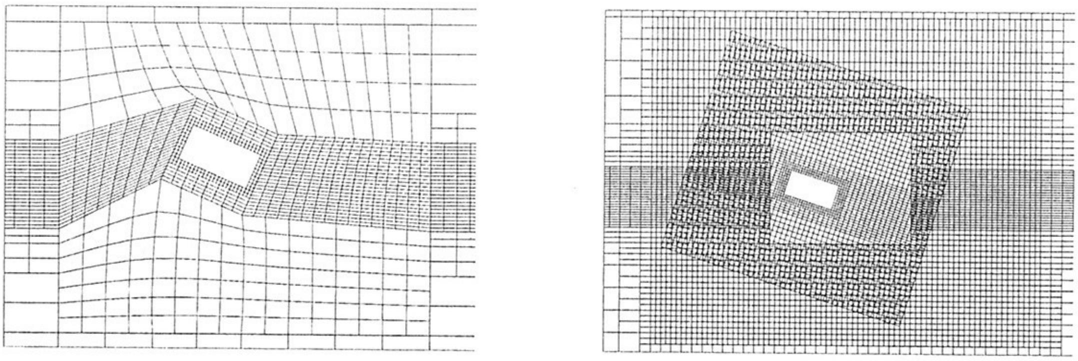
(a) deformation of the grid around the body (b) overlapping grid

Fig. 1: Adaptation of the grid to body motion.

4 Results and Discussion

4.1 RoRo vessel in head waves

The RoRo vessel designed by Flensburg Schiffbau-Gesellschaft (FSG) has been selected as one of the test models to check the accuracy and reliability of the present method. Results are compared to the experiments conducted in HSVA within the framework of Roll-S project.

The ship model has a length of 5.364 m between perpendiculars and a breadth of 0.765 m; the model scale is 1/34. The self-propelled ship model runs with a speed of 1.6 m/s ($F_n = 0.22$) and keeps its straight course in an incoming regular wave with 4.0 m wave length and 0.15 m wave height. The numerical simulation has been set up in a similar way as the model test. The heave and pitch motion are set free. Roll motion has been kept fixed in the simulation since in this case the ship is running in head waves and the wave frequency is still far from the resonance frequency of the ship for roll motion. Therefore the roll motion is not expected to be significant, which has been proved by the experimental measurement.

The computed wave patterns at two time instants are shown as a top view in Fig. 2. As can be observed, the spread angle of the wave crests at the ship bow is about $2 \cdot 19.5$ degree, which coincides with the analytical prediction of the steady wave system due to forward speed of the ship. This indicates the computed wave system is actually the superposition of this steady wave system and the unsteady wave system due to incoming waves and resulting ship motion. Results of ship's heave and pitch motions in time history are compared to the experimental data. As shown in Fig. 3, the agreement is satisfactory.

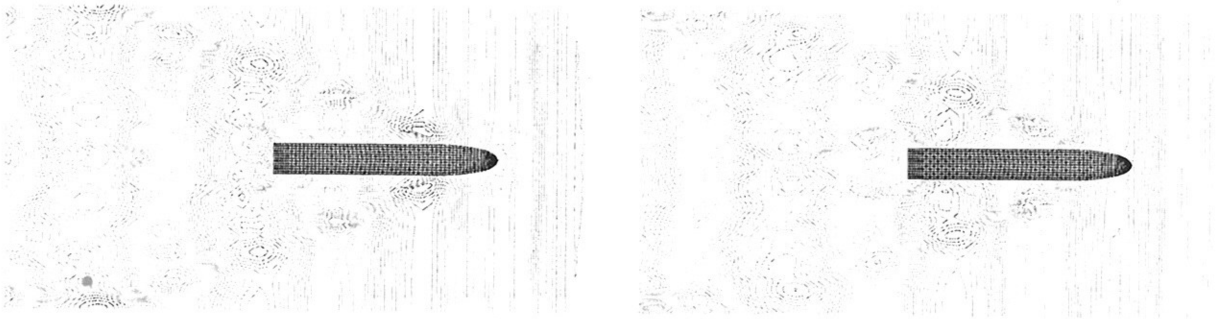
(a) time = 9.75 s (b) time = 10.20s

Fig. 2 Wave pattern of ship running with forward speed ($F_n = 0.22$) in head waves.

4.2 Computation of propeller and rudder

To simulate ship maneuvering with operating rudder, rudder and propeller have to be modeled in addition to the ship hull. The rudder of the RoRo vessel has the HSVA-73 profile, it has been modeled geometrically and computed in free stream condition first. The computed force coefficients

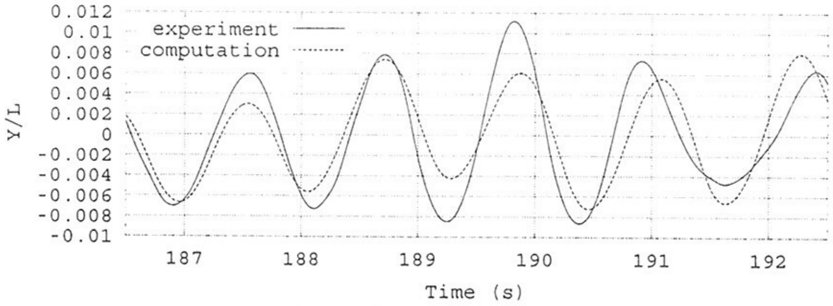

(a) heave motion

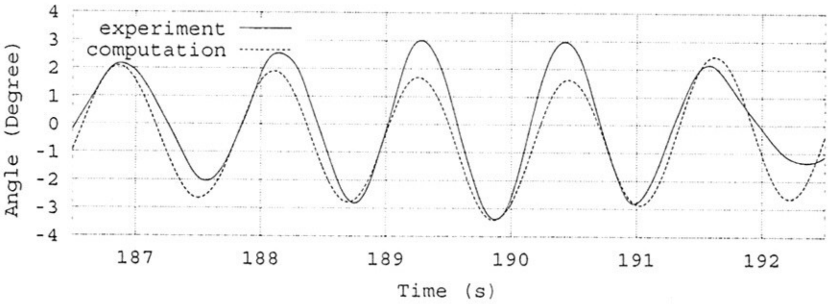

(b) pitch motion

Fig. 3: Time history of the RoRo ship motion in waves.

are plotted in Fig. 4. The propeller has been simulated by a body force distribution according to analytical prediction [5]. Computation has been conducted for the rudder in propeller slipstream, where the propeller is located at 60% of rudder length before the rudder. The comparison of the computed rudder forces inside slipstream and in free stream is shown in Fig. 5. As one can see, the rudder lift force in slipstream is about 1.5 times larger than in free stream (the thrust loading coefficient C_{Th} is 1.94). The pressure distribution on the rudder and the velocity vectors at the planes before and behind the rudder are plotted in Fig. 6.

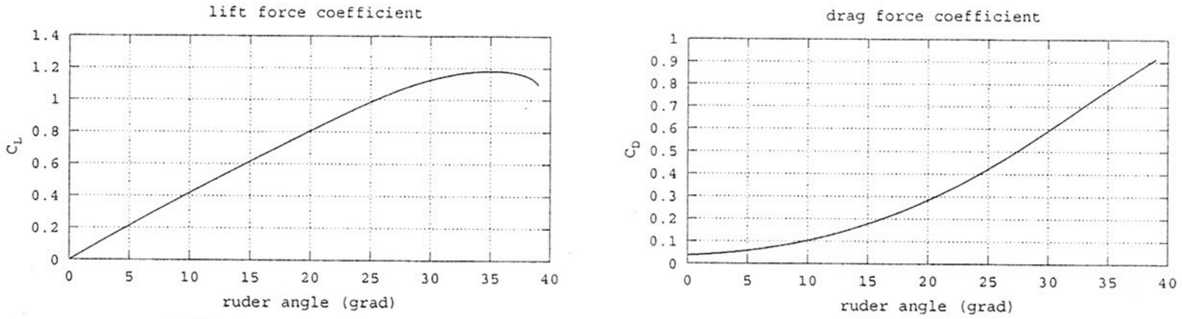

(a) lift force coefficient (b) drag froce coefficient

Figure 4: computed force coefficients for ruder in three-dimensional flow.

5 Conclusions

Finite volume method has been used to compute the viscous fluid flow with free surface. The standard body dynamics has been taken to compute the motion of the body under flow-induced forces. A coupled method has been developed to capture the interaction between fluid flow and solid bodies in time domain. Favorable agreement has been shown for a RoRo vessel running with forward speed in incoming regular waves. The interaction of propeller and rudder has been computed with body-force modeled propeller and geometrically modeled rudder. All results demonstrate the

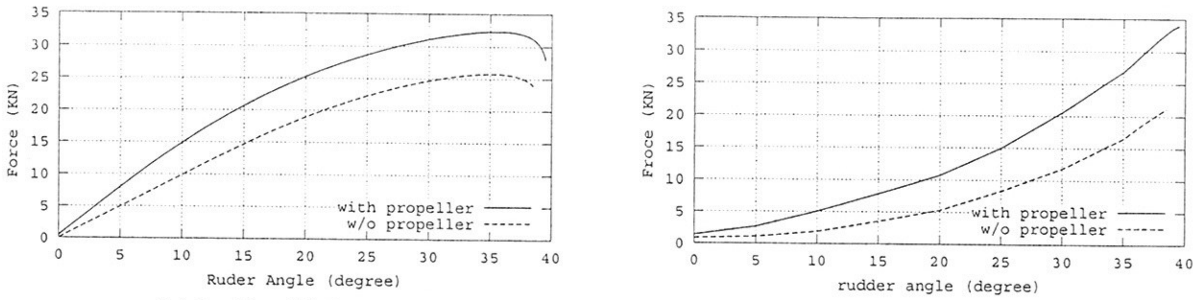

(a) Rudder lift force (b) Rudder drag force

Fig. 5: Rudder forces in propeller slipstream (C_{Th} = 1.94) and in free stream

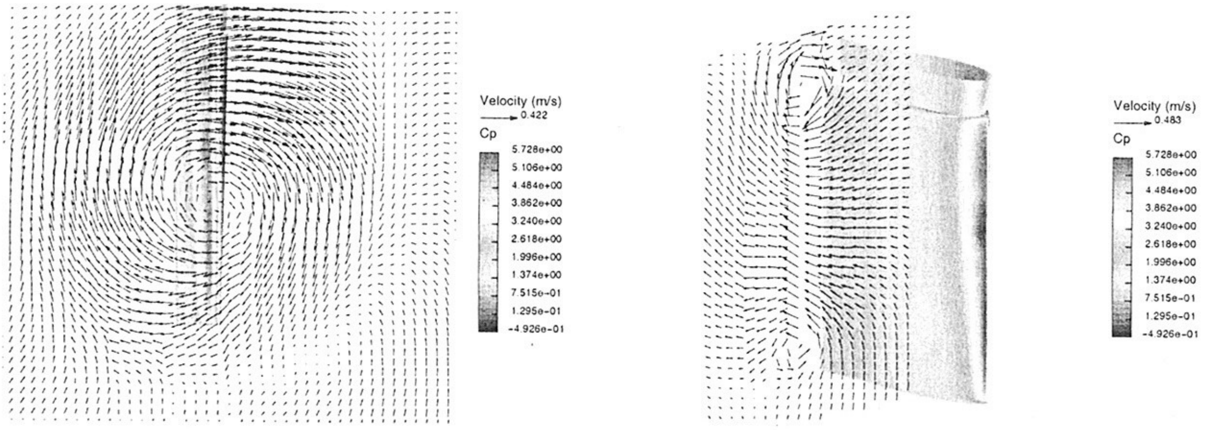

(a) velocity at 30% of rudder length in front of rudder (b) velocity at 30% of rudder length behind rudder

Fig. 6: Pressure distribution on rudder and velocity vectors at two planes in front of and behind rudder.

accuracy and applicability of the present method for the application in ship maneuvering. These elementary steps are important for such a simulation of ship maneuvering, which will be conducted in near future.

References

[1] Muzaferija S. and Perić M. Computation of free surface flow using interface-tracking and interface-capturing methods, Chap. 2 in O. Mahrenholtz and M. Markiewicz (eds.), Nonlinear Water Wave Interaction, pp. 59-100, WIT Press, Southampton, 1999.

[2] Demirdžić I. and Muzaferija S. Numerical method for coupled fluid flow, heat transfer and stress analysis using unstructured moving meshes with cells of arbitrary topology, Comput. Methods Appl. Mech. Eng., vol. 125, pp. 235-255, 1995.

[3] Demirdžić I., Muzaferija S. and Perić, M. Computation of turbulent flows in complex geometries, chap.7̃ in G. Tzabiras et al. (eds.), Calculation of Complex Turbulent Flows, pp2̃49-299, WIT press, Southampton, 2000.

[4] Hadzic I., Muzaferija S., Peric M. and Xing Y. Numerical Simulation of Interaction of a Floating Body and a Free-Surface Flow with Waves, Fifth World Congress on Computational Mechanics, Vienna/Austria, 2002.

[5] Stern F., Kim H.T., Patel V.C. and Chen H.C. A viscous-flow approach to the computation of propeller-hull interaction, Journal of Ship Research, vol. 32, no. 4, pp. 246-262, 1988.

6th Numerical Towing Tank Symposium (NuTTS'03)

Rome, Italy, 29 September - 1 October 2003
Sponsored by INSEAN

Topics:

- Nonlinear flows around marine structures (LES, RANSE, Euler with or w/o free surface)
- Free-surface flows around marine structures (3-d seakeeping, free-surface viscous flows)
- Related topics (validation experiments, numerical techniques, grid generation, etc)

Deadlines:	Early feedback:	15 July 2003
	Abstracts received:	**15 August 2003**
	Notification of acceptance:	22 August 2003
	Last possible update:	15 September 2003

You are invited to participate in the above event. The objective of the event is to provide a forum for informal discussions among experts in the field and to disseminate latest results. Younger workers and Ph.D. students are especially encouraged to participate. The event will be held at INSEAN (Sala Leonardo), with participants staying at Casa Domitilla in Rome. All participants stay and have meals together to maximize interaction and discussion.

The extended abstracts of the proposed talk will be directly reproduced in the proceedings. Work in progress, encountered problems, etc. should be discussed in an open, informal atmosphere (no ties!) among colleagues. The first page of the extended abstract should be headed with the title and authors' names and address (incl. email) in a compact form to economize on space. Extended abstracts are limited to 6 pages in a field 17cm by 25cm per page.

An early reply will help us in organizing the event better. For the early feedback, a tentative title or topic will suffice. An initial abstract may be as short as several lines.

Following the tradition of previous NuTTS events, the fees will be kept low to allow a maximum number of scientists to attend. The fees including accommodation (4 nights starting from Saturday) and meals during the symposium will be:

500/400/250 EUR for regular participants/for authors/for students incl. PhD candidates

<u>Early registration is vital</u> as reserved rooms at Casa Domitilla are limited.

Volker Bertram, bertram@waves.insean.it
Maurizio Landrini, maulan@waves.insean.it